A STUDY OF FOCUSSED ION BEAM PATTERNED THIN MAGNETIC FILMS WITH SOFT X-RAY AND MAGNETO-OPTICAL MICROSCOPY

PAUL COOK

Materials & Physics Research Centre
School of Computing, Science and Engineering
University of Salford, Salford, UK

Submitted in Partial Fulfilment of the Requirements of the Degree of Doctor of Philosophy, February 2010

CONTENTS

TABLES AND ILLUSTRATIONS

ACKNOWLEDGEMENTS

I would like to take this opportunity to express my sincere gratitude to all of the people who have helped make this research possible, and to those who have supported me throughout my studies.

Firstly, I would like to thank my supervisor Dr. Tiehan Shen, whose enthusiasm first inspired me as an undergraduate to begin this work. His support and guidance over the last few years have been unwavering. For that I am extremely grateful.

Special thanks are given to Prof. Phil Grundy for his help with TEM analysis, his support and time spent proof reading this thesis. I would like to extend my thanks to Dr. Grenville Jones, whose critical reading and comments have also been greatly appreciated.

I wish to express my appreciation to Dr. Simon Morton, Dr. David Kilcoyne, Dr. Mi-Young Im and Dr. Peter Fischer at the Advanced Light Source, Berkeley, for their valuable contributions to the X-ray microscopy work. I would especially like to thank Simon and David, who spent a considerable amount of their time helping me during my visits to Berkeley.

Thank you to Kerry Abrams for development of the TEM micrographs, Dr. Geoff Hill at the University of Sheffield for assistance with UV photolithography, Dr. Wei Guan for conducting EDX measurements and Geoff Parr for assistance with Lorentz Microscopy.

I have had the great pleasure of working with some wonderful colleagues over the last few years. Dr. Wuxia Li, Dr. Jamie Thompson, Dr. Wei Guan, Dr. Lang Qin, Dr. Ning Wang, have not only assisted with their helpful discussions but their friendship has been most highly valued.

Thank you to my family and friends. To Stephanie, whose friendship I have relied upon and treasured over the last three years, and to my parents and brothers for their unconditional support, without which, none of this would have been possible.

Finally, this work was largely funded by the EPSRC. Additional funding also been provided by the Institute of Physics through the C. R. Barber Trust, CMMP Division and Nanoscale Physics & Technology Group. I would also like to thank the Pro-Vice-Chancellor (Research) of Salford University for providing the special travel grant.

ABBREVIATIONS

BPM	Bit-Patterned Media
CB	Circular Birefringence
CCD	Charge-Coupled Device
CD	Circular Dichroism
CP	Circularly Polarised
D-MOKE	Diffracted Magneto-Optical Kerr Effect
EDX	Energy Dispersive X-Ray Spectroscopy
EP	Elliptically Polarised
***e*-ray**	Extraordinary Ray
EXAFS	Extended X-Ray Absorption Fine Structure
FIB	Focussed Ion Beam
FWHM	Full-Width-Half-Maximum
GMR	Giant Magnetoresistance
LB	Linear Birefringence
LD	Linear Dichroism
LMIS	Liquid Metal Ion Source
LP	Linearly Polarised
MCB	Magnetic Circular Birefringence
MCD	Magnetic Circular Dichroism
MFM	Magnetic Force Microscopy
MLB	Magnetic Linear Dichroism
MOKE	Magneto-Optical Kerr Effect
MRAM	Magnetic Random Access Memory
MTXM	Magnetic Transmission X-Ray Microscope
OA	Optic Axis
OD	Optical Density
***o*-ray**	Ordinary Ray
OSA	Order Selection Aperture
PEM	Photoelastic Modulator
SAD	Selected Area Diffraction
SEM	Scanning Electron Microscope
SEMPA	Scanning Electron Microscopy with Polarisation Analysis
SIM	Scanning Ion Microscopy
Si-PIN	Silicon photodiode with a p-type/intrinsic/n-type structure
SPLEEM	Spin-Polarised Low-Energy Electron Microscopy
SRIM	The Stopping and Range of Ions in Matter
STEM	Scanning Transmission Electron Microscope
STXM	Scanning Transmission X-Ray Microscope
TEM	Transmission Electron Microscope
TMR	Tunnel Magnetoresistance
TRIM	Transport of Ions in Matter
XANES	X-Ray Absorption Near Edge Structure
XAS	X-Ray Absorption Spectroscopy
XMCD	X-Ray Magnetic Circular Dichroism
XMLD	X-Ray Magnetic Linear Dichroism
X-PEEM	X-Ray Photoemission Electron Microscopy
ZP	Zone-Plate

ABSTRACT

Until the last few years, focussed ion beam systems were primarily used within the semiconductor industry as tools for modifying prototype integrated circuits, but owing to the development of commercial systems and the concomitant reduction in costs, they are rapidly becoming more popular within academic institutions for research purposes. This work investigates the potential application of the focussed ion beam to the study of patterned magnetic media, which is an area of increasing interest as new methods of extending the performance limits of current magnetic storage media are sought. The effects of quasi-homogeneous Ga ion implantation and micro-machining on the structural properties and magnetic behaviour of thin Fe films have been studied by various microscopy techniques. Doses on the order of 8×10^{15} ions cm^{-2} were found to induce structural changes in the polycrystalline microstructure, but the ferromagnetic properties were found to be reasonably resistant to ion implantation. The formation of magnetic domains within patterned arrays of simple geometric shapes was studied using magnetic transmission X-ray microscopy and X-ray magnetic circular dichroism. Hysteresis properties of the patterns were determined by magneto-optical measurements using a specially designed dual photoelastic modulator-based polarimeter. A detailed description of the polarimeter is given along with a new calibration method, which improved the accuracy of the measurement system in comparison to a more conventional approach.

CHAPTER 1 Introduction

1.1 *Nanoscale Magnetism*

Magnetism has been studied for centuries, maybe even millennia. The oldest references to magnetic materials originate from ancient Greece and China as far back as the 6th century BCE[1.1], although it was not until the 19th century that real progress in understanding the origin of magnetism began. In 1820, Hans Christian Ørsted became the first to realise the link between magnetism and electricity. His initial experiments were shortly followed by a formulation of the electromagnetic phenomenon by André-Marie Ampère[1.1], who also made a prediction that magnetism in matter occurs as a result of circular electric currents on a microscopic scale[1.1, 2] Astonishingly, he proposed this before the discovery of electrons which we now know to be responsible for the magnetic moments[1.1, 3] of atoms. In 1907 Pierre-Ernest Weiss predicted that a local ordering of the magnetic moments takes place via a "molecular force", which leads to the spontaneous magnetisation of ferromagnetic materials[1.1, 3]. Weiss also postulated that the moments were aligned such that the material was magnetised to the saturation value in localised regions but the direction of the magnetisation could vary from one area of the material to the next[1.1, 3]. This was a crucial step in understanding the behaviour of ferromagnetic materials, since it explained how they could exhibit any degree of average magnetisation, from zero up to the saturation level. These areas of differing magnetisation are now known as "domains".

The formation and mechanics of magnetic domains within a material of restricted physical geometry, particularly on the sub-micron and nano scales[1.4-19], is currently of great interest for various applications, especially the development of magnetism-based memory devices[1.20]. If the dimensions of a material are reduced to a scale comparable with the width of a domain wall (i.e. the transitional region from one domain to the next), it will contain just a single domain[1.4]. There may be a preferential direction along which the magnetisation in this domain lies, which will be determined by the physical boundaries of the material. A certain amount of energy is required to change the direction of the magnetisation, which is usually

supplied by an external magnetic field, or if the magnetic particle is reduced to just a few nanometres, then thermal energy may be sufficient to randomise the magnetic moments. In this latter case, the magnetisation will become unstable and may fluctuate randomly. The point at which this occurs is known as the superparamagnetic limit and is of major concern in the magnetic storage industry[1.21-23].

In conventional magnetic storage devices, data is written to a nanocrystalline magnetic layer (CoCrPt), with each data bit spanning several tens of crystallites (also called grains) approximately 10 nm in size[1.21]. The grains are effectively isolated from one another by the non-magnetic grain boundaries, thus behave as isolated single domain elements. As the data bits become smaller, in order that an acceptable signal-to-noise ratio is maintained, the grain size must also decrease, and therein lies the problem. The grains cannot be reduced significantly otherwise the data would eventually degrade as thermal energy causes random fluctuation of the magnetisation in the individual grains[1.21]. Considering the rate at which areal densities are currently increasing (30-50 % per year)[1.22], the superparamagnetic limit will be reached within a few years, perhaps as soon as 2012[1.23]. If the magnetic data-storage industry is to continue to grow, new technologies must be developed.

The rapid increase in storage density has been attributed to a series of developments within the last 20 years. The giant magnetoresistance effect (GMR) discovered simultaneously by Albert Fert and Peter Grünberg in 1988, was the crucial breakthrough that allowed these developments to occur[1.24]. Ten years after the discovery of GMR, IBM released the first commercial hard disk drive that made use of the effect. The read-head within the drive contained a spin-valve[1.25] which made it much more sensitive to the stray magnetic fields created by the data bits on the disk, and allowed them to be reduced in size, increasing the capacity of the media to 2.69 Gbits/in^2. GMR read-heads became the industry standard and further increases in capacity followed. The longitudinal media used, however, had density limits of around 100 Gbits/in^2 [1.26, 27]. Since the magnetisation of each bit lay in the plane of the media, neighbouring bits were strongly coupled. In 2005, Toshiba began the industry-wide transition from longitudinal[1.23, 27] to perpendicular recording where the bits were magnetised out-of-plane. This allowed them to be packed closer together, pushing the areal density up to 133 Gbits/in^2. In 2006 Seagate improved read-head technology and introduced the first commercial hard disk drive that used the tunnel magnetoresistance (TMR) effect, and predicted it would allow areal densities beyond 300 Gbits/in^2 to be achieved[1.28]. This was

indeed true and at the time of writing, the capacity currently available is around 400 Gbits/in^2. It is thought that current perpendicular storage media may be pushed to around 1 Tbit/in^2 [1.22, 27], but in order to surpass this limit, amongst other options[1.22], the development of bit-patterned media (BPM)[1.22, 23, 29-32] has been proposed. This involves patterning the disk surface with discrete single-domain magnetic elements which each represent a single data bit. Although the idea has been considered since the 1990s, there are still several technical aspects that need addressing in order to realise BPM with densities of 1 Tbit/in^2 and beyond[1.30]. The bit-pitch is likely to be on the order of 25 nm[1.30] at most, which is already approaching the limits of current lithography and imaging techniques.

Although the hard disk drive industry is probably the main driving force behind current research into nano-scale magnetism, there is also a desire to develop a better understanding of the seemingly random nature of domain wall formation and propagation. When magnetic elements are reduced down to the micron scale, shape anisotropy begins to dominate the magnetic behaviour[1.4], which consequently becomes more predictable as the physical boundaries begin to limit the number of possible domain states. Therefore, by controlling the element shape it is possible to have some control over the domain formation. For example, stable vortex and so-called "onion state" domain formations have been observed in nanoscale ring structures[1.13]. The onion-state occurs where the ring splits into two domains, with the two halves magnetised in opposite senses. Separating the two domains are 180° domain walls, which may be reliably manipulated or trapped at lateral constrictions (notches) cut into the edges of the ring. These domain wall traps have also been created in long, thin magnetic wires[1.16, 33-37]. The position of the domain walls can be easily moved by application of a magnetic field or by electrical current injection[1.37]. Combined with high resolution magnetic imaging techniques, these structures allow studies of domain wall mechanics on the nanometre scale, the results of which may be of importance for emerging technologies such as magnetoresistive random access memory (MRAM)[1.20, 38]

There are various lithography techniques that may be used to fabricate nano-scale magnetic structures[1.5], although unfortunately none of which are currently capable of producing BPM with the required bit-density on a commercial scale. UV lithography as used in the semiconductor industry requires advanced techniques to achieve a resolution that is more easily obtained with electron beam (e-beam) lithography, which is on the order of 5-20 nm depending on the approach[1.5, 30]. Currently this resolution limit appears to be determined by

the resist technology not the e-beam itself[1.30], therefore this technique is the most likely candidate to be developed for the commercial production of BPM[1.30].

Researching magnetism on a scale of tens or hundreds of nanometres, however, does not require such high demands on the lithography technique, allowing some of the alternative approaches[1.5] to be used. One such alternative is focussed ion beam (FIB) lithography[1.39-42]. It is a "top-down" technique analogous to e-beam lithography, but uses ions to irradiate the sample instead of electrons. Since ions have much greater mass, the implantation process itself is enough to modify the material structure without the need for resists and lift-off procedures (although resists are also used in some cases). Using FIB milling, a direct transfer of a pattern from design to substrate is possible without the need for mask fabrication or additional processing steps. This is sometimes referred to as a "direct-write" process. It may considerably speed up the fabrication of small-scale patterns, making it ideal for device prototyping. The resolution of the process is on the order of several tens of nanometres so is not likely to be a candidate for commercial use, but it can be used quite successfully to create nanoscale magnetic elements[1.43] or even produce bit-patterned media on a small experimental scale[1.44].

The study of nanoscale elements has only been made possible by the development of magnetic imaging techniques such as Lorentz microscopy[1.45], magnetic force microscopy (MFM)[1.46] and more recently, various forms of X-ray microscopy[1.47, 48] Despite being a lower resolution technique, the convenience of magneto-optical microscopy (or Kerr microscopy as it is also known)[1.49, 50] means that it is still a widely used and important imaging method. However, it often only provides normalised quantitative information, where the images are normalised to a saturated state, making direct comparison between samples difficult. If combined with Stokes polarimetry, as will be described in later chapters, a true quantitative analysis of a sample is possible. By reducing the wavelength of the light down to the soft X-ray regime, not only is it possible to achieve a higher spatial resolution, but also as a result of core-level electron excitations, a quantitative, element specific analysis of magnetic materials is possible using the X-ray magnetic circular dichroism effect[1.48]. This makes X-ray microscopy probably one of the most powerful tools for the study of magnetic materials.

1.2 *Outline of the Thesis*

This work is primarily a study of FIB-patterned ferromagnetic thin films and the modifications to their structural and magnetic properties as a result of the energetic ion-target interactions, sputtering effects and Ga implantation. There is also a second aspect to the work that involves the exploration of two analysis techniques, namely, magnetic transmission X-ray microscopy (MTXM) and magneto-optical Stokes polarimetry.

Firstly, the focussed ion beam instrument is introduced in Chapter 2, where some of its applications as a general purpose micro-machining tool are discussed. The discussion then focuses on some of the mechanisms that are known to occur during ion irradiation of magnetic materials and ways in which they have been used to control their magnetic behaviour.

Chapter 3 then describes some of the fundamental concepts behind the analysis techniques used in this work. Those are: transmission electron microscopy, the magneto-optical phenomena, and X-ray absorption and microscopy.

Chapter 4 then expands on the optical aspects and introduces the concept of Stokes polarimetry using photoelastic modulators. The construction of a magneto-optical microscope with a dual-photoelastic modulator-based polarimeter is described in detail. While the microscope does not provide domain images in the way a conventional magneto-optical (or Kerr) microscope would (although this would be possible), it analyses the polarisation state of a magnified image of the sample to provide a quantitative measure of the average magnetisation. In order to achieve this, the polarimeter had to be calibrated. A comparison of polarimeter calibration methods was performed, including a new approach, which in principle allows for a more accurate determination of the Stokes parameters.

Many of the ion irradiation studies to date have focussed on materials with magnetic properties that are very sensitive to stoichiometry, crystal structure or interfacial properties. Some report a reduction in coercivity after ion irradiation while others, an increase. In Chapter 5 the focus is placed on simple single-layer Fe films, and to a lesser extent, Ni/Fe bi-layers. Although such materials are not at the forefront of magnetic media research, studying

a 3*d* ferromagnetic material allows the process of Ga ion implantation to be studied more effectively without the added complications encountered with more complex magnetic systems.

In Chapter 6, MTXM is explored as a domain imaging tool. Thanks to the high resolution capabilities of the microscope used (XM-1), domains can be seen within small magnetic elements less than 500 nm in size. These observations are used to interpret irregular hysteresis loops generated by magneto-optical measurements on arrays of such elements.

Since the FIB also has ability to deposit electrically conductive materials, there is the potential to fabricate prototype magnetoresistive devices almost entirely from scratch. However, the process of deposition involves the application of very high ion doses. For magnetoresistive applications, such contacts would have to be placed on top of the magnetic layer, which may be adversely affected as a result. A preliminary exploration of this issue is presented in Chapter 7.

Finally, Chapter 8 summarises the findings and discusses some additional work that may form an extension to that presented here.

References

1.1 E. du Trémolet de Lacheisserie, "Magnetism, from the dawn of civilization to today," in *Magnetism: Fundamentals*, E. du Trémolet de Lacheisserie, D. Gignoux and M. Schlenker, Eds. New York: Springer, 2005, pp. 3-18.

1.2 J. R. Hofmann, *André-Marie Ampère*. New York: Cambridge University Press, 1995.

1.3 A. Aharoni, *Theory of Ferromagnetism*, 2nd ed. New York: Oxford University Press, 2000.

1.4 C. L. Dennis, R. P. Borges, L. D. Buda, U. Ebels, J. F. Gregg, M. Hehn, E. Jouguelet, K. Ounadjela, I. Petej, I. L. Prejbeanu and M. J. Thornton, Journal of Physics-Condensed Matter **14** (49), R1175-R1262 (2002).

1.5 J. I. Martín, J. Nogués, K. Liu, J. L. Vicent and I. K. Schuller, Journal of Magnetism and Magnetic Materials **256** (1-3), 449-501 (2003).

1.6 T. Schrefl, J. Fidler, K. J. Kirk and J. N. Chapman, Journal of Magnetism and Magnetic Materials **175** (1-2), 193-204 (1997).

1.7 J. Fidler, T. Schrefl, V. D. Tsiantos, W. Scholz and D. Suess, Computational Materials Science **24** (1-2), 163-174 (2002).

1.8 W. Scholz, D. Suess, T. Schrefl and J. Fidler, Journal of Applied Physics **91** (10), 7047-7049 (2002).

1.9 S. B. Choe, Y. Acremann, A. Scholl, A. Bauer, A. Doran, J. Stöhr and H. A. Padmore, Science **304** (5669), 420-422 (2004).

1.10 M. Kläui, C. A. F. Vaz, J. A. C. Bland, W. Wernsdorfer, G. Faini, E. Cambril, L. J. Heyderman, F. Nolting and U. Rüdiger, Physical Review Letters **94** (10), 4 (2005).

1.11 C. Brownlie, S. McVitie, J. N. Chapman and C. D. W. Wilkinson, Journal of Applied Physics **100** (3), 9 (2006).

1.12 S. Bance, T. Schrefl, G. Hrkac, D. Suess, C. Brownlie, S. McVitie, J. N. Chapman and D. A. Allwood, IEEE Transactions on Magnetics **42** (10), 2966-2968 (2006).

1.13 C. A. F. Vaz, T. J. Hayward, J. Llandro, F. Schackert, D. Morecroft, J. A. C. Bland, M. Kläui, M. Laufenberg, D. Backes, U. Rüdiger, F. J. Castano, C. A. Ross, L. J. Heyderman, F. Nolting, A. Locatelli, G. Faini, S. Cherifi and W. Wernsdorfer, Journal of Physics-Condensed Matter **19** (25) (2007).

1.14 G. Meier, M. Bolte, U. Merkt, B. Krüger and D. Pfannkuche, Journal of Magnetism and Magnetic Materials **316** (2), E966-E968 (2007).

1.15 C. C. Wang, J. Wang, A. O. Adeyeye and N. Singh, Journal of Magnetism and Magnetic Materials **320** (11), 1781-1786 (2008).

1.16 T. Komine, I. Murakami, T. Nagayama and R. Sugita, IEEE Transactions on Magnetics **44** (11), 2516-2518 (2008).

1.17 O. A. Tretiakov, D. Clarke, G. W. Chern, Y. B. Bazaliy and O. Tchernyshyov, Physical Review Letters **100** (12) (2008).

1.18 H. T. Zeng, D. Read, D. Petit, A. V. Jausovec, L. O'Brien, E. R. Lewis and R. P. Cowburn, Applied Physics Letters **94** (10), 3 (2009).

1.19 M. T. Bryan, P. W. Fry, P. J. Fischer and D. A. Allwood, Journal of Applied Physics **103** (7) (2008).

1.20 X. C. Zhu and J. G. Zhu, IEEE Transactions on Magnetics **39** (5), 2854-2856 (2003).

1.21 H. J. Richter, Journal of Magnetism and Magnetic Materials **321** (6), 467-476 (2009).

1.22 Y. Shiroishi, K. Fukuda, I. Tagawa, H. Iwasaki, S. Takenoiri, H. Tanaka, H. Mutoh and N. Yoshikawa, IEEE Transactions on Magnetics **45** (10), 3816-3822 (2009).

1.23 S. N. Piramanayagam and K. Srinivasan, Journal of Magnetism and Magnetic Materials **321** (6), 485-494 (2009).

1.24 A. Fert and P. Grünberg, Physics Today **60** (12), 12-14 (2007).

1.25 B. Dieny, Journal of Magnetism and Magnetic Materials **136** (3), 335-359 (1994).

1.26 H. N. Bertram and M. Williams, IEEE Transactions on Magnetics **36** (1), 4-9 (2000)

1.27 M. H. Kryder and R. W. Gustafson, Journal of Magnetism and Magnetic Materials **287**, 449-458 (2005).

1.28 S. N. Mao, Y. H. Chen, F. Liu, X. F. Chen, B. Xu, P. L. Lu, M. Patwari, H. W. Xi, C. Chang, B. Miller, D. Menard, B. Pant, J. Loven, K. Duxstad, S. P. Li, Z. Y. Zhang, A. Johnston, R. Lamberton, M. Gubbins, T. McLaughlin, J. Gadbois, J. Ding, B. Cross, S. Xue and P. Ryan, IEEE Transactions on Magnetics **42** (2), 97-102 (2006).

1.29 H. J. Richter, A. Y. Dobin, O. Heinonen, K. Z. Gao, R. J. M. Van der Veerdonk, R. T. Lynch, J. Xue, D. Weller, P. Asselin, M. F. Erden and R. M. Brockie, IEEE Transactions on Magnetics **42** (10), 2255-2260 (2006).

1.30 A. Kikitsu, Journal of Magnetism and Magnetic Materials **321** (6), 526-530 (2009).

1.31 C. A. Ross, H. I. Smith, T. Savas, M. Schattenburg, M. Farhoud, M. Hwang, M. Walsh, M. C. Abraham and R. J. Ram, Journal of Vacuum Science & Technology B **17** (6), 3168-3176 (1999).

1.32 E. Chunsheng, D. Smith and J. Wolfe, Journal of Applied Physics **98** (2), 024505 (2005).

1.33 M. Kläui, C. A. F. Vaz, J. Rothman, J. A. C. Bland, W. Wernsdorfer, G. Faini and E. Cambril, Physical Review Letters **90** (9), 4 (2003).

1.34 M. Kläui, C. A. F. Vaz, A. Lapicki, T. Suzuki, Z. Cui and J. A. C. Bland, Microelectronic Engineering **73-74**, 785-789 (2004).

1.35 A. Olziersky, A. Vilà, M. Rubio-Roy, E. Bertran and J. Fontcuberta, Microelectronic Engineering **86** (4-6), 878-881 (2009).

1.36 M. Y. Im, L. Bocklage, P. Fischer and G. Meier, Physical Review Letters **102** (14), 4 (2009).

1.37 Y. Jang, S. Yoon, K. Lee, S. Lee, C. Nam and B. K. Cho, Nanotechnology **20** (12), 4 (2009).

1.38 S. Tehrani, J. M. Slaughter, E. Chen, M. Durlam, J. Shi and M. DeHerrera, IEEE Transactions on Magnetics **35** (5), 2814-2819 (1999).

1.39 K. Gamo, Semiconductor Science and Technology **8** (6), 1118-1123 (1993).

1.40 S. Nagamachi, M. Ueda and J. Ishikawa, Journal of Vacuum Science & Technology B **16** (4), 2515-2521 (1998).

1.41 K. Arshak, M. Mihov, S. Nakahara, A. Arshak and D. McDonagh, Journal of Vacuum Science & Technology B **22** (6), 3016-3020 (2004).

1.42 A. A. Tseng, Small **1** (10), 924-939 (2005).

1.43 G. Xiong, D. A. Allwood, M. D. Cooke and R. P. Cowburn, Applied Physics Letters **79** (21), 3461-3463 (2001).

1.44 C. T. Rettner, IEEE transactions on magnetics **37** (4), 1649-1651 (2001).

1.45 M. S. Cohen, IEEE Transactions on Magnetics **MAG1** (3), 156-167 (1965).

1.46 A. Yacoot and L. Koenders, Journal of Physics D-Applied Physics **41** (10), 46 (2008).

1.47 J. Stöhr and S. Anders, IBM Journal of Research and Development **44** (4), 535-551 (2000).

1.48 P. Fischer, D. H. Kim, W. L. Chao, J. A. Liddle, E. H. Anderson and D. T. Attwood, Materials Today **9** (1-2), 26-33 (2006).

1.49 P. Kasiraj, R. M. Shelby, J. S. Best and D. E. Horne, IEEE Transactions on Magnetics **22** (5), 837-839 (1986).

1.50 F. Schmidt and A. Hubert, Journal of Magnetism and Magnetic Materials **61** (3), 307-320 (1986).

CHAPTER 2 Introduction to Focussed Ion Beams and Magnetic Patterning

2.1 *Focussed Ion Beam Techniques*

Development of focussed ion beam (FIB) systems began in the 1970s, with a desire to emulate the capabilities of transmission electron microscopes using a beam of ions[2.1, 2]. The idea was to make use of the stronger interactions that take place between fast ions and matter to achieve contrast mechanisms not readily seen in electron microscopy[2.1]. FIBs eventually became the ion beam counterpart of scanning electron microscopes. The greater mass of the ions means that a FIB can be used for micro-machining as well as imaging. Furthermore, it is also possible to deposit metallic and semiconducting materials by ion-induced decomposition of chemical precursors. This ability to remove and deposit material resulted in the extensive use of FIBs within the semiconductor industry, where they are ideally suited to defect analysis, integrated circuit rewiring and lithography mask repair[2.3-7]. The last 10 years or so have seen the development of commercial FIB systems[2.7], which has resulted in increased popularity amongst academic institutes and use across a wide range of research disciplines. As a lithography tool, the resolution obtainable is not quite as high as that possible with e-beam lithography, being on the order of a few tens of nanometres. However, the direct-write nature is highly convenient since it offers a simpler, quicker approach to lithography on a scale of tens to hundreds of microns. In addition, it is also possible to pattern non-planar surfaces comparatively easily.

2.1.1 Principles of Operation

A focussed ion beam, in terms of operation, is very similar to a scanning electron microscope (SEM). As can be seen from Fig. 2.1.1, the two systems have many common features. In the FIB ions are generated by a liquid metal ion source (LMIS) situated at the top of the optical column, then accelerated and focussed by the column optics to a small spot upon the sample surface. A schematic diagram of a LMIS is shown in Fig. 2.1.2. It consists of a needle, usually made of tungsten, which protrudes from a ceramic reservoir containing the metal. When heated by an element coiled around the outside of the reservoir, the melted metal flows

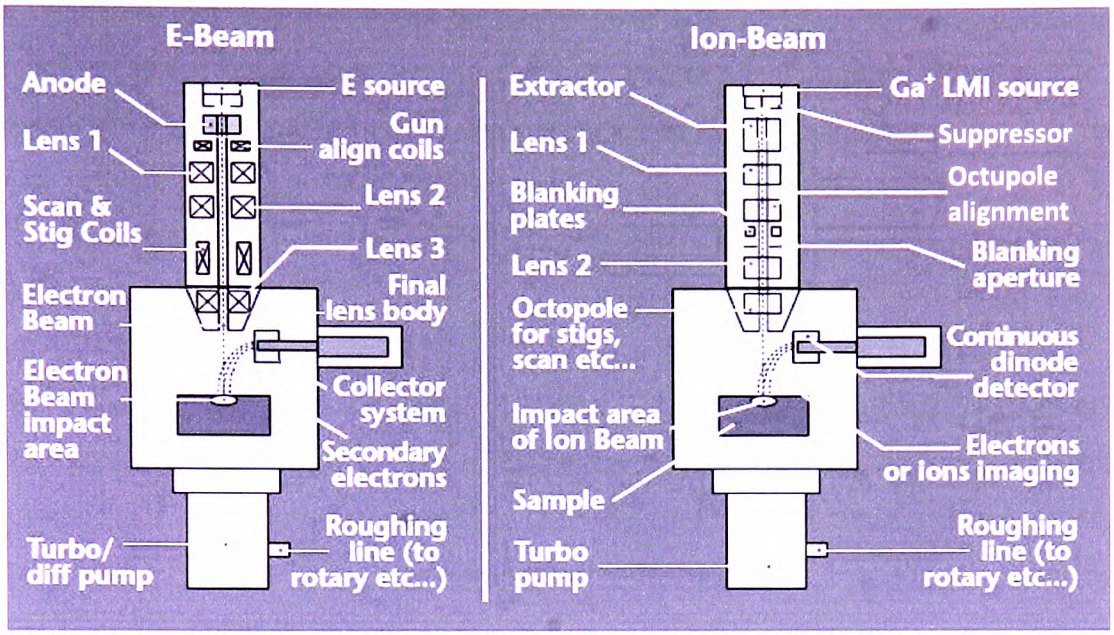

Figure 2.1.1 - Comparison between SEM and FIB column optics. Cited from Ref. (2.7).

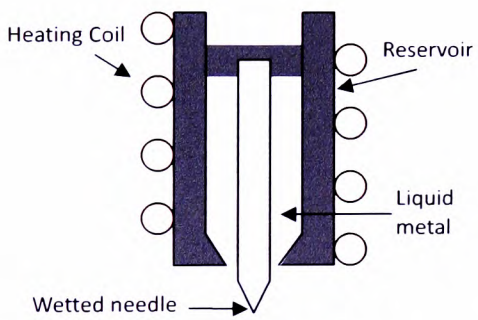

Figure 2.1.2 - Needle liquid metal ion source (LMIS)

through grooves in the outer surface of the needle down to the tip. The Ga-LMIS is the most commonly used source for general-purpose FIB applications and is supplied as standard in virtually all commercially available systems. This is the case for several reasons, one of which is that the melting point of Ga is just above room temperature, reducing the demands placed upon the heating coil and reservoir assembly. Ga also has a low vapour pressure when in the molten state, meaning that it is less likely to evaporate, conserving the supply. These attributes make for a long lasting, stable source which is ideal for use within a vacuum.

In order to extract the ions, a potential difference in the region of 7-12 kV is applied between the extraction electrode and source. As the voltage is raised, the liquid metal at the tip begins to deform and the balance between surface tension and electrostatic forces results in the formation of a Taylor cone*. As the extraction voltage is further increased, a narrow jet of

* A Taylor cone is typically observed in electrospraying of liquids. It is a steady state of equilibrium between the electrostatic forces deforming the liquid drop at the emission tip and the surface tension. For this state to occur, the liquid must form a cone with a half-angle of 49.3°.

ions is ejected from the very tip of the Taylor cone which quickly diverges into a conical spray owing to the mutual repulsion amongst the ions. In addition to the acceleration energy, the eletrostatic interactions between the ions result in a random energy spread, ΔE, which greatly influences the resolution of the system. For a Ga-LMIS operating at a typical extractor current of 1-2 μA, ΔE is only about 5 eV (FWHM), which is relatively low in comparison to other sources[2.8].

When focussing the ions, the minimum spot size is determined by several factors, predominantly the size of the ion source, chromatic aberration and to a lesser extent, spherical aberration. The emitting tip of a LMIS is typically only 5 nm in diameter and is one of the reasons for the high resolution capabilities of a modern FIB[2.9]. Chromatic aberration occurs when the ions have different energies in the axial direction and are consequently focussed to different points on the sample. It becomes more pronounced at higher currents because of the increasing number of ion-ion interactions within the beam, therefore a source with a small ΔE is desirable. Spherical aberration occurs due to off-axis variations in the focal length of the lenses, but is likely to be negligible in comparison to chromatic aberration in the typical operating range of most commercial FIB systems[2.8]. As a consequence of stochastic beam broadening and the lens aberrations, the ion beam takes an approximate Gaussian distribution profile which becomes broader with decreasing accelerating voltage. Therefore to achieve optimum resolution, one would use a low probe current at high beam energy, although this is not always practical.

The position of the ion beam spot is controlled by electrostatic octupole lenses and may be raster-scanned across the sample, having the effect of homogeneously irradiating the scan area. Alternatively, the spot may be precisely positioned in specific areas when controlled by lithography software/hardware systems.

2.1.2 Ion-Target Interactions and Sputtering

As illustrated in Fig. 2.1.3, during a collision with a target, the primary ions produce cascades of secondary particles (electrons, atoms and ions) beneath the sample surface. It is this ion-target interaction that makes the FIB such a versatile tool. Only a small fraction of the cascading particles will leave the target surface, with typical energies ranging up to a few tens of eV. If the ion beam is raster-scanned over the sample, the secondary electrons may be

detected to generate an image of the surface. This is known as scanning ion microscopy (SIM) and is identical in principle to secondary electron imaging in an SEM. 30 keV Ga ions typically penetrate a few tens of nanometres beneath the target surface[2.10] (Fig. 2.1.3*A*), whereas equally energetic electrons would penetrate as deep as several microns. Consequently, FIB-generated secondary electron images exhibit contrast that is more sensitive to the material structure and surface chemistry. An example often used to illustrate this point is a mechanism known as channelling contrast, visible in Fig. 2.1.4. Crystallites orientated such that the crystal planes are parallel to the beam appear dark on the image as they allow the ions to penetrate to a depth where the secondary electrons cannot easily escape. Where the planes are at an appreciable angle to the beam, the detected electron yield is higher, since it is generated closer to the target surface.

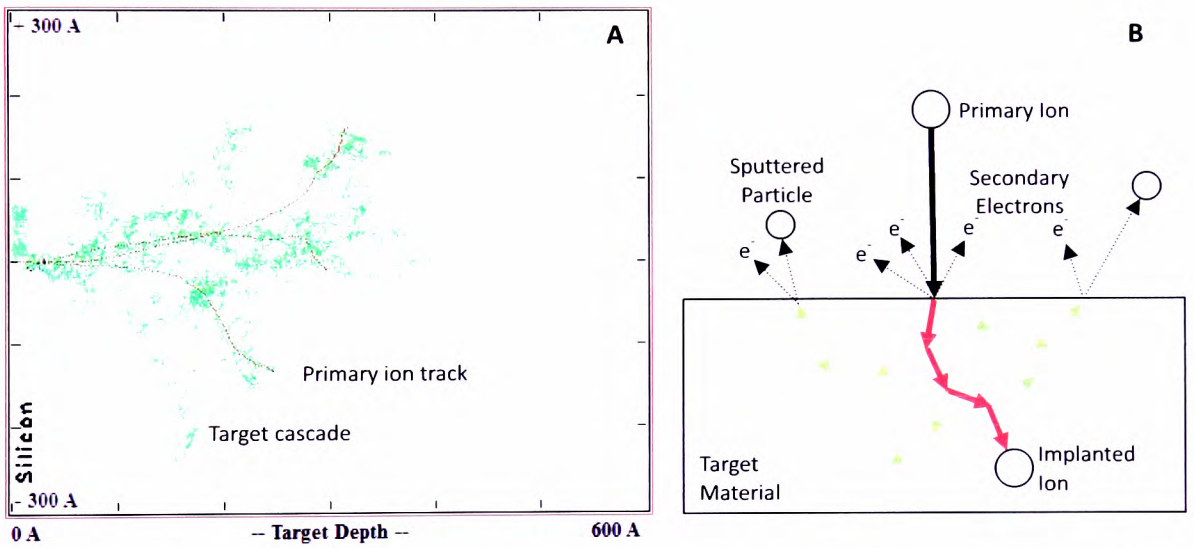

Figure 2.1.3 – Illustrations of the ion-target interactions. *A*: A simulated collision between three 30 keV Ga ions and an amorphous Si target[2.10]. The red lines illustrate the Ga ion tracks, while the green lines and dots illustrate the Si cascades and final positions. *B*: A schematic diagram of the ion-target interaction.

Not only are electron cascades generated during the ion-target interaction, but atomic cascades also. For every primary ion collision, there may be several hundred target atoms displaced within the interaction volume. Those that are displaced near the surface may go on to knock out a surface atom, producing a sputter yield. In order for this to happen, the surface atom must gain enough kinetic energy to overcome the surface binding energy of the material, which can vary with roughness and chemistry. Typically, there are several sputtered atoms for every primary ion, but this depends on many factors, including the primary ion species, beam energy, target composition and structure, particularly at the surface. Polycrystalline materials show a variation in sputter yield depending on the crystallite orientations[2.11]; this is again a result of the ion channelling effect.

The sputtering action turns the FIB into a micro-machining tool, allowing a user to etch away a sample surface to reveal underlying features, or to machine intricate patterns on a sub-micron scale. This is only made possible by the sophisticated computer software/hardware lithography packages that can be used to control the beam movement. The software allows a user to capture an image of the sample and then draw an overlay of features to be milled, containing anything from simple shapes to complex images, in any location within the field of view.

One of the most common applications of FIB-machining is the production of transmission electron microscope lamella[2.3, 13]. It is quite easily achievable to position a cross-section with sub-micron precision. Fig. 2.1.4 shows a typical example of such a lamella prepared by FIB milling. This is an extreme example of sputtering however. In Chapter 6, FIB milling is used much less aggressively in order remove layers of magnetic material only a few nanometres in thickness.

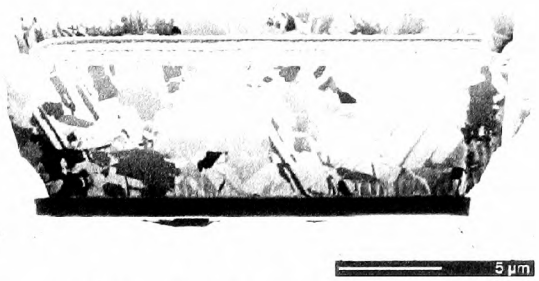

Figure 2.1.4 – A FIB-milled TEM lamella in polycrystalline Cu. Ion channelling contrast reveals the individual crystals. Cited from Ref. (2.13).

The major disadvantage to the FIB machining technique is the significant quantity of the primary ion species that gets implanted within the interaction volume. In addition, the cascades that are essential for the sputtering action can change the structure of the sample in often undesirable ways. The atomic reorganisation that occurs within collision cascades can cause amorphisation in crystalline samples[2.14, 15] and sometimes recrystallisation[2.15, 16]. In some cases it is possible to remove amorphised or contaminated areas by tilting the sample such that the ions are incident at a glazing angle, then reduced probe current and beam energy are used to sputter only the top surface without causing further significant damage. This approach is not always possible, but alternative post-processing methods may potentially be used to alleviate some of the side effects of ion beam induced damage. While not an integral part of this thesis, a wet etching technique has been explored as a possible approach to removing damaged areas of FIB-machined GaAs. Fe on GaAs forms a Schottky diode, where the current-voltage characteristics are highly sensitive to the properties of metal-semiconductor interface and consequently are sensitive to FIB-induced damage. Circular

trenches were milled into an Fe film in order to form discs that were physically isolated from the surrounding film. The diode characteristics of the discs were significantly worsened by the Ga contamination and damage to the GaAs. However, after wet-etching, their performance was virtually restored to that of the original, undamaged Fe/GaAs interface.

2.1.3 Focussed Ion Beam Induced Deposition

In addition to sputtering, it is also possible to deposit metallic or insulating materials using a FIB-induced chemical vapour deposition technique (FIBID)[2.5, 17-19]. This involves injecting a chemical precursor around the focal point of the ions which adsorbs onto the sample surface. Incident ions transfer energy to the sample and the resulting cascades locally decompose the molecules into volatile and non-volatile components. The non-volatile component forms a residue on the sample surface, while the volatile component is removed by the vacuum system. The precursor vapour is supplied from a reservoir and injected into the sample chamber through small needles positioned approximately 100 μm from the focal point of the ion beam. One of the most commonly used precursors for metallic deposition is tungsten hexacarbonyl ($W(CO)_6$)[2.17]. When irradiated by ions or electrons, the molecules dissociate such that the carbon and oxygen are released, leaving tungsten on the surface. This allows for electrically conductive wires to be formed for modifying circuits, or creating interconnects in prototype devices. FIBID is briefly explored later in Chapter 7 as a possible means of fabricating electrical interconnects for magnetoresistive studies.

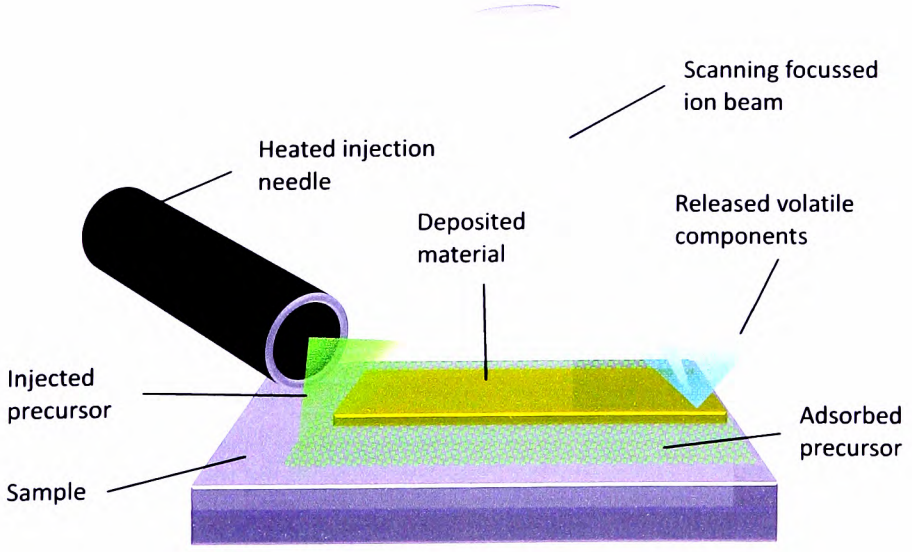

Figure 2.1.5 – Schematic illustration of focussed ion beam induced deposition.

2.2 *Magnetic Patterning by Ion Irradiation*

The atomic reorganisation that occurs during energetic ion irradiation of a sample is very effective at altering any magnetic properties it may have, particularly if they depend strongly upon micro-structure or composition. The properties of the irradiated material may be altered through changes in the shape, magnetocrystalline, interface and exchange anisotropies, or by introducing defects that affect the magnetic domain nucleation and propagation behaviour. Patterning by ion irradiation may be performed using stencil masks or resist masks deposited directly upon the media, but the direct-write nature of the FIB makes it a particularly attractive approach. There have been a large number of studies using both methods, a few of which are discussed here.

Probably the most obvious form of magnetic patterning involves structurally modifying the film such that shape anisotropy is artificially introduced. Sufficiently high doses are selectively applied to areas of a sample such that the magnetic layers are entirely removed. If many discrete elements are patterned in the form of an array, when observed as a whole, its hysteretic behaviour reflects the shape anisotropy of the individual elements[2.20, 21]. Examples of this form of surface patterning using FIB lithography are illustrated in Ref. (2.21) where arrays of permalloy wires, elongated hexagons and circles, with dimensions as small as 100 nm were produced.

It is often unnecessary to remove the entire thickness of a magnetic layer in order to introduce artificial anisotropy. Simply the presence of an ion-irradiated region where the magnetic properties differ from the rest of the film may affect domain wall propagation or domain nucleation in the local vicinity. Owen *et al.* implanted Ga ions into 30 nm thick permalloy films in the form of "anti-dot" arrays of various dimensions[2.22] The ions, implanted at a relatively low dose of 10^{16} ions cm^{-2}, were confined to discrete square regions arranged periodically across the film. As a result, the anisotropy of the permalloy was affected and trapped domains states were observed at remanence. This method is approaching what can be considered to be pure magnetic patterning, where the magnetic properties are altered using ion doses well below those required for topographical patterning.

Pure magnetic patterning was first demonstrated by Chappert[2.23], where Co/Pt multilayers with perpendicular magnetic anisotropy were irradiated with 30 keV He^+ ions at doses ranging from 2×10^{15} to 2×10^{16} ions cm^{-2}. A reduction in coercivity and a switch to in-plane anisotropy was observed as the ion dose was increased. The perpendicular anisotropy of the Co/Pt system is highly dependent upon interfacial properties between the individual Co and Pt layers, thus mixing at these interfaces was thought to be responsible for the perpendicular to in-plane transition. There have been many subsequent studies of ion irradiation effects on the Co/Pt system[2.24-30], all reporting reductions in perpendicular anisotropy. Bonder *et al.* clearly illustrate[2.28] the interlayer mixing that occurs during ion irradiation with high resolution cross-sectional TEM images of the Co/Pt structure before and after irradiation with 80 keV (effective) Ar^{++} ions. After a dose of 10^{15} ions cm^{-2}, there was no hint of any multilayer structure remaining. A similar atomic mixing effect was also considered to be responsible for a reduction in anisotropy within an ordered CoPt alloy[2.31]. In this system, strong magnetocrystalline anisotropy results from the highly ordered alternating planes of Co and Pt which can be easily disordered by ion irradiation.

The ability to create a magnetically patterned yet structurally flat surface is highly desirable for magnetic storage applications. Rettner described a process where small areas of granular $Co_{70}Cr_{18}Pt_{12}$ perpendicular recording media were patterned using a Ga FIB[2.32]. Rettner irradiated the 20 nm thick magnetic layer and 5 nm carbon capping layer with a dose of 2.5×10^{17} ions cm^{-2} in order to produce arrays of isolated square single-domain islands. Read-write operations on the patterned media were later demonstrated[2.33, 34] and showed improved jitter* in comparison to the performance of the continuous film. Albrecht later demonstrated[2.35] read/write operations along tracks of the single-domain islands at higher areal densities up to 200 Gbit/$inch^2$. The trenches between the magnetic islands were only 6 nm deep, thus the relatively thick 20 nm magnetic layer remained continuous. Despite this, the neighbouring islands were only coupled through magneto-static interactions. Implantation of Ga from the ion beam and migration of C from the capping layer were thought to contribute to the reduced direct exchange coupling between the islands[2.34].

* Jitter is an important read-back noise characteristic that results from randomised transitions in the magnetisation of the media from one bit to the next.

A similar reduction in exchange forces in CoCrPt layers, with in-plane anisotropy, was observed by Georgieva *et al*[2.36]. In this case, various CoCrPt/Cr multilayers were irradiated with Ar^{++} ions at effective energies of 80 keV. The coercivity and saturation magnetisation of the media were significantly reduced after irradiation with just 10^{14} ions cm^{-2}. This was attributed to local intermixing of Cr into the magnetic layers resulting in dilution of the Co magnetic moments. Consequently, exchange coupling between individual grains and layers was reduced. Slightly higher ion doses of 3×10^{15} ions cm^{-2} rendered the film nonmagnetic allowing patterning of magnetic and non-magnetic features.

Most of the examples above involve adjusting the magnetic properties by atomic intermixing and reducing order. However, order can actually be reintroduced to some extent by application of a magnetic film during irradiation. McGrouther *et al.* reported that Ga irradiation affected the coupling between exchange-biased CoFe and IrMn layers, such that the bias strength was reduced with increasing dose[2.37]. After a dose of 6×10^{14} ions cm^{-2}, the bias strength was reduced by 70 % in comparison to that of the as-grown film. This was, as previously described, due to disordering at the interface between the two layers. However, in a later work[2.38] a much lower dose of 6×10^{13} ion cm^{-2} was applied to the same film in the presence of an external field applied anti-parallel to the bias direction. As a result, the bias within the irradiated film was reversed and had a strength around 50 % of that exhibited by the original film. This is clear evidence of atomic order during irradiation, which in effect, is like thermal annealing in an applied field.

This atomic ordering has been used by Woods and co-workers as a method of locally modifying the uniaxial anisotropy of 5 nm thick permalloy films[2.39]. In this case, ion irradiation was performed through a resist mask with very high energy (200 keV) Ar ions at a dose of 2×10^{14} ions cm^{-2}. The use of heavier 30 keV Ni ions has also been reported[2.40], where doses as low as 5×10^{13} ions cm^{-2} were found to be sufficient. Using a Ni ion source to irradiate permalloy allows the effects of the ion-target interactions to be studied more effectively without the issue of Ga contamination that is usually encountered with FIB irradiation. It was found that doses up to 1×10^{16} ion cm^{-2} increased the coercivity of the 20 nm thick $Ni_{81}Fe_{19}$ films, which was attributed to an increased number of pinning sites. A reduction in saturation magnetisation was also observed and was attributed to a combination of film thinning due to sputtering, atomic mixing at the interface between the permalloy film and a Ta under-layer, and an change in the stoichiometry as a result of the Ni implantation.

Interface mixing was significant as reported in Ref. (2.41) and produced a magnetically dead amorphous layer, which expanded upwards into the NiFe with increasing ion dose.

Of course, most commercial FIB systems use Ga ion sources, so one usually has to accept the fact that contamination will occur. Kaminsky *et al.* described the effects of irradiating areas of 15.5 nm thick $Ni_{80}Fe_{20}$ with 30 keV Ga ions[2.42]. The thickness and stoichiometry of the permalloy was comparable to that studied in Ref. (2.40), with the addition of a 9 nm $Ni_{80}Cr_{20}$ capping layer. The reported effects, however, are quite different. The coercivity was seen to *reduce* with applied doses up to 8.5×10^{15} ions cm^{-2}, and eventually a dose of 1×10^{16} ions cm^{-2} rendered the film non-ferromagnetic at room temperature. Compositional changes resulting from indirect implantation of Cr was suggested as the reason behind the modification of the magnetic behaviour at low ion doses, but direct Ga implantation was considered to be the most likely explanation for the loss of observable ferromagnetism at the highest dose. Conversely, Ozkaya *et al.* reported that a Ga dose of 1×10^{16} ions cm^{-2} *increased* the coercivity of a 30 nm thick $Ni_{81}Fe_{19}$ film within relatively small 10 μm × 10 μm implanted regions[2.43]. This was mostly attributed to an enlarged lattice parameter within the irradiated areas, increasing strain and impeding domain wall movement. No protective layer was deposited and consequently 7 % of the material was sputtered. Different sputtering rates for the Fe and Ni were seen to alter the composition of the permalloy which was also considered as a possible factor affecting the magnetic behaviour.

The studies on permalloy films seem to suggest that although a capping layer prevents unwanted sputtering, migration of this material into magnetic layer can be detrimental to the ferromagnetic properties. This may be taken advantage of if one wished to render a film non-magnetic with as lower dose as possible.

References

2.1 W. H. Escovitz, T. R. Fox and R. Levisetti, Proceedings of the National Academy of Sciences of the United States of America **72** (5), 1826-1828 (1975).

2.2 J. H. Orloff and L. W. Swanson, Journal of Vacuum Science & Technology **12** (6), 1209-1213 (1975).

2.3 R. Krueger, Micron **30** (3), 221-226 (1999).

2.4 L. R. Harriott, A. Wagner and F. Fritz, Journal of Vacuum Science & Technology B **4** (1), 181-184 (1986).

2.5 H. Komano, H. Nakamura and T. Takigawa, Journal of Vacuum Science & Technology B **9** (5), 2653-2665 (1991).

2.6 H. W. P. Koops, R. Weiel, D. P. Kern and T. H. Baum, Journal of Vacuum Science & Technology B **6** (1), 477-481 (1988).

2.7 FEI Company, "Focused ion beam technology, capabilities and applications," 2006 [Online]. Available: http://www.fei.com/uploadedFiles/Documents/Content/2006_06_FIB_Overview_pb.pdf. [Accessed: May, 2009].

2.8 P. D. Prewett and G. L. R. Mair, *Focused Ion Beams from Liquid Metal Ion Sources*. Somerset: Research Studies Press Ltd., 1991.

2.9 F. A. Stevie, L. A. Giannuzzi, B. I. Prenitzer, "The focused ion beam instrument," in *Introduction to Focused Ion Beams: Instrumentation, Theory, Techniques and Practice*, L. A. Giannuzzi, F. A. Stevie, Eds. New York: Springer, 2005, pp. 1-12.

2.10 J. F. Ziegler, SRIM-2008, http://www.srim.org.

2.11 B. W. Kempshall, S. M. Schwarz, B. I. Prenitzer, L. A. Giannuzzi, R. B. Irwin and F. A. Stevie, Journal of Vacuum Science & Technology B **19** (3), 749-754 (2001).

2.12 L. A. Giannuzzi, B. I. Prenitzer, B. W. Kempshall, "Ion – solid interactions," in *Introduction to Focused Ion Beams: Instrumentation, Theory, Techniques and Practice*, L. A. Giannuzzi, F. A. Stevie, Eds. New York: Springer, 2005, pp. 13-52.

2.13 R. M. Langford and C. Clinton, Micron **35** (7), 607-611 (2004).

2.14 Z. G. Wang, T. Kato, T. Hirayama, N. Kato, K. Sasaki and H. Saka, Applied Surface Science **241** (1-2), 80-86 (2005).

2.15 S. Rubanov and P. R. Munroe, Journal of Microscopy-Oxford **214**, 213-221 (2004).

2.16 W. Voegeli, K. Albe and H. Hahn, Nuclear Instruments & Methods in Physics Research Section B-Beam Interactions with Materials and Atoms **202**, 230-235 (2003).

2.17 H. Langfischer, B. Basnar, H. Hutter and E. Bertagnolli, Journal of Vacuum Science & Technology a-Vacuum Surfaces and Films **20** (4), 1408-1415 (2002).

2.18 T. Tao, J. S. Ro, J. Melngailis, Z. L. Xue and H. D. Kaesz, Journal of Vacuum Science & Technology B **8** (6), 1826-1829 (1990).

2.19 M. J. Vasile and L. R. Harriott, Journal of Vacuum Science & Technology B **7** (6), 1954-1958 (1989).

2.20 R. P. Cowburn, D. K. Koltsov, A. O. Adeyeye and M. E. Welland, Applied Physics Letters **73** (26), 3947-3949 (1998).

2.21 G. Xiong, D. A. Allwood, M. D. Cooke and R. P. Cowburn, Applied Physics Letters **79** (21), 3461-3463 (2001).

2.22 N. Owen, H. Y. Yuen and A. Petford-Long, IEEE Transactions on Magnetics **38** (5), 2553-2555 (2002).

2.23 C. Chappert, Science **280** (5371), 1919-1922 (1998).

2.24 J. Ferré, C. Chappert, H. Bernas, J. P. Jamet, P. Meyer, O. Kaitasov, S. Lemerle, V. Mathet, F. Rousseaux and H. Launois, Journal of Magnetism and Magnetic Materials **199**, 191-193 (1999).

2.25 D. Weller, J. E. E. Baglin, A. J. Kellock, K. A. Hannibal, M. F. Toney, G. Kusinski, S. Lang, L. Folks, M. E. Best and B. D. Terris, Journal of Applied Physics **87** (9), 5768-5770 (2000).

2.26 G. J. Kusinski, G. Thomas, G. Denbeaux, K. M. Krishnan and B. D. Terris, Journal of Applied Physics **91** (10), 7541-7543 (2002).

2.27 R. Hyndman, P. Warin, J. Gierak, J. N. Chapman, J. Ferré, J. P. Jamet, V. Mathet and C. Chappert, Journal of Magnetism and Magnetic Materials **240** (1-3), 50-52 (2002).

2.28 M. J. Bonder, N. D. Telling, P. J. Grundy, C. A. Faunce, T. Shen and V. M. Vishnyakov, Journal of Applied Physics **93** (10), 7226-7228 (2003).

2.29 G. J. Kusinski, K. M. Krishnan, G. Denbeaux and G. Thomas, Scripta Materialia **48** (7), 949-954 (2003).

2.30 S. W. Shin, S. G. Lee, J. Lee, C. N. Whang, J. H. Lee, I. H. Choi, T. G. Kim and J. H. Song, Nanotechnology **16** (8), 1392-1395 (2005).

2.31 M. Abes, J. Venuat, D. Muller, A. Carvalho, G. Schmerber, E. Beaurepaire, A. Dinia and V. Pierron-Bohnes, Journal of Applied Physics **96** (12), 7420-7423 (2004).

2.32 C. T. Rettner, IEEE transactions on magnetics **37** (4), 1649-1651 (2001).

2.33 J. Lohau, IEEE transactions on magnetics **37** (4), 1652-1656 (2001).

2.34 C. T. Rettner, IEEE transactions on magnetics **38** (4), 1725-1730 (2002).

2.35 M. Albrecht, Applied physics letters **81** (15), 2875-2877 (2002).

2.36 M. T. Georgieva, P. J. Grundy and N. D. Telling, Applied Physics Letters **90** (4), 3 (2007).

2.37 D. McGrouther, J. N. Chapman and F. W. M. Vanhelmont, Journal of Applied Physics **95** (12), 7772-7778 (2004).

2.38 D. McGrouther, W. A. P. Nicholson, J. N. Chapman and S. McVitie, Journal of Physics D-Applied Physics **38** (18), 3348-3353 (2005).

2.39 S. I. Woods, S. Ingvarsson, J. R. Kirtley, H. F. Hamann and R. H. Koch, Applied Physics Letters **81** (7), 1267-1269 (2002).

2.40 J. Fassbender and J. McCord, Applied Physics Letters **88** (25), 3 (2006).

2.41 J. Fassbender, J. von Borany, A. Müecklich, K. Potzger, W. Möller, J. McCord, L. Schultz and R. Mattheis, Physical Review B **73** (18), 8 (2006).

2.42 W. M. Kaminsky, G. A. C. Jones, N. K. Patel, W. E. Booij, M. G. Blamire, S. M. Gardiner, Y. B. Xu and J. A. C. Bland, Applied Physics Letters **78** (11), 1589-1591 (2001).

2.43 D. Ozkaya, R. M. Langford, W. L. Chan and A. K. Petford-Long, Journal of Applied Physics **91** (12), 9937-9942 (2002).

CHAPTER 3 Analysis Techniques

3.1 *Transmission Electron Microscopy*

Transmission electron microscopy (TEM) is a technique that was developed in the 1930s in which electrons are transmitted through thin samples (typically up to 100 nm in thickness). While scanning electron microscopy (SEM) generates images of surface topography, TEM provides information about inner structure. The very first electron microscope was developed by Knoll and Ruska in 1931, but the performance of optical microscopes was not surpassed until Ruska later developed an improved microscope in 1933. TEM is now probably one of the most commonly used techniques for materials analysis, achieving spatial resolutions down to 0.1 – 0.3 nm[3.1].

3.1.1 Electron Diffraction

As the high energy electrons (typically 80-200 keV) pass through the sample, they interact with its periodic structure and undergo elastic and inelastic scattering. Analogous to light through a periodic grating, the electrons are diffracted by the atomic planes in the crystal, which results in the formation of a diffraction pattern. This process is called selected area diffraction (SAD) and is one of the most common modes of TEM operation. The scattering of electrons by the periodic potential in the lattice can be described by a reflection from atomic planes with an interplanar spacing, d_{hkl} (where h, k and l are the Miller indices). This is conveyed by the Bragg Law:

$$2d_{hkl}\sin\theta = n\lambda \tag{3.1.1}$$

where θ is the scattering angle, λ is the de Broglie wavelength of the electrons and n is an integer representing the diffraction order. For a cubic crystal, the interplanar spacing is given by:

$$d_{hkl} = \frac{na}{\sqrt{h^2 + k^2 + l^2}} = \frac{na}{\sqrt{N}} \tag{3.1.2}$$

where a is the lattice parameter and $N = h^2 + k^2 + l^2$. Therefore, from the scattering angle, it is possible to find the lattice parameter of the crystal. For single crystal samples the diffraction pattern will appear as discrete spots corresponding to the different (*hkl*) planes. In the case of a polycrystalline sample, the spots produced by each of the many randomly orientated crystallites form diffraction rings as shown in Fig. 3.1.1. The radius of each ring is given by:

$$R = \frac{n\lambda D}{d_{hkl}} \tag{3.1.3}$$

where D is the distance from the sample to the imaging screen (or the camera length). Then by combining Eqns. 3.1.2 and 3.1.3, for a cubic crystal:

$$R^2 = \frac{N\lambda^2 D^2}{a^2} = \frac{N\gamma^2}{a^2} \tag{3.1.4}$$

where γ is the camera constant, $\gamma = \lambda D$. From this relation it is evident that the ring radius squared is proportional to N and inversely proportional to the lattice parameter. If the first (smallest) ring is denoted R_1 and the last (largest) ring R_i, we may write:

$$\frac{R_i^2}{R_1^2} = \frac{N_i}{N_1} \tag{3.1.5}$$

If the type of cubic system (primitive, face or body centring) is known, then the ratio R_i^2 / R_1^2 may be matched to the expected values of N_i / N_1 in order to index the rings.

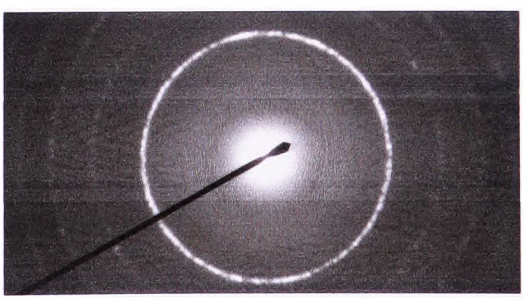

Figure 3.1.1 – SAD pattern generated by a polycrystalline Fe film. The individual spots from the randomly orientated crystallites form rings.

A real-space image can be formed if just the transmitted beam (the central spot in the SAD image) is allowed to reach the imaging plane. This is achieved by inserting and objective aperture as shown in Fig. 3.1.2. This is known as bright field imaging, where sample thickness and diffraction contrast can be seen. Alternatively, one or more of the diffracted spots may be used to form a real-space image. This is known as dark field imaging which can provide extra information about planar defects or grain sizes.

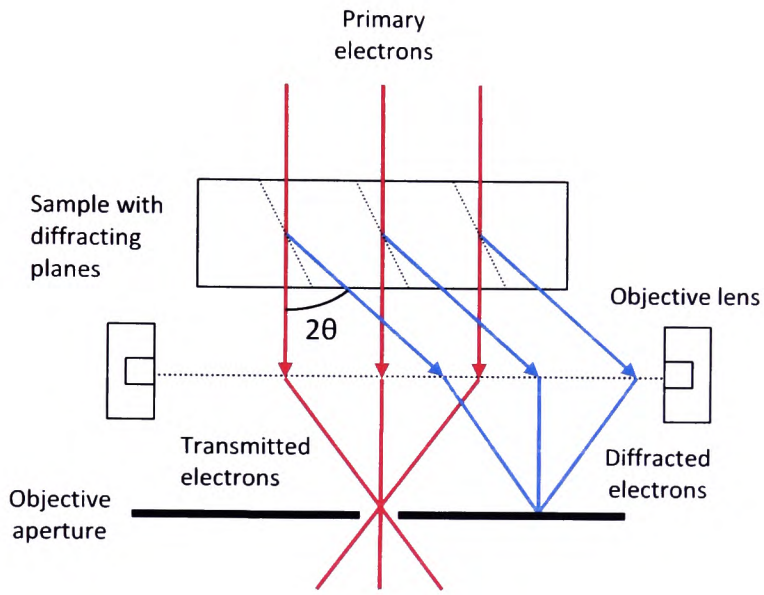

Figure 3.1.2 – The diffracted electrons are blocked in bright field imaging mode.

3.1.2 Lorentz Microscopy

Another TEM technique that is used specifically for imaging magnetic samples is known as Lorentz microscopy. As the electrons are transmitted through a sample with in-plane anisotropy, they are deflected by the Lorentz forces generated by the magnetisation of the sample. Where a change in the magnetisation occurs, i.e. at a domain wall, the electrons are deflected in different directions and areas of enhancement and depletion give rise to a contrast mechanism that may be observed by slightly over- or under-focussing. The over-focussed case is shown in Fig. 3.1.3. This is known as Fresnel imaging, and is the most easily achieved out of two possible modes. The second, more difficult approach, known as Foucault mode, involves off-centring the objective aperture such that only the electrons deflected by domains orientated in a given direction may pass through. The result is an in-focus image of the full magnetic domains, not just the domain walls.

The physical separation between the sample and objective lens is generally quite small and as a result, the lens field may cause undesirable magnetisation of the sample such that the domain structure is lost. Therefore, in order to perform Lorentz microscopy, the objective lens is usually switched off and a secondary lens installed further away from the sample. In some TEMs, the design of the objective lens is such that this procedure is not necessary and the magnetic contrast can be observed at low magnification where the lens field is small. The sample may be magnetised in a given direction by tilting it with respect to the field (which is parallel to beam axis). As the angle of tilt is increased, the component of the field in-plane increases such that the magnetisation may switch. The magnetisation can then be reversed by tilting in the opposite direction. For samples that are easily saturated in-plane, the angle of tilt may only be a few degrees, depending on the strength of the field.

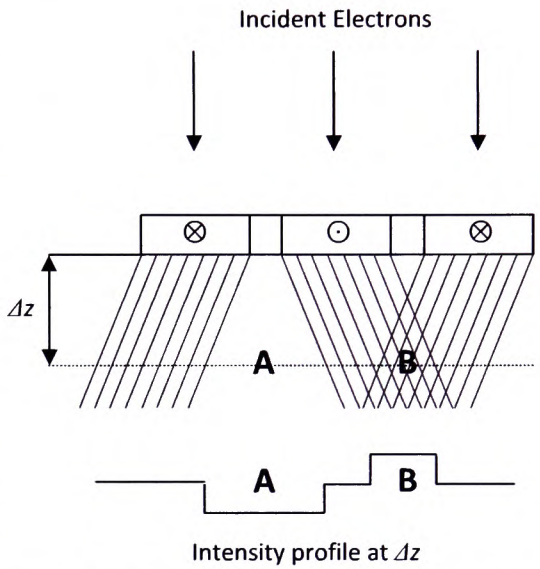

Figure 3.1.3 – Schematic diagram illustrating the deflection of transmitted electrons as they pass through a magnetised material. At the domain walls, there is depletion (A) and reinforcement (B) of the electron intensity at over focus Δz.

3.2 *Optical and Magneto-Optical Effects*

There are two optical phenomena that are absolutely fundamental to the analysis techniques used in this work, namely, birefringence and dichroism. The effects may arise naturally as a result of material structure, induced strain or the application of a magnetic field. In any case, the origins of the effects lie with the interactions that take place between the oscillating electric field vector of a light ray and the electronic configuration of the medium through which it propagates.

3.2.1 Natural Birefringence

Natural birefrinence is an optical effect resulting from anisotropy within a material's crystal structure. The simplest case is where a crystal has a single axis of anisotropy; this is called the optic axis (OA). In such a crystal (calcite for example) there are two principal values of refractive index along two orthogonal crystallographic axes. Rays propagating at an angle to the optic axis will experience different values of refractive index depending on the polarisation of the electric field vector, **E**. The component of **E** that is perpendicular to the optic axis (ordinary-ray or *o*-ray) will experience the ordinary refractive index, n_o, while the parallel component (extraordinary ray or *e*-ray) will experience the extraordinary refractive index, n_e. The difference between refractive indices, $\Delta n = n_e - n_o$, is called the birefringence.

Birefringence causes the light to propagate through the crystal at different velocities depending on its polarisation state[3.2]. If a point light source is embedded within a birefringent crystal, as shown in Fig. 3.2.1, the *o*-rays propagate outwards isotropically with speed $v_\perp$, since they are everywhere polarised perpendicular to the optic axis. The *e*-rays also propagate with this speed along the optic axis, but with a different speed perpendicular to it ($v_{//}$). If $n_o < n_e$, then $v_\perp > v_{//}$, in which case the crystal is positive uniaxial. If $n_o > n_e$ then $v_\perp < v_{//}$ and the crystal is negative uniaxial.

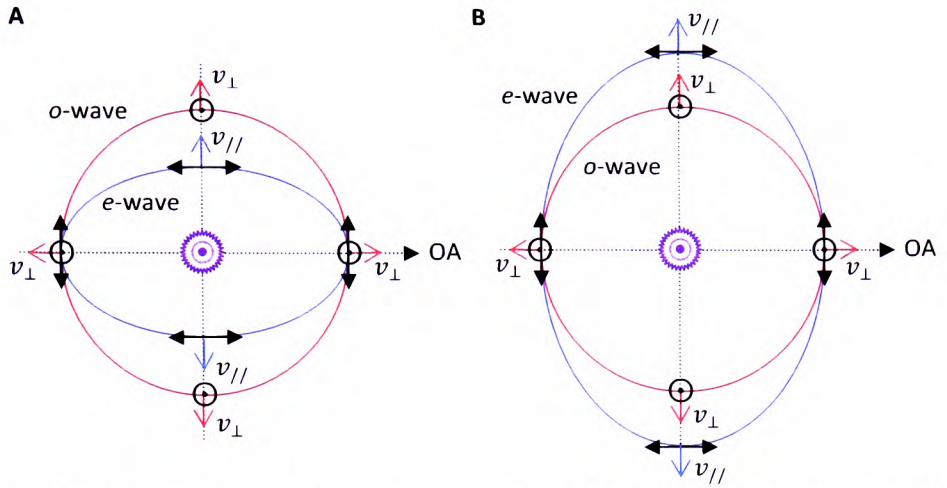

Figure 3.2.1 – Schematic illustrations of *o*- and *e*-wave propagation in positive (*A*) and negative (*B*) uniaxial crystals. The black dots and arrows indicate the axes along which **E** lies for the *o*- and *e*-waves respectively. Adapted from Ref. (3.2).

Figure 3.2.2*A* shows an example of a linearly-polarised ray passing through a positive uniaxial birefringent crystal perpendicular to the optic axis. The electric field vector is at 45° to the optic axis and thus is decomposed into two equal but orthogonal components, $\mathbf{E}_x$ and $\mathbf{E}_y$. The difference in the velocities of the two components induces a phase difference, the result of which is that the light emerges elliptically polarised (EP). With specific crystal thicknesses it is possible to create circularly polarised (CP) light, or rotate the plane of polarisation by 90° (Fig. 3.2.2*B*). Circular polarisation occurs when the induced phase difference between $\mathbf{E}_x$ and $\mathbf{E}_y$ becomes 90° (Fig. 3.2.2*C*), while a phase difference of 180° will flip the plane of polarisation (Fig. 3.2.2*D*). Crystals engineered to produce such phase differences are called quarter- and half-wave plates.

It may also be the case that a material has two different refractive indices for left- and right-circularly polarised light; this effect is known as circular birefringence or optical activity. Augustin-Jean Fresnel explained optical activity by visualising plane-polarised light in terms of two coherent, circularly polarised components of equal amplitude but opposite handedness. In an optically active material, they propagate independently with different values of refractive index and thus a phase difference is introduced (Fig. 3.2.3*A*) which increases with optical path length. This causes a gradual rotation of the resultant electric field vector as the light propagates through the material, as shown in Fig. 3.2.3*B*.

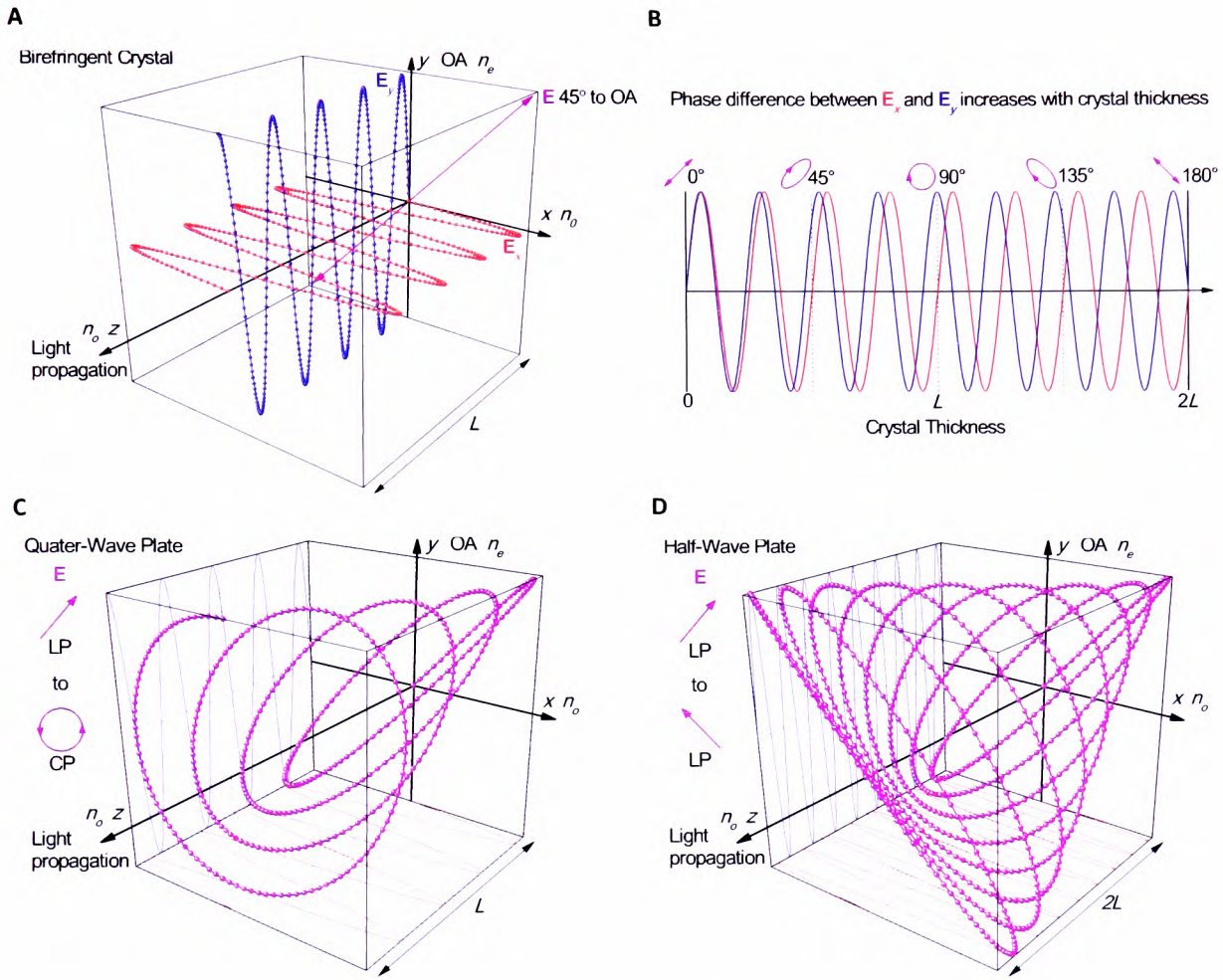

Figure 3.2.2 - Linear birefringence. *A*: The vertical component ($\mathbf{E}_y$) of the electric field vector **E** lags behind the horizontal component ($\mathbf{E}_x$). *B*: The phase difference between $\mathbf{E}_x$ and $\mathbf{E}_y$ changes with the thickness of the birefingent crystal. *C*: A quarter-wave plate creates a phase shift of 90°, producing circularly polarised light. *D*: A half-wave plate produces a phase shift of 180°, rotating **E** by 90°.

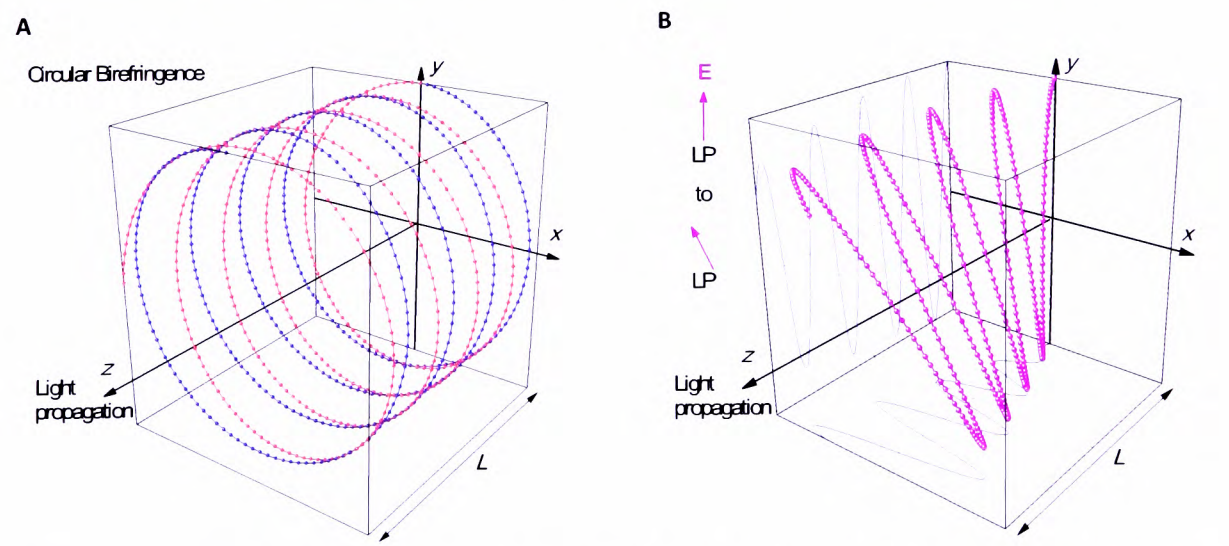

Figure 3.2.3 – An illustration of circular birefringence. Linearly polarised light consists of equal components of left- and right- circular polarisation, one of which lags behind the other in an opticaly active material (*A*). This causes the resultant electric field vector to rotate as the light propagates through the material (*B*).

3.2.2 Natural Dichroism

Dichroism is the differential absorption of light with different polarisation states. It arises naturally as a result of material or molecular structure and may be observed with both linearly and circularly polarised light. Stretched molecules or anisotropic crystals may exhibit linear dichroism (LD), where two orthogonal components of linearly polarised light are absorbed differently, resulting in a rotation of the electric field vector. Circular dichroism (CD) is the differential absorption of light with left- and right-handed circular polarisation and occurs naturally when light interacts with chiral molecules. When transmitted through a circularly dichroic medium, linearly polarised light will have one of its circular components absorbed to a greater extent (Fig. 3.2.4*A*). This results in the light becoming elliptically polarised, but with the major axis of the ellipse remaining parallel to the original plane of polarisation (Fig. 3.2.4*B*).

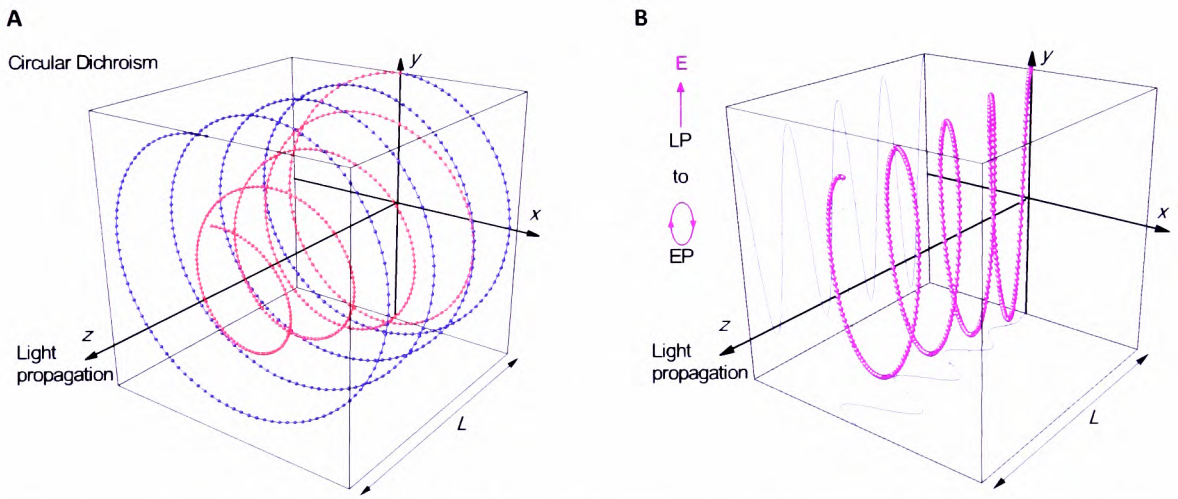

Figure 3.2.4 – An illustration of circular dichroism. One component of circular polarisation is absorbed more than the other (*A*), resulting in the initially linearly polarised electric field vector becoming elliptically polarised (*B*).

3.2.3 Magneto-Optical Effects

Dichroism and birefringence were discussed above in terms of the natural structure of materials, but both forms of optical phenomena may arise as a result of the interaction between an applied magnetic field and the electronic charge within a material. Michael Faraday was the first to observe such phenomena in 1845, with an effect called magnetic circular birefringence (MCB), now commonly referred to as the Faraday effect. Faraday found that a linearly polarised ray of light had its plane of polarisation rotated as it was transmitted through a piece of lead borate glass in the presence of an applied magnetic field. In fact most transparent dielectric materials will exhibit this effect to some extent. The Faraday rotation (θ_F) is proportional to the magnetic flux density (B) along the direction of light propagation:

$$\theta_F = v B l \tag{3.2.1}$$

where v is the material-specific Verdet constant and l is the optical path length. Unlike optical activity, MCB is nonreciprocal and breaks time-reversal symmetry. If, for example, light propagates through an optically active material and then is reflected directly back along the same path, there will be no net rotation of the polarisation. However, with MCB the reflected light will undergo a further rotation in the same sense, doubling the effect.

The origin of MCB is closely related to the Zeeman effect[3.3], where the application of a magnetic field causes a splitting of the optical transitions responsible for absorption. The phenomenon is often explained from a classical point of view [3.2, 4], where we again treat linearly polarised light as two independent circularly polarised components. The rotating electric field vectors of the two components drive electrons in the material in circular orbits. A magnetic field applied perpendicular to the orbital plane will generate a force on the electrons either towards or away from the centre of the orbit depending on the direction of the field and the handedness of the light. Therefore, for a given magnetic field there are two possible values for the radius of the orbit and hence two possible values for the permittivity and refractive index. Consequently, the speed of light in the material is different for the two circularly polarised components.

Where absorptive materials are concerned, such as a thin ferromagnetic film, dichroic effects are also produced, predominantly, magnetic circular dichroism (MCD). This introduces a degree of ellipticity into the polarisation state of the transmitted light. On transmission through a magnetised ferromagnetic film, a combination of MCB and MCD will result in linearly polarised light becoming elliptically polarised, with the major-axis of the ellipse rotated relative to the incident plane of polarisation. In theory, either the Faraday rotation (θ_F) or ellipticity (ϕ_F) may be used as a measure of the average **M** versus **H** behaviour of the sample. Over 30 years after Faraday's discovery, in 1877, John Kerr found that the very same effects also occurred with reflected light; the so-called magneto-optic Kerr effect (MOKE). However, in reflection, the Kerr rotation (θ_K) and ellipticity (ϕ_K) are associated with MCD and MCB respectively.

In a ferromagnetic material the Faraday and magneto-optical Kerr effects are proportional to the magnetisation of the material, not the applied field, which makes the effects incredibly large in comparison to those produced by nonmagnetic materials[3.5]. However, these large effects cannot be explained by the magnetic field within the material alone. There is in fact a contribution from the spin-orbit interaction, which, although present in all materials, is only observed in ferromagnetic materials because of the net magnetic moments produced by the imbalance between occupied spin-up and spin-down 3*d*-states[3.5]. This will be discussed further in the next section.

Consider a ferromagnetic thin film illuminated with linearly polarised light, where the plane of polarisation is perpendicular to the plane of incidence (*s*-polarised), as shown in Fig. 3.2.5. If the film were nonmagnetic, the reflected and transmitted beams would also be *s*-polarised,

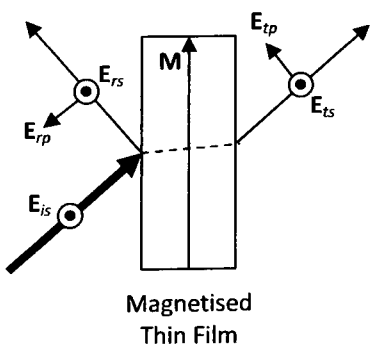

Figure 3.2.5 – The magnetisation induces small components of polarisation in the reflected and transmitted light that are orthogonal to the incident plane of polarisation.

but because of the Faraday and Kerr effects, components polarised parallel to the plane of incidence (p-polarised) are generated. In the figure, E_{is}, (E_{rs}, E_{rp}) and (E_{ts}, E_{tp}) are the complex amplitudes of the incident, reflected and transmitted electric field vector components. The Fresnel reflection matrix for the thin film is given by[3.6]:

$$R = \begin{pmatrix} r_{pp} & r_{ps} \\ r_{sp} & r_{ss} \end{pmatrix} \tag{3.2.2}$$

where r_{ij} is a complex ratio of the incident j-polarised electric field to the reflected i-polarised electric field. Similarly, the Fresnel transmission matrix is:

$$T = \begin{pmatrix} t_{pp} & t_{ps} \\ t_{sp} & t_{ss} \end{pmatrix} \tag{3.2.3}$$

where t_{ij} is a complex ratio of the incident j-polarised electric field to the transmitted i-polarised electric field. In some cases the complex Fresnel coefficients generated by the Faraday and Kerr effects, which would be t_{ps} and r_{ps} in this example, are called the Faraday and Kerr coefficients, f and k, respectively. The complex Kerr rotation for p- and s-polarised light is given by[3.6]:

$$\Theta_K^p = \frac{r_{sp}}{r_{pp}} = \frac{k}{r_{pp}} \qquad \text{and} \qquad \Theta_K^s = \frac{r_{ps}}{r_{ss}} = \frac{k}{r_{ss}} \tag{3.2.4}$$

The complex Faraday rotation for p- and s-polarised light is given by:

$$\Theta_F^p = \frac{t_{sp}}{t_{pp}} = \frac{f}{t_{pp}} \qquad \text{and} \qquad \Theta_F^s = \frac{t_{ps}}{t_{ss}} = \frac{f}{t_{ss}} \tag{3.2.5}$$

The above relations may be expressed in the form of the Kerr rotation (θ_K), ellipticity (ϕ_K), Kerr coefficient (k) and Fresnel reflection coefficient (r)[3.7]:

$$\Theta_K = \theta_K + \mathrm{i}\phi_K = \frac{k}{r} \tag{3.2.6}$$

or the Faraday rotation (θ_F), ellipticity (ϕ_F), Faraday coefficient (f) and Fresnel transmission coefficient (t):

$$\Theta_F = \theta_F + i\phi_F = \frac{f}{t} \tag{3.2.7}$$

Measurement of the magneto-optical effects is usually performed in one of three different experimental arrangements, polar, longitudinal or transverse (Fig. 3.2.6). These arrangements are often associated with MOKE, but they also apply in the case of the Faraday effects. In the polar geometry, the light is incident normal to the sample surface and parallel to the magnetisation. All planes of incident polarisation yield equivalent effects. The longitudinal or transverse geometries have to be used for samples with in-plane anisotropy, where the light is incident on the sample at an oblique angle such that a component of the magnetisation lies along the wave vector. In the longitudinal arrangement, the plane of incidence is parallel to the magnetisation and the polarisation state is sensitive only to the average component of the magnetisation in this plane (m_l). The incident light can be polarised in any orientation, but for simplicity is usually polarised parallel (p-polarised) or perpendicular (s-polarised) to the plane of incidence. Unlike in the polar geometry, s and p polarisations are not equivalent. Although the Faraday (or Kerr) coefficient will be the same for the two states, the Fresnel transmission (or reflection) coefficient will not be and thus the complex Faraday (or Kerr) rotation differs in each case. The transverse geometry is unique in that there are no magnetisation dependent polarisation effects, but instead the intensity of the transmitted or reflected light is modulated. The incident light has to p-polarised and the intensity is sensitive only to the component of magnetisation perpendicular to the plane of incidence (m_t).

In the case where the light is incident normal to both the sample surface and the magnetisation, the first-order Faraday and Kerr effects disappear and instead second-order Voigt effects can be observed[3.8]. These effects are in fact magnetic linear birefringence

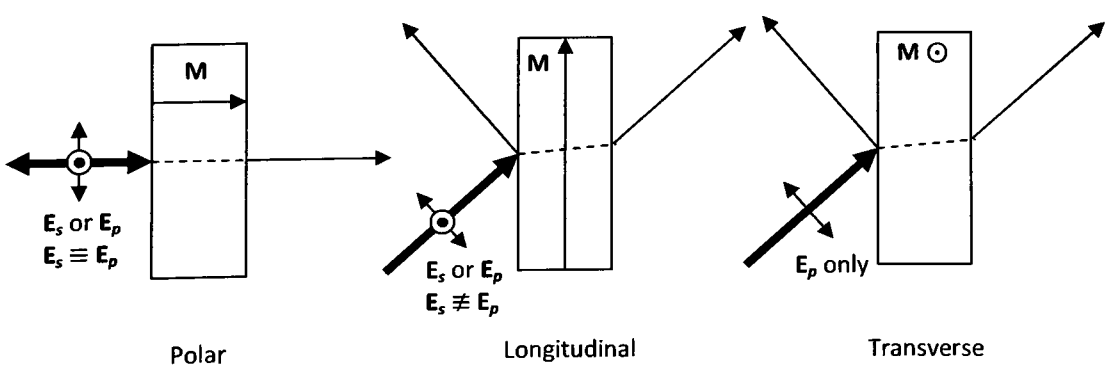

Figure 3.2.6 – The three commonly used geometries for magneto-optical measurements.

(MLB) and dichroism (MLD) where there are differential rates of propagation and differential absorption of the light polarised parallel and perpendicular to the magnetisation. Since the effects are quadratic in magnetisation, there is no directional sensitivity, only axial.

3.2.4 Diffracted-MOKE

The limited resolution of optical techniques makes performing magneto-optical measurements on nanoscale elements difficult to achieve, although it has been demonstrated[3.9, 10]. It is most easily performed by measuring the behaviour of an array of many identical elements[3.9, 10]. Depending on the geometry and periodicity of the array, complex combinations of diffraction, polarisation and magneto-optical effects can lead to unusual hysteresis loops. The zeroth- and higher-order diffracted spots may be measured separately using a technique known as diffracted-MOKE (D-MOKE), or sometimes Bragg-MOKE[3.12] While the hysteresis loops obtained with conventional MOKE depend on the average component of magnetisation along the sensitivity direction, the loop generated by the n^{th} diffraction order represents the n^{th} Fourier component of the magnetisation distribution, which is given by the magnetic form factor[3.12, 13]:

$$f_n^m = \int m(\mathbf{r}) \exp\{\mathrm{i}\, n\mathbf{G}\mathbf{r}\} \mathrm{d}\, S \tag{3.2.8}$$

where $m(\mathbf{r})$ is the component of magnetisation at point $\mathbf{r}$ in a unit cell of the array and $\mathbf{G}$ is the reciprocal lattice vector. The form factor is the Fourier transform of the domain structure within a unit cell of the array and obviously changes with applied field. As a result, the hysteresis loops can show features not seen with conventional MOKE[3.12-18]. These features are sensitive to the domain formation as a result of small fluctuations in the reflectivity and transmittance of the magnetic film corresponding to the local magnetisation distribution. Such features can be difficult to interpret, thus D-MOKE is often supported with micromagnetic simulations that predict the domain structure at each value of the applied field so that the form factor may be calculated and a theoretical loop can be generated for comparison.

3.3 *X-Ray Microscopy*

When visible light interacts with matter, the processes responsible for absorption and the magneto-optical effects primarily involve interactions with weakly bound valance and conduction electrons, in the case of X-ray absorption these interactions involve more tightly bound core electrons. These interactions provide us with powerful techniques with which we can probe the structural and magnetic properties of materials.

3.3.1 X-ray Absorption Spectroscopy (XAS)

If the energy of an X-ray photon is such that it causes a core electron transition, a strong peak in absorption occurs. By measuring the X-ray absorption as a function of photon energy it is possible to determine the composition and chemistry of the absorbing material. The most direct method of measuring the absorption spectra is by detection of X-rays transmitted through semi-transparent samples. If the transmitted intensity is converted to optical density (OD), the absorption is sensitive to the sample composition, thickness and density:

$$\mathrm{OD} = \ln\left(\frac{I_t}{I_0}\right) = -\rho\mu t \tag{3.3.1}$$

where μ is the mass absorption coefficient (in units of $\mathrm{cm}^2\ \mathrm{g}^{-1}$), ρ is the density of the material, and I_t and I_0 are the transmitted and incident intensities. For depolarised X-rays, μ depends only upon the photon energy and the atomic number of the absorbing species.

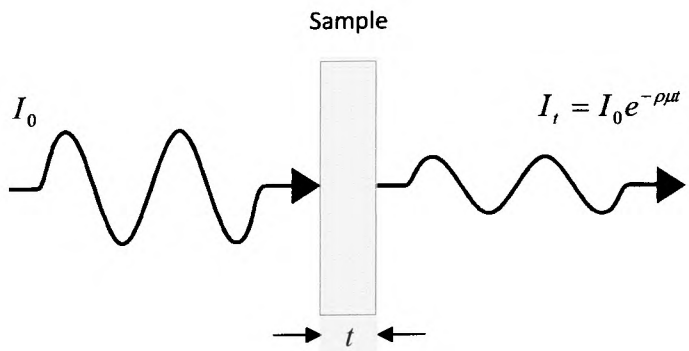

Figure 3.3.1 - X-ray transmission through a semi-transparent sample

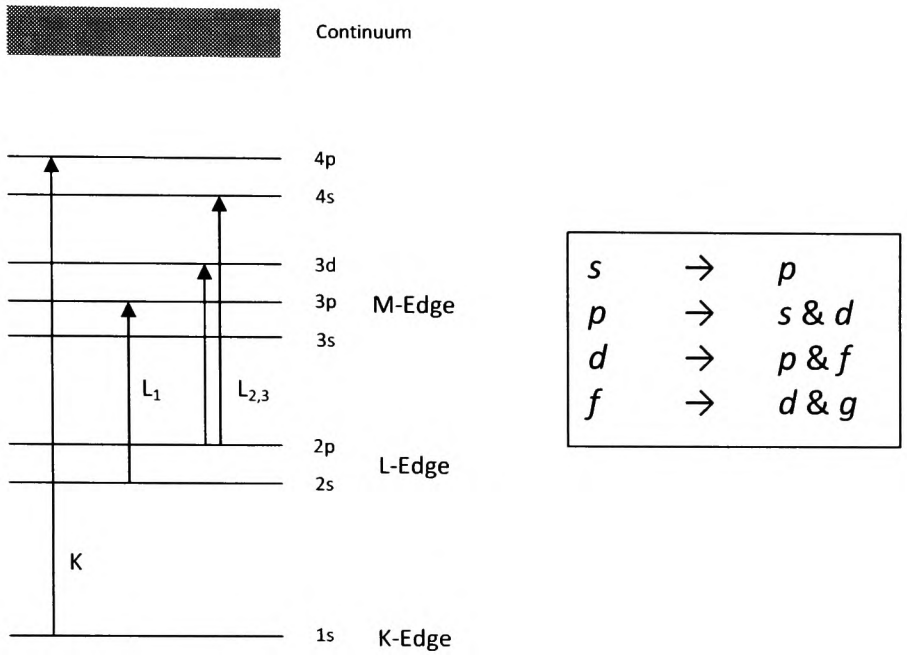

Figure 3.3.2 The K and L edge transitions. The selection rules only allow certain transitions. The $2p$ state is spin-orbit split giving rise to two transition channels, the $L_{2,3}$ edges. Adapted from Ref. (3.18).

The mechanism behind XAS is the selective excitation of core electrons into unoccupied states above the Fermi-level in metals or the conduction band of semi-conductors. Dipole selection rules stemming from Fermi's Golden Rule restrict the possible transitions such that there must be a change in the azimuthal quantum number ($\Delta\ell$) of ± 1 [3.19]. The probability of any given transition is proportional to the availability of empty final states, so a photon is more likely to be absorbed if there are more available states into which it can promote an electron. Therefore, the absorption scales directly with number of empty states. Scanning the photon energy while measuring the absorption provides the transition probability within a range of energies; this is the X-ray absorption spectrum. Large increases in absorption are measured where the energy corresponds to a core electron transition into an empty state just below the continuum. The area under an absorption peak is called the resonance intensity and is directly proportional to the number of empty states. The energies at which the peaks occur are element specific, allowing XAS to be used as a quantitative measure of the composition of a sample. Depending on the energy range scanned, absorption spectra can also provide structural and chemical information.

The spectra are usually treated as two separate regions from which different information may be extracted. The first part is known as the X-ray absorption near edge structure (XANES),

which extends from the pre-edge to around 50 eV after the absorption edge. The pre-edge region may contain peaks where core electrons are excited into the lowest unoccupied states. Increasing the photon energy past the pre-edge region results in a rapid increase in absorption where the core electrons are excited into the highest unoccupied states just below the binding energy; this is known as the absorption edge. The peak in absorption then occurs when the photon energy matches the electron binding energy and provides the electron with just enough energy to transition into continuum states. Increasing the energy a further 50 eV in excess of the binding energy produces low-energy photoelectrons. The photoelectron wave backscatters off surrounding atoms producing fine structure on the measured spectrum, from which electronic and bonding information may be extracted. The second part of the spectrum extends from 50 eV to 1000 eV after the absorption edge; this is called the extended X-ray absorption fine structure (EXAFS). Here, the photoelectron has higher kinetic energy and undergoes single scattering events with nearest-neighbour atoms. Oscillations are seen in the spectrum where there is constructive and destructive interference between the outgoing and backscattered photoelectron waves. Nearest neighbour information, such as the number of atoms surrounding the absorber, their spacing and approximate atomic number may be determined from the oscillations.

3.3.2 Scanning Transmission X-ray Microscope – ALS Beamline-5.3.2

XAS is usually performed using synchrotron sources because of the intense polychromatic radiation they are able to provide. The scanning transmission X-ray microscope (STXM) at the Advanced Light Source (ALS) beamline-5.3.2[3.20] uses bending magnet radiation to produce a beam with a usable energy range of 200 to 1200 eV. A spherical-grating monochromator and slit aperture are used to tune the energy of the beam, which is then focussed onto a transparent sample using a Fresnel zone-plate. An order selection aperture (OSA) allows only the first order diffracted radiation to pass through. The transmitted intensity can be measured as a function of energy or sample position to obtain absorption spectra or images with 40 nm spatial resolution. XAS may be performed by moving the sample such that the beam spot is at the desired location and the transmitted intensity is simply measured as a function of beam energy. Alternatively, a single pixel line may be scanned across the sample at each energy step. Every pixel along the line in represents an absorption spectrum for the corresponding area on the sample. The final mode, and the most time consuming, involves capturing an entire image at each energy step to produce a "stack".

Each image is a map of the absorption at a single energy and thus provides topographic information. When the entire stack is analysed, spatially resolved chemical and topographical information can be extracted simultaneously. This is extremely useful for determining elemental distribution.

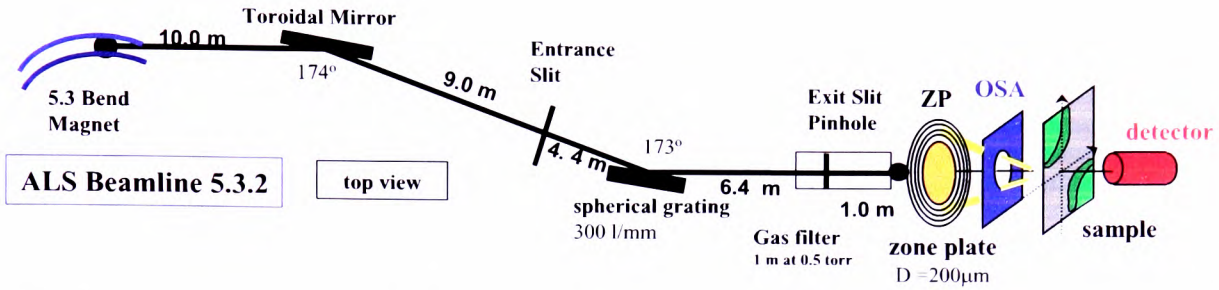

Figure 3.3.3 - A schematic diagram showing the key components of the STXM at the ALS beamline-5.3.2. Cited from Ref. (3.21).

3.3.3 X-Ray Magnetic Circular Dichroism (XMCD)

As stated previously, the absorption coefficient μ depends only upon atomic number and photon energy when depolarised light is used. When polarised light is used, the absorption coefficient then becomes sensitive to anisotropy within the sample. Naturally occurring dichroism originates from orientational order, such as anisotropy within a crystal structure or bonding orientation in molecules and polymer chains[3.22]. The absorption coefficient of linearly polarised X-rays differs when the electric field vector lies parallel or perpendicular to the axis of anisotropy. A related and often indistinguishable effect occurs in magnetic materials where the aligned spins of the electrons distort the charge distribution around the atoms relative to the spin direction. This occurs as a result of the spin-orbit interaction and gives rise to *induced* orientational order. X-rays polarised along the distorted axis will be absorbed more than those polarised perpendicular to it, resulting in X-ray magnetic linear dichroism (XMLD)[3.23].

When dealing with magnetic samples, it is usually desirable to determine the direction of the magnetic moments rather than just the axis along which they are aligned. To achieve this, circularly polarised X-rays are used, which have an angular momentum of $\pm\hbar$ determined by the helicity. The absorption then shows a dependence upon the projection of the

magnetisation onto the angular momentum of the photon. This is known as X-ray magnetic circular dichroism (XMCD)[3.24, 25].

The first attempts to measure MCD effects using X-rays, began with Chapman in 1913[3.26]. Success was limited however, as was that of others who attempted in later years. Eventually, Schütz became the first to publish observations of the XMCD effect in 1987, where synchrotron radiation was transmitted through magnetised iron at the K-edge[3.27]. In 1990 Chen *et al.* reported a much stronger XMCD effect at the $L_{2,3}$-edges of Ni, almost two orders of magnitude greater than at the K-edges of transition metals[3.28]. The XMCD effect in transition metals has its origins in the 3*d*-states, where the exchange interaction causes a splitting of the density of states (Stoner model)[3.24, 25]. The density of spin-up and -down states become shifted with respect to one another, as illustrated in Fig. 3.3.4, which creates an imbalance between spin-up and -down electrons below the Fermi level, resulting in a net magnetic moment. Since the density of states are only shifted with respect to one another, the difference in occupied states below the Fermi-level is equal (but opposite in sign) to the difference in empty states above the Fermi-level. By probing the number of empty spin-up and -down states with excited 2*p*-electrons, a "hole moment" is measured and therefore, it is possible to determine the real magnetic moment produced by the 3*d*-electrons. In reality, as shown in Fig. 3.3.2, the $L_{2,3}$ edges also involve $p \rightarrow s$ transitions, although these are negligible in comparison to the $p \rightarrow d$ transitions and may be neglected[3.29].

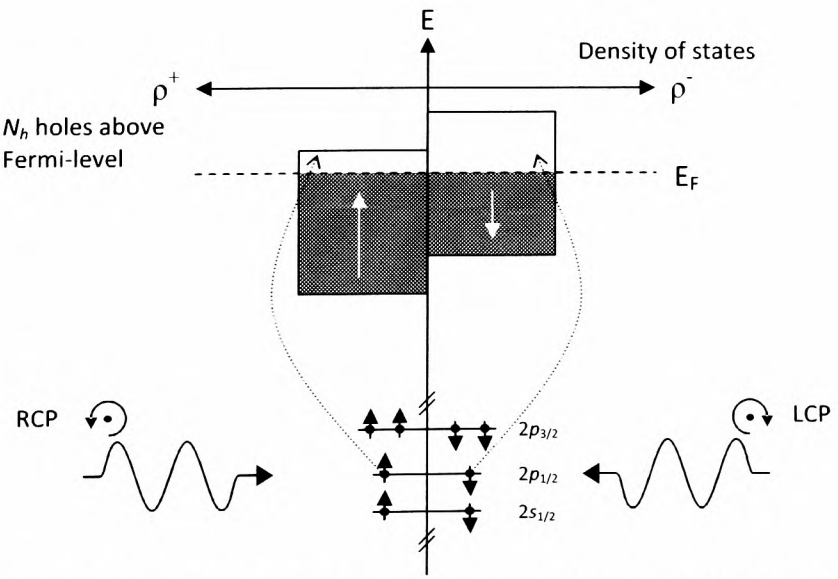

Figure 3.3.4 – Schematic illustration of the split density of 3*d*-states that gives rise to a net magnetic moment in ferromagnetic metals. This may be probed using soft-X-rays to excite core 2*p*-electrons into the empty 3*d*-states.

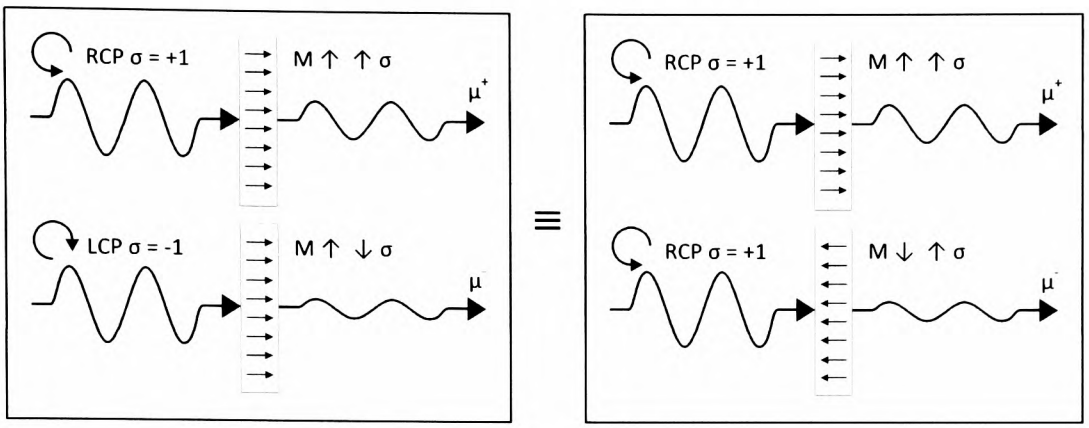

Figure 3.3.5 - XMCD measurement is performed by either switching the polarisation of radiation or the magnetisation of the sample. σ is the photon helicity.

When a circularly polarised photon excites an electron out of a $2p$-state, the photon's angular momentum is transferred in part to the electron through the spin-orbit coupling[3.24, 25]. This does not occur in pure spin states such as the s-states, where the incident photon can only affect the orbital angular momentum. In states where the azimuth quantum number (ℓ) is non-zero, the electron spin is coupled to the orbital momentum, and thus the photon will be able to transfer angular momentum to both parts. As a result of this coupling, spin-polarised photoelectrons are generated, with the polarisation depending on the helicity of the photons. During a dipolar transition spin flips are forbidden, so a "spin-up" photoelectron, for example, must go into a spin-up final state. Since X-ray absorption scales with the number of empty states, it is possible to selectively measure the number of empty spin-up and -down states by switching the polarisation of the photon, or equivalently by switching the magnetisation of the sample as shown in Fig. 3.3.5. The difference between the spectra measured in both cases gives the XMCD signal as illustrated in Fig. 3.3.6. Note the XMCD intensities A and B are opposite in sign for the $2p_{3/2}$ (L_3) and $2p_{1/2}$ (L_2) levels, reflecting the opposite spin-orbit coupling, $(\ell + s)$ and $(\ell - s)$, respectively.

If quantitative analysis of the XMCD signal is required, there are two fundamental sum rules that relate the areas A and B in the XMCD signal to the spin (m_s) and orbital (m_o) components of the total magnetic moment[3.25]:

$$m_s = \frac{\mu_B \langle -A + 2B \rangle}{C} \tag{3.3.2}$$

$$m_o = \frac{-2\mu_B \langle A + B \rangle}{3C} \tag{3.3.3}$$

where μ_B is the Bohr magneton and the constant C is a transition matrix element. A third very important sum rule relates the resonant intensities at the $L_{2,3}$-edges to the total number of *d*-holes, N_h[3.25].

$$N_h = \frac{\langle I_{L_3} + I_{L_2} \rangle}{C} \tag{3.3.4}$$

The resonant intensities I_{L_2} and I_{L_3} are measured with *depolarised* X-rays since both spin-up and -down states need to be included.

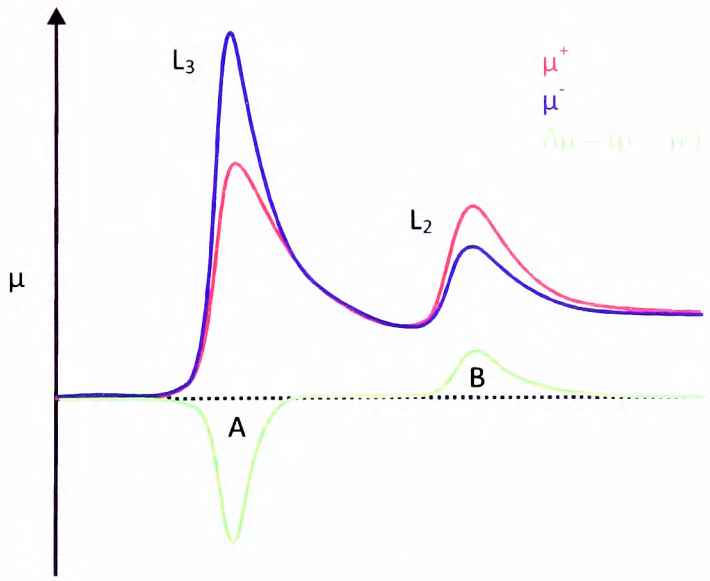

Figure 3.3.6 - The absorption coefficient vs. photon energy at the $L_{2,3}$ edges of Fe. The XMCD signal shown in green can be obtained by taking the difference between the spectra recorded with the photon wave vector parallel and anti-parallel to the magnetisation.

If the transmitted intensity is recorded as a function of sample position, the XMCD effect provides a contrast mechanism by which we can image magnetic domain structure[3.30-33]. Fig. 3.3.7 illustrates an example of this. The magnetic transmission X-ray microscopy (MTXM) image in *A* shows an ALS logo milled into an Fe polycrystalline film with a focussed ion beam. The contrast is mostly due to the variations in the thickness of the Fe, but faint

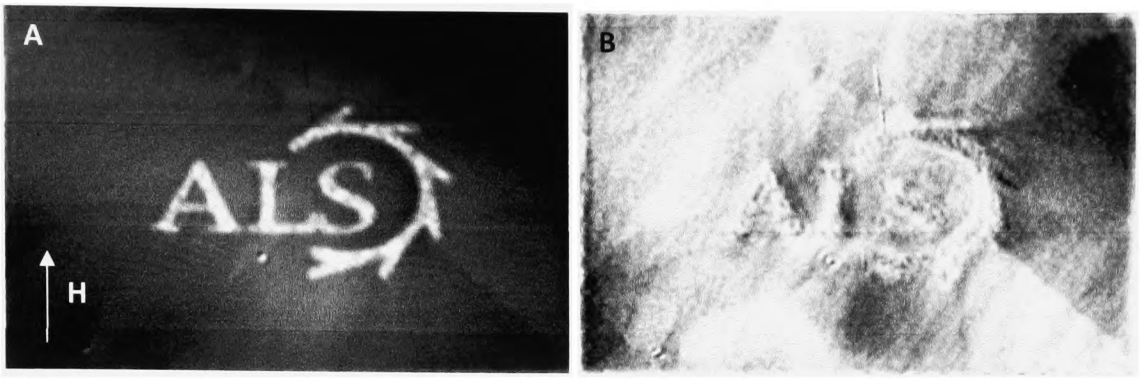

Figure 3.3.7 – An MTXM image of the ALS logo milled into a polycrystalline Fe film using a focussed ion beam at Salford University (*A*). The contrast is mostly due to thickness differences, but faint magnetic contrast can be seen also. By taking images at opposing external magnetic fields and taking the difference provides the XMCD image of the magnetic domains (*B*).

magnetic contrast can be seen, particularly in the right bottom corner. Taking the difference between two images recorded at opposing field values generates an XMCD image as shown in *B*. Here the contrast is mostly caused by variations in the magnetisation direction, thus the magnetic domains can be seen easily.

The example in Fig. 3.3.7 shows imaging of a magnetic film where the magnetisation lies in-plane, but there must be a component of the magnetisation along the photon wave vector. To achieve this, the sample is mounted so that the normal of the surface makes an angle with the wave-vector[3.31], as illustrated below in Fig. 3.3.8. The domains magnetised along the *x*-axis give rise to magnetic contrast, whereas those magnetised along the *y*-axis are indistinguishable. This is analogous to the longitudinal magneto-optical arrangement discussed in section 3.2.

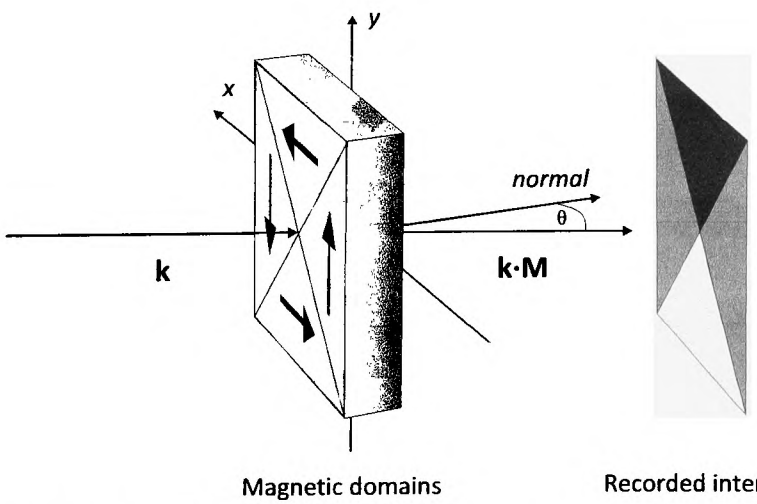

Figure 3.3.8 - A schematic diagram illustrating the measurement of in-plane magnetisation. Only the magnetisation with a component along the photon wave vector gives rise to magnetic contrast on the recorded image.

3.3.4 Magnetic Transmission X-ray Microscopy – ALS Beamline-6.1.2 (XM-1)

The magnetic transmission X-ray microscope (MTXM) at the ALS beamline 6.1.2 (XM-1) is a full-field microscope using Fresnel zone-plates (ZP) to achieve a spatial resolution of 15 nm[3.30, 34]. X-rays from a bending magnet are focussed onto the sample by a condenser ZP. The focal length of the ZP is wavelength-dependent, making it possible to tune the energy through the relative positioning of an OSA[3.34]. The OSA position is adjusted to allow the first order of the desired wavelength through, blocking the unwanted wavelengths. This ZP/OSA combination acts as a liner monochromator, providing a usable energy range of 300-1300 eV. A second zone-plate positioned after the sample projects a full-field image of the sample onto an X-ray-sensitive charge coupled device (CCD).

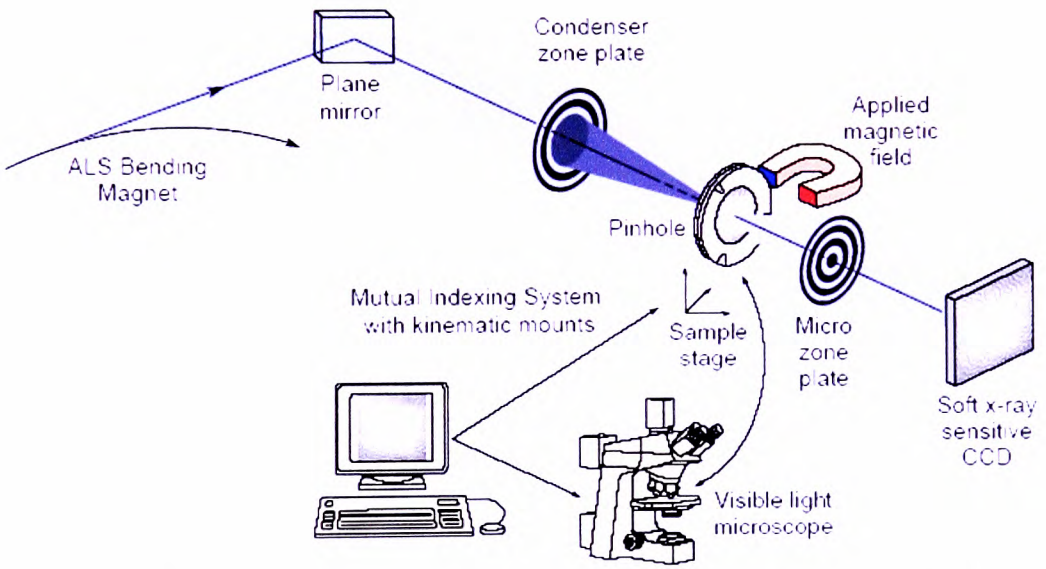

Figure 3.3.9 - A schematic diagram showing the key components of the ALS beamline- 6.2.1 (XM-1). Cited from Ref. (3.33).

The necessary circular polarisation is achieved simply by observing the X-rays emitted a few milliradians off the orbital axis of the bending magnet. This natural polarisation of the light may be visualised by imagining the circular orbit of the electrons in a magnetic field. When viewed along the orbital plane, the electrons appear to move along a horizontal line. When above the axis, an observer will see the electrons circling in one sense, and in the opposite sense when viewing from below the axis, therefore the radiation is naturally polarised depending upon the observer position. XM-1 uses variable slit apertures that may be positioned above or below the orbital plane to provide up to 60-70 % circular polarisation. By adjusting the apertures, the polarisation may be switched to produce the XMCD contrast.

Rather than switching the polarisation, it is often more convenient to flip the magnetisation of the sample. This is achieved using an externally applied magnetic field, which in principle can be as strong as one can produce and orientated in any direction.

The application of an external field also allows domain reversal processes to be studied. This involves applying a field such that the sample is saturated in a given direction, then reversed from zero in discrete steps until saturation is achieved in the opposite direction. A magnified image of the sample is captured at each field step, thus providing an image sequence of the magnetisation reversal mechanism. The process is then repeated in the opposite direction, returning the sample to its original saturated state. Magnetic domain information shows up on the recorded images as additional contrast superimposed upon the structural information (Fig. 3.3.7*A*). In principle, the variations in the pixel values (proportional to the transmitted intensity) at each position throughout the MTXM image sequence represent magnetic hysteresis loops characterising the switching behaviour of the corresponding areas of the sample[3.35].

XMCD images (Fig. 3.3.7*B*) can be produced by either dividing each image within the sequence by one of the sample when saturated (a base image), or alternatively by dividing each image by the one that precedes it in the sequence (sequential difference). The first approach provides a complete picture of the domains at any point during the reversal process with respect to the saturation condition, while the second method shows only the parts of the sample that switch between two successive images. During image acquisition certain artefacts may arise, which can be related to changes in polarisation factor, background intensity or alignment of the optics. Differences in the artefacts tend to be greatest between images recorded at maximum opposing fields, presumably due to shifting of the sample or optics. Also, intensity variations between initial and final images can sometimes occur. These artefacts are more problematic if a single base image is used to generate the XMCD images. The sequential difference technique is advantageous in this respect since artefacts between two successive images are usually minimal and the resulting XMCD images tend to reveal the magnetic signals more effectively. In this thesis, the approach used depends upon which portrays the magnetisation cycle most clearly. Also to shorten acquisition time, the section of the reversal process that goes from maximum $\pm\mathbf{H}$ to $\mathbf{H} = 0$ is often disregarded, or performed with coarser field steps.

3.3.5 Alternative Magnetic Imaging Techniques

When it comes to magnetic imaging, there are numerous possible techniques each with their own strengths and weaknesses. There are several based upon electron microscopy, including scanning electron microscopy with polarisation analysis (SEMPA)[3.36], spin-polarised low energy electron microscopy (SPLEEM)[3.37], X-ray photoemission electron microscopy (X-PEEM)[3.38] and of course, Lorentz microscopy[3.39].

SEMPA works on the principle that secondary electrons emitted from a magnetised surface are spin-polarised. The conventional secondary electron detector is replaced with a spin-analysing detector, which allows for the magnetisation to be mapped. Contrast mechanisms that are observed in conventional SEM can also be observed, providing topographic images as well as magnetic images. The technique can provide high spatial resolution of approximately 10 nm[3.36], and is surface sensitive since the polarised electrons originate from the topmost layers. The disadvantage is that the sample has to be conductive in order to prevent charging.

SPLEEM also has high lateral resolution and surface sensitivity comparable to SEMPA, but spin polarisation is induced by *reflecting* the primary low energy electron beam off the magnetic surface.

Probably one of the most flexible electron microscopy techniques is X-PEEM. It is a combination of PEEM and XAS. In PEEM, ultraviolet light is used to generate photoelectrons, that are subsequently analysed to provide topographical and work function contrast at a high spatial resolution of 10 nm. X-PEEM uses soft X-rays to generate the photoelectrons, which means a slightly lower resolution compared to UV PEEM due to the photoelectrons having a larger energy spread[3.38] However, in addition to the UV PEEM imaging modes, X-PEEM also provides element specificity, and is capable of XAS and XMCD measurements (although spatial resolution of the system in Ref. (3.38) is reduced in XMCD mode).

Lorentz microscopy is probably one of the most widely used of all the electron microscopy techniques for magnetic imaging. Although there is no element specificity, or chemical sensitivity, it offers high spatial resolution (2-20 nm in magnetic imaging mode[3.39]). Unfortunately, the easiest method of obtaining magnetic contrast (Fresnel mode) does not

provide a complete picture of the domains, only the domain walls. There is however, an effect known as magnetisation ripple[3.40] which arises in polycrystalline films as a result of local fluctuations in the magnetisation. Quantification of this effect is rather difficult, but it can at least provide an indication of properties such as local anisotropy[3.40]. These fluctuations in magnetisation are not generally apparent in MTXM images, but might be seen if the resolution could be improved.

All electron microscopy techniques unfortunately require a high vacuum environment and may not be suitable for some samples. Also, the in-situ application of a magnetic field is limited since there are complications with the electron trajectories and column optics. This makes monitoring of the magnetisation reversal processes impossible where high fields are required to saturate the sample.

Magneto-optic techniques described earlier are very popular and since they are convenient for use in a laboratory environment and relatively inexpensive to set up. Using photons to probe the material means measurements don't have to be performed in a vacuum and radiation damage to the sample is rare. What is more, in theory any magnetic field can be applied freely without impairing the measurement system. High temporal resolution is possible, but obviously the spatial resolution is relatively low and there is a lack of element specificity and surface sensitivity. Quantitative comparisons between different samples are not always possible, depending on the setup.

Another popular technique for use in the laboratory is magnetic force microscopy (MFM)[3.41], which again is easily performed. The spatial resolution varies depending on the sharpness of the probe, with a few tens of nanometres being typical[3.41]. The magnetic tip interacts with the stray field produced by the domains in the sample, and consequently there may be a degree of uncertainty as to the origin of the magnetic structure observed. Also, where flux closure states are present, there may not be a large enough stray field for the tip to interact with. The technique is not generally quantitative unless extra measures are taken to calibrate the magnetic tip[3.41].

While the aforementioned techniques are by no means inferior, some of their shortcomings are addressed with MTXM. To summarise the discussion above, MTXM is a quantitative, element specific imaging technique that can provide spatially resolved, element specific maps

of the magnetic moments using the XMCD effect. The photon-in, photon-out nature allows magnetisation reversal processes to be imaged without the magnetic field causing significant disruption to the imaging process. The 15 nm spatial resolution of XM-1 allows these reversal processes to be observed in sub-micron-scale elements. Furthermore, MTXM can be performed in air, making it suitable for a wider variety of samples then electron microscopy-based methods. What it cannot do is provide surface sensitivity, for which the related X-PEEM technique can be used.

References

3.1 L. Reimer, H. Kohl, *Transmission Electron Microscopy: Physics of Image Formation*, 5th ed. New York: Springer, 2008.

3.2 E. Hecht, *Optics*, 4th ed. San Francisco: Addison Wesley, 2002.

3.3 M. J. Freiser, IEEE Transactions on Magnetics **MAG4** (2), 152 (1968).

3.4 K. Brennemann, *Nonlinear Optics in Metals*. New York: Oxford University Press, 1998.

3.5 N. Argyres, Physical Review **97** (2), 334-345 (1955).

3.6 C. Y. You and S. C. Shin, Journal of Applied Physics **84** (1), 541-546 (1998).

3.7 B. Heinrich and J. Bland, *Ultrathin Magnetic Structures: Volume 2*. Berlin: Springer, 2005.

3.8 R. Carey and B. W. J. Thomas, Journal of Physics D-Applied Physics **7** (17), 2362-2368 (1974).

3.9 R. P. Cowburn, D. K. Koltsov, A. O. Adeyeye and M. E. Welland, Applied Physics Letters **73** (26), 3947-3949 (1998).

3.10 D. A. Allwood, G. Xiong, M. D. Cooke and R. P. Cowburn, Journal of Physics D-Applied Physics **36** (18), 2175-2182 (2003).

3.11 G. Xiong, D. A. Allwood, M. D. Cooke and R. P. Cowburn, Applied Physics Letters **79** (21), 3461-3463 (2001).

3.12 M. Grimsditch and P. Vavassori, Journal of Physics-Condensed Matter **16** (9), R275-R294 (2004).

3.13 I. Guedes, N. J. Zaluzec, M. Grimsditch, V. Metlushko, P. Vavassori, B. Ilic, P. Neuzil and R. Kumar, Physical Review B **62** (17), 11719-11724 (2000).

3.14 I. Guedes, M. Grimsditch, V. Metlushko, P. Vavassori, R. Camley, B. Ilic, P. Neuzil and R. Kumar, Physical Review B **66** (1), 9 (2002).

3.15 O. Geoffroy, D. Givord, Y. Otani, B. Pannetier, A. D. Santos, M. Schlenker and Y. Souche, Journal of Magnetism and Magnetic Materials **121** (1-3), 516-519 (1993).

3.16 T. Schmitte, K. Westerholt and H. Zabel, Journal of Applied Physics **92** (8), 4524-4530 (2002).

3.17 J. L. Costa-Krämer, A. Bengoechea, R. Alvarez-Sánchez and F. Briones, IEEE Transactions on Magnetics **41** (11), 4229-4235 (2005).

3.18 A. Westphalen, K. Theis-Bröhl, H. Zabel, K. Rott and H. Brückl, Journal of Magnetism and Magnetic Materials **302** (1), 181-189 (2006).

3.19 C. Cartier dit Moulin, "Interaction of X-rays with matter: Absorption spectroscopy," in *Magnetism and Synchrotron Radiation*, E. Beaurepaire, B. Carrière and J.-P. Kappler, Eds. Les Ulis: Les Éditions de Physique, 1997 pp. 1-18.

3.20 T. Warwick, H. Ade, D. Kilcoyne, M. Kritscher, T. Tylisczcak, S. Fakra, A. Hitchcock, P. Hitchcock and H. Padmore, Journal of Synchrotron Radiation **9**, 254-257 (2002).

3.21 T. Araki, *STXM 5.3.2 User Manual*.

3.22 J. Stöhr and S. Anders, IBM Journal of Research and Development **44** (4), 535-551 (2000).

3.23 G. van der Laan, Physical Review Letters **82** (3), 640-643 (1999).

3.24 J. Stöhr, Journal of Electron Spectroscopy and Related Phenomena **75**, 253-272 (1995).
3.25 J. Stöhr, Journal of Magnetism and Magnetic Materials **200** (1-3), 470-497 (1999).
3.26 J. C. Chapman, Philosophical Magazine **25**, 792-802, 1913.
3.27 G. Schütz, W. Wagner, W. Wilhelm, P. Kienle, R. Zeller, R. Frahm and G. Materlik, Physical Review Letters **58** (7), 737-740 (1987).
3.28 C. T. Chen, F. Sette, Y. Ma and S. Modesti, Physical Review B **42** (11), 7262-7265 (1990).
3.29 H. Ebert, J. Stöhr, S. S. P. Parkin, M. Samant and A. Nilsson, Physical Review B **53** (23), 16067-16073 (1996).
3.30 P. Fischer, D. H. Kim, W. L. Chao, J. A. Liddle, E. H. Anderson and D. T. Attwood, Materials Today **9** (1-2), 26-33 (2006).
3.31 P. Fischer, T. Eimüller, G. Schütz, M. Kohler, G. Bayreuther, G. Denbeaux and D. Attwood, Journal of Applied Physics **89** (11), 7159-7161 (2001).
3.32 T. Eimüller, P. Fischer, G. Schütz, P. Guttmann, G. Schmahl, K. Pruegl and G. Bayreuther, Journal of Alloys and Compounds **286** (1-2), 20-25 (1999).
3.33 T. Eimüller, P. Fischer, M. Köhler, M. Scholz, P. Guttmann, G. Denbeaux, S. Glück, G. Bayreuther, G. Schmahl, D. Attwood and G. Schütz, Applied Physics A-Materials Science & Processing **73** (6), 697-701 (2001).
3.34 P. Fischer, G. Denbeaux, T. Ono, T. Okuno, T. Eimüller, D. Goll and G. Schütz, Journal of Physics D-Applied Physics **35** (19), 2391-2397 (2002).
3.35 D. H. Kim, P. Fischer, W. L. Chao, E. Anderson, M. Y. Im, S. C. Shin and S. B. Choe, Journal of Applied Physics **99** (8), 08H303 (2006).
3.36 M. R. Scheinfein, J. Unguris, M. H. Kelley, D. T. Pierce and R. J. Celotta, Review of Scientific Instruments **61** (10), 2501-2526 (1990).
3.37 E. Bauer, T. Duden and R. Zdyb, Journal of Physics D-Applied Physics **35** (19), 2327-2331 (2002).
3.38 S. Anders, H. A. Padmore, R. M. Duarte, T. Renner, T. Stammler, A. Scholl, M. R. Scheinfein, J. Stöhr, L. Séve and B. Sinkovic, Review of Scientific Instruments **70** (10), 3973-3981 (1999).
3.39 M. S. Cohen, IEEE Transactions on Magnetics **MAG1** (3), 156-& (1965).
3.40 K. D. Leaver, Thin Solid Films **2** (1-2), 149-& (1968).
3.41 A. Yacoot and L. Koenders, Journal of Physics D-Applied Physics **41** (10), 46 (2008).

CHAPTER 4 Stokes Polarimetry for Magneto-Optical Techniques

4.1 Stokes Polarimetry using Photoelastic Modulators

As has been discussed in the preceding chapters, a quantitative analysis of magnetic materials is desirable. In order for this to be achieved with magneto-optical methods, a full and accurate characterisation of the polarisation state of the transmitted or reflected light must be performed, ideally in real-time.

4.1.1 The Stokes Parameters

In 1852 George Stokes introduced four parameters, now known as the Stokes parameters, which provide an experimentally convenient approach to characterising any arbitrarily polarised state of light. Each quantity, commonly denoted as I, Q, U and V, is the sum or difference of two measurable intensities. They are defined as:

$$I = I_{0^\circ} + I_{90^\circ} = I_{45^\circ} + I_{-45^\circ} = I_r + I_l \tag{4.1.1}$$

$$Q = I_{0^\circ} - I_{90^\circ} \tag{4.1.2}$$

$$U = I_{45^\circ} - I_{-45^\circ} \tag{4.1.3}$$

$$V = I_l - I_r \tag{4.1.4}$$

The quantities Q and U both represent differences in detected intensity when light is transmitted through a polariser orientated at two specific angles. Q represents the intensity difference between polariser angles of 0° (I_{0°) and 90° (I_{90°), while for U these angles are ±45° (I_{+45°, I_{-45°). V is the difference between the intensities of the left- and right-handed circularly polarised components. I is the total intensity, which, for fully polarised light should satisfy the following condition:

$$I = \sqrt{Q^2 + U^2 + V^2} \tag{4.1.5}$$

If the light is not fully polarised, then we have a situation where $I > \sqrt{Q^2 + U^2 + V^2}$, in which case we must distinguish between the total intensity, I, and the intensity of the polarised component, I_p, where:

$$I_p = \sqrt{Q^2 + U^2 + V^2} \tag{4.1.6}$$

We may also find the depolarised component, I_{dp}, which is defined here as:

$$I_{dp} = \sqrt{I^2 - I_p^{\,2}} \tag{4.1.7}$$

Once the Stokes parameters have been determined, different aspects of the polarisation state may be calculated. The orientation (or azimuth angle) of the polarisation maybe be obtained using:

$$\Psi = \frac{1}{2}\tan^{-1}\left(\frac{U}{Q}\right) \tag{4.1.8}$$

For elliptically polarised light, the ellipticity angle is given by:

$$\chi = \frac{1}{2}\sin^{-1}\left(\frac{V}{I_p}\right) \tag{4.1.9}$$

The polarisation factor is usually defined as the ratio of the polarised and total intensities:

$$P = \frac{I_p}{I} \tag{4.1.10}$$

The polarisation factor may also be described in terms of the linearly and circularly polarised components, P_L and P_C respectively, given by:

$$P_L = \frac{\sqrt{Q^2 + U^2}}{I} \qquad \text{and} \qquad P_C = \frac{V}{I} \tag{4.1.11}$$

A problem with the definitions in Eqns. 4.1.10 and 4.1.11 is that, rather confusingly, $P \neq P_L + P_C$. Therefore it may be more appropriate to redefine them in the following way. The polarisation factor may be written as:

$$P = \frac{I_p^2}{I^2} \tag{4.1.12}$$

Similarly a depolarisation factor, D, can be defined:

$$D = \frac{I_{dp}^2}{I^2} \tag{4.1.13}$$

The linear and circular polarisation factors, P_L and P_C may also be redefined as:

$$P_L = \frac{Q^2 + U^2}{I^2} \tag{4.1.14}$$

and,

$$P_C = \frac{V^2}{I^2} \tag{4.1.15}$$

This leads to a much more logical situation, where it is always true that $P = P_L + P_C$ and $P + D = 1$.

4.1.2 Dual-Photoelastic Modulator Polarimetry

The influence of a material on the polarisation state of light is measured using a polarimeter, which may be as simple as two crossed polarisers and a detector. If a transparent material placed between the two polarisers changes the polarisation state of the transmitted light, an increase in the intensity is observed at the detector. The angle through which the analysing polariser must be rotated to minimise the detected intensity is equivalent to the optical rotation generated by the sample. Analysis of the magneto-optical effects is sometimes performed using a wave-plate/polariser combination[4.1]. The wave-plate is used to turn the elliptical light transmitted or reflected by the sample into linearly polarised light, which is then analysed by the polariser. Such an approach requires iterative adjustment of the wave-plate and polariser in order to determine the magneto-optical rotation and ellipticity. Consequently hysteresis loops are often just normalised to the saturated state or presented as a modulation of an arbitrary detected intensity[4.1, 2]. In order directly compare the magneto-optical characteristics of different samples an absolute measure of the polarisation state is needed. For this, the wave-plate/polariser combination may be replaced with a photoelastic modulator/polariser combination[4.3].

The photoelastic modulator (PEM), invented by Billardon and Badoz in 1966[4.4], is an optically transparent element (usually fused silica) that is used to modulate the state of polarised light using the photoelastic effect. The optical element vibrates at a natural resonant frequency when driven by a piezoelectric transducer and is shaped in such a way that standing sound waves are setup within it. The stresses generated by the sound waves cause the silica to become birefringent (photoelastic effect), where the optic axis is aligned parallel to the modulated axis. As the crystal is compressed (or stretched), the component of **E** parallel to the modulated axis travels faster (or slower) than the perpendicular component. The phase difference between the two components varies with time, and a modulation of the polarisation state occurs.

In 1969 James Kemp presented a general description of photoelastic modulation[4.5], in which he outlined potential applications for PEM-based polarimeters, including measuring the polarisation state of starlight with an accuracy of 10^{-6}. The application of PEMs in astronomy led to the first direct evidence of the existence of black holes; they now have applications in many different fields.

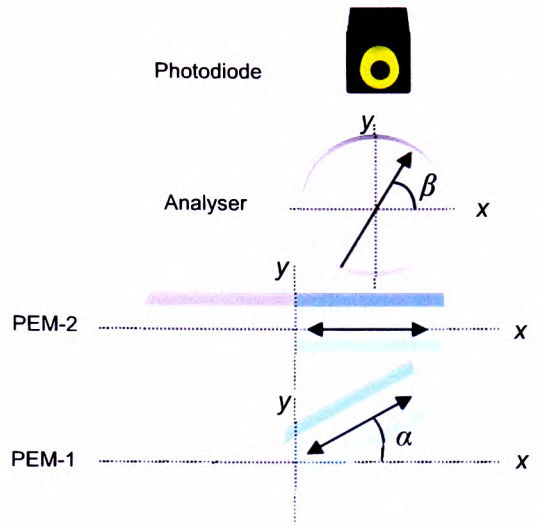

Figure 4.1.1 – Dual-PEM arrangement.

A PEM-based polarimeter may comprise one[4.3, 6-11] or two[4.3, 12-17] PEMs. For real-time measurement of the Stokes parameters, a dual-PEM arrangement is required. While single-PEM polarimeters are simpler, in order to determine all four parameters they require measurements to be made at two dispositions of the PEM and analyser. Figure 4.1.1 shows a schematic diagram of a dual-PEM polarimeter, consisting of PEM-1, PEM-2, an analyser and a photodiode. The analyser, orientated at an angle β to the x-axis, is a linear polariser that converts the modulating polarisation state into an intensity modulation that can be detected by the photodiode. The signal generated by the photodiode contains both *ac* and *dc* components. For monochromatic light passing through the two PEMs and analyser, it can be shown[4.17] that the theoretical intensity, I', at the photodiode is given by Eqn. 4.1.16, where δ_{i0} is the PEM retardation amplitude (in radians), and Ω_i is the modulation frequency (i = 1, 2 for PEM-1 and PEM-2 respectively). $J_0(\delta_{i0})$, $J_m(\delta_{i0})$ and $J_n(\delta_{i0})$ represent standard Bessel functions of the first kind where m and n are odd and even non-zero integers.

$$
\begin{aligned}
I' = {} & \frac{1}{2}I + \frac{1}{2}Q\cos^2(2\alpha)\cos(2\beta) + \frac{1}{4}U\sin(4\alpha)\cos(2\beta) && \text{1-3}\\
& + \frac{1}{2}\sin(2\alpha)\cos(2\beta)[Q\sin(2\alpha) - U\cos(2\alpha)]J_0(\delta_{10}) && 4\\
& + \frac{1}{2}\sin(2\alpha)\sin(2\beta)[Q\cos(2\alpha) + U\sin(2\alpha)]J_0(\delta_{20}) && 5\\
& - \frac{1}{2}\cos(2\alpha)\sin(2\beta)[Q\sin(2\alpha) - U\cos(2\alpha)]J_0(\delta_{10})J_0(\delta_{20}) && 6\\
& + \{\sin(2\alpha)\sin(2\beta)[1 - J_0(\delta_{10})][Q\cos(2\alpha) + U\sin(2\alpha)] + U\sin(2\beta)J_0(\delta_{10})\}\sum_n^{\infty} J_n(\delta_{20})\cos(n\Omega_2 t) && 7\\
& + [\sin(2\alpha)\cos(2\beta) - \cos(2\alpha)\sin(2\beta)J_0(\delta_{20})][Q\sin(2\alpha) - U\cos(2\alpha)]\sum_n^{\infty} J_n(\delta_{10})\cos(n\Omega_1 t) && 8\\
& \mp \sin(2\beta)[Q\sin(2\alpha) - U\cos(2\alpha)]\sum_{m_1}^{\infty}\sum_{m_2}^{\infty} J_{m_1}(\delta_{10})J_{m_2}(\delta_{20})\cos[(m_1\Omega_1 \pm m_2\Omega_2)t] && 9\\
& - \cos(2\alpha)\sin(2\beta)[Q\sin(2\alpha) - U\cos(2\alpha)]\sum_{n_1}^{\infty}\sum_{n_2}^{\infty} J_{n_1}(\delta_{10})J_{n_2}(\delta_{20})\cos[(n_1\Omega_1 \pm n_2\Omega_2)t] && 10\\
& + V\sin(2\beta)J_0(\delta_{10})\sum_m^{\infty} J_m(\delta_{20})\sin(m\Omega_2 t) && 11\\
& + V[\cos(2\alpha)\sin(2\beta)J_0(\delta_{20}) - \sin(2\alpha)\cos(2\beta)]\sum_m^{\infty} J_m(\delta_{10})\sin(m\Omega_1 t) && 12\\
& + V\cos(2\alpha)\sin(2\beta)\sum_m^{\infty}\sum_n^{\infty} J_m(\delta_{10})J_n(\delta_{20})\sin[(m\Omega_1 \pm n\Omega_2)t] && 13\\
& \pm V\sin(2\beta)\sum_n^{\infty}\sum_m^{\infty} J_n(\delta_{10})J_m(\delta_{20})\sin[(n\Omega_1 \pm m\Omega_2)t] && 14
\end{aligned}
\tag{4.1.16}
$$

The first six terms make up the *dc* component, I_{dc}, which is proportional to I, Q and U. The remaining eight terms constitute the *ac* component, which is proportional to Q, U and V. In order to determine both Q and U, it is necessary to measure the 7th term along with any one of the 8th, 9th or 10th terms. The 7th term is denoted here as I_{QU2}, and the additional term as I_{QU1}. V is provided by any one of the last four terms, which we denote I_V. We can then write:

$$I_{dc} = c_1 I + c_2 Q + c_3 U \tag{4.1.17}$$

$$I_{QU1} = c_4 Q + c_5 U \tag{4.1.18}$$

$$I_{QU2} = c_6 Q + c_7 U \tag{4.1.19}$$

$$I_V = c_8 V \tag{4.1.20}$$

where the constants c_i (i = 1..8) contain the terms associated with the angular settings of α and β, and the PEM parameters δ_{i0} and Ω_i.

The *ac* components of I' that represent I_{QU1}, I_{QU2} and I_V may be extracted from the photodiode signal using lock-in amplifiers locked to the Ω_1, $2\Omega_1$, Ω_2 or $2\Omega_2$ PEM reference signals or various combinations thereof. The pure frequencies are generally preferred since composite frequencies require additional electronics to sum the appropriate reference signals. The *dc* component may be measured using a *dc* electrometer. Owing to various characteristics of the experimental arrangement, such as the efficiency of the photodiode and the frequency response of the electronics, I_{dc}, I_{QU1}, I_{QU2} and I_V are not the actual signals that are measured. The measured signals S_{dc}, S_{QU1}, S_{QU2} and S_V are related to I_{dc}, I_{QU1}, I_{QU2} and I_V through proportionality constants v_1, v_2, v_3 and v_4 respectively.

$$S_{dc} = v_1 I_{dc} = g_1 I + g_2 Q + g_3 U \tag{4.1.21}$$

$$S_{QU1} = v_2 I_{QU1} = g_4 Q + g_5 U \tag{4.1.22}$$

$$S_{QU2} = v_3 I_{QU2} = g_6 Q + g_7 U \tag{4.1.23}$$

$$S_V = v_4 I_V = g_8 V \tag{4.1.24}$$

The above equations are then written in matrix form:

$$\begin{pmatrix} S_{dc} \\ S_{QU1} \\ S_{QU2} \\ S_V \end{pmatrix} = \begin{pmatrix} g_1 & g_2 & g_3 & 0 \\ 0 & g_4 & g_5 & 0 \\ 0 & g_6 & g_7 & 0 \\ 0 & 0 & 0 & g_8 \end{pmatrix} \begin{pmatrix} I \\ Q \\ U \\ V \end{pmatrix} = G \begin{pmatrix} I \\ Q \\ U \\ V \end{pmatrix} \tag{4.1.25}$$

A matrix inversion on G is required, the result of which may be written as:

$$\begin{pmatrix} I \\ Q \\ U \\ V \end{pmatrix} = \begin{pmatrix} k_1 & k_2 & k_3 & 0 \\ 0 & k_4 & k_5 & 0 \\ 0 & k_6 & k_7 & 0 \\ 0 & 0 & 0 & k_8 \end{pmatrix} \begin{pmatrix} S_{dc} \\ S_{QU1} \\ S_{QU2} \\ S_V \end{pmatrix} = K \begin{pmatrix} S_{dc} \\ S_{QU1} \\ S_{QU2} \\ S_V \end{pmatrix} \tag{4.1.26}$$

where K is a set of constants that are specific to the experimental setup and need to be determined before the Stokes parameters can be calculated. This is achieved through a calibration process, which will be described in detail in section 4.3.

4.2 *A Practical Magneto-Optical Stokes Polarimeter*

A schematic diagram of a polarimeter constructed for the purpose of characterising optically transparent magnetic samples is shown in Fig. 4.2.1. Photographs of the system are shown in Fig. 4.2.2. The measurement system can be described in terms of three sections: a light source, sample stage assembly and polarimeter.

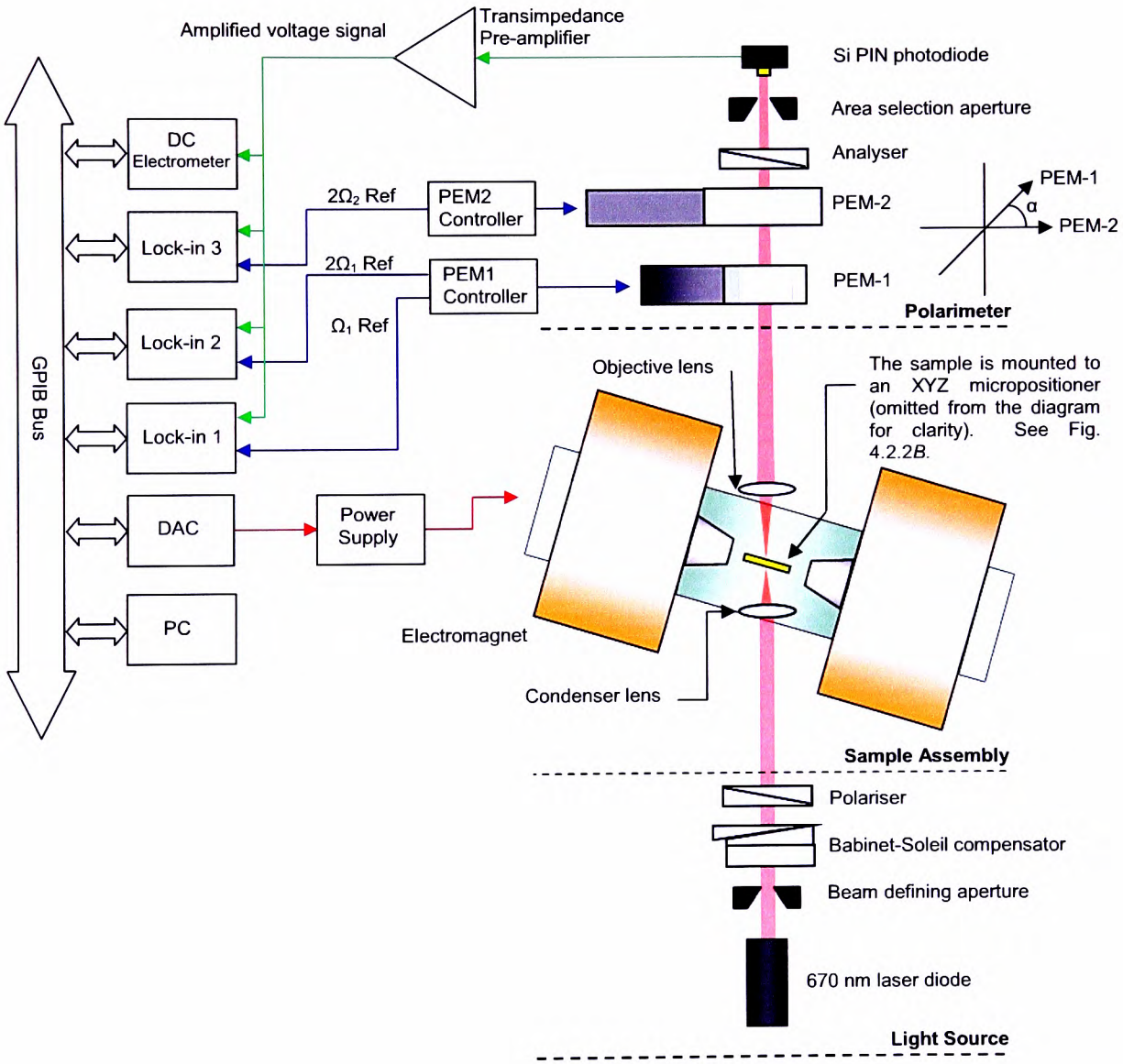

Figure 4.2.1 - A schematic diagram of the magneto-optical Stokes polarimeter.

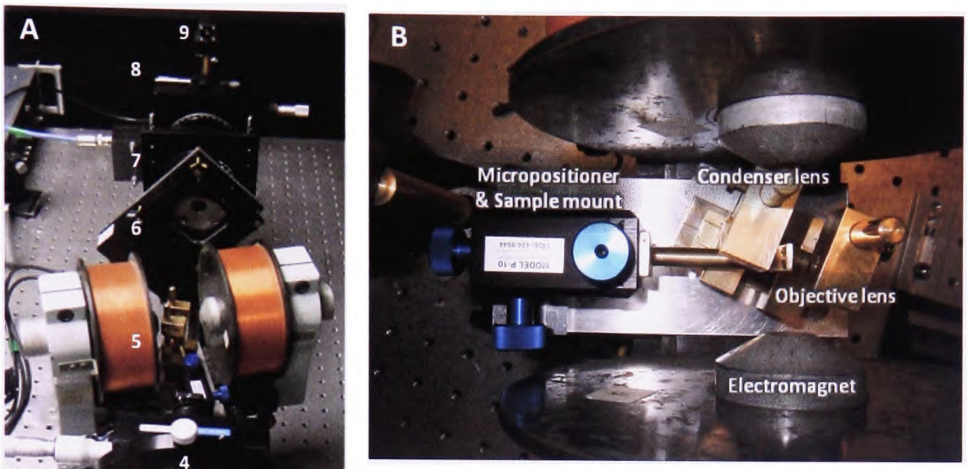

Figure 4.2.2 – *A*: A photograph of the polarimeter. The components visible are the: (1) laser, (2) neutral density filter, (3) polariser, (4) Babinet-Soleil compensator, (5) electromagnet/sample mount and lenses, (6) PEM-1, (7) PEM-2, (8) analysing polariser (hidden behind 7) and (9) Si-PIN photodiode. *B*: A close-up photograph of the sample mount and lens assembly.

The Light Source: The light source comprises a 6 mW laser diode with a wavelength of 670 nm, and the various optical components for conditioning the light beam. The polarisation state of the light is controlled using a combination of a Babinet-Soleil compensator (Spectral Optics 8-400) and a Glan-Thompson polariser. The polariser angle is denoted here as θ, and is measured with respect to the laboratory x-axis. Since laser light is already linearly polarised to a large degree (typically 99%), there is a large variation in the beam intensity as the polariser is rotated. To avoid this, the compensator can be calibrated to produce close to a quarter-wave retardation and then placed between the laser and the polariser such that it effectively "depolarises" the laser light. When circularly polarised light is required, the polariser and compensator are interchanged. The polariser then has to be set within an appropriate range of angles such that the intensity is sufficiently high. With the fast-axis of the compensator orientated parallel to the laboratory x-axis, circular polarisation is achieved by rotating the polariser to ±45°.

Sample Stage Assembly: The sample stage assembly consists of an electromagnet, a three-axis micropositioner to which the sample is mounted, a condenser lens to focus light onto the sample and an objective lens to focus the transmitted light through the polarimeter. The sample is mounted with its surface always fixed parallel to the applied field, but the whole assembly may be rotated such that the sample surface normal makes an angle up to 25-30°

with the beam direction; this is necessary when characterising films with in-plane magnetisation. The lenses may be rotated independently of the sample and electromagnet to ensure their optical axes remain parallel to the beam direction. A short focal length condenser lens focuses the light through the sample, which is then collected by the objective lens and projected to form a magnified image of the sample upon an adjustable aperture in front of the photodiode. The arrangement effectively operates as a simple full-field microscope with a variable field of view and magnification. The size of the illuminated area may be varied by adjusting the condenser lens position relative to the sample. A spot size of less than 20 μm is achievable, but 50-100 μm is typical for sample measurement. By observing the projected image, the desired area of the sample is brought into the field of view using the micropositioner. The aperture diameter and position are then adjusted to allow only the light from a specific area of the image to pass through to the photodiode.

The Polarimeter: The polarimeter, as previously described in section 4.1, uses two PEMs, an analysing polariser and a photodiode. It is essential that the resonant frequencies of the two PEMs are different in order that the signals be can be recovered by the electronics; typically a 2 kHz difference is sufficient. The two PEMs used in this system, denoted as PEM-1 and PEM-2, are from the Hinds Instruments PEM-90 series with natural resonant frequencies of 42 kHz and 50 kHz respectively.

In order to set the orientation of PEM-1 to the desired value of α, it is first necessary to determine the x-axis of the polarimeter. With both PEMs removed from the beam path, the polariser is orientated at 0° as indicated by its own rotary mount. This initial setting determines the orientation of the polarimeter x-axis. The analyser is then rotated until the *dc* signal from the photodiode is minimised, indicating that the passing axes of the polariser and analyser are orthogonal. In turn, the PEMs are placed back into the beam path and orientated such that the modulated axes are parallel (or perpendicular) to the polariser by adjusting them such that the *dc* signal is at a minimum. Once aligned, the orientation of PEM-2 should remain unchanged since its modulated axis defines the x-axis of the polarimeter. PEM-1 may then be rotated to the desired value of α.

The final component in the polarimeter is the Si-PIN photodiode. It is essential that the photodiode responds linearly to the variations in light intensity typically encountered during normal operation of the polarimeter. To test photodiode response, the photocurrent was

measured as a function of light intensity. A laser was used as the light source and the intensity was varied by adjusting the relative angle between the passing axes of two polarisers (γ). According to Malus' law, the intensity of the light transmitted through the second polariser is proportional to $\cos^2(\gamma)$. The plot of photodiode current versus $\cos^2(\gamma)$ in Fig. 4.2.3 shows a linear response up to the maximum photocurrent of 60 μA. Even the full intensity of the laser was insufficient to saturate the photodiode.

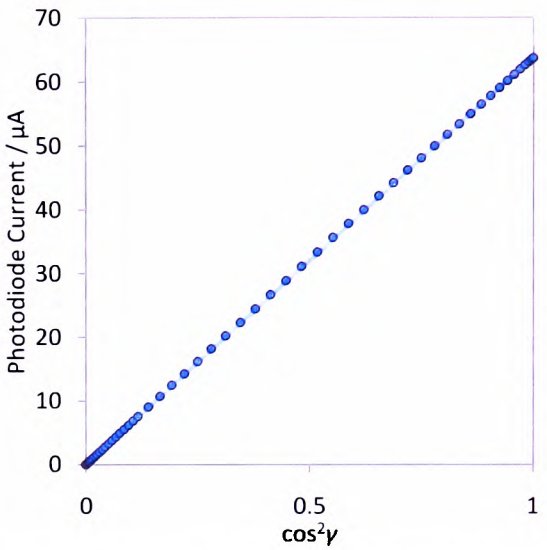

Figure 4.2.3 – The photodiode response is linearly proportional to the incident intensity.

Data Acquisition: The small photocurrent generated by the photodiode is converted into a larger voltage signal by a transimpedance pre-amplifier*, allowing the four signals to be measured simultaneously using a Keithley 6517 electrometer and three separate lock-in amplifiers; a Stanford Research Systems SR810 DSP, an EG&G 5209 and a PerkinElmer 7265. The lock-in amplifiers measure the *ac* signals, S_{QU1}, S_{QU2} and S_V, by locking to the $2\Omega_1$, $2\Omega_2$ and Ω_1 PEM frequencies respectively. Data acquisition is performed by a personal computer running custom software, which is also responsible for controlling the energising voltage applied to the electromagnet, allowing automated measurement of hysteresis loops.

To ensure the electronics were operating linearly, the S_{dc}, S_{QU1}, S_{QU2} and S_V signals were measured as a function of intensity (Fig. 4.2.4). Since the S_{dc} signal is not always a direct measure of the true intensity, this was determined with the PEMs switched off. All amplifiers appeared to respond linearly with intensity apart from that used to measure the S_V signal. When the Ω_1 *ac* component dropped to approximately 0.6 mV, as measured by the lock-in amplifier, the signal response was no longer linear. This was found to be an issue with the amplifier's ability to track the phase of very small signals reliably. For sample measurement purposes, a small degree of ellipticity was introduced to increase the Ω_1 *ac* component of the signal to a level more suitable for the amplifier.

* Details of a pre-amplifier that may be used for low frequency signals are given in Appendix 1. A commercial pre-amplifier was used for most of the work presented here.

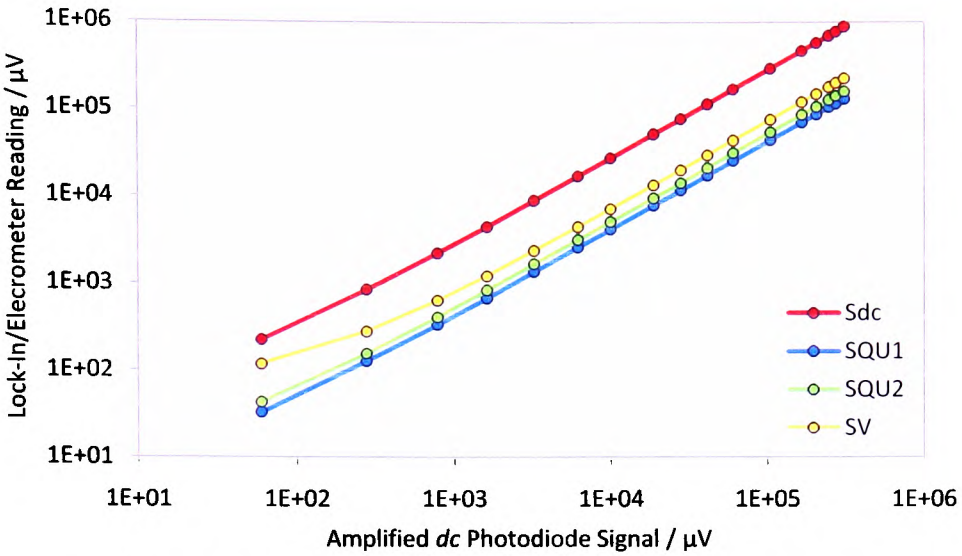

Figure 4.2.4 – The S_{dc}, S_{QU1}, S_{QU2} and S_V signals are measured as a function of light intensity. The light intensity was measured with the PEMs switched off to obtain the true *dc* signal. Logarithmic scales have been used to show the low signal region more clearly.

4.3 *Dual-PEM Polarimeter Calibration Methods*

In order for the polarimeter to provide quantitative measurements of the polarisation state, the matrix of constants, K, must first be determined. It is possible to compute the theoretical values of k_i (i = 1..8) by choosing specific values of α, β, δ_{10} and δ_{20} and evaluating each term in Eqn. 4.1.16, but doing so will inevitably bring about the introduction of errors into the measurement if the physical arrangement differs[4.17]. In addition, the bandwidth limitations of the electronics may result in an attenuated signal at the higher frequencies, which, coupled with differences between the internal electronics of the three lock-in amplifiers, will make the actual constants somewhat different to those theoretically calculated. It is therefore preferable to perform a calibration procedure to account for these issues.

4.3.1 Linear Regression

Linear regression is the simplest approach to calibration, but requires the polarimeter to be configured in one of three ways[4.17], the most commonly used being: $\alpha = 45°$, $\beta = 22.5°$ and $\delta_{10} = \delta_{20} = 2.4048$ rad[4.3, 12, 13]. δ_{10} and δ_{20} are set such that $J_0(\delta_{i0})$ in Eqn. 4.1.16 reduces to zero. Other terms are also eliminated by setting $\alpha = 45°$, which leads to the diagonalisation of K ($k_2 = k_3 = k_5 = k_6 = 0$) and we find that S_{dc}, S_{QU1}, S_{QU2} and S_V are all proportional to individual Stokes parameters. Assuming negligible depolarisation occurs (P = 1), Eqn. 4.1.5 will be satisfied, then from Eqn. 4.1.26 it becomes apparent that:

$$k_1^2 S_{dc}^{\ 2} = k_4^2 S_{QU1}^{\ 2} + k_7^2 S_{QU2}^{\ 2} + k_8^2 S_V^{\ 2} \tag{4.3.1}$$

The first constant, k_1, can only be determined if the quantum efficiency of the detector is known; it will suffice for most purposes to give this the value of unity. If the four signals are measured using a wide range of linear and elliptical polarisation states, then k_4^2, k_7^2 and k_8^2 can be determined using linear regression. While this is mathematically convenient, it may not provide an accurate determination of the constants, since any deviation from the indented values of α, δ_{10} and δ_{20} will result in non-zero values for k_2, k_3, k_5 and k_6. Determining K then becomes a non-linear problem to which linear regression cannot be applied. A commercially available dual-PEM polarimeter[4.12] fixes α at 45° to reduce this error as much as possible, but there is still the matter of ensuring $J_0(\delta_{10})$ and $J_0(\delta_{20})$ are close to zero.

4.3.2 Four-State Calibration Method

An alternative method of calibration is available[4.18], in which K is determined by reducing the terms in Eqn. 4.1.16, not by setting δ_{10} and δ_{20}, but by forcing certain Stokes parameters to zero. This is achieved by controlling the polarisation state of the light source.

The calibration begins with the use of linearly polarised light such that $P = P_L = 1$, therefore all terms associated with V are reduced to zero. Provided that $\alpha = 45°$, it is also possible to reduce the terms associated with either Q or U to zero, by setting the polariser angle (θ) to four specific values, they are 0°, 45°, 90° and -45°. At $\theta = 0°$ and 90° the condition ($I = \pm Q$, $U = V = 0$) occurs, and similarly when $\theta = \pm 45°$, ($I = \pm U$, $Q = V = 0$). Using Eqn. 4.1.26, expressions can be obtained for each relationship as shown in Table 4.3.1. From these expressions, k_2, k_3, k_4 and k_7 normalised to k_1 (where $k_1 = 1$) can be calculated as follows:

$$\frac{k_2}{k_1} = -\frac{a+c}{2} \tag{4.3.2}$$

$$\frac{k_3}{k_1} = -\frac{b+d}{2} \tag{4.3.3}$$

$$\frac{k_4}{k_1} = \frac{a-c}{2} \tag{4.3.4}$$

$$\frac{k_7}{k_1} = \frac{b-d}{2} \tag{4.3.5}$$

where a, b, c and d are ratios of two measured signals at each polariser orientation.

What is apparent here is that this method allows k_2 and k_3 to be determined. These constants are associated with the values of $J_0(\delta_{10})$ and $J_0(\delta_{20})$ which usually have to be zero (or close to), requiring specific PEM retardation settings. The ability to experimentally determine k_2 and k_3 means that these retardation settings can be relaxed and any error associated with setting them is eliminated.

The final step in the calibration is to determine k_8. For this, a component of circular polarisation is generated by inserting an arbitrary retardation plate after the polariser. All four signals (S_{dc}, S_{QU1}, S_{QU2} and S_V) are measured, from which I, Q and U are calculated using the

previously determined constants. Assuming negligible depolarisation occurs within each optical element, V may be calculated by rearranging Eqn. 4.1.5, and subsequently k_8 using the relation:

$$V = \frac{k_8}{k_1} S_v \tag{4.3.6}$$

Unfortunately there is the disadvantage that any errors in k_2, k_3, k_4 and k_7 will be summed together in the determination of k_8.

θ	Forced Relationships Between *I*, *Q* and *U*	Derived Expression	Measured Signals
0°	*I*=*Q*, *U*=0	$\frac{S_{dc}}{S_{QU1}} = \frac{k_4 - k_2}{k_1} = a$	$S_{dc,0}$, $S_{QU1,0}$
45°	*I*=*U*, *Q*=0	$\frac{S_{dc}}{S_{QU2}} = \frac{k_7 - k_3}{k_1} = b$	$S_{dc,45}$, $S_{QU2,45}$
90°	*I*=-*Q*, *U*=0	$\frac{S_{dc}}{S_{QU1}} = -\frac{k_2 + k_4}{k_1} = c$	$S_{dc,90}$, $S_{QU1,90}$
-45°	*I*=-*U*, *Q*=0	$\frac{S_{dc}}{S_{QU2}} = -\frac{k_7 + k_3}{k_1} = d$	$S_{dc,-45}$, $S_{QU2,-45}$

Table 4.3.1 – The relationships set up between I, Q and U give rise to four expressions. Two measurements are required at each of the four special polariser angles.

4.3.3 Non-Linear Optimisation

During the course of this work, a more flexible calibration method has been developed which uses an iterative algorithm to fit values to each of the constants based on a several measurements of known linear polarisation states and unknown elliptical states. All constants may be found, including k_5 and k_6, thus in principle, all constraints previously imposed on the polarimeter configuration may be relaxed.

This method is demonstrated here using the standard Microsoft Excel Solver, which uses a version of the Generalised Reduced Gradient Algorithm (GRG2) to solve non-linear optimisation problems[4.19]. The algorithm must be supplied with a continuous function that minimises, maximises or has a known value when the specified variables, reach their ideal values. The algorithm estimates the partial derivatives of the function with respect to each variable using a finite difference method. The values of the variables are then shifted in the direction of reducing gradient. In a non-linear function there may be a number of points at

which the gradient is minimised and thus the algorithm will find the local optimum solution. In this case, global optimisation may require several executions of the algorithm with randomly selected starting values of the variables.

A model is presented here for the purpose of polarimeter calibration, where a value derived from errors associated with the polarisation factor and azimuth angle of various polarisation states must be minimised by fitting appropriate values to the constants, k_i ($i = 2...8$). Since all measurements are of fully polarised states (assuming virtually no depolarisation) the deviation of P from unity can be considered an error. This leads to two expressions that should have values close to zero when the constants are correctly fitted, the first of which is:

$$\varepsilon_{1i} = \gamma_1 \left(I_i^2 - I_{p_i}^2 \right)^2 = \gamma_1 I_{dp_i}^4 \tag{4.3.7}$$

The second error is defined as:

$$\varepsilon_{2i} = \gamma_2 \left(\frac{I_i^2}{I_{p_i}^2} - 1 \right)^2 = \gamma_2 \frac{I_{dp_i}^4}{I_{p_i}^4} \tag{4.3.8}$$

where γ_1 and γ_2 are scaling factors that may be adjusted in order to improve optimisation procedure.

Although ε_{1_i} and ε_{2_i} depend upon all of the constants, alone they are not sufficient to establish the correct relationship between k_4, k_5, k_6 and k_7. Take ε_{1_i} for example, k_4, k_5, k_6 and k_7 only enter the expression through Q and U in I_p (see Eqn. 4.1.6). Rewriting Eqn. 4.3.7 with I_p in terms of the individual Stokes parameters gives:

$$\varepsilon_{1i} = \gamma_1 \left(I_i^2 - Q_i^2 - U_i^2 - V_i^2 \right)^2 \tag{4.3.9}$$

Then, writing Q and U in terms of the measured signals and k_4, k_5, k_6 and k_7 gives:

$$\varepsilon_{1i} = \gamma_1 \left(I_i^2 - \left(k_4 S_{QU1_i} + k_5 S_{QU2_i} \right)^2 - \left(k_6 S_{QU1_i} + k_7 S_{QU2_i} \right)^2 - V_i^2 \right)^2 \tag{4.3.10}$$

The algorithm tries to reduce the value of ε_{1_i} to a minimum, but it can be seen from Eqn. 4.3.10 that there is no explicit relationship between k_4, k_5, k_6 and k_7 that will lead the

algorithm to the correct solution. There could be any number of combinations of the constants that satisfy the condition $\varepsilon_{1_i} = 0$ since the relationship between Q and U is not defined. The same can be said for ε_{2i}, therefore another expression is needed. The most obvious way to relate Q and U is through calculation of the azimuth angle, which is usually performed using Eqn. 4.1.8. However, since a continuous function is desired for the algorithm to work most effectively, the tangent function should be avoided. Alternatively, the azimuth angle may be calculated using:

$$\Psi = \frac{1}{2}\cos^{-1}\left(\frac{Q}{I_l}\right) \qquad \text{or} \qquad \Psi = \frac{1}{2}\sin^{-1}\left(\frac{U}{I_l}\right) \tag{4.3.11}$$

where I_l is the intensity of the linearly polarised component, i.e. $I_l = \sqrt{Q^2 + U^2}$. If linearly polarised states are measured, then the difference between the set polariser angle and the measured azimuth angle can provide a third error that must be minimised by the algorithm. This leads to the following expression:

$$\varepsilon_{3i} = \gamma_3\left(\frac{Q_i}{I_{l_i}} - \cos(2\theta_i)\right)^2 + \gamma_3\left(\frac{U_i}{I_{l_i}} - \sin(2\theta_i)\right)^2 \tag{4.3.12}$$

where γ_3 is another scaling factor.

Where there are a total of m measured polarisation states, the first n of which are linear, the function supplied to the algorithm is then:

$$\varepsilon_{total} = \varepsilon_{1t} + \varepsilon_{2t} + \varepsilon_{3t} = \sum_{i=1}^{m}\varepsilon_{1i} + \sum_{i=1}^{m}\varepsilon_{2i} + \sum_{i=1}^{n}\varepsilon_{3i} \tag{4.3.13}$$

A practical example of this calibration method is given in the next section.

4.4 *A Practical Comparison of Calibration Methods*

4.4.1 Experimental Arrangement

In order to allow for a direct comparison between each calibration method, the polarimeter described in section 4.2 was configured such that $\alpha = 45°$ and $\delta_{10} = \delta_{20} = 2.4048$ rad. This is one of the three arrangements that permit linear regression[4.17]. Three sets of data were collected: set *A* comprises measurements of linearly polarised light at the four special polariser angles (0°, 45°, 90° and -45°); set *B* includes a large range of elliptical polarisation states; finally, set *C* contains measurements of linearly polarised light at known values of θ, ranging from 0° to 45°. The measurements as recorded by the lock-in amplifiers and *dc* electrometer are listed in Appendix 2.

The validity of the calibration constants obtained using each method was tested in three ways. Firstly, by combining data sets *A*, *B* and *C*, a plot of I^2 versus I_p^2 was created, the gradient of which represents the average polarisation factor (as defined in Eqn. 4.1.12) and should be very close to unity. Secondly, the polarisation factor was calculated for each individual measurement. The deviation in the measured *P* from unity is:

$$\varepsilon_P = |P - 1| \tag{4.4.1}$$

The average and maximum deviations in *P*, $\langle \varepsilon_P \rangle$ and $\varepsilon_{P\max}$, then provided additional checks of the correlation between *I* and I_p. The final check, for the linearly polarised states in set *C*, is the difference between the measured azimuth angle and the intended polariser setting. This provided an indication of the validity of k_4 and k_7. The deviation in the azimuth measurement, ε_Ψ, is defined as:

$$\varepsilon_\Psi = \big||\Psi| - |\theta|\big| \tag{4.4.2}$$

At polariser angles of 0°, 45°, 90° and -45°, either one of S_{QU1} or S_{QU2} becomes very small and thus can fluctuate randomly between positive and negative values. As a result, it is often the case that the sign of Ψ is opposite to that of θ, for this reason the absolute value of Ψ and θ are taken in Eqn. 4.4.2. Setting of the polariser angle is limited by the precision of its rotary

mount: 5 arc-min in this case. Therefore the average and maximum ($\langle \varepsilon_\Psi \rangle$ and $\varepsilon_{\Psi\,\max}$) azimuth errors should be approximately 2.5 arc-min (0.04°).

4.4.2 Linear Regression

With all of the measurements in data sets *A*, *B* and *C*, linear regression was performed using Eqn. 4.3.1. The values obtained for k_4, k_7 and k_8 were 2.5596, 1.9864 and 2.2790 respectively. A plot of I^2 versus I_p^2 is shown in Fig. 4.4.1, from which it is evident that linear regression did not provided an adequate fit to the constants. Consequently, the azimuth errors are large, with the average and maximum values being 0.21° and 0.37° respectively. The values of $\langle \varepsilon_P \rangle$ and $\varepsilon_{P\,\max}$ are also relatively large, with values of 0.07 and 0.17 respectively.

A clue to the source the error may be found by observing the data points corresponding to data set *A* in Fig. 4.4.1. Firstly, it is worth clarifying that at $\theta = 0°$ it *should* be the case that $I = I_p = Q$ and $U = 0$. Similarly, at $\theta = 90°$, $I = I_p = -Q$ and $U = 0$, thus the following is obtained from Eqn. 4.1.26:

$$S_{dc0} = k_4 S_{QU1_0} \qquad \text{and} \qquad S_{dc90} = -k_4 S_{QU1_{90}} \tag{4.4.3}$$

From Fig. 4.4.1, it is evident that at a polariser angle of 0°, $I^2 > I_p^2$, which means $S_{dc0} > k_4 S_{QU1_0}$. At 90°, $I^2 < I_p^2$, therefore $S_{dc90} < -k_4 S_{QU1_{90}}$. If it is now assumed that k_2 is in fact non-zero and the matrix *K* is not diagonalised, then the following is true:

$$S_{dc0} + k_2 S_{QU1_0} = k_4 S_{QU1_0} \qquad \text{and} \qquad S_{dc90} + k_2 S_{QU1_{90}} = -k_4 S_{QU1_{90}} \tag{4.4.4}$$

It now becomes apparent that in order to make *I* equal to I_p, then k_2 has to be made small and negative. Applying the same argument to the cases where $\theta = \pm 45°$, we find that k_3 should also be small and negative. This suggests that that the actual values of δ_{10} and δ_{20} are such that $J_0(\delta_{10}) \neq J_0(\delta_{20}) \neq 0$, in which case linear regression is not applicable and an alternative calibration method must be used.

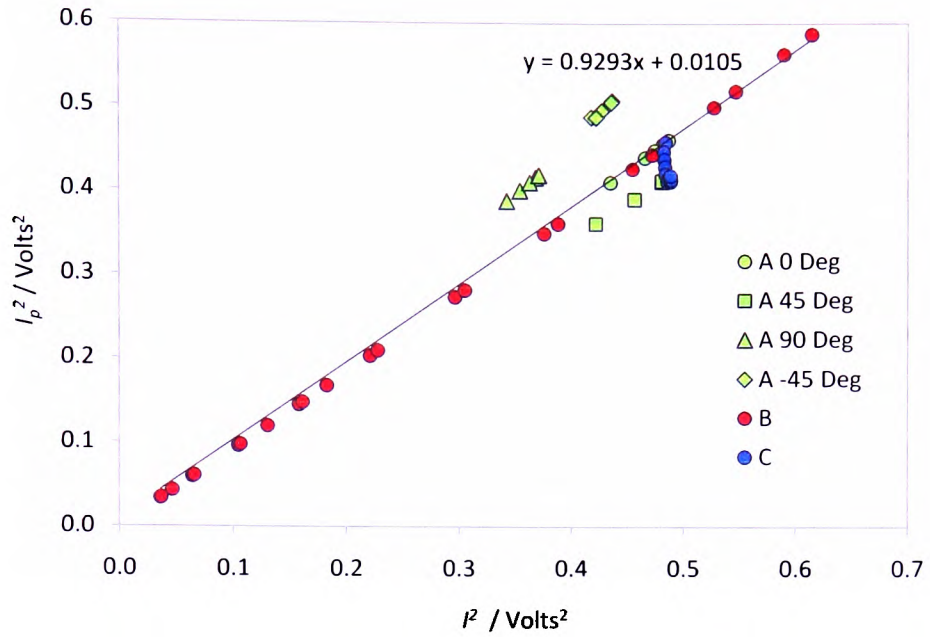

Figure 4.4.1 – I^2 vs. I_p^2 for each measurement in data sets *A*, *B* and *C*, calculated using the constants determined by linear regression.

4.4.3 Four-State Calibration Method

Using data set *A*, the first stage of the calibration was performed, where the values *a*, *b*, *c* and *d*, and subsequently k_2, k_3, k_4 and k_7 were calculated using equations 4.3.2 to 4.3.5. In theory, only one set of measurements at polariser angles of 0°, 45°, 90° and -45° is required, however, each of the four states was measured several times in order to determine the degree of reproducibility. The values of the constants calculated from each sub-set of measurements are listed in Table 4.4.1.

The final constant, k_8, was then determined using the measurements of elliptically polarised states in data set *B*. When the component of circular polarisation (P_C) is low, the calculation of k_8 becomes susceptible to small errors in *I* and either *Q* or *U*. Consequently, in the plot of k_8 versus ellipticity angle (χ) (Fig. 4.4.2), k_8 begins to decrease rapidly as χ falls below 15°. For this reason, the mean value of k_8 was calculated using ellipticity angles greater than 15°. At χ = 5°, k_8 deviates from the mean by 13%, but this may be corrected by just a 0.35 % change to either *I* or *Q*, illustrating the degree of sensitivity to small errors.

Calibration Set	k_2	k_3	k_4	k_7
1	-0.1133	-0.1534	2.5187	1.9897
2	-0.1142	-0.1523	2.5160	1.9926
3	-0.1124	-0.1508	2.5162	1.9930
4	-0.1120	-0.1510	2.5169	1.9936
5	-0.1117	-0.1482	2.5174	1.9943
Mean	-0.1127	-0.1511	2.5170	1.9926
Standard Deviation	0.0010	0.0019	0.0011	0.0018
Standard Deviation (%)	0.89	1.26	0.04	0.09

Table 4.4.1 – The calibration constants obtained from five different sets of measurements of S_{dc}, S_{QU1} and S_{QU2} at the four special polariser angles.

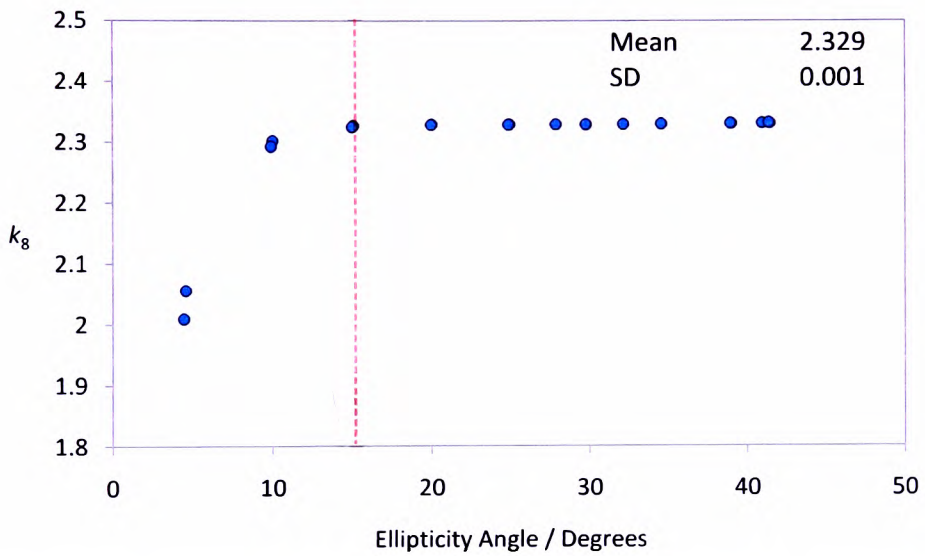

Figure 4.4.2 – The calculated values of k_8 across a wide range of elliptically polarised states. The mean and standard deviation are only calculated for states where $\chi > 15°$ (marked by red dashed line).

The ability to determine k_2 and k_3 allows for a much improved correlation between I^2 and I_p^2 as illustrated by Fig. 4.4.3. Accordingly, the values of $\langle \varepsilon_P \rangle$ and $\varepsilon_{P\max}$ reduced to 1.9×10^{-3} and 9×10^{-3} respectively and there was a simultaneous reduction in $\langle \varepsilon_\Psi \rangle$ and $\varepsilon_{\Psi\max}$ to 0.05° and 0.11° respectively. While $\langle \varepsilon_\Psi \rangle$ is acceptable, $\varepsilon_{\Psi\max}$ appears to be too large considering that the polariser may be set to within ±0.04°.

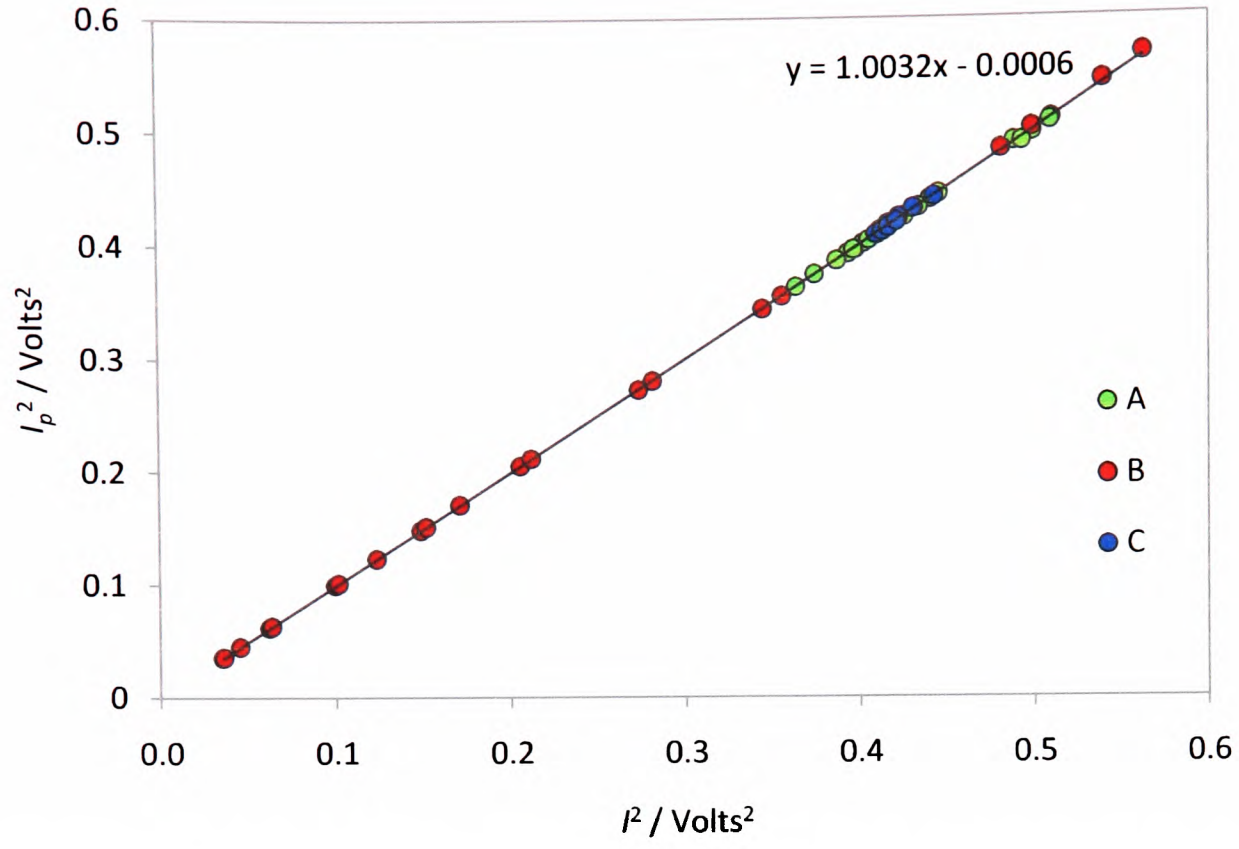

Figure 4.4.3 – I^2 vs. I_p^2 for each measurement in data sets *A*, *B* and *C*, calculated using the constants determined using the four-state calibration method.

4.4.4 Non-Linear Optimisation

For all measurements in data sets *A*, *B* and *C*, the values ε_{1_t}, ε_{2_t} and ε_{3_t} were calculated and summed together to give ε_{total} (Eqn. 4.3.13). With k_5 and k_6 set to zero, and all other non-zero constants given the initial value of unity, the optimisation procedure provided a solution to *K* that resulted in a small reduction in all of the errors in comparison to the previous calibration procedures. Moreover, by also allowing the algorithm to fit values to k_5 and k_6 a further reduction in the errors was possible. It was found that the solution was sensitive to the relative magnitude of the error functions. Several executions of the procedure were required using a range of values for γ_1, γ_2 and γ_3 in order to determine that setting $\gamma_1 = \gamma_2 = 1$ and $\gamma_3 = 10$ provided the most significant overall improvement in the measurement errors. Using this configuration, the following solution was obtained:

$$K = \begin{bmatrix} 1 & -0.1107 & -0.1509 & 0 \\ 0 & 2.5139 & -0.0002 & 0 \\ 0 & 0.0046 & 1.9933 & 0 \\ 0 & 0 & 0 & 2.3310 \end{bmatrix} \tag{4.4.5}$$

A plot of I^2 versus I_p^2 in Fig. 4.4.4 shows that the average polarisation factor is slightly closer to unity than in the previous case, which is a result of $\langle \varepsilon_P \rangle$ and $\varepsilon_{P\max}$ being reduced to 1.8×10^{-3} and 6×10^{-3} respectively. The most significant improvement was seen in the azimuth errors $\langle \varepsilon_\Psi \rangle$ and $\varepsilon_{\Psi\max}$, which were reduced to 0.030° and 0.052°. These values are more comparable with the expected error in θ.

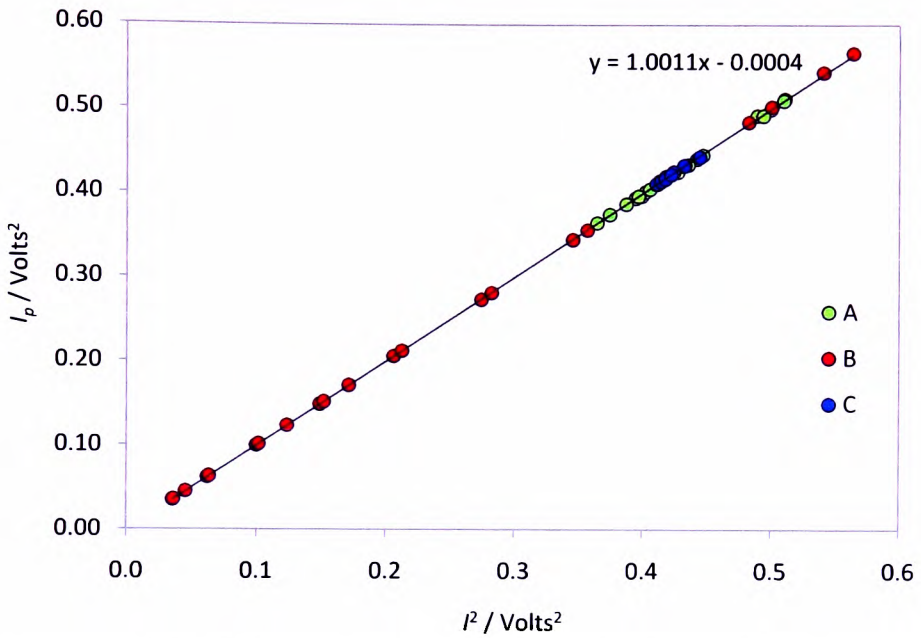

Figure 4.4.4 – I^2 vs. I_p^2 for each measurement in data sets *A*, *B* and *C*, calculated using the constants determined using non-linear optimisation.

To illustrate the behaviour of $\varepsilon_{1_t}, \varepsilon_{2_t}, \varepsilon_{3_t}$ and ε_{total} in the vicinity of the global minimum, each error has been plotted as functions of k_i (i = 2...8), as shown in Fig. 4.4.5. In each plot, a single constant was varied while keeping the other seven at their ideal values. From Figs. 4.4.5, *C* and *F* it would seem that the functions $\varepsilon_{3_t}(k_4)$ and $\varepsilon_{3_t}(k_7)$ are non-smooth as k_4 and k_7 approach zero, however, it only appears so because of the plot scaling. The functions are in fact always continuous and smoothly varying. Even so, to ensure the algorithm was not hindered in any way, the optimisation procedure was performed a number of times with randomly selected starting values for each of the constants. In each case the algorithm returned identical solutions, so long as the starting values were non-zero. This confirms both the robustness of the model and also that the solution corresponds to the global minimum and not one of many local minima.

It is evident from Figs. 4.4.5, *C* and *F* that ε_{3_t} does not assist significantly in defining the values of k_4 and k_7, but plays a crucial role in determining the correct signs. This is clearly shown in Fig. 4.4.6, where $\varepsilon_{3_t}(k_4)$ and $\varepsilon_{3_t}(k_7)$ are plotted for various polariser angles. Figures 4.4.5, *D* and *E* show that ε_{3_t} actually plays a vital role in defining the values of k_5 and k_6, which are most effectively found using polariser angles of 45° (or -45°) and 0° (or 90°), respectively, as illustrated by Fig. 4.4.7. Although it is not absolutely necessary to measure these particular angles, they are more effective at leading the algorithm to the correct solution. In fact they are sufficient by themselves to fit the constants k_i (i = 2...7), as has already been proven with the four-state calibration method.

From Fig. 4.4.5*G*, it is evident that k_8, may be either positive or negative, since the function $\varepsilon_{total}(k_8)$ is symmetrical about zero. The sign cannot be determined through calibration, but if the handedness of the light used during calibration is known, the correct sign may be applied.

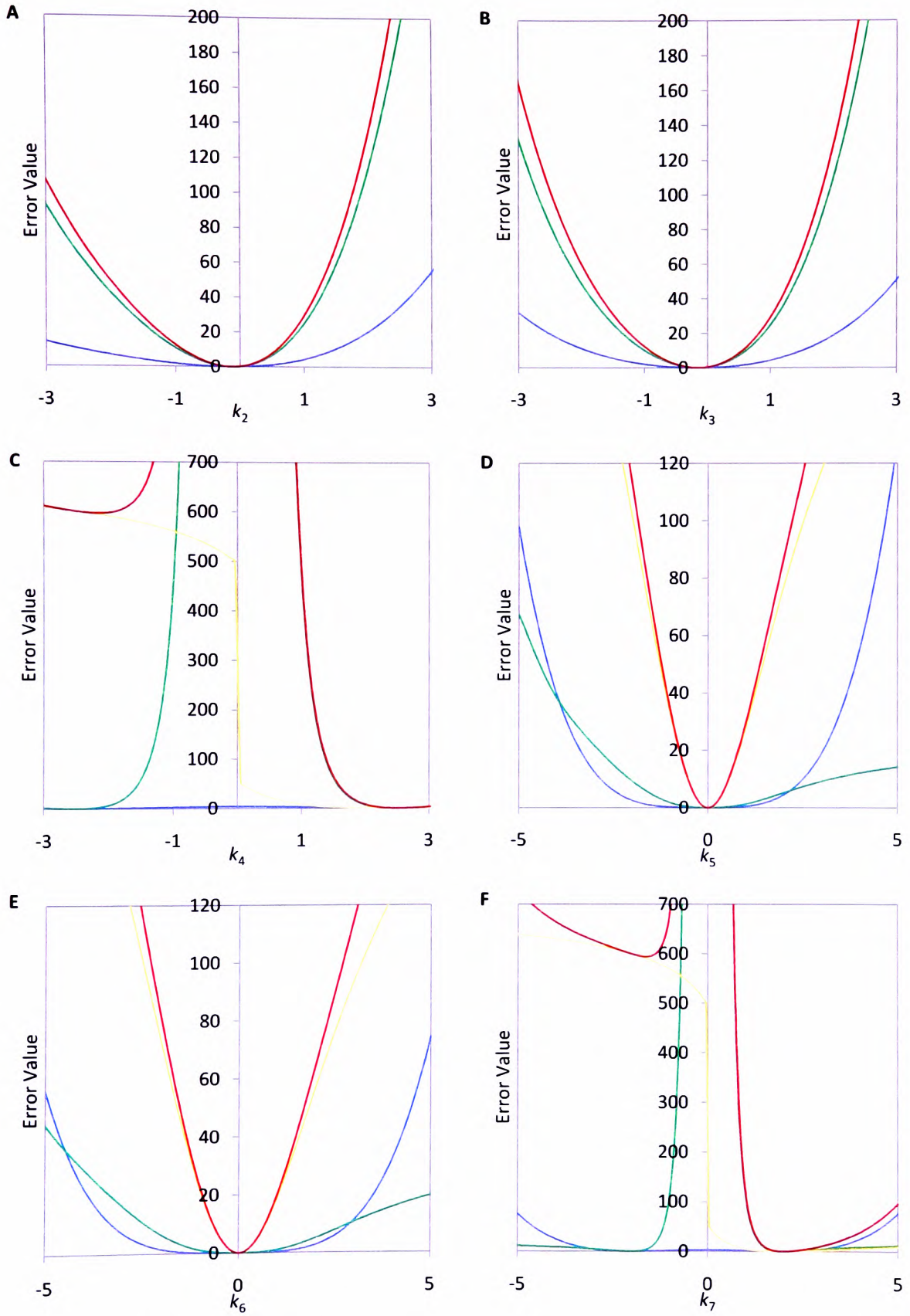

Figure 4.4.5 – Errors ε_{1_t} (blue), ε_{2_t} (green), ε_{3_t} (yellow) and ε_{total} (red) plotted as functions of : k_2 (*A*), k_3 (*B*), k_4 (*C*), k_5 (*D*), k_6 (*E*) and k_7 (*F*).

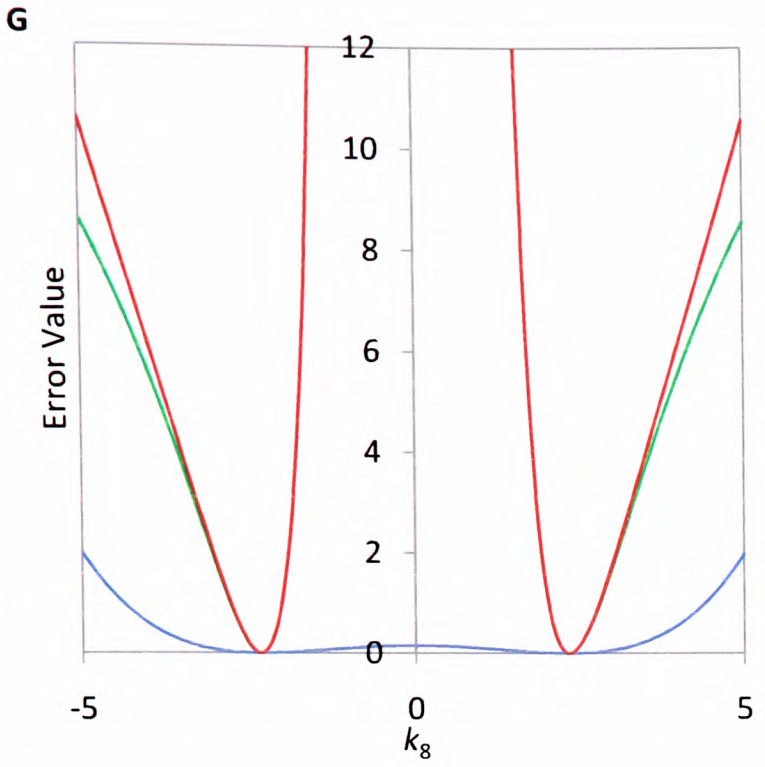

Figure 4.4.5 cont. – Errors ε_{1t} (blue), ε_{2t} (green) and ε_{total} (red) plotted as functions of k_8.

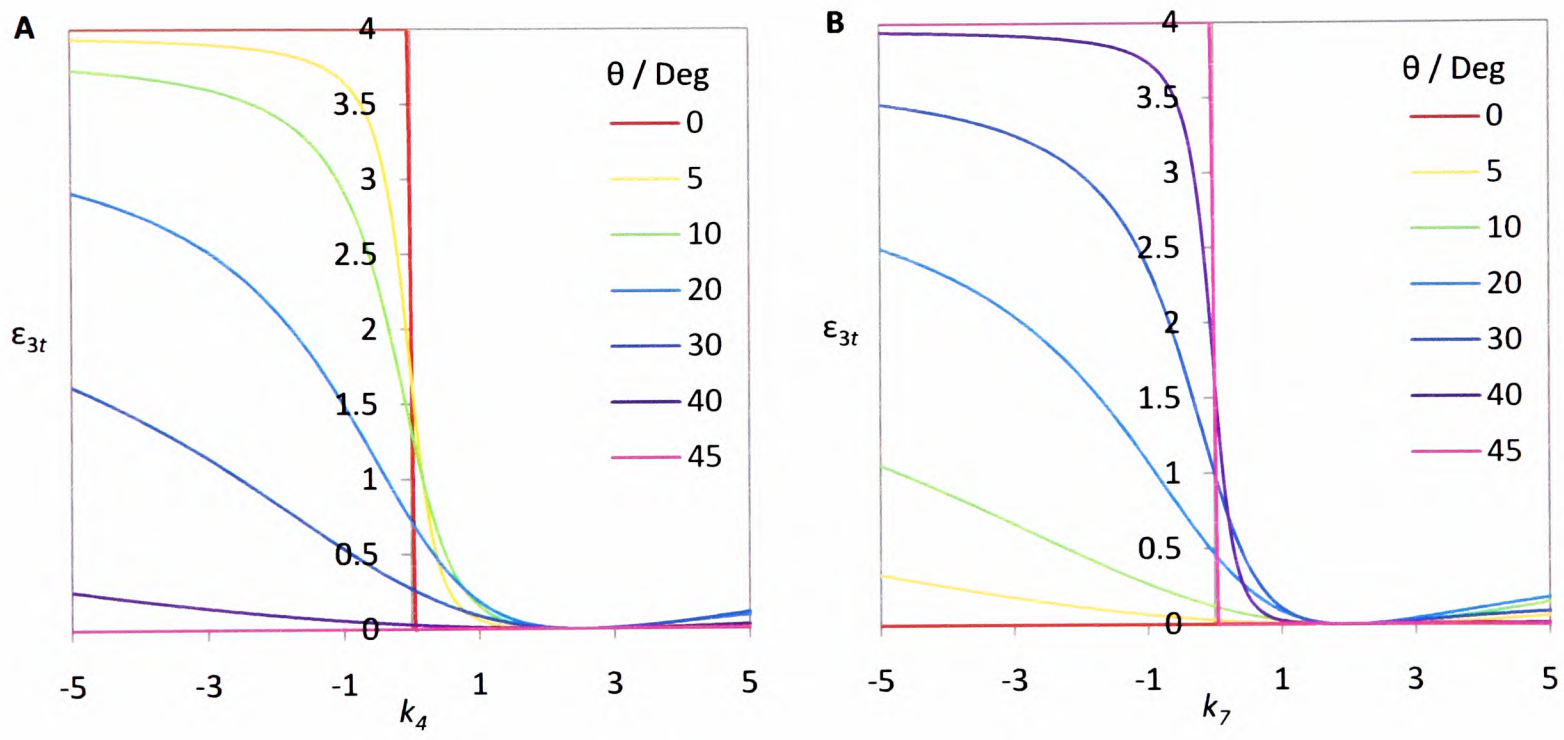

Figure 4.4.6 – ε_{3t} as a function of: k_4 (*A*) and k_7 (*B*) at various polariser angles.

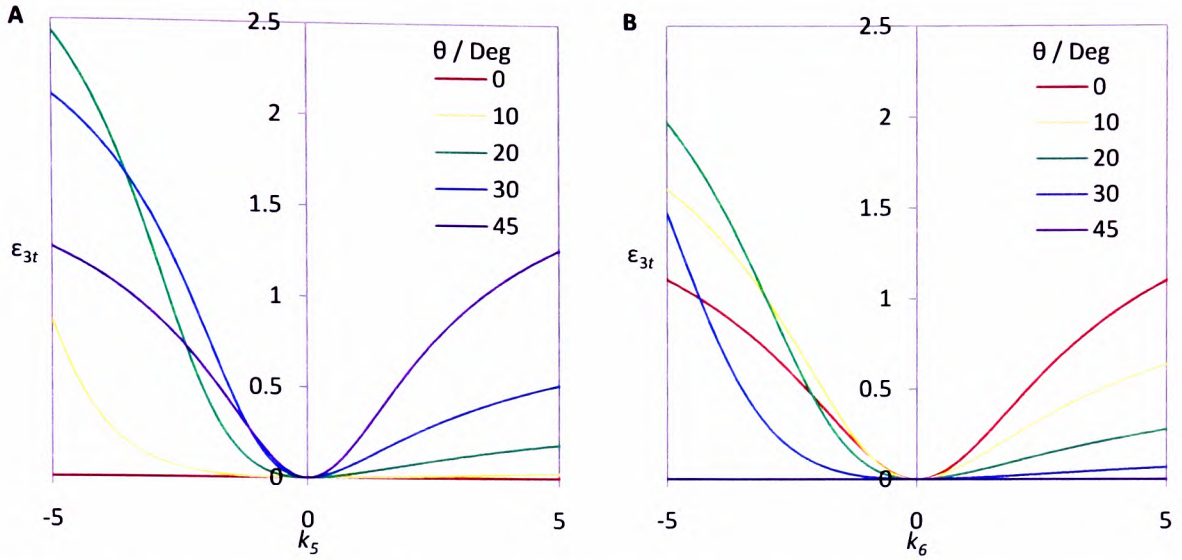

Figure 4.4.7 – ε_{3_t} as a function of k_5 (*A*) and k_6 (*B*) at various polariser angles.

4.4.5 Summary

The results obtained from each calibration procedure are summarised in Tables 4.4.2 and 4.4.3. Although the polarimeter parameters required to diagonalise K were set accordingly, this did not reduce the off-diagonal components sufficiently for linear regression to provide an adequate result. It is evident from the values of k_2 and k_3 (associated with $J_0(\delta_{i0})$), and the comparatively small values of k_5 and k_6 (associated with α) obtained using the optimisation algorithm, that the retardation settings of the PEMs are the primary sources of error. This may be a combination of several factors, including miscalibration of the PEM controllers, and a deviation of the laser wavelength from the quoted value.

While the four-state calibration method is very reliable, non-linear optimisation is the most versatile approach, which in principle allows any polarimeter configuration to be used. In the case presented here, it also provides the lowest errors. However, a degree of caution must be exercised when fitting multiple unknown variables, since there can be any number of solutions at which the algorithm may arrive. It is advisable to execute the procedure several times with different starting values for each of the constants to ensure the solution corresponds to the global minimum. If the configuration being used involves setting α to 45°, then the first step of the four-state calibration method may be performed, in which case reasonably accurate values of k_2, k_3, k_4 and k_7 will be known before the optimisation is

performed. The main disadvantage to both the four-state and non-linear optimisation methods is that they require the polariser to be set very accurately and errors in θ will inevitably affect the calibration result. Despite this, both procedures offer a much greater accuracy than that obtainable using linear regression when the values of k_2 and k_3 are non-zero. This allows δ_{10} and δ_{20} to take any value, allowing for further refinement of the polarimeter configuration, as discussed in the next section.

	k_2	k_3	k_4	k_5	k_6	k_7	k_8
Linear Regression			2.5596			1.9864	2.2790
Four-State Calibration	-0.1127	-0.1511	2.5170			1.9927	2.3293
Non-Linear Optimisation	-0.1107	-0.1509	2.5139	-0.0002	0.0046	1.9933	2.3310

Table 4.4.2 – Summary of the calibration constants obtained using each calibration method.

	$\langle \varepsilon_P \rangle$	$\varepsilon_{P\max}$	$\langle \varepsilon_\Psi \rangle$	$\varepsilon_{\Psi\max}$
Linear Regression	0.0730	0.1701	0.2067°	0.3688°
Four-State Calibration	0.0019	0.0090	0.0521°	0.1116°
Non-Linear Optimisation	0.0018	0.0060	0.0299°	0.0524°

Table 4.4.3 – The errors associated with each set of constants.

4.5 *Optimised Polarimeter Configuration*

In the previous section, it was shown how the off-diagonal constants in K can be found using the four-state calibration and non-linear optimisation methods. Since these methods relax the condition that $\delta_{10} = \delta_{20} = 2.4048$ rad., from Eqn. 4.1.16, it can be seen that the Ω_1, $2\Omega_1$ and $2\Omega_2$ components of the *ac* signal, proportional to $J_1(\delta_{10})$, $J_2(\delta_{10})$ and $J_2(\delta_{20})$ respectively, may be increased by maximising the relevant Bessel functions. This would be advantageous in a situation where the sample being measured induces only very small changes in the polarisation state and the signal-to-noise ratio becomes more important. $J_2(\delta_{20})$ and hence S_{QU2} may be maximised by setting $\delta_{20} = 3.054$ rad. The maxima of $J_1(\delta_{10})$ and $J_2(\delta_{10})$ occur at different values of δ_{10} which means that S_{QU1} and S_V cannot be maximised simultaneously. A compromise can be made where δ_{10} is set to 2.630 rad, such that $J_1(\delta_{10}) = J_2(\delta_{10})$. Also, by adjusting the analyser angle (β), a balance between the maximum attainable S_{QU1} and S_{QU2} signals can be found.

Using this PEM configuration (and keeping $\alpha = 45°$), the four-state calibration method was performed as outlined in the previous section. Five sets of measurements were taken at the four special polariser angles (0°, 45°, 90° and -45°), referred to as data set D. Then several elliptical states were measured making up data set E. The constants obtained from set D are shown in Table 4.5.1. The final constant k_8 was then obtained from set E as shown in Fig. 4.5.1.

Calibration Set	k_2	k_3	k_4	k_7
1	-0.2645	-0.4773	2.4005	1.9029
2	-0.2638	-0.4758	2.3995	1.8989
3	-0.2628	-0.4662	2.3996	1.8953
4	-0.2623	-0.4656	2.3993	1.8964
5	-0.2630	-0.4662	2.3995	1.8956
Mean	-0.2633	-0.4702	2.3997	1.8978
Standard Deviation	0.0009	0.0058	0.0005	0.0032
Standard Deviation (%)	0.34	1.23	0.02	0.09

Table 4.5.1 – The calibration constants obtained from five different sets of measurements of S_{dc}, S_{QU1} and S_{QU2} at the four special polariser angles.

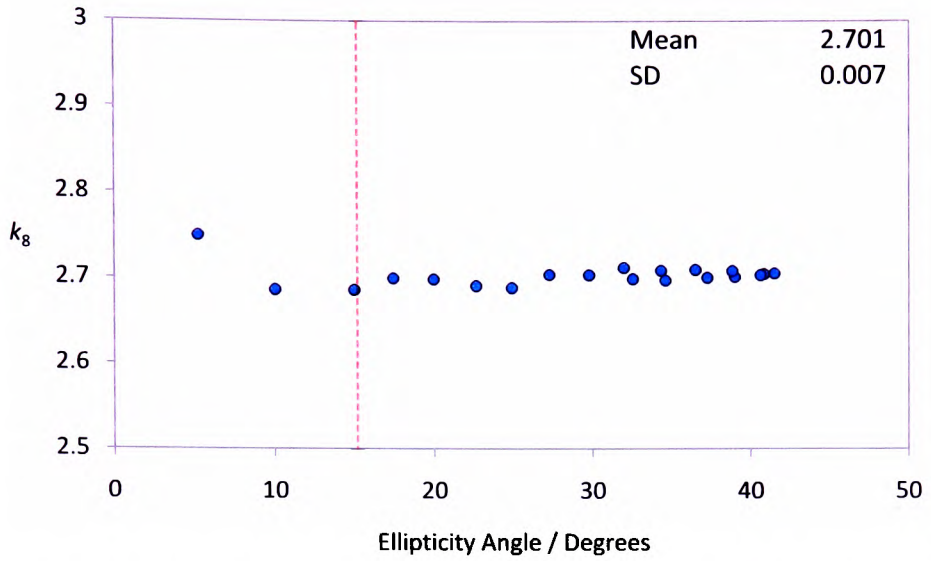

Figure 4.5.1 – The calculated values of k_8 across a wide range of elliptically polarised states. The mean and standard deviation are only calculated for states where $\chi > 15°$ (marked by red dashed line).

As a check of the validity of k_4 and k_7, the azimuth errors were calculated for linearly polarised states at various settings of the polariser; these measurements made up data set F. On average, the deviation of the measured azimuth angle from the intended polariser setting, $\langle \varepsilon_\Psi \rangle$, was only 0.030°, with a maximum deviation , $\varepsilon_{\Psi max}$, of 0.053°. This indicates a very good fit to the two constants. Then taking all measurements in the three data sets into account, the average deviation of the polarisation factor from unity, $\langle \varepsilon_P \rangle$, was found to be 3.0×10^{-3} with a maximum deviation, $\varepsilon_{P max}$, of 0.013.

Then applying the non-linear optimisation to all measurements using scaling factors of $\gamma_1 = \gamma_3 = 1$ and $\gamma_2 = 2$. The values of the constants obtained were:

$$K = \begin{bmatrix} 1 & -0.2624 & -0.4688 & 0 \\ 0 & 2.3997 & -0.0024 & 0 \\ 0 & -0.0006 & 1.8967 & 0 \\ 0 & 0 & 0 & 2.7038 \end{bmatrix} \tag{4.5.1}$$

This time both methods yielded very similar results, in fact k_4 is the same (to 4 d.p.). As a result, the optimisation did not improve the statistics significantly. There was only a 1 % reduction in $\langle \varepsilon_\Psi \rangle$, but $\varepsilon_{\Psi max}$ was reduced by 16 % to 0.045. $\varepsilon_{P max}$ actually increased by 20 % to 0.015, yet $\langle \varepsilon_P \rangle$ reduced by 16 % to 2.5×10^{-3}. These differences are of negligible

consequence to the actual sample measurement, but owing to the overall reduction in the errors provided by the optimisation, the constants in Eqn. 4.5.1 were used.

	k_2	k_3	k_4	k_5	k_6	k_7	k_8
Four-State Calibration	-0.2633	-0.4702	2.3997	-	-	1.8978	2.7015
Non-Linear Optimisation	-0.2624	-0.4688	2.3997	-0.0024	-0.0006	1.8967	2.7038

Table 4.5.2 – Summary of the calibration constants obtained using the four-state and non-linear optimisation calibration methods.

	$\langle \varepsilon_P \rangle$	$\varepsilon_{P\max}$	$\langle \varepsilon_\Psi \rangle$	$\varepsilon_{\Psi\max}$
Four-State Calibration	0.0030	0.0127	0.0302	0.0529
Non-Linear Optimisation	0.0025	0.0153	0.0298	0.0446

Table 4.5.3 – The errors associated with each set of constants.

4.6 *A Typical Fe Film Measurement*

With the polarimeter calibrated, a 10-12 nm thick nanocrystalline Fe film, typical of those used throughout this work, was placed in the magneto-optical microscope. The probing light was conditioned to have a low ellipticity angle (3°) in order to raise the V signal to aid the lock-in amplifier. The film was then measured using predominantly p-polarised ($\Psi = 3°$) and s-polarised ($\Psi = 87°$) light. Using each polarisation state, to check for intrinsic anisotropy, the sample was measured at two orientations, where its x-y axes were rotated through 90°. The Faraday rotation (θ_F) and ellipticity angle (ε_F) are plotted in Figs. 4.6.1, A and B, respectively.

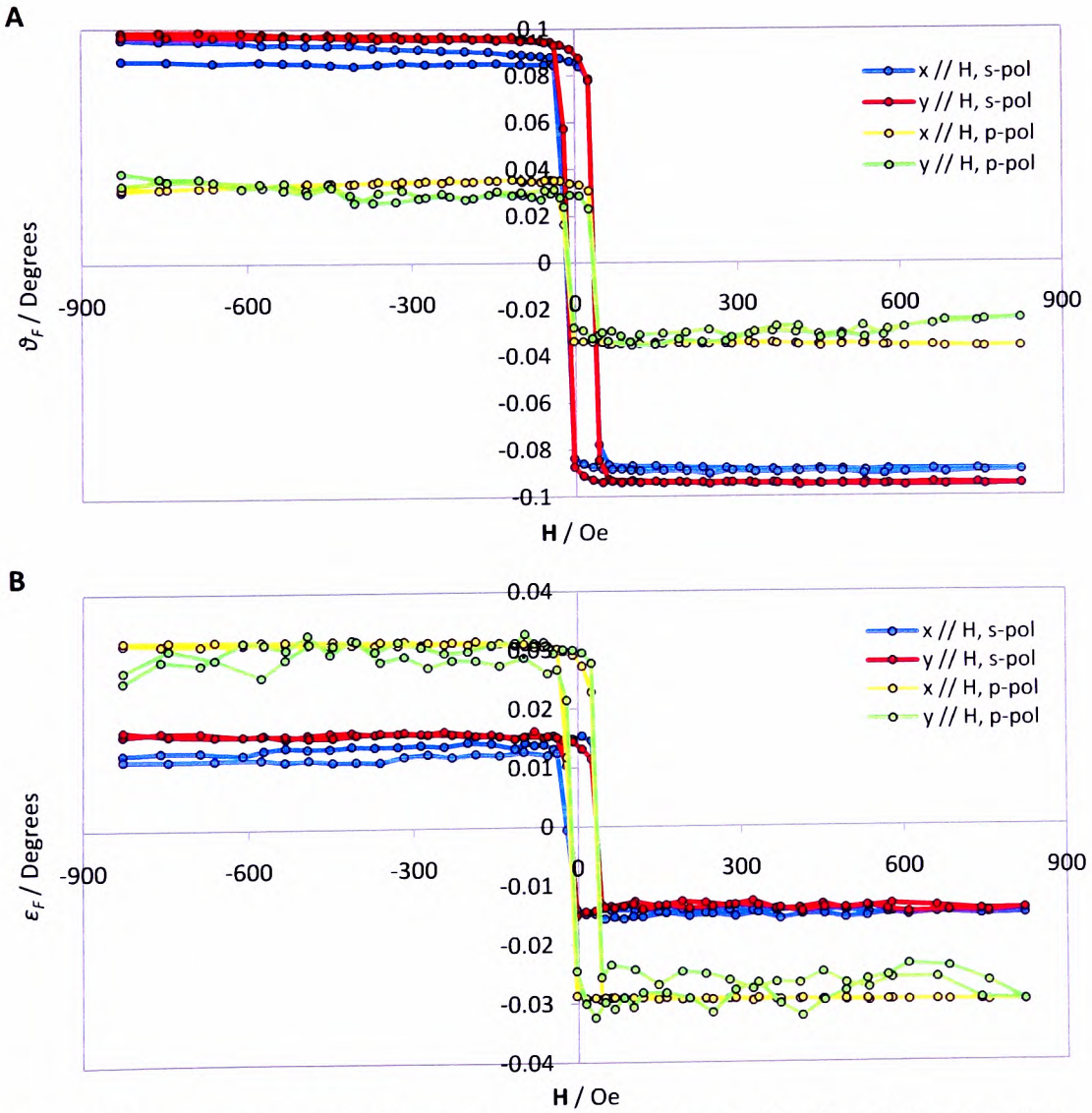

Figure 4.6.1 – A: Faraday rotation hysteresis loops obtained from the Fe film. B: Corresponding ellipticity angle loops.

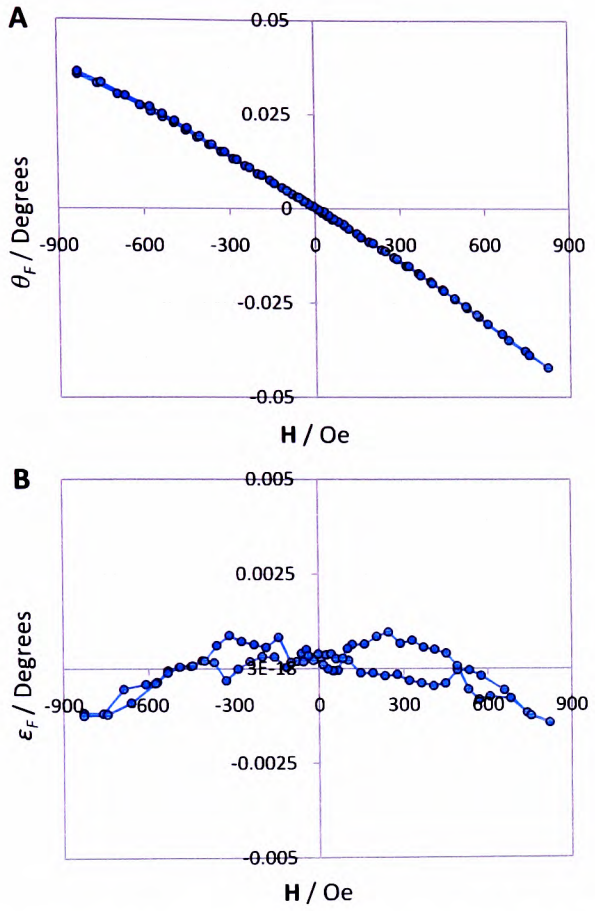

Figure 4.6.2 – *A*: Faraday rotation caused by the lenses. *B*: Changes in the ellipticity angle caused by a small degree of MCD or MLB.

An unfortunate consequence of the system design is that the lenses are located in the magnetic field, thus have their own contribution to the Faraday rotation signal, as shown in Fig. 4.6.2*A*. Since it is approximately linear with applied field, it may simply be subtracted to leave only the sample contribution. This correction was performed in order to obtain the loops in Fig. 4.6.1*A*. Figure 4.6.2*B* shows that the lenses have negligible contribution to the ellipticity, although small MCD or MLB effects are detectable. They may be ignored unless very small signals are being measured. For this reason, it is sometimes advantageous to measure the ellipticity angle instead of the Faraday rotation with this particular experimental set-up.

References

4.1 D. A. Allwood, G. Xiong, M. D. Cooke and R. P. Cowburn, Journal of Physics D-Applied Physics **36** (18), 2175-2182 (2003).

4.2 G. Xiong, D. A. Allwood, M. D. Cooke and R. P. Cowburn, Applied Physics Letters **79** (21), 3461-3463 (2001).

4.3 T. Oakberg, "Stokes polarimetry," Hinds Instruments, Appl. Note, 1993 [Online]. Available: http://www.hindspem.com/media/pem-90-sp.pdf. [Accessed: Feb, 2010].

4.4 M. Billardon and J. Badoz, C. R. Acad. Sci. Ser. B **262**, 1672-1675 (1966).

4.5 J. C. Kemp, Journal of the Optical Society of America **59** (8P1), 950-954 (1969).

4.6 W. Hipps and G. A. Crosby, Journal of Physical Chemistry **83** (5), 555-562 (1979).

4.7 D. Yang, J. C. Canit and E. Gaignebet, Journal of Optics-Nouvelle Revue D Optique **26** (4), 151-159 (1995).

4.8 J. W. Lee, J. R. Jeong, D. H. Kim, J. S. Ahn, J. Kim and S. C. Shin, Review of Scientific Instruments **71** (10), 3801-3805 (2000).

4.9 M. W. Wang, F. H. Tsai and Y. F. Chao, Thin Solid Films **455**, 78-83 (2004).

4.10 A. J. Zeng, L. H. Huang, Z. R. Dong, J. M. Hu, H. J. Huang and X. Z. Wang, Applied Optics **46** (5), 699-703 (2007).

4.11 S. Polisetty, J. Scheffler, S. Sahoo, Y. Wang, T. Mukherjee, X. He and C. Binek, Review of Scientific Instruments **79** (5) (2008).

4.12 B. L. B Wang and T. Oakberg, "Dual PEM systems: Polarimetry applications," Hinds Instruments, Appl. Note, 2005 [Online]. Available: http://www.hindspem.com/media/Dual%20PEM%20Systems%20-%20Polarimetry%20Applications.pdf. [Accessed: Feb, 2010].

4.13 G. R. Boyer, B. F. Lamouroux and B. S. Prade, Applied Optics **18** (8), 1217-1219 (1979).

4.14 B. L. B. Wang, J. List and R. R. Rockwell, in *Polarization Measurement, Analysis, and Applications V*, edited by D. H. Goldstein and D. B. Chenault (Spie-Int Soc Optical Engineering, Bellingham, 2002), Vol. 4819, pp. 1-8.

4.15 M. Kuldkepp, N. C. Hawkes, E. Rachlew and B. Schunke, Applied Optics **44** (28), 5899-5904 (2005).

4.16 Y. W. Liu, G. A. Jones, Y. Peng and T. H. Shen, Journal of Applied Physics **100** (6), 7 (2006).

4.17 W. Guan, G. A. Jones, Y. W. Liu and T. H. Shen, Journal of Applied Physics **103** (4) (2008).

4.18 W. Guan, P. J. Cook, G. A. Jones and T. H. Shen. Applied Optics, in press (2010).

4.19 D. Fylstra, L. Lasdon, J. Watson and A. Waren, Interfaces **28** (5), 29-55 (1998).

CHAPTER 5 Ga-Ion Irradiation of Nanocrystalline Ferromagnetic Thin Films

Gallium ion irradiation can bring about significant changes to a material's structure, which are generally limited to within the first few tens of nanometres beneath the surface. While such modifications might not prove significant in relatively thick materials, in the case of very thin films the structure will be modified throughout and consequently its magnetic behaviour can be very sensitive to ion irradiation. Here, the effects of 30 keV Ga+ ion irradiation on the structural, compositional and magnetic properties of thin nanocrystalline Fe single-layer and Ni/Fe bi-layer films have been investigated using TEM, STXM, EDX and magneto-optical techniques.

5.1 *Structure and Composition of Ga-Irradiated Thin Films*

5.1.1 TEM Analysis

It is known that atomic reorganisation induced by ion irradiation can result in an increase in the average grain size in nanocrystalline materials[5.1-3]. Each highly energetic Ga ion can displace several hundred target atoms, thus with a sufficiently high ion dose, it is possible that every atom within a thin film will be displaced many times over. The grain enlargement effect is illustrated in Fig. 5.1.1, where TEM images show how the microstructure of a 12 nm thick Fe film changes with increasing ion dose. Figure 5.1.1*A* shows the lowest ion dose of 7.68×10^{15} ions cm^{-2} increased the average grain size from approximately 15 nm to 26 nm. The largest grains are seen in *C* and *D*, some of which measure around 60 nm. It is also apparent in *C* that the film begins to segregate into clusters after being irradiated with 2.29×10^{16} ions cm^{-2}. This is much more noticeable in *D*, where clusters of various sizes appear to be surrounded by an apparent amorphous matrix. In *E* and *F* there is hardly any Fe film left at all. What remains is a random distribution of isolated Fe-Ga grains of various irregular shapes and sizes.

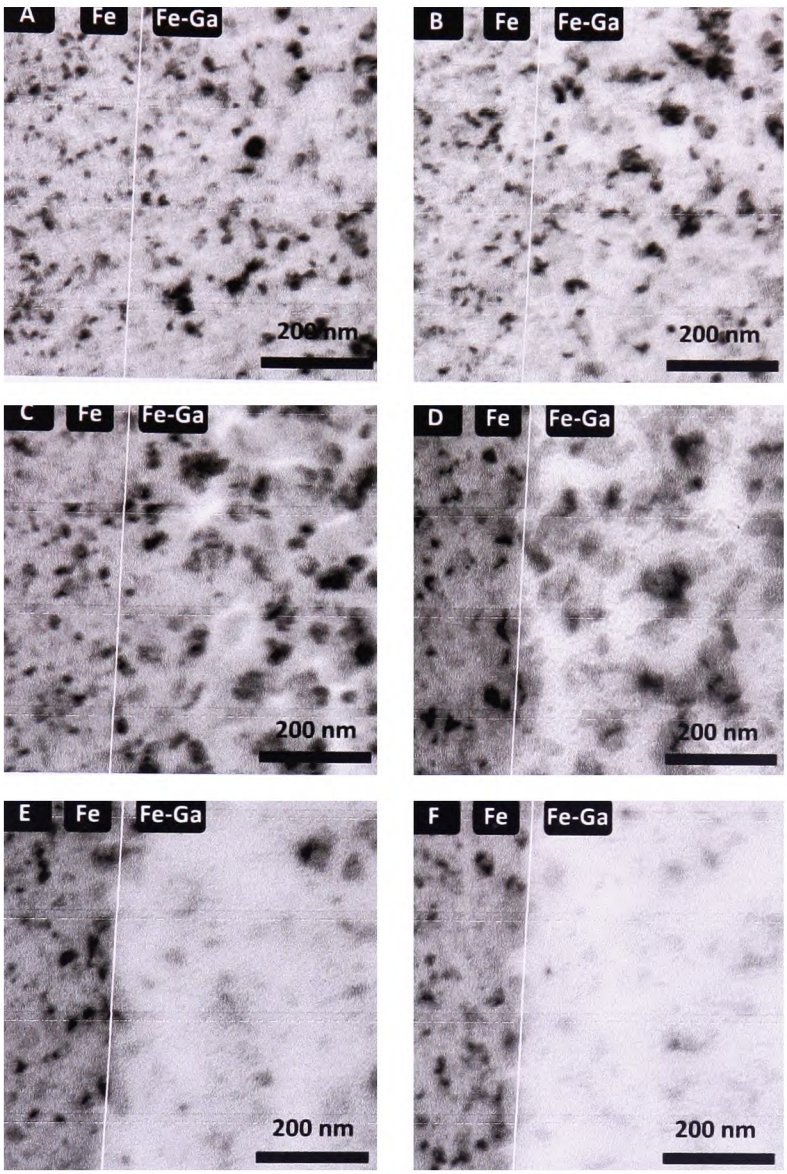

Figure 5.1.1 – Bright-field TEM images of a 12 nm thick Fe film irradiated with Ga ion doses (in 10^{16} ions cm^{-2}) of 0.768 (*A*), 1.15 (*B*), 2.29 (*C*), 3.44 (*D*), 4.59 (*E*) and 5.16 (*F*).

Selected area diffraction (SAD) patterns were recorded on the as-grown Fe film and each of the irradiated regions, as shown in Fig. 5.1.2. Unfortunately, the photographs were overexposed and as a result the central region of the pattern was saturated. An *ad hoc* correction method, which involved removing the amorphous contribution from the silicon nitride membrane, recovered the contrast to some extent. However, the first ring was still obscured in most cases. The structural changes observed in the bright-field images above are clearly reflected in the diffraction patterns. In its original as-grown state, the film produces bright, continuous rings that are indicative of the very small grains (*A*). After ion irradiation, the rings become discontinuous since the grains included in the field of the diffraction

aperture are considerably larger in size and less in number. After a dose of 4.59×10^{16} ions cm^{-2}, some of the reflections from individual grains can be distinguished (*F*). Indexing the rings as described in Chapter 3 confirmed the presence of the (200), (211), (220), (310) and (222) reflections in all areas apart from the highest dosed area. What is interesting is that this indicates a body-centred cubic (bcc) crystal structure is present even after the highest ion doses. The brighter (211) and (310) rings in Figs. 5.1.2, *A*, *B* and *C* signify a preferential orientation (texturing) on deposition, which persisted until an ion dose of 2.29×10^{16} ions cm^{-2} was applied. In Figs. 5.1.2, *D* and *E*, all of the rings appear similar in brightness which indicates that this texturing was destroyed, possibly by recrystallisation.

Figure 5.1.3 shows the normalised lattice parameters for several of the Fe-Ga areas plotted as a function of ion dose. The variations are small (< 1 %), but a definite trend is noticeable. The two lowest doses resulted in a small increase in *a* of about 0.6 %, followed by a decrease back down to the original value after applying 2.29×10^{16} ions cm^{-2}. An apparent compression of the lattice occurs after applying 3.44×10^{16} ions cm^{-2}, although it is possible that this may be a further relaxation compared to the as-grown state. The initial increase is comparable to that observed in Ref. (5.4), where 60-82 nm thick Fe films were irradiated with various ion species. The authors considered a reduction in the intrinsic film stress as a result of the ion irradiation to be responsible for the rise in lattice parameter. Here, the actual value of the lattice parameter in the as-grown film is unknown, therefore it is not possible to judge from the data whether the film was initially under compressive stress.

EDX measurements (discussed later) and TRIM simulations suggest that after applying a dose of 1.15×10^{16} ions cm^{-2}, the Ga content was approximately 9-10 at. %. In view of this, in addition to film stress, alloying of the Fe and Ga must also be considered, since the increase in *a* is consistent with the formation of an $Fe_{90}Ga_{10}$ alloy[5.5, 6] Applying a higher Ga dose of 2.29×10^{16} ions cm^{-2} results in an increase in the Ga content to roughly 20 at. %, which according to Refs. (5.5) and (5.6) is the point at which short range ordering of the Ga becomes significant. The loss in texture as observed in Fig. 5.1.2*D* suggests recrystallisation, which could be associated with the Ga ordering. However, it is possible that the high energy implantation might prevent any ordering from occurring. Additionally, the film can be seen to become discontinuous in Fig. 5.1.1*C*, which implies changes in stress. Consequently, firm conclusions regarding the increased lattice parameter cannot be made.

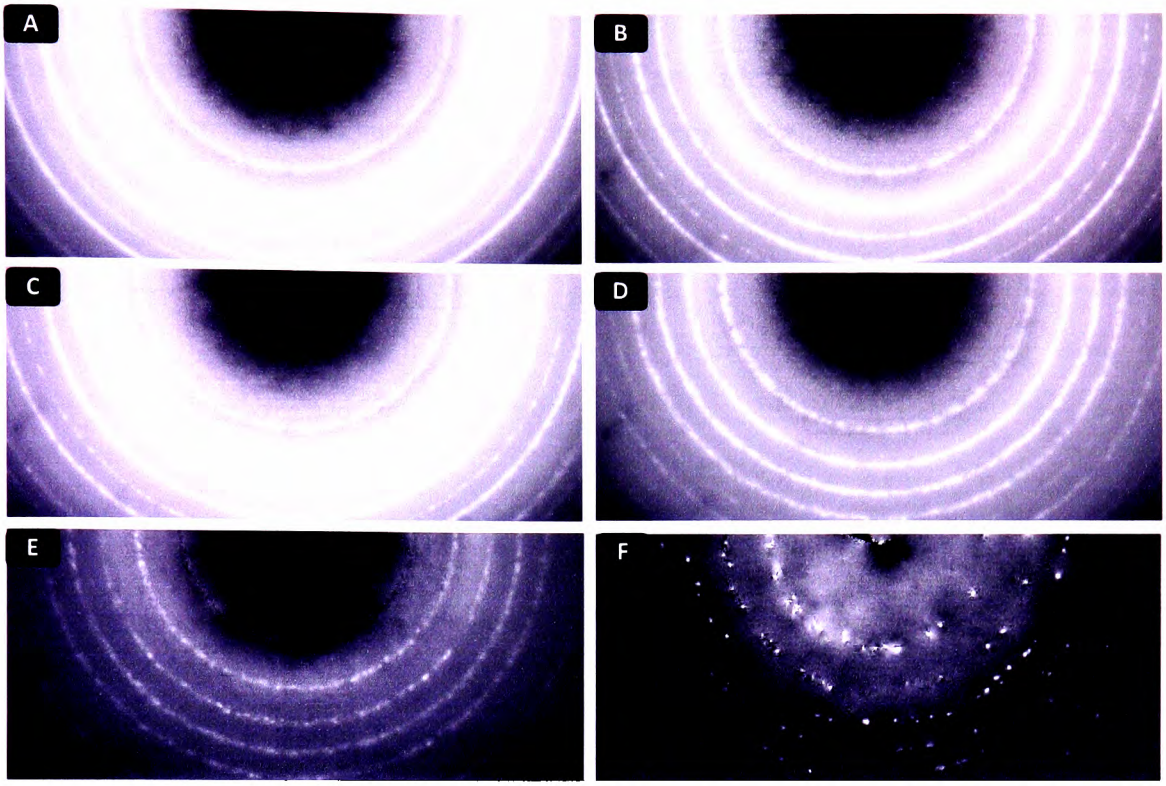

Figure 5.1.2 – Selected area diffraction patterns taken from the as-grown Fe film (*A*), and the areas irradiated with doses of 0.768 (*B*), 1.15 (*C*), 2.29 (*D*), 3.44 (*E*) and 4.59 (*F*) $\times 10^{16}$ ions cm^{-2}. The photographs were slightly overexposed and as a result the (110) reflection is missing from most of the patterns. An *ad-hoc* correction was made to recover some of the contrast; this included removing the amorphous contribution from the silicon nitride membrane. The first five rings in *A* to *D* are the (200), (211), (220), (310) and (222) reflections. In *E* and *F*, the (110) reflections can also be seen.

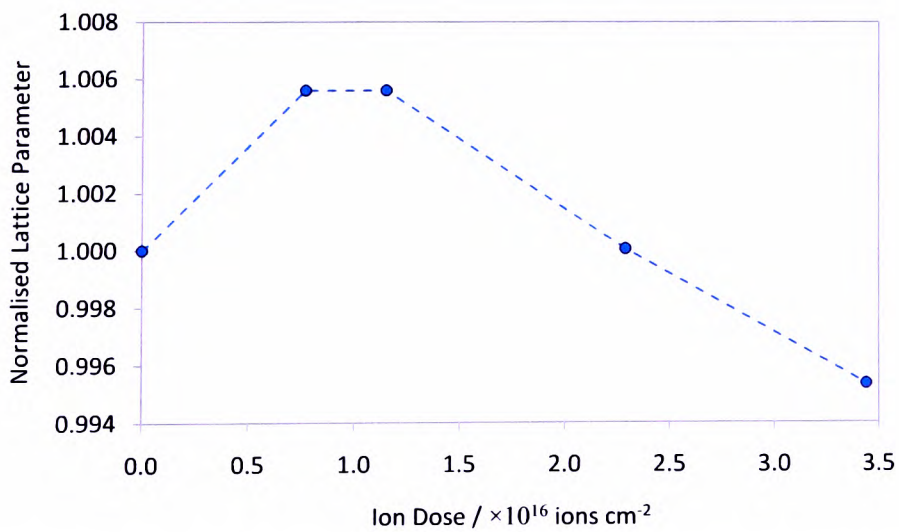

Figure 5.1.3 – Relative changes in the lattice parameters of the Fe-Ga with increasing ion dose.

The EDX measurements mentioned above are shown in Fig. 5.1.4. They were performed on a 12 nm Ga-irradiated Fe film and show the relative proportions of Fe and Ga at different ion doses. EDX is not a surface sensitive technique, therefore not only does the Ga within the Fe film contribute to the detected signal, but also that within the silicon nitride membrane. TRIM simulations suggest that 60 % of the Ga ions will come to rest in a 12 nm thick Fe film, but this fraction decreases linearly to 23 % in 2 nm of Fe. Taking this into account, the Ga content is thought to be on the order of 9-15 % for the three lowest ion doses, but discontinuities developing at higher doses make it difficult to judge the portion of Ga ions that stop within the film.

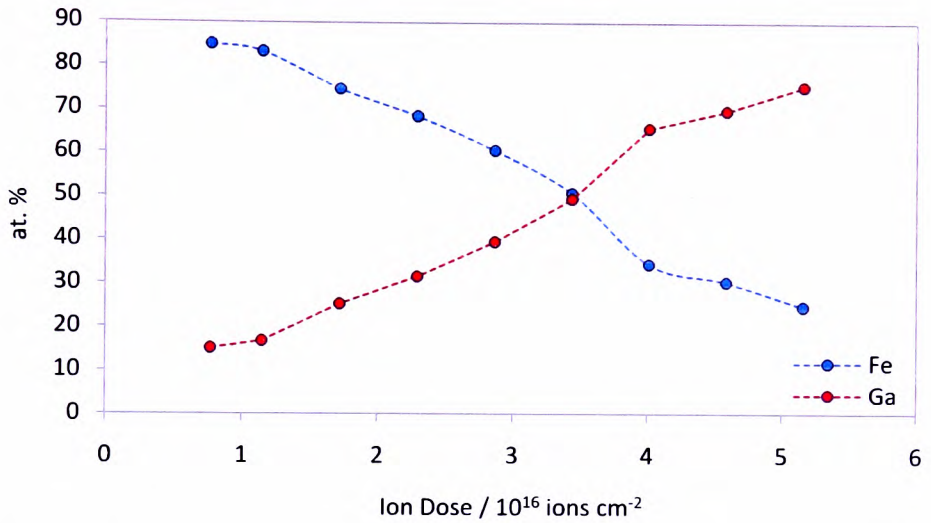

Figure 5.1.4 – EDX measurements showing approximate Fe and Ga content as a 10-12 nm Fe film deposited on 100 nm thick silicon nitride membrane is subjected to Ga irradiation at increasing doses. The indicated Ga content is not restricted to the Fe film, but also includes that implanted within the membrane.

5.1.2 Scanning X-Ray Microscopy

The reduction in Fe thickness with increasing ion dose has been estimated using STXM images of the irradiated films. Fig. 5.1.5 shows an example STXM image of an irradiated Fe film, recorded at the Fe L_3-edge (708 eV). The image shows an array of 7 μm × 7 μm squares that were irradiated with 30 keV Ga ions using a range of ion doses. The image has been converted to optical density (see Chapter 3) so the higher dosed squares appear darker because of the reduced quantity of Fe. The pixel values are proportional to the amount of Fe (Eqn. 3.3.1), therefore by measuring the average pixel value within each irradiated square and normalising to the optical density of a known thickness of Fe, a plot of film thickness versus

ion dose can be created. Such thickness measurements for two Fe films with initial thicknesses of 12 nm and 5.3 nm are plotted in Fig. 5.1.6, along with estimated sputter yields. These were calculated based on the changes in the Fe thickness with increasing ion dose.

.

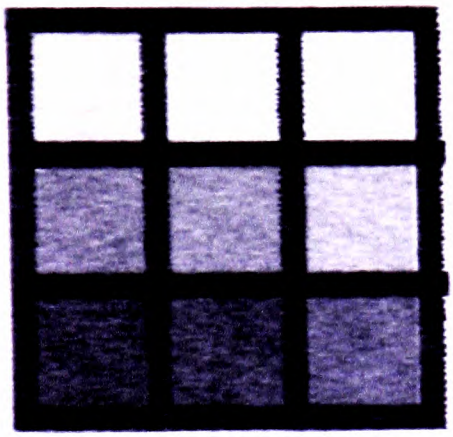

Figure 5.1.5 – An example STXM OD image of an irradiated Fe film. The darker areas show where the Fe has been thinned or milled away completely.

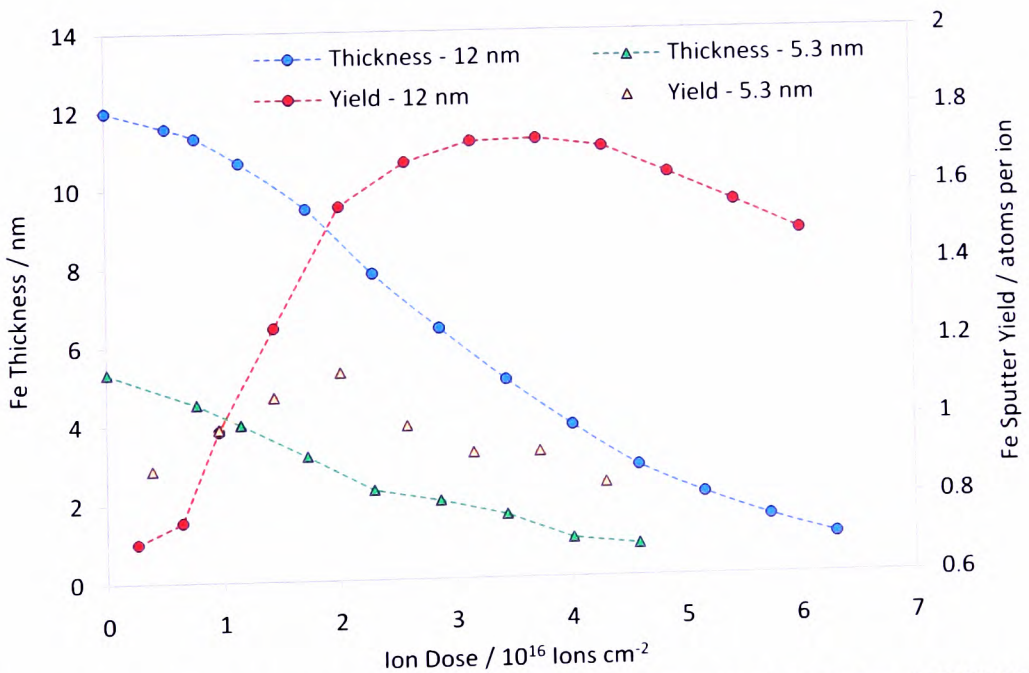

Figure 5.1.6 – Thickness measurements and sputter yield estimates obtained from STXM OD images of Fe films with initial thicknesses of 12 nm and 5.3 nm.

It is immediately apparent from Fig. 5.1.6 that the sputtering rates from the two films are different, but the general behaviour is similar in both cases. There is an initial rise followed by a reduction in sputter rate, due the combination of structural and compositional changes as the ion dose is increased. Initially, yields from both samples increased approximately linearly up until an ion dose of 2×10^{16} ions cm^{-2}. This may be explained if the surface roughening effect of ion beam milling is considered. Surface atoms are bound by fewer bonds than those in the bulk and require less energy to escape. Sputtering increases the roughness and hence number of surface atoms, and effectively lowers the binding energy allowing for a higher sputter yield[5.7].

When the 12 nm Fe layer was irradiated with a dose of 4.3×10^{16} ions cm^{-2}, or maybe more significantly, reduced to a thickness of approximately 3 nm, the sputter yield began to reduce linearly with further increasing ion dose. A reduction in yield also occurred in the case of the 5.3 nm layer, after it too was thinned to 3 nm. Potentially, increasing Ga content may contribute to the reduction in Fe sputter rate since an increasing portion of the sputter yield will be Ga. TRIM simulations show that, as might be expected, the Fe sputter yield is inversely proportional the Fe content. In alloys, lighter atoms are usually preferentially sputtered, however the similar atomic masses of Fe and Ga may mean that the yields primarily depend on the quantity of each element. Probably a more significant factor affecting the Fe yield is the reduction in the number of Fe cascades as the film becomes thinner. The sputtered atoms are generally produced by a series of knock-on collisions at the surface, but the origin of the cascades may be deeper. The sputter yield estimates suggest that this may be as deep as 3-4 nm beneath the surface. Reducing the thickness below this threshold effectively reduces the number of cascading particles and inevitably reduces the sputter yield. The significance of the 3 nm threshold was supported by further TRIM simulations, which show that the yield decreases marginally as the Fe thickness is reduced below 4 nm, and decreases rapidly below 3 nm (Fig. 5.1.7). The theoretical sputter yields, however, are considerably larger

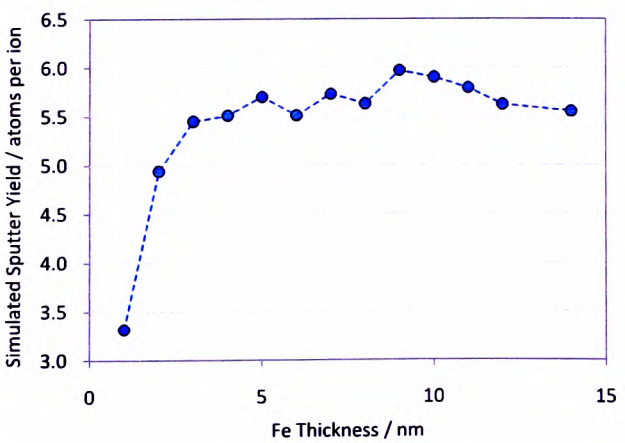

Figure 5.1.7 – TRIM simulation of the sputter yield from an amorphous Fe film of reducing thickness on silicon nitride.

than those determined experimentally. Redeposition of sputtered material may be partially responsible for the comparatively low experimental yields, which is an effect not accounted for in the simulation. Also not accounted for is the nanocrystalline nature of the film which can significantly affect the ion-target interaction[5.5]. In the case of the thinner 5.3 nm film, the initial rise in Fe yield was not as rapid as that observed from the thicker film, which may suggest that cascades generated even deeper than 3 nm may be involved in sputtering. Also, the initial Ga dose would account for a greater portion of the film, possibly further suppressing the Fe yield.

Thickness and sputter yield estimates were also calculated for Ni/Fe and Fe/Ni bi-layers, with initial Fe layer thicknesses of 4.5 and 4.3 nm, respectively (Fig. 5.1.8). The thicknesses of the Ni layers were not measured using the STXM because of practical limitations at the Ni absorption edge, but based on thickness monitor readings during film deposition they were determined to be between 4 and 6 nm.

It is generally thought that sputtering only occurs from the surface region of a material, therefore, the Ni layer should have been more than sufficient to prevent sputtering of the Fe. Interestingly, the Fe yield from the Ni/Fe film is in fact greater than that from the Fe/Ni film at low ion doses. Figure 5.1.9*A* shows an STXM image of the Ni/Fe bi-layer recorded at 390

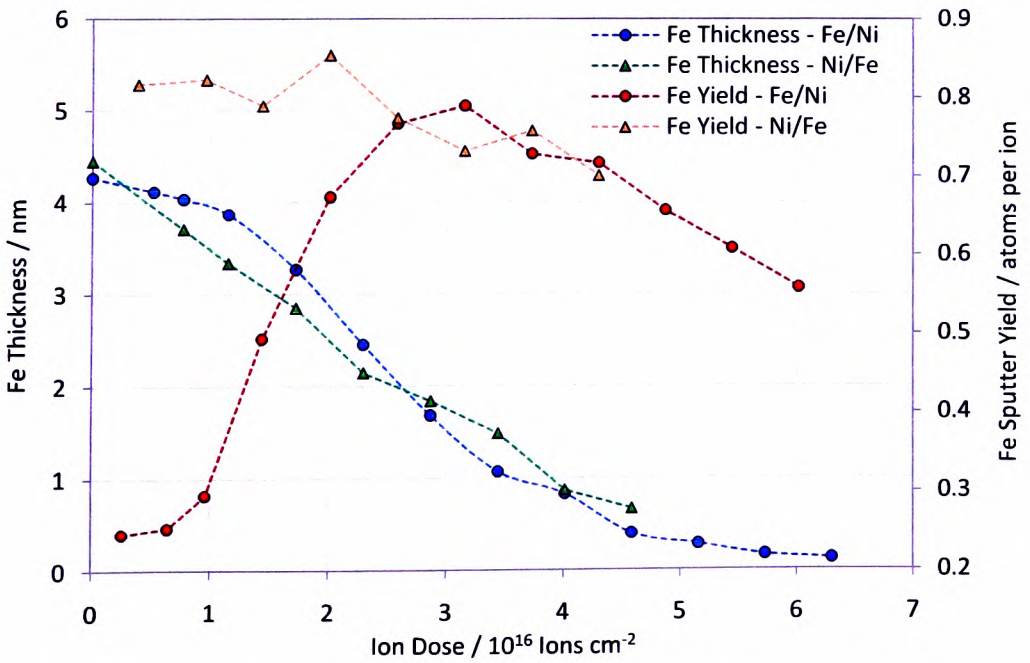

Figure 5.1.8 – Fe thickness measurements and sputter yield estimates from an STXM OD image of Ni/Fe and Fe/Ni bi-layer films.

eV, where the Fe and Ni absorb similarly. It is possible to distinguish between the three thicknesses: the silicon nitride membrane, the single Fe layer and finally the Fe with the Ni capping layer. Variations in the contrast between the different areas suggest that the Fe and Ni layers are of comparable thickness. In principle the Ni layer should be the first to be sputtered away, therefore the contrast variation from one small square to the next in the irradiated grid pattern (from light to dark) should be a result of the Ni layer becoming thinner. The small square with an OD that matches that of the Fe layer alone should be the point at which all of the Ni has been sputtered away. This point corresponds to a dose of just over 3.4×10^{16} ions cm^{-2}, which is somewhere between the two squares marked with black arrows in *A*. If the energy is increased to the Fe L_3-edge, Ni becomes almost completely transparent. This is illustrated in Fig. 5.1.9*B*, where there is virtually no difference in contrast between the Fe and Ni/Fe areas. Therefore, the contrast in *B* can only be attributed to variations in the Fe thickness. It is quite clearly apparent that even the lowest ion doses reduce the Fe thickness, which indicates that the Ni layer provides no protection against sputtering. TRIM simulations suggest that the Fe sputter yield should be insignificant with a Ni capping layer present, even if the thickness is just 1 nm, but the nature of the simulation means that ion channelling and progressive atomic mixing are not accounted for. It is well known that the ion channelling effect in polycrystalline materials allows the incident ions to travel much deeper into the sample[5.7, 8]. Ga ions could therefore be channelled through the Ni grains to the Fe layer below, where higher energy Fe cascades could be generated. Layer intermixing may consequently be more significant allowing the Fe to migrate towards the surface. In addition, channelling of high energy Fe atoms through appropriately orientated Ni grains or voids in the Ni layer could potentially result in an Fe sputter yield.

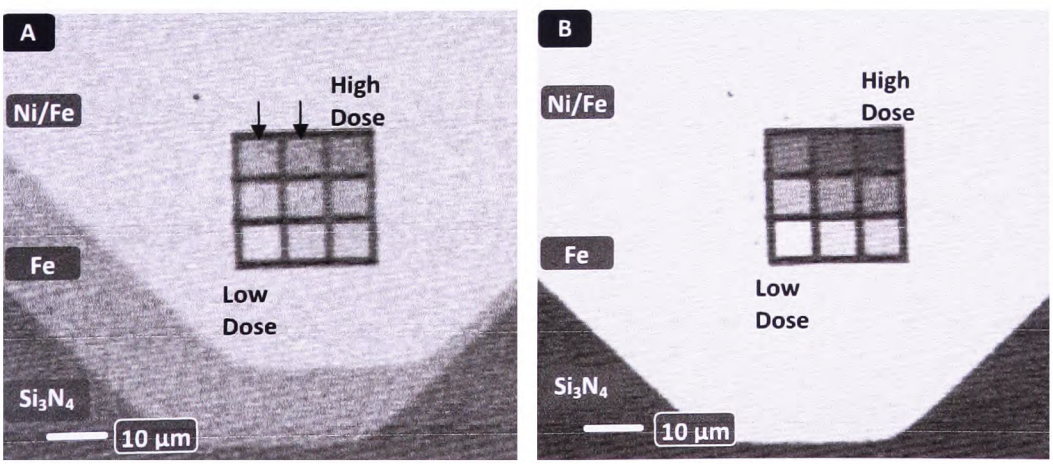

Figure 5.1.9 – STXM OD images of the Fe and Ni/Fe regions recorded at 390 eV (*A*) and 708 eV (*B*). The point at which the Ni is expected to be removed occurs between the squares marked with arrows. However this does not correlate with the variation in the Fe thickness shown in *B*.

It is apparent from Fig. 5.1.8 that there is no initial increase in Fe yield from the Ni/Fe bi-layer. This suggests the sputtering mechanism is independent of the Ni surface roughness which may support the theory of ion channelling. In order for the Fe atoms to sputter through the Ni layer they are most likely going to be very energetic, probably having energies much greater than the Ni surface binding energy. Modifications to the binding energy of a few eV brought about by erosion of the Ni surface would be of no consequence to such energetic particles.

5.1.3 X-Ray Absorption Spectroscopy

It has previously been discussed how Ga may become incorporated into the Fe lattice structure during ion irradiation. In addition, alloying at the Fe/substrate interface is certain to occur to some extent. By comparing the position and shape of the X-ray absorption peaks produced by the Fe-Ga to those produced by the as-grown film, any chemical changes to the Fe such as the formation of compounds will be revealed. Shown in Fig. 5.1.10 are the absorption spectra from several areas of Fe-Ga. Due to an absence of a true I_0 (see Eqn. 3.3.1) the spectra have been normalised to that from the as-grown film. Consequently, the peaks appear inverted, where a deeper trough indicates less absorption in comparison to the as-grown Fe. For all measured areas, the peaks in absorption occurred at 708 eV and 721 eV, corresponding to the L_3 and L_2 edges, respectively. This indicates that any alloying that occurred during Ga irradiation did not result in the formation of chemical compounds.

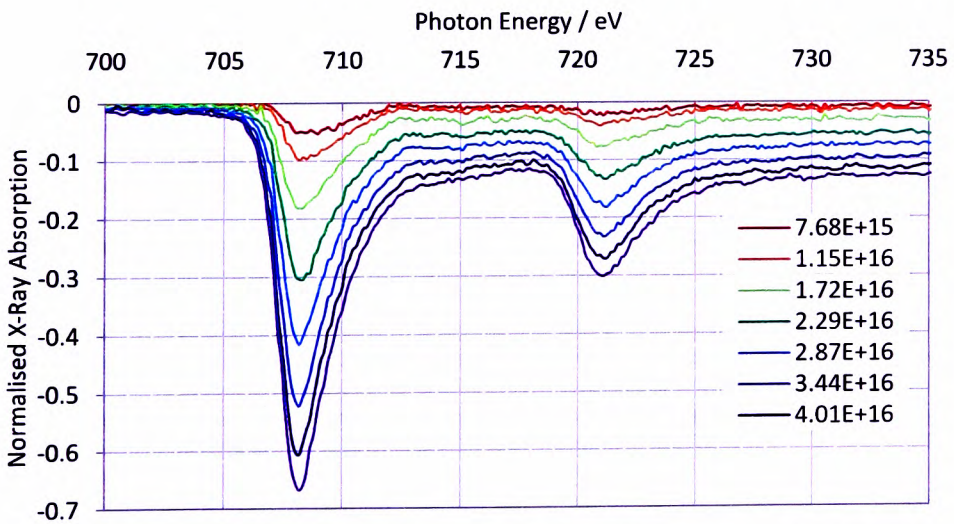

Figure 5.1.10 – XAS from the Fe-Ga regions. The spectra have been normalised to that from the as-grown film, thus the graph shows the relative absorption by different film thicknesses.

5.2 *Magnetic Properties of Ga-Irradiated Fe Films*

The effects of ion irradiation on the magnetic properties of a 12 nm thick Fe film were determined by magneto-optical and Lorentz microscopy. Eight squares measuring 40 μm × 40 μm were irradiated with a range of Ga ion doses. Each irradiated area was isolated from the surrounding film by a 2 μm wide frame, milled using an ion dose high enough to sputter away the full thickness of the Fe. In addition, a ninth square was defined within which the Fe was left in the original as-grown state.

5.2.1 Magneto-Optical Measurements

The probing light used for the MO measurements was conditioned to have a low degree of ellipticity such that the signal associated with the circular component was raised above zero to aid the signal recovery electronics, as previously discussed in Chapter 4. The azimuth and ellipticity angles of the light after passing through the lenses, without the sample in place, were found to be 0.345° and 10.065° respectively. The sample was then inserted into the beam path such that the angle of incidence was 25-30°, ensuring a component of the in-plane magnetisation was along the photon propagation direction. The spot size was adjusted such that it was just large enough to over-illuminate a single square and an image of the sample was projected onto the detector aperture. This was then adjusted to allow only the light

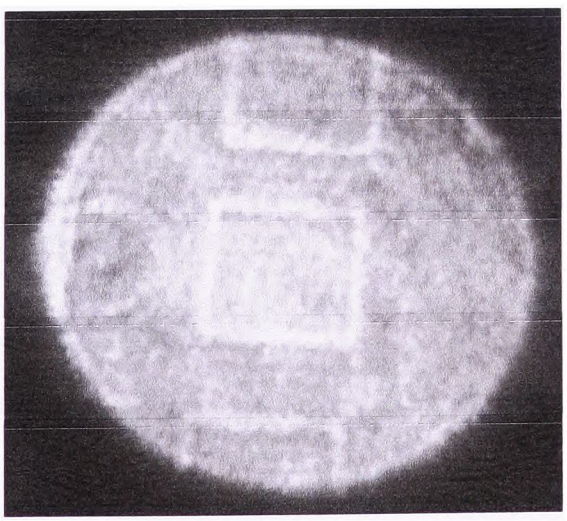

Figure 5.2.1 – A projected image of an irradiated region of an Fe film. The light square is the milled border surrounding the irradiated area.

transmitted through the centre of the square to reach the photodiode. A projected image of three of the FIB-irradiated areas is shown in Fig. 5.2.1.

Magnetic hysteresis loops were obtained from each of the nine squares, by taking the average of approximately 30 full cycles of the magnetic field. To avoid having to account for the lens contribution to the Faraday rotation as discussed in Chapter 4, the change in the ellipticity angle (ε_F) was used as a measure of the magnetisation. The loops from the areas irradiated with doses up to 1.72×10^{16} ions cm^{-2} are plotted in Fig. 5.2.2*A*, while those from the higher dosed areas have been plotted on a different scale in Fig. 5.2.2*B*.

The thin film in its original state has a narrow hysteresis loop with a low coercivity (H_C) of about 10 Oe. The relatively sharp switching at low values of the applied field is indicative of easy domain wall displacement that is typical in soft magnetic materials. The loop appears slightly offset to the right of the origin, which is likely to be a result of the remanent magnetisation of the iron cores in the electromagnet. The square of Fe left in the as-grown state shows an increase in H_C of approximately 5 Oe above that of the original continuous film, suggesting that there may be a pinning effect introduced by the milled edges of the frame.

The measurements on the Fe-Ga squares show that Ga irradiation can have a dramatic effect on the magnetic behaviour as shown in Fig. 5.2.3*A*, where H_C is plotted as a function of ion dose. At the lowest ion dose of 7.68×10^{15} ions cm^{-2} there is only a marginal increase in H_C above that of the Fe square but there is already a marked reduction in the saturation magnetisation (M_S), which can be attributed to sputtering of a small volume of material, as revealed by the STXM data. At a dose of 1.15×10^{16} ions cm^{-2}, H_C increased to 40 Oe but the sharp switching shown by the loop squareness suggests that domain wall propagation across the film was still unrestricted. The introduction of domain wall pinning only became apparent at a higher dose of 1.72×10^{16} ions cm^{-2}, where the slightly reduced squareness of the loop suggests that the reversal occurred in several steps. At this point H_C had increased to 108 Oe. It reached a maximum of 205 Oe (almost 14 times that of the Fe square) at a dose of 2.87×10^{16} ions cm^{-2}, after which it rapidly reduced along with M_S and the signal-to-noise ratio on the application of higher doses.

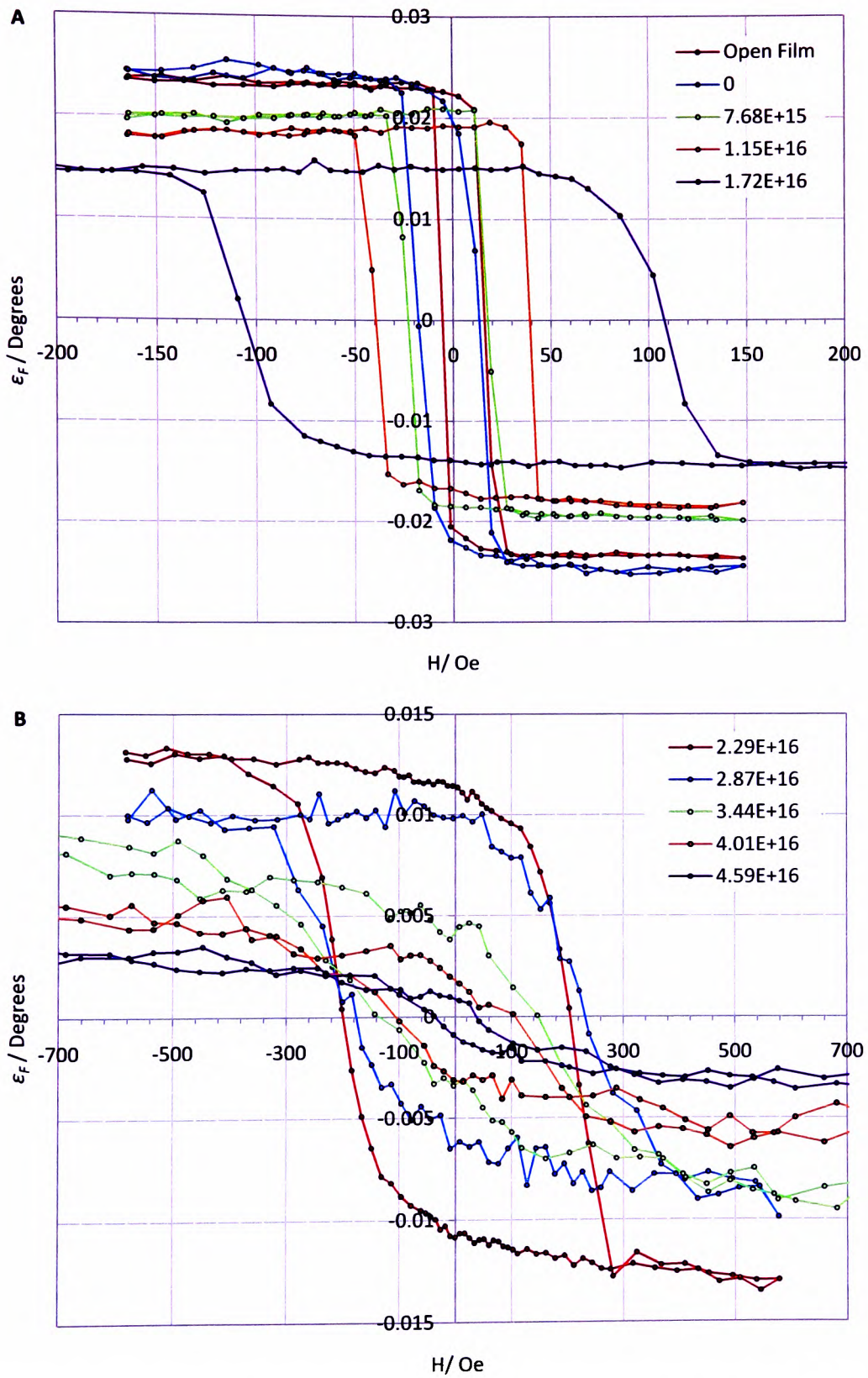

Figure 5.2.2 – Magnetic hysteresis loops showing the variation in ellipticity angle of the light transmitted through the as-grown and Fe-Ga regions as a function of applied field. The loops corresponding to the low and high ion doses are shown in *A* and *B* respectively.

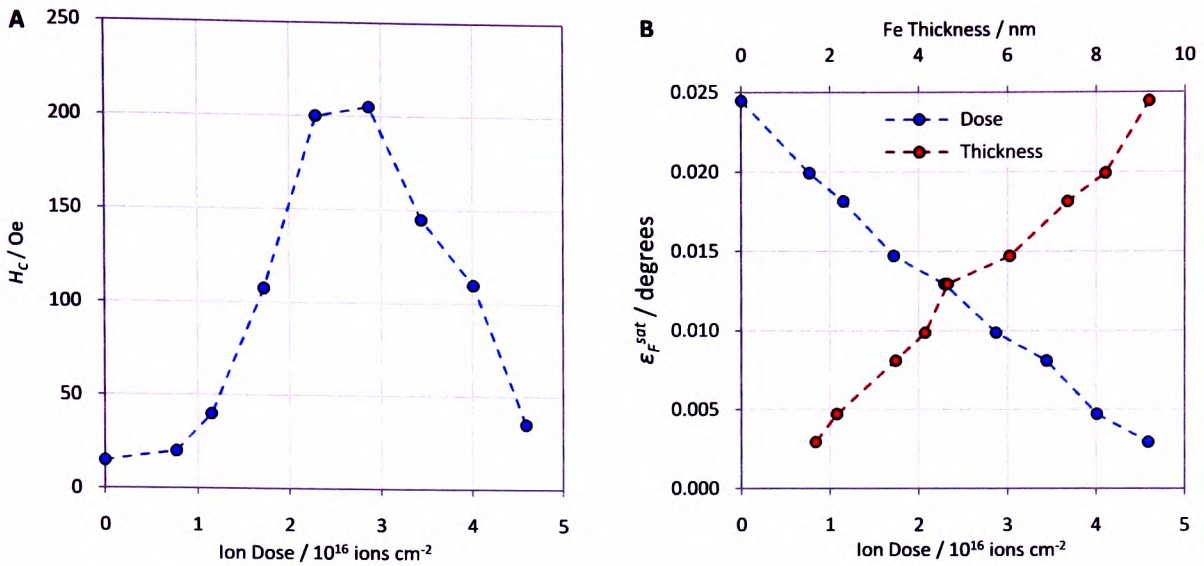

Figure 5.2.3 – *A*: Coercivity plotted as a function of ion dose. *B*: Ellipticity angle at saturation (ε_F^{sat}), as a function of ion dose and expected film thickness. The film thicknesses have been inferred from the thickness vs. dose measurements in Fig. 5.1.6.

The reduction in saturation magnetisation ($\varepsilon_F^{sat} \propto M_S$), shown in Fig. 5.2.3*B*, is approximately linear with ion dose. There may be a reduction in M_S as a result of alloying, but it is more likely to be attributed to the reduced volume of magnetic material[5.10]. For single-crystal Fe films with thicknesses in the range of 1 nm to 5.5 nm, the coercivity has been shown to be relatively consistent, on the order of 20 Oe[5.11]. For thicker polycrystalline films, an increase in coercivity was observed as the thickness was reduced towards 40 nm, but was attributed to a switch from Bloch to Néel domain walls[5.10]. Since the films studied here are too thin to support Bloch walls, this mechanism is not responsible for the large range of coercivities observed, which is most likely a result of changes to the structure and composition of the film. It is well known that the coercivity of polycrystalline materials is determined by domain wall pinning at the grain boundaries, provided that the grains are larger than the exchange correlation length (domain wall width), $L_0 = (A/K_1)^{1/2}$ (where A is the exchange stiffness and K_1 is the magnetocrystalline anisotropy constant). In this regime, the coercivity is inversely proportional to the grain size[5.10, 12-15], but is also dependent upon other aspects of the microstructure such as surface roughness, stress and oxidation state[5.10]. Larger grains mean fewer grain boundaries and consequently fewer pinning sites. Each grain will have an easy-axis defined by its shape, which may differ from one grain to the next. In this case the magnetic behaviour is determined by the anisotropy constant, K_1[5.12, 13]. The Fe film in Fig. 5.1.1, in its as-grown state, comprises grains approximately 15 nm in size; this is slightly smaller than the 18 nm exchange correlation length in Fe[5.14]. In this regime the

magnetisation cannot align along the easy-axis of each individual grain, so there is an averaging of the magnetocrystalline anisotropy over several grains that are coupled by the exchange interaction. This leads to a smaller effective anisotropy constant $\langle K \rangle$[5.12, 13]. The stronger coupling between grains and averaging of the crystalline anisotropy makes nanocrystalline materials, magnetically, very soft. Increasing the grain size within this regime will result in an increase in the coercivity. In fact, the random anisotropy model[5.12, 13] predicts H_C increases with the sixth power of the grain size. This dependency is not so strong in thinner films where the thickness is less than L_0, as shown by Georgieva *et al.*[5.15].

From Figs. 5.1.1, *A* and *B*, it can be seen that doses of 7.68×10^{15} ions cm^{-2} and 1.15×10^{16} ions cm^{-2}, increase the grain size past the exchange correlation length, which could be accountable for the increased coercivity. The easy domain wall displacement in these Fe-Ga regions, indicated by the hysteresis loop squareness, may suggest that the defects introduced by the Ga implantation are smaller than L_0, thus their effects are effectively averaged out. The incorporation of Ga may also affect coupling between grains, particularly if it accumulates at the grain boundaries. At doses of 1.72×10^{16} ions cm^{-2} and above, the discontinuities as observed in Figs. 5.1.1, *C* and *D* are large and probably provide pinning sites for the domain walls, increasing the coercivity. At the highest ion doses, the intergranular distance is increased such that the remaining Fe-Ga grains are only weakly coupled through the magnetostatic interactions and magnetisation of each region occurs almost independently. As a result, the hysteresis loops show progressive hardening of the Fe-Ga.

5.2.2 Lorentz Microscopy

Lorentz TEM imaging of the sample provided some insight into the changes occurring to the magnetic structure of the Fe as the ion dose was increased. Fig. 5.2.4 comprises a series of Fresnel images of the as-grown Fe and several of the irradiated areas at remanence after magnetising the film somewhat by inclining the TEM sample stage (see Chapter 2). The field values cannot be given because of a lack of objective lens field data. Some of the images show clear ripple contrast, where alternating light and dark bands form perpendicular to the magnetisation direction. The effect occurs almost exclusively in polycrystalline films and arises as a result of fluctuations in the magnetisation direction of the individual grains. Following the first description of magnetisation ripple by Fuller and Hale in 1960, several theories have been developed in an attempt to quantify this phenomena[5.16] and relate it to the

structural and magnetic properties of the sample.

In Fig. 5.2.4*A*, the ripple contrast occurring in the as-grown film, well away from any implanted features can be seen. In *B*, the film is enclosed by a square frame which causes a rotation of the ripple with respect to the direction in *A*, but the wavelength remains similar. In order to reduce magnetostatic energy, the magnetisation of the film near the milled frame tries to align parallel to the edges. Inside the frame, it appears as though the magnetisation has tried to align parallel to the vertical edges and consequently has rotated clockwise by 35° with respect to the direction in *A*. At the lower frame edge, the magnetisation has rotated anti-clockwise by 20°. The direction of magnetisation is also inferred from the relative positions of the light and dark contrasting square outlines. The bright outline corresponds to the position of the milled frame where all the Fe has been removed. The electron beam is transmitted through this area without being deflected by the Lorentz force and it therefore serves as a reference image. The image of the magnetised film then appears shifted relative to this bright outline because of the Lorentz deflection, and may be used to determine the direction of magnetisation.

The effect of ion irradiation is illustrated in images Figs. 5.2.4 *C* to *G*, where the ion doses applied were 7.68×10^{15}, 1.15×10^{16}, 1.72×10^{16}, 2.29×10^{16} and 2.87×10^{16} ions cm^{-2},

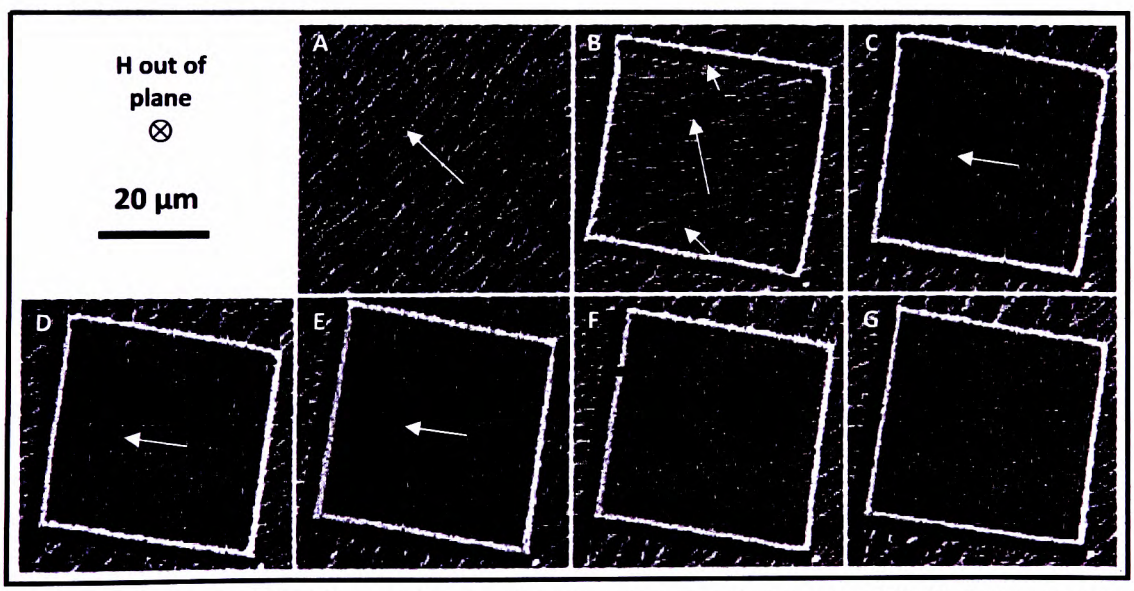

Figure 5.2.4 – Fresnel TEM images showing the remanent magnetic structure of the Fe in its as-grown state without (*A*) and with (*B*) a milled frame. The areas irradiated with ion doses of: 0.768 (*C*), 1.15 (*D*), 1.72 (*E*), 2.29 (*E*) and 2.87 (*G*) $\times10^{16}$ ions cm^{-2}. The white arrows indicate the direction of magnetisation inferred from the ripple contrast and Lorentz deflection along the frame edges. The objective lens field strength is not known, but is applied perpendicular to the sample.

respectively. The square with the lowest ion dose still shows ripple, however the wavelength and contrast appear slightly reduced, indicating reduced magnetic dispersion. The direction of the ripple and the lack of a dark band at the right frame edge both indicate that the magnetisation lies parallel to the top and bottom frame edges. This suggests that the coercive force is larger in the Fe-Ga and restricts the magnetisation from rotating away from its former magnetised state. The magnetisation ripple disappears almost completely at higher doses where the grain boundaries are too disordered to give rise to any noticeable contrast. The direction of magnetisation can still be determined from the direction of the Lorentz deflection, but this too becomes smaller as the film becomes thinner until virtually all magnetic contrast in the Fe-Ga region disappears in images *F* and *G*.

In summary, Ga ion implantation has been shown to drastically affect the magnetic behaviour of thin Fe films, although the Fe-Ga remained ferromagnetic even after a dose of 4.59×10^{16} ions cm^{-2} was applied. The coercivity increased up until a dose of 2.29×10^{16} ions cm^{-2} at which point the film started to become discontinuous. At low doses the increase in coercivity may have been a consequence of reduced exchange coupling between the grains as a result of enlargement to a size greater than the exchange correlation length. Higher doses introduced discontinuous regions that mostly likely inhibited the domain wall displacement across the film. After a dose of 2.87×10^{16} ions cm^{-2}, the coercivity began to reduce significantly but still remained higher than that of the as-grown film.

References

5.1 D. Ozkaya, R. M. Langford, W. L. Chan and A. K. Petford-Long, Journal of Applied Physics **91** (12), 9937-9942 (2002).

5.2 R. Hyndman, P. Warin, J. Gierak, J. N. Chapman, J. Ferré, J. P. Jamet, V. Mathet and C. Chappert, Journal of Magnetism and Magnetic Materials **240** (1-3), 50-52 (2002).

5.3 W. Voegeli, K. Albe and H. Hahn, Nuclear Instruments & Methods in Physics Research Section B-Beam Interactions with Materials and Atoms **202**, 230-235 (2003).

5.4 G. A. Müller, E. Carpene, R. Gupta, P. Schaaf, K. Zhang and K. P. Lieb, European Physical Journal B **48** (4), 449-462 (2005).

5.5 R. A. Dunlap, J. D. McGraw and S. P. Farrell, Journal of Magnetism and Magnetic Materials **305** (2), 315-320 (2006).

5.6 R. A. Dunlap, N. C. Deschamps, R. E. Mar and S. P. Farrell, Journal of Physics-Condensed Matter **18** (20), 4907-4920 (2006).

5.7 V. Ignatova, D. Karpuzov, I. Chakarov and I. Katardjiev, Progress in Surface Science **81** (6-7), 247-335 (2006).

5.8 Y. Stark, R. Frömter, D. Stickler and H. P. Oepen, Journal of Applied Physics **105** (1), 5 (2009).

5.9 T. Ishitani and T. Ohnishi, Journal of Vacuum Science & Technology a-Vacuum Surfaces and Films **9** (6), 3084-3089 (1991).

5.10 Y. K. Kim and M. Oliveria, Journal of Applied Physics **74** (2), 1233-1241 (1993

5.11 Y. W. Liu, PhD Thesis, University of Salford, 2005.

5.12 G. Herzer, IEEE Transactions on Magnetics **26** (5), 1397-1402 (1990).

5.13 G. Herzer, Scripta Metallurgica Et Materialia **33** (10-11), 1741-1756 (1995).

5.14 A. Hernando, Journal of Physics-Condensed Matter **11** (48), 9455-9482 (1999).

5.15 M. T. Georgieva, N. D. Telling and P. J. Grundy, Materials Science and Engineering B-Solid State Materials for Advanced Technology **126** (2-3), 287-291 (2006).

5.16 K. D. Leaver, Thin Solid Films **2** (1-2), 149-172 (1968).

CHAPTER 6 FIB-Patterned Ferromagnetic Films and Magnetic Domain Imaging

This chapter is an exploration of FIB-patterned media using magneto-optical and X-ray microscopy analysis techniques. Several patterns have been studied, including arrays of discrete Fe elements, composite Fe/Fe-Ga structures, and anti-dots. MTXM images of some patterns provide detailed information about the domain structure within each individual element, while the magneto-optical measurements provide the average hysteretic behaviour.

6.1 *Experimental Prerequisites*

All patterns were milled into 12 nm nanocrystalline Fe films, grown on 100 nm thick silicon nitride membranes. The physical arrangement of the magneto-optical Stokes polarimeter made it impossible to perform D-MOKE in the usual manner but the image of the sample formed at the detector were superstitions of all diffracted orders collected by the objective lens, thus the measurements still contained the extra information provided by the diffracted light. In addition to the magneto-optical measurements, the structural and magnetic properties of typical arrays were studied using the STXM and MTXM at ALS beamlines 5.3.2 and 6.1.2, respectively.

Magneto-optical and MTXM measurements were performed with an incidence angle of 25-30°, where the plane of incidence was parallel to the applied magnetic field (see Chapter 3). As previously discussed (Chapter 4) a slightly elevated circular polarisation factor is required. However, since most of the patterns were optically anisotropic, the ellipticity was kept as low as possible to avoid a potentially complex combination of polarisation-dependent effects. Therefore, the measurements were performed using *p*-polarised ($\Psi = 3°$) or *s*-polarised ($\Psi = 87°$) light with a low ellipticity angle of approximately 3°; in some cases both polarisation states were used. Each pattern was measured at two orientations, with the applied field along the pattern's *x*- or *y*-axis, as indicated in the relevant figures. There were then four possible arrangements: i) x // **H**, *p*-polarisation; ii) x // **H**, *s*-polarisation; iii) y // **H**, *p*-polarisation; iv) y // **H**, *s*-polarisation.

6.2 *Nanocrystalline Fe Gratings*

Probably the simplest pattern with which to observe the combined magneto-optical and diffraction effects is a grating made up of magnetic and non-magnetic elements[6.1-5]. Schmitte *et al.* reported D-MOKE measurements on a number of polycrystalline Fe gratings with various strip widths and a fixed period of 5 μm[6.2]. Strips of width 2.1 μm and 2.5 μm generated peaks in the Kerr signals around the switching fields, which were only seen in the second-order diffracted beams. These effects were attributed to the formation of domains. On the other hand, gratings with different strip widths did not show any dependence of the loop shape on diffraction order. It was stated that even though the domain structure within strips of comparable width were similar, the loop shapes were very sensitive to the ratio of the strip width to the grating parameter. Westphalen *et al.* reported vector- and D-MOKE measurements on a grating comprising alternating wide (1.9 μm) and narrow (0.9 μm) Fe strips and found more varied hysteresis loop shapes, which again were attributed to domain formation[6.3].

Here, the FIB was used to mill away rectangular sections of film such that gratings were produced with Fe strips of width w_m, separated by milled spacer regions of width w_s. The film thickness variations across the gratings are much less than the wavelength of the light (670 nm) so the phase differences introduced as a result of the structure would be negligible, but because of absorption and reflectivity variations, the patterns functioned as transmission amplitude gratings. The resulting diffraction patterns contain contributions from both the Fe and spacer strips, but only those from the Fe change with magnetisation. Even without considering magnetic effects, a metallic grating couples the polarisation of the incident light with the geometry of the grating[6.6, 7] resulting in a polarisation dependant transmittance. Inoue *et al.* define three regimes for magnetic gratings[6.6]: i) $2(w_m+w_s) < \lambda$; ii) $w_m > \lambda$; iii) $w_m < \lambda < 2(w_m+w_s)$. A grating that satisfies the first condition is said to behave as a wire grid polariser, while one that satisfies the second behaves as a continuous film in terms of the magneto-optical effects. The third regime is effectively a transition between the first two, where complex combinations of the magneto-optical and polarisation effects can occur.

6.2.1 X-Ray Microscopy

Before the magneto-optical measurements on the FIB-patterned gratings were performed, the structural and magnetic properties were studied using STXM and MTXM. Fig. 6.2.1 shows a three-dimensional surface plot (generated from the STXM OD image in *A*) of a grating with equal strip and spacer widths of 0.4 μm. The *z*-axis has been scaled such that the thickness variations are greatly exaggerated to clearly show the profile of the pattern. Each strip was irradiated with a different ion dose, ranging from zero up to 5.16×10^{16} ions cm^{-2}. It is apparent that the strips do not have well-defined sharp edges, but approximate Gaussian profiles, reflecting the ion distribution in the FIB. Even the strip that was not intentionally irradiated (strip 10) has been reduced in thickness by about 2 nm as a result of the FIB tails (*B*). XMCD images of the grating (included in Appendix 3) reveal that there is in fact no correlation between ion dose and coercivity for the strips irradiated with doses up to 1.15×10^{16} ions cm^{-2} (Strips 7-10). In fact strips 8, 9 and 10 simultaneously undergo complete reversal at field values of +426 Oe and -413 Oe. The effect of the ion irradiation can only really be observed after applying doses of 2.29×10^{16} ions cm^{-2} or higher, where domain wall

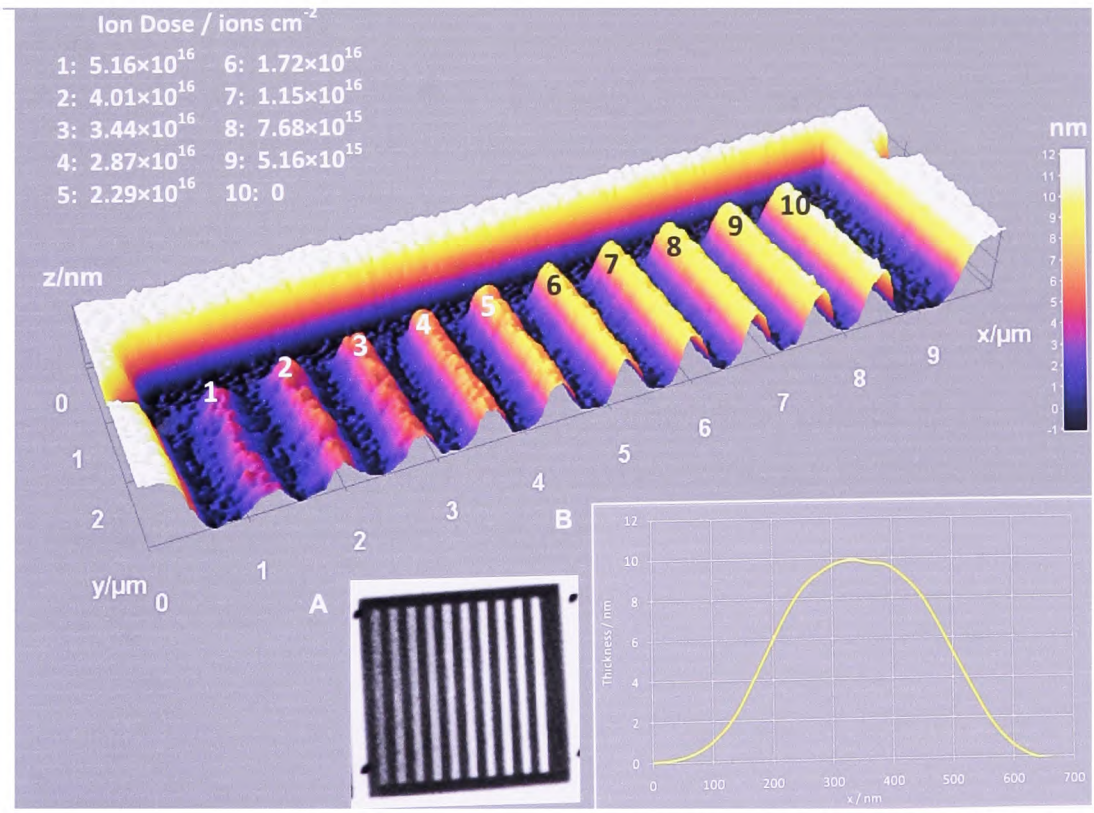

Figure 6.2.1 – A 3-D surface plot generated from an STXM OD image (*A*) of a grating with $w_m = w_s =$ 0.4 μm. Each strip was irradiated with a different ion dose and therefore had a different thickness as indicated by the colour scale. The z-scale has been plotted in order to exaggerate the thickness variations. The surface profile of strip 10 is show in *B*.

pinning is observed and magnetisation reversal takes place over several field increments.

Figure 6.2.2 shows an MTXM image of a grating where all Fe strips are identical and received no additional ion dose apart from that from the FIB tails. The spacer strips were irradiated with a lower ion dose than those shown in Fig. 6.2.1 and as a result, clusters of Fe-Ga remain between the Fe strips. The Fe-Ga clusters increase the surface roughness around the strip edges and seem to provide extra pinning sites that restrict the domain wall motion during magnetisation along the strip length (easy-axis), as illustrated by the XMCD images in Fig. 6.2.3. Although the strips were created identical, the individual hysteresis loops (Fig. 6.2.4*A*) show a wide range of coercivity values, possibly due to differences in the microstructure along the edges. Some loops are also displaced from the origin, which may indicate a degree of pinning via magnetostatic interactions between the neighbouring strips, depending on whether their magnetisation was parallel or anti-parallel. The variations in coercivity and switching field of the individual strips gave the grating an effective coercivity of just over 100 Oe (Fig. 6.2.4*B*). Averaging the behaviour in this way is effectively what happens during magneto-optical measurements.

The grating was also magnetised with the applied field perpendicular to the strips (hard-axis). The images of this process are not shown here since no XMCD contrast could be observed suggesting that either there was no domain structure, or that it did not change significantly from one image to the next. However, a small magnetic signal became apparent when the average intensity of the X-rays transmitted through each strip was plotted as a function of applied field (Fig. 6.2.4*C*). The magnitude of this signal is only 18 % of that observed during easy-axis magnetisation. The lack of any magnetic features in the images would imply coherent rotation of the magnetisation vector rather than reversal by domain wall displacement. Interestingly, the plot shows that on average, the strips have a small component of magnetisation perpendicular to their length at remanence.

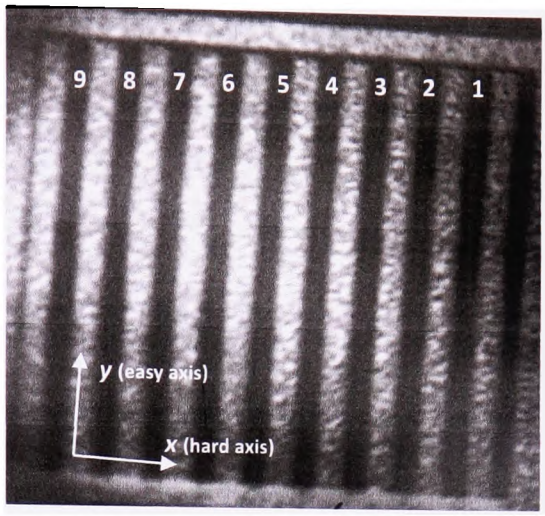

Figure 6.2.2 – MTXM image of a polycrystalline Fe grating with $w_m = w_s = 0.4$ μm. This is not an optical density image, so the Fe regions appear dark and the thinner milled regions are bright.

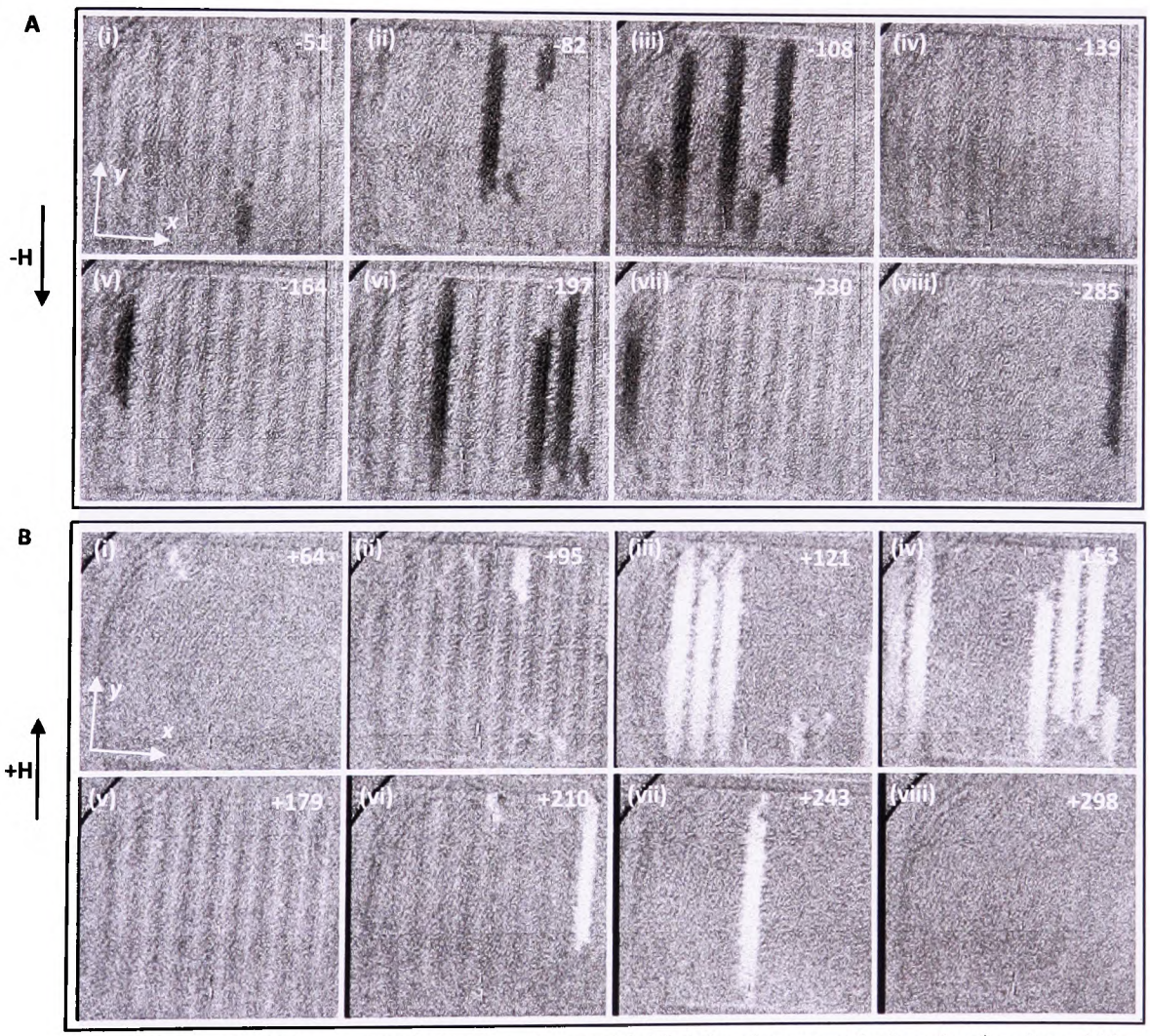

Figure 6.2.3 – XMCD sequential difference images highlighting the magnetic domains forming within strips of nanocrystalline Fe while stepping the applied field from +369 Oe to -357 Oe (*A*) then back to +369 Oe (*B*). The field values (in Oe) are shown in each image.

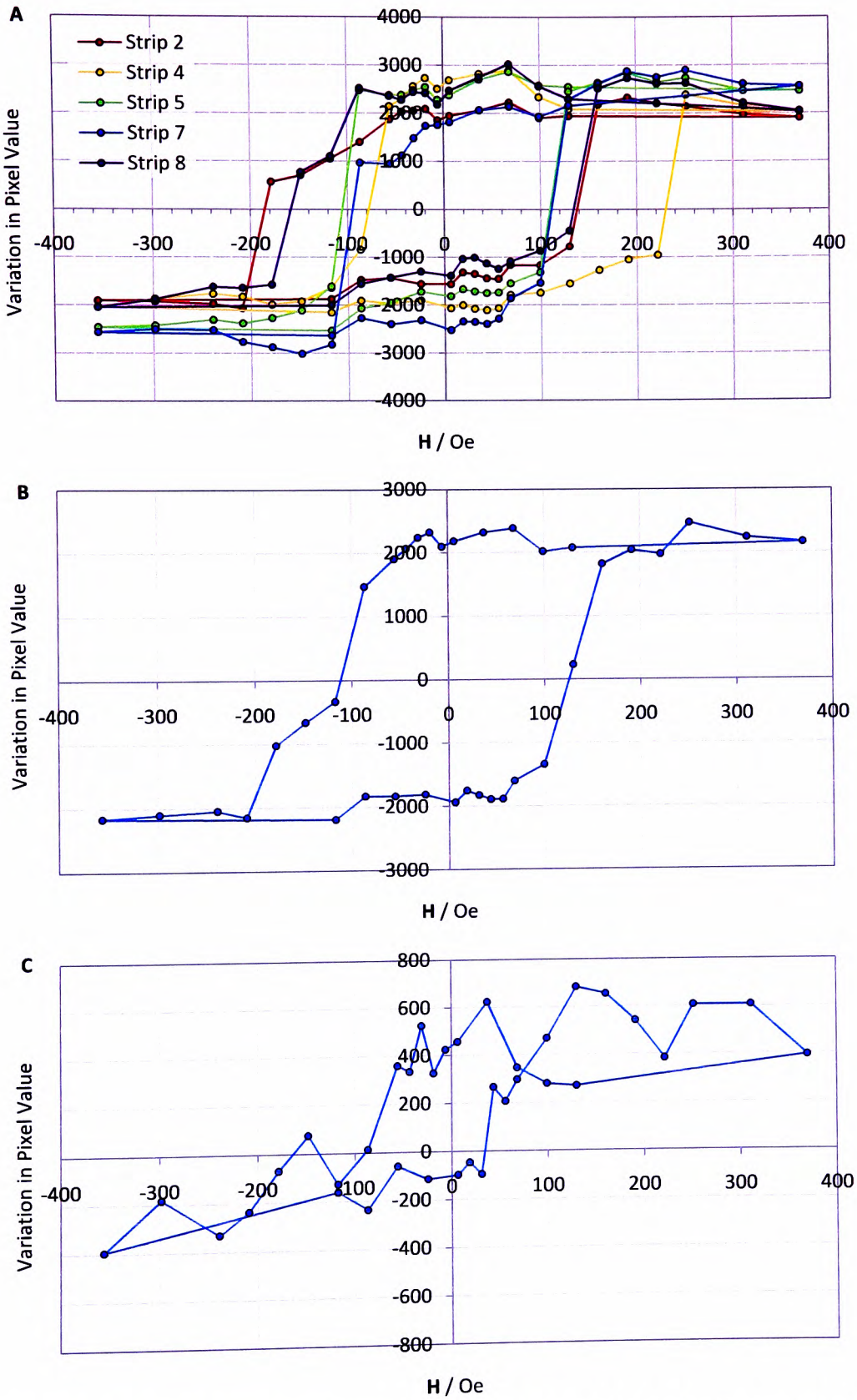

Figure 6.2.4 – Hysteresis loops derived from the MTXM images showing the behaviour of several of the individual strips (*A*) and the entire grating (*B*) during easy-axis magnetisation. The average behaviour of the grating during hard-axis magnetisation is shown in *C*.

6.2.2 Magneto-Optical Properties

For the purpose of magneto-optical characterisation, gratings were patterned over much larger areas of the film measuring 58 μm × 58 μm. The Fe strips were formed slightly wider by 0.1 μm (w_m = 0.5 μm) to allow for the extra irradiation caused by the FIB tails. Three separate gratings were produced with strip separation widths (w_s) of 0.5 μm, 1 μm and 1.5 μm. SEM images of the gratings are shown in Figs. 6.2.5, *A*, *B* and *C* respectively.

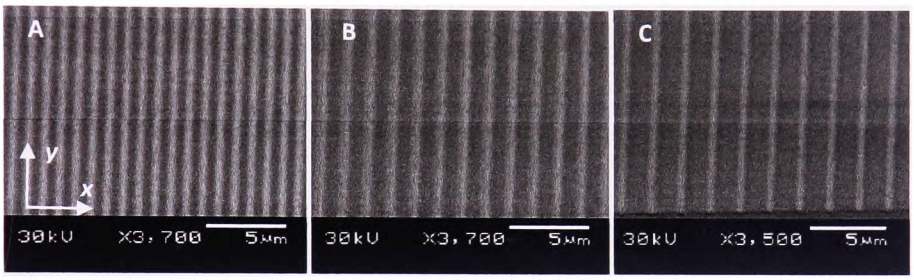

Figure 6.2.5 – SEM images of the grid patterns with w_m = 0.5 μm and w_s = 0.5 μm (*A*), 1 μm (*B*) and 1.5 μm (*C*). The scale in *C* is different to that in *A* and *B*.

The wavelength of the light used to probe the structures was 670 nm, thus each grating falls into the so-called resonance domain, where the grating period is comparable to the wavelength of the light. The Stokes parameters were averaged over 30 cycles of the applied field, from which the Faraday rotation and ellipticity angles were calculated and plotted as a function of **H** in Figs. 6.2.6 and 6.2.7. The θ_F loops show that the gratings with strip separation widths of 0.5 μm and 1.5 μm, both have values of easy-axis coercivity on the order of 150 Oe, but the grating with w_s = 1 μm had a much higher coercivity of 230 Oe. Reduced magnetostatic coupling between the strips could potentially increase the coercivity as the strip separation increases[6.7], but the fact that only the grating with an intermediate value of w_s shows an increase would suggest this is not the case. As previously discussed, the microstructure around the strip edges may induce pinning. Any beam drift during milling would have resulted in poorly defined edges, as well as unintentional irradiation of the Fe strips, producing a greater number of pinning sites; this is considered to be the most likely explanation for the increased coercivity.

The θ_F loops obtained during hard-axis magnetisation are quite clearly asymmetric. Again, the loops in *A* and *C* are similar in shape, but those in *B* differ substantially. The two polarisation states result in not just a variation in the magnitude of the signal as seen on the continuous film in Chapter 4, but also very different loop shapes. The loop measured with *s*-

polarised light is typical of hard-axis magnetisation, while that produced using *p*-polarisation bears no resemblance to what might be expected from the **M** versus **H** behaviour. The magnetic reversal mechanism is obviously going to be the same in both cases, therefore the different results can only be attributed to polarisation effects.

Unlike in the case of a continuous film, the hysteresis loops plotted using the ε_F measurements (Fig. 6.2.7) do not emulate the behaviour of corresponding θ_F loops. This is particularly noticeable during hard-axis magnetisation, where the asymmetry of the resulting loops is so pronounced that the two branches of the cycles cross one another. Again, changing the polarisation state from *s* to *p* affects the loop shape. The grating with w_s = 1 μm appears to be a special case where both polarisation states yield similar loops. The period of the grating is 1.5 μm, but because of the angle of incidence of around 27°, it is effectively reduced to 1.34 μm which is twice the wavelength of the probing light. This may be coincidental but invites further theoretical analysis. As well as increased asymmetry, the hard-axis ε_F loops measured with *s*-polarised light reveal additional features during magnetisation reversal. Each loop has small steps between field values of +21 and +42 Oe during the $-\mathbf{H} \rightarrow +\mathbf{H}$ branches, and between -21 and -39 Oe during the $+\mathbf{H} \rightarrow -\mathbf{H}$ branches. These features correspond approximately to the switching observed in the X-ray transmission hysteresis loop in Fig. 6.2.4. These steps are virtually unnoticeable in the θ_F measurements which might imply ε_F is more sensitive to the mechanism by which the magnetisation reverses.

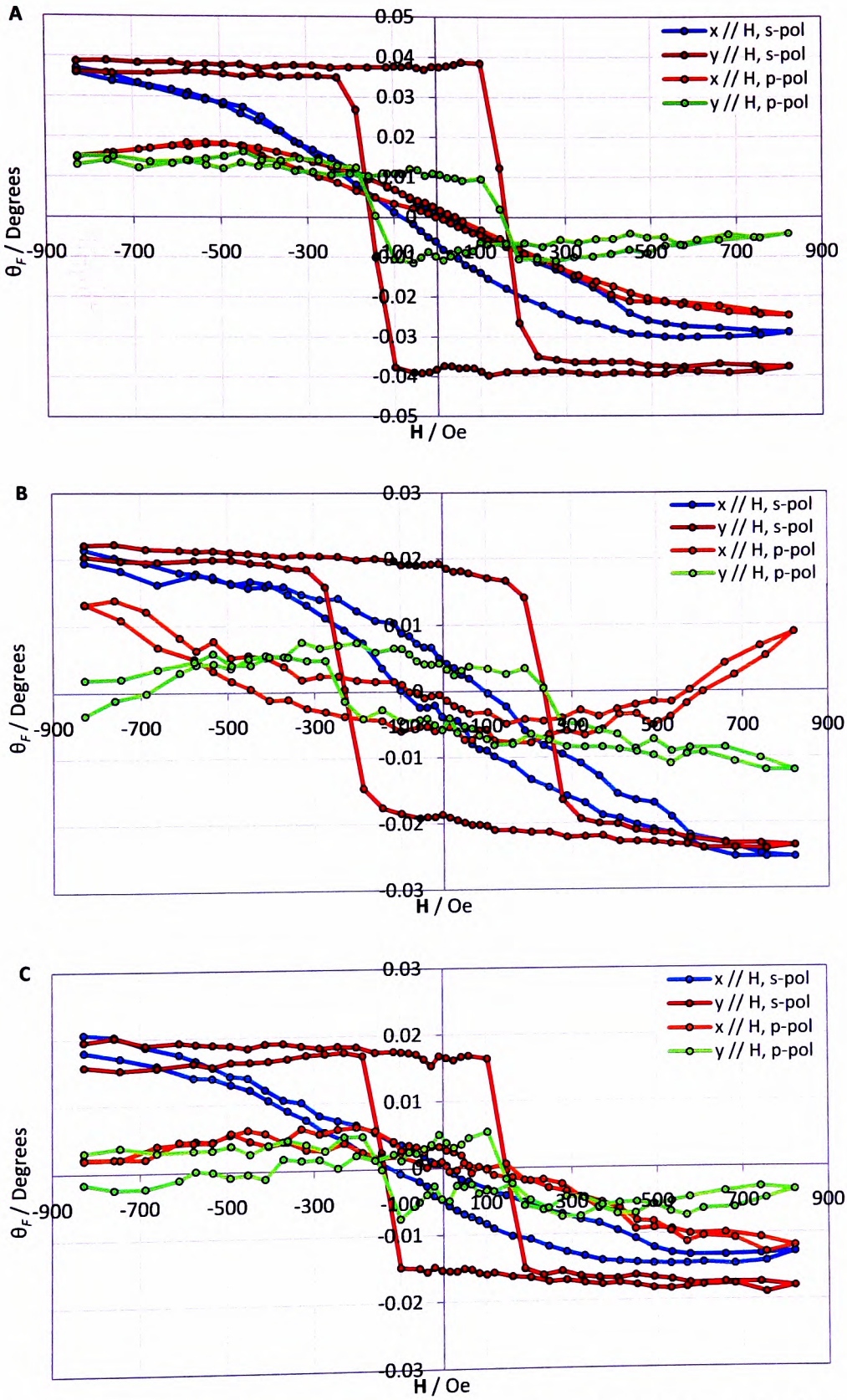

Figure 6.2.6 –Hysteresis loops showing the θ_F produced by gratings with w_m = 0.5 and w_s = 0.5 μm (*A*), 1.0 μm (*B*) and 1.5 μm (*C*), at various applied field strengths.

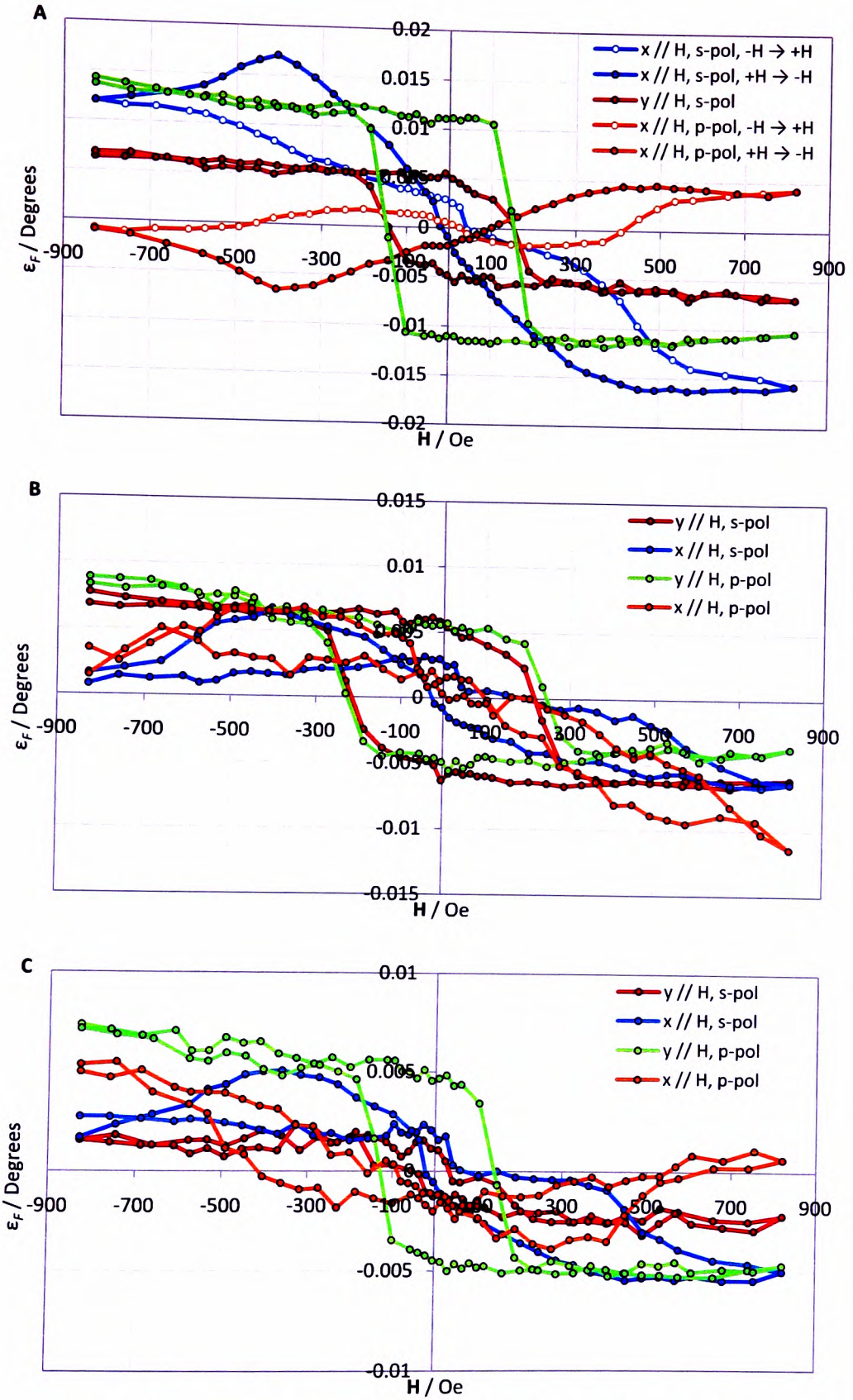

Figure 6.2.7 – Hysteresis loops showing the ε_F produced by gratings with $w_m = 0.5$ and $w_s = 0.5$ μm (*A*), 1.0 μm (*B*) and 1.5 μm (*C*), at various applied field strengths. In *A*, the two branches of the hard-axis cycles, (**-H** → **+H**) and (**+H** → **-H**), have been plotted using different symbols.

The reason behind the irregular shape of some of the hysteresis loops in Figs. 6.2.6 and 6.2.7 is not fully understood, but it is clear that the grating period has a significant effect, particularly during hard-axis magnetisation. The magnetic reversal process occurring within each grating is not thought to change significantly as a result of increasing w_s, but diffraction effects caused by the grating geometry will. Not only may the loop shapes produced by the diffracted light vary with w_s[6.2, 3], but in addition, the number of diffracted orders that comprise the image at the photodiode may also vary as a result of the limited aperture of the objective lens. As w_s increases, more of the higher orders can be collected since the diffracted beams become less dispersed, possibly changing the apparent behaviour of the gratings.

It is also possible that anomalous loops could originate from the second-order magneto-optical effects. Osgood *et al.*, used a longitudinal MOKE arrangement to measure the hard-axis magnetisation of Fe(110) films[6.9]. Asymmetrical loops of various shapes were obtained, some of which were similar to the "distorted lemniscate" shaped loops in Fig. 6.2.7*A*. This anomalous behaviour was associated with the magneto-optical effects second-order in **M** which are proportional to the product of the longitudinal and transverse components of the magnetisation, $m_l \cdot m_l$ (Fig. 6.2.8). It was explained in Ref. (6.4) that this behaviour is observed when **H** is applied at a small angle to the hard-axis.

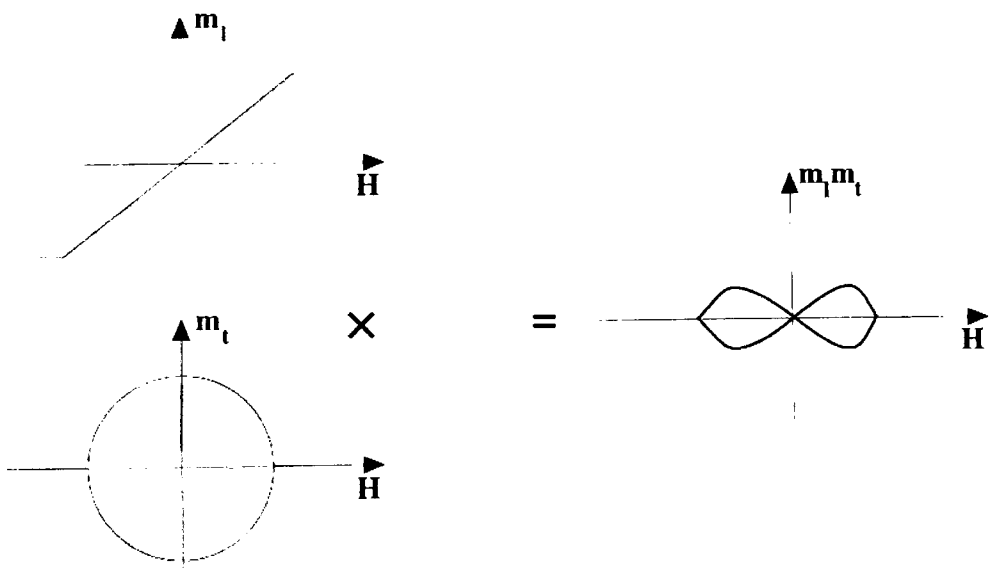

Figure 6.2.8 – A schematic diagram of $m_l \cdot m_t$ vs. **H** applied almost parallel to the hard axis. The second-order magneto-optical effects are proportional to the product of m_l and m_t. Adapted from Ref. (6.9).

The $m_l \cdot m_t$ proportionality term is in fact intuitive, considering the second-order effects are magnetic linear birefringence and dichroism. The light polarised parallel or perpendicular to the magnetisation (effectively the optic axis) will pass through the material with the polarisation state unchanged, while the largest effects occur when **E** makes an angle of 45° with **M**. Linear birefringence affects the ellipticity of the light, while dichroism results in a rotation of the azimuth angle. The presence of these effects is indicative, but not necessarily purely a consequence, of coherent rotation of the magnetisation during reversal[6.2, 3, 9, 10]. The degree of asymmetry in the measured loops may be used as an indication of how well the coherent rotation model applies to the sample[6.9, 11]. In cases where domain wall displacement dominates, the asymmetry will be reduced. In order to determine the magnitude of $m_l \cdot m_t$ a technique analogous to vector-MOKE[6.3] would be required, where m_l and m_t are measured separately by rotating both the sample and magnetic field by 90° with respect to the plane of incidence.

The XMCD imaging suggests that there may be coherent rotation occurring during hard-axis magnetisation owing to the narrow geometry of the strips, which may be partially responsible for the asymmetry observed in Figs. 6.2.6 and 6.2.7. Where second-order effects are present, the resulting anomalies will manifest in the zeroth- and higher-order diffracted beams, while any effects associated with domain structure only appear in the high-order beams[6.2]. Thus by blocking the all diffracted orders with a spatial filter, the origin of the asymmetry may be determined. Alternatively, since the second-order effects become larger and the first order effects smaller as the angle of incidence approaches zero, some additional measurements of the gratings at various angles of incidence could also provide a clue as to the origin of the loop shape.

6.3 *Composite Fe and Fe-Ga Arrays*

In the previous section the gratings consisted only of Fe strips and thus the magnetic reversal was determined primarily by their shape anisotropy and to some extent their microstructure. Here, the arrays described were produced using lower ion doses such that Fe-Ga regions were created within the Fe, but still remained ferromagnetic allowing interactions to take place between all elements.

6.3.1 Fe and Fe-Ga Gratings

In an attempt to further understand the origin of the asymmetry previously observed during magneto-optical characterisation of the discrete Fe gratings, arrays of alternating 0.5 μm wide strips of as-grown and Ga-irradiated Fe were created using ion doses of 1.15×10^{16}, 1.72×10^{16}, 2.87×10^{16}, 3.44×10^{16} and 4.01×10^{16} ions cm^{-2}. As with the previous gratings, the length of the strips lay parallel to the sample *y*-axis. TEM observations in Chapter 5 show that the Fe should remain connected until an ion dose between 2.29×10^{16} and 3.44×10^{16} ions cm^{-2} is applied. In light of this, coherent rotation of the magnetisation might be considered as an unlikely occurrence in gratings irradiated with lower doses and reversal by domain wall displacement may be expected to dominate. At higher doses, the Fe becomes discontinuous and the Fe strips will become more isolated. However, the Fe-Ga remains ferromagnetic and should still allow domain formation between the strips. A combination of domain wall nucleation and coherent rotation may be expected in these gratings.

The θ_F hysteresis loops measured with **H** parallel to the length of the strips (*y*-axis) are shown in Fig. 6.3.1*A*. The two gratings implanted with 1.15×10^{16} and 1.72×10^{16} ions cm^{-2} behaved in a similar manner to the as-grown film, but exhibited slightly increased coercivity, having values of 25 and 50 Oe respectively. The gratings implanted with 2.87×10^{16} ions cm^{-2} or greater have a much higher coercivity of 140 Oe. The loops measured with **H** perpendicular to the strips in Fig. 6.3.1*B* clearly show the introduction of hard-axes after applying 2.87×10^{16} ions cm^{-2}. Interestingly, the two gratings that received the lowest ion doses display lower coercivity in this orientation than when the field is parallel to the strips. In fact, the grating that received the lowest dose has a coercivity of around 12 Oe, which is almost as low as that of the as-grown film (10 Oe). This is probably a result of domain formation at remanence, as indicated by the reduced squareness of the loops.

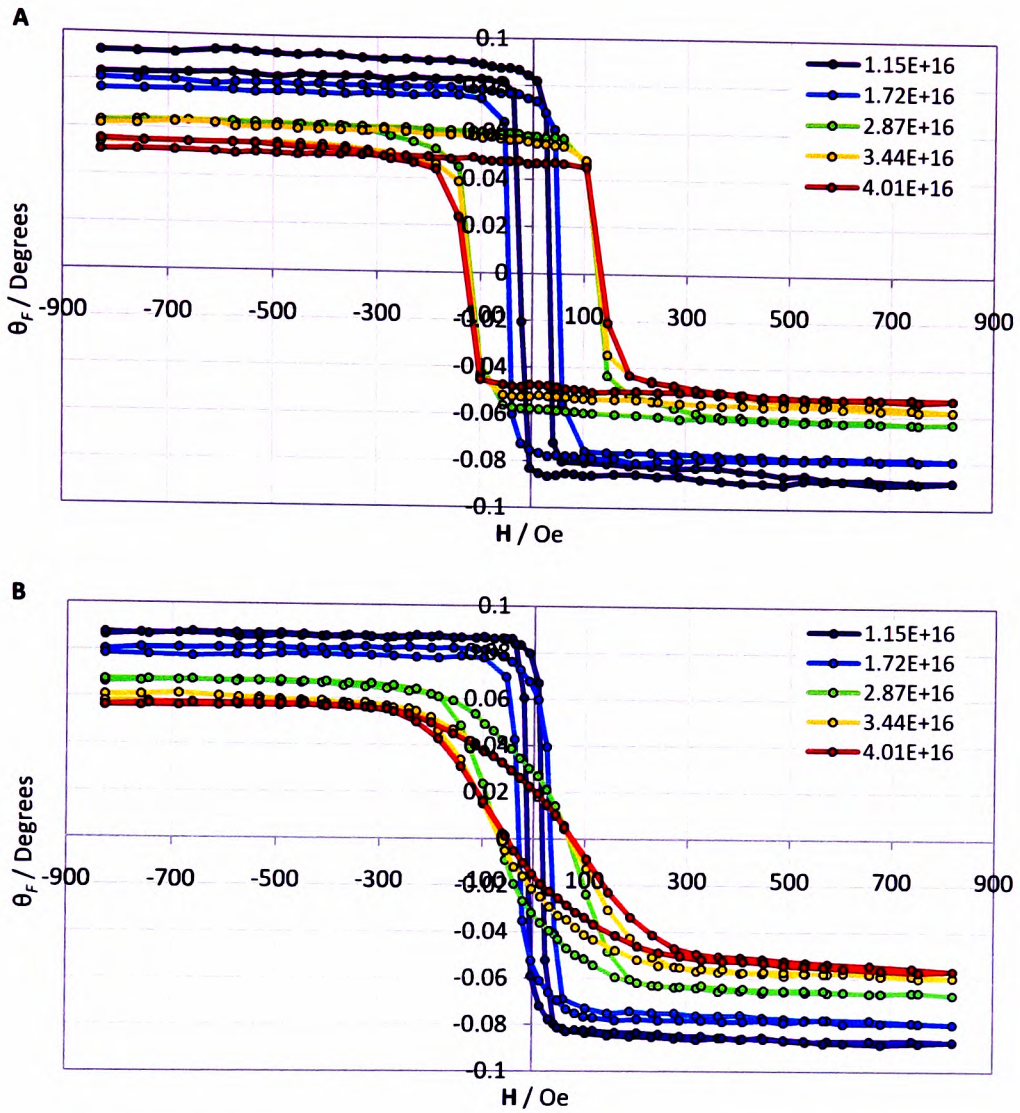

Figure 6.3.1 – Faraday rotation as a function of **H** applied parallel (*A*) and perpendicular (*B*) to the length of the strips.

Hysteresis loops showing the variation in ε_F as **H** is applied parallel to the strips are shown in Fig. 6.3.2*A*. As observed with the discrete gratings, irregular features are seen that are not apparent on the θ_F loops. In this case, the features appear at various points in the loops depending upon the ion dose applied. Surprisingly, the two gratings irradiated with the lowest doses exhibit greatest asymmetry, although it is not immediately apparent at first glance. Peaks in the magnitude of the ellipticity angle (marked with black arrows) manifest around **H** = 0, but only during the **+H** → **-H** branch of the cycle. Slightly larger peaks are present when the gratings are magnetised perpendicular to the strips, but instead occur during the **-H** → **+H** branch as shown in Fig. 6.3.2*B*.

As can be seen in Fig. 5.1.1 in Chapter 5, ion doses of 1.15×10^{16} and 1.72×10^{16} ions cm^{-2} do not produce well-defined edges between the as-grown Fe and irradiated Fe-Ga. In which case, diffraction effects produced by the gratings irradiated with these ion doses are likely to be weak. Also considering that the θ_F loops indicate weak anisotropy and a slightly reduced squareness, particularly in Fig. 6.3.1*B*, it would seem logical that the peaks at **H** = 0 are not a result of diffraction effects, but of domain formation at remanence. Schmitte *et al.* stated that domain-dependent features were only observable in the loops measured with diffracted light[6.2], but if domains form across the grating such that a significant component of the magnetisation is at an oblique angle to the plane of incidence, this could give rise to appreciable second-order effects that are observable with the specular beam.

The gratings irradiated with the three highest ion doses produce more symmetrical loops when magnetised parallel to the strips. The high shape anisotropy of the pattern creates a well-defined easy-axis parallel to the strip length, thus the magnetisation does not rotate when the field is removed and no peaks in ε_F are observed. It is also apparent that the gratings become slightly harder to saturate following the initial switch of the magnetisation. Within this region from **H** = ±150 Oe to saturation, the magnetisation reversal occurs step-by-step, which can be attributed to the magnetically harder Fe-Ga. Although this second stage of the reversal is perceptible in the θ_F loops in Fig. 6.3.1*A*, it is much more so here and most obvious after a dose of 3.44×10^{16} ions cm^{-2}. This is where the Fe-Ga is not a continuous film, but is still present in the form of large clusters of several hundred nanometres. The result is a loop that reveals both hard and relatively soft magnetic behaviour, as might be observed with a dual-phase material. At the highest dose of 4.01×10^{16} ions cm^{-2}, this second stage begins to disappear as the Fe-Ga is milled away.

When **H** is applied perpendicular to the strips in the three higher dosed gratings, asymmetrical hysteresis loops are generated with anomalous regions occurring at non-zero values of **H**. This effect is associated with the introduction of the hard-axes, as evident in Fig. 6.3.1*B*. Where **H** = -100 Oe, the two branches of the loops intersect as previously observed with the discrete gratings. Additionally, the magnitude of the magnitude of ε_F^{sat} appears to increase with ion dose, yet intuitively one would expect M_S to reduce as material is removed, as is clearly shown by the corresponding θ_F loops. Naturally, higher ion doses reduce the thickness of the Fe-Ga such that the differences in transmittance through the alternating strips become

more pronounced. At magnetic saturation, any contribution from the second-order magneto-optical effects can be ruled out since the magnetisation lies parallel to **H** and accordingly, m_t will be negligible. Domain structure can also be neglected which leads to the conclusion that the apparent increase in the M_S with ion dose must be an effect produced by a superstition of contributions from the specular and diffracted light.

A similar 0.4 μm Fe/Fe-Ga grating was patterned over a smaller area of 7 μm × 7 μm using an ion dose of 2.5×10^{16} ions cm^{-2} for the purpose of conducting MTXM imaging (Fig. 6.3.3*A*). The XMCD image sequence has been included in Appendix 3, but fails to show any significant pinning induced by the Fe-Ga strips. In fact, the shape of the milled border dictated the domain formation as shown in Fig. 6.3.3*B*.

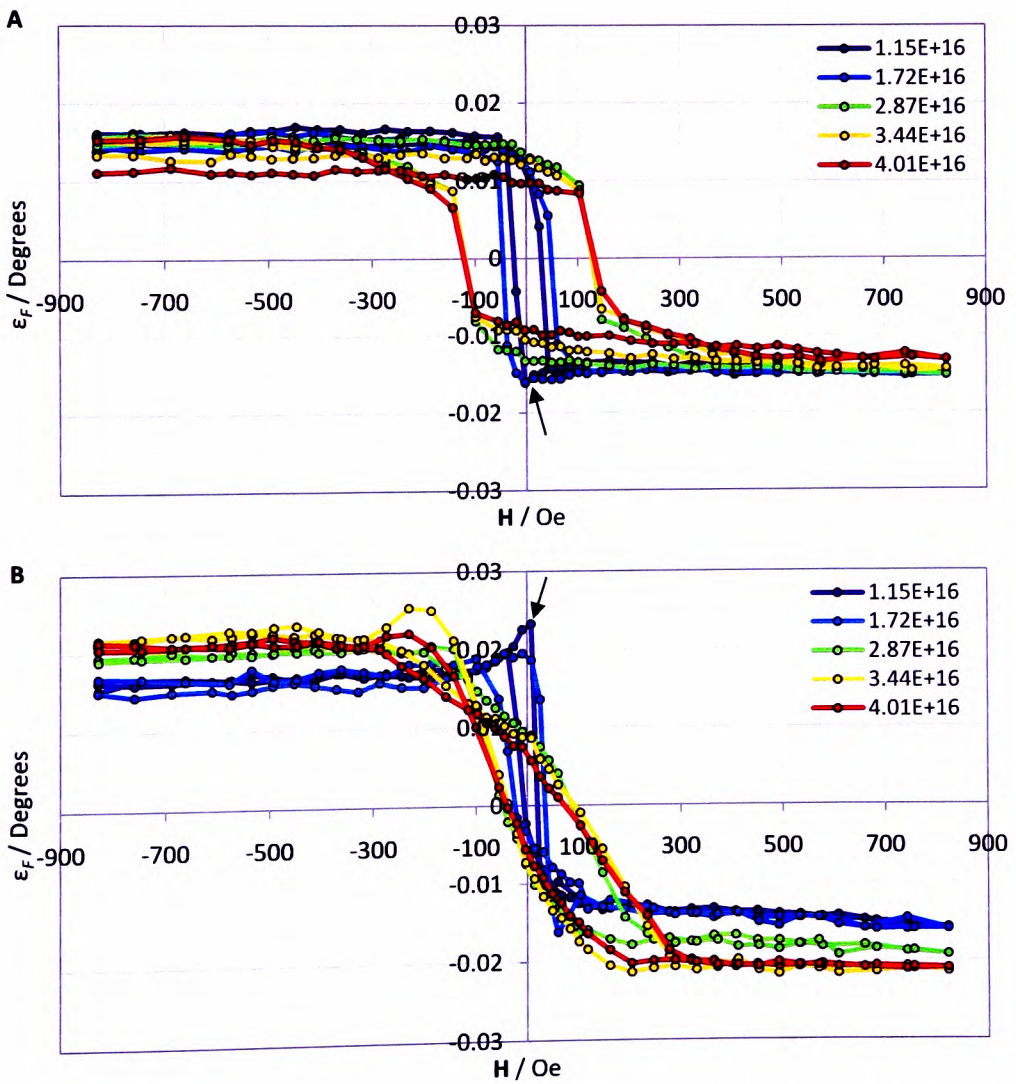

Figure 6.3.2 – Faraday rotation as a function of field strength applied parallel (*A*) and perpendicular (*B*) to the length of the strips. The arrows mark peaks in the loops at **H** = 0.

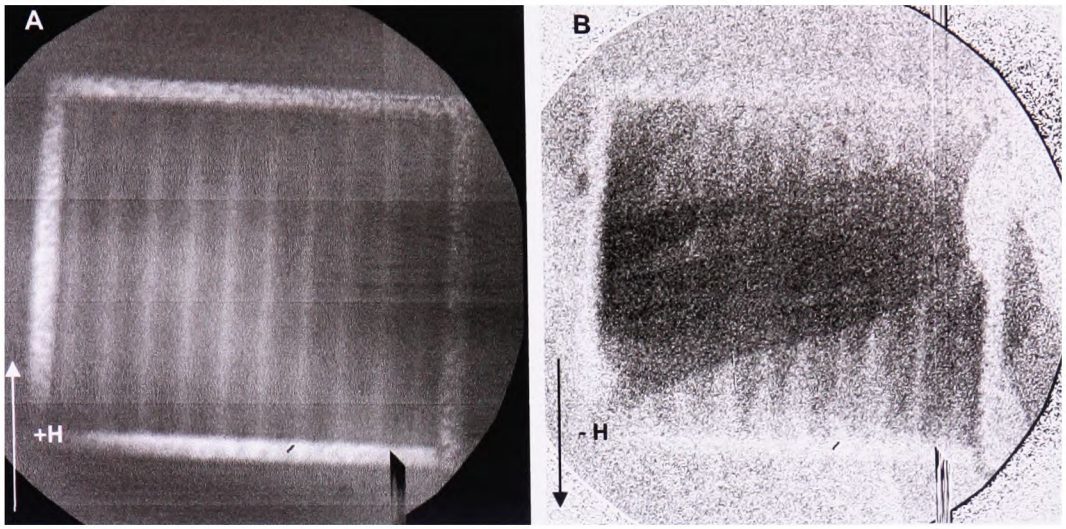

Figure 6.3.3 – *A*: MTXM image of a saturated grating with Fe-Ga strips irradiated with a dose of 2.5×10^{16} ions cm^{-2}. This is not an OD image, so light areas represent the thinner Fe-Ga. *B*: An XMCD image showing a large area of the grating switching its magnetisation as **H** is reversed to -56 Oe (dark regions).

6.3.2 "Meta-Material" Array

Using a Ga ion dose of 2×10^{16} ions cm^{-2}, a pattern inspired by the "split-ring resonators" that are often used to give rise to the negative magnetic permeability in meta-materials[6.12] was implanted into an Fe film. Such patterns were chosen not only because of the interesting domain structures they may produce, but also to illustrate the versatility of the FIB and highlight its potential application within the field of meta-material research. The pattern covered a large area of 40 μm × 40 μm, but only a small section could be observed at any one time using the MTXM. The selected area is shown in Fig. 6.3.4, where the light regions represent the irradiated film. Surrounding the pattern is a 1 μm wide frame that was irradiated with a dose of 2×10^{16} ions cm^{-2}.

XMCD sequential difference images of the magnetisation reversal process are shown in Fig. 6.3.5 where each image highlights only the areas that switch between successive field steps. It is apparent that the presence of the border did not seriously affect the domain structure within the patterned area as was previously observed in Fig. 6.3.3, but provided a sufficient enough barrier to prevent interactions with the surrounding film. The as-grown film is one of the first areas

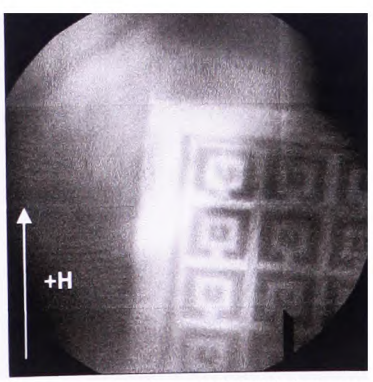

Figure 6.3.4 – MTXM image (not OD) of a corner of the "split-ring" array.

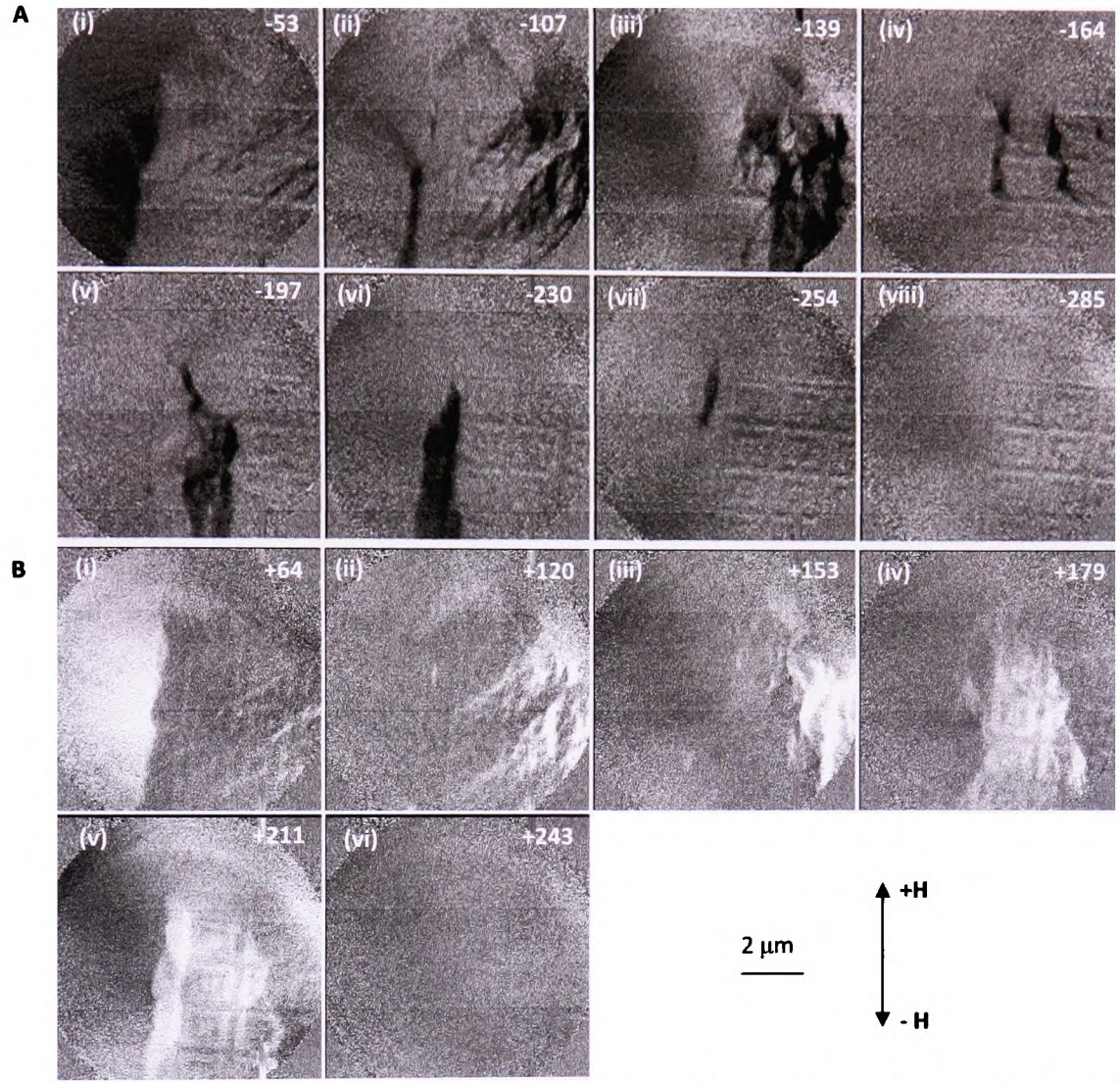

Figure 6.3.5 – XMCD sequential difference images showing the domain formation across the array of "split-rings" during cycling of the applied field from +914 Oe to -893 Oe (*A*) then back to +914 Oe (*B*). The field values (in Oe) are shown in each image.

to switch at -53 Oe, along with some small domains running diagonally through the pattern. Larger areas of the pattern then follow with domains nucleating rather haphazardly, although pinning along the ring edges can clearly be seen in some areas. The reverse cycle appears similar with domains spanning sections of Fe and Fe-Ga. In *B*, (iv) and (v), the same large area of the pattern is highlighted twice, which indicates the magnetisation effectively rotated over two successive field steps. Such a rotation may cause second-order magneto-optical effects to occur if this pattern were to be measured optically.

6.4 *Chessboard Arrays*

6.4.1 Domain Imaging

The magnetic structure occurring in small ferromagnetic elements changes according to their aspect ratio. Long rectangular elements can easily support single domains aligned parallel to their length, but lower aspect ratios tend to result in domain configurations such as the diamond state, or the four-domain Landau state[6.13-16] as illustrated by the schematic diagrams in Fig. 6.4.1. On application of a magnetic field, **H**, the domains that are parallel and anti-parallel to **H** expand and shrink accordingly. The flux closure domains that are perpendicular to **H** on average cancel out, therefore $m_r \cdot m_t$ should be close to zero and no second-order magneto-optical effects should be observed from such elements.

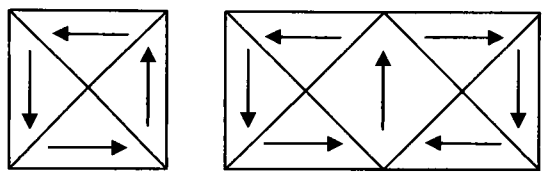

Figure 6.4.1 – Possible remanent states in small magnetic elements.

Real domain configurations forming within small nanocrystalline Fe elements defined by FIB milling are shown in Fig. 6.4.2. MTXM images of two different, but identically proportioned arrays, recorded with a field of +369 Oe applied parallel and perpendicular to the length of the strips are shown in Figs. 6.4.2, *A* and *B*, respectively. Selected XMCD images from the full magnetisation cycles (included in Appendix 3) are shown in Figs. 6.4.2, *C* and *D*.

The remanent states formed after removing the +369 Oe field are shown in *C*, (i) and *D*, (i) where the darker contrast represents the areas of Fe that have switched relative to the magnetised states in *A* and *B*, i.e. the base images. The dark spots visible within the smaller elements indicate the formation of flux-closure vortex states, such as the Landau and diamond configurations. In *C*, (i), the longer elements remained magnetised along their length at remanence as previously observed with the gratings. In *D*, (i), faint contrast can be seen within the longer strips, probably resulting from interactions between neighbouring strips and clusters of Fe within the milled regions. Such interactions are seen in *D*, (ii) where the field was reversed to -357 Oe and the domains formed across the gaps between strips through the small clusters of Fe-Ga. Both orientations of the array, the smaller 0.4 μm × 0.4 μm squares and the 0.4 μm × 0.8 μm rectangles reversed their magnetisation by domain wall displacement.

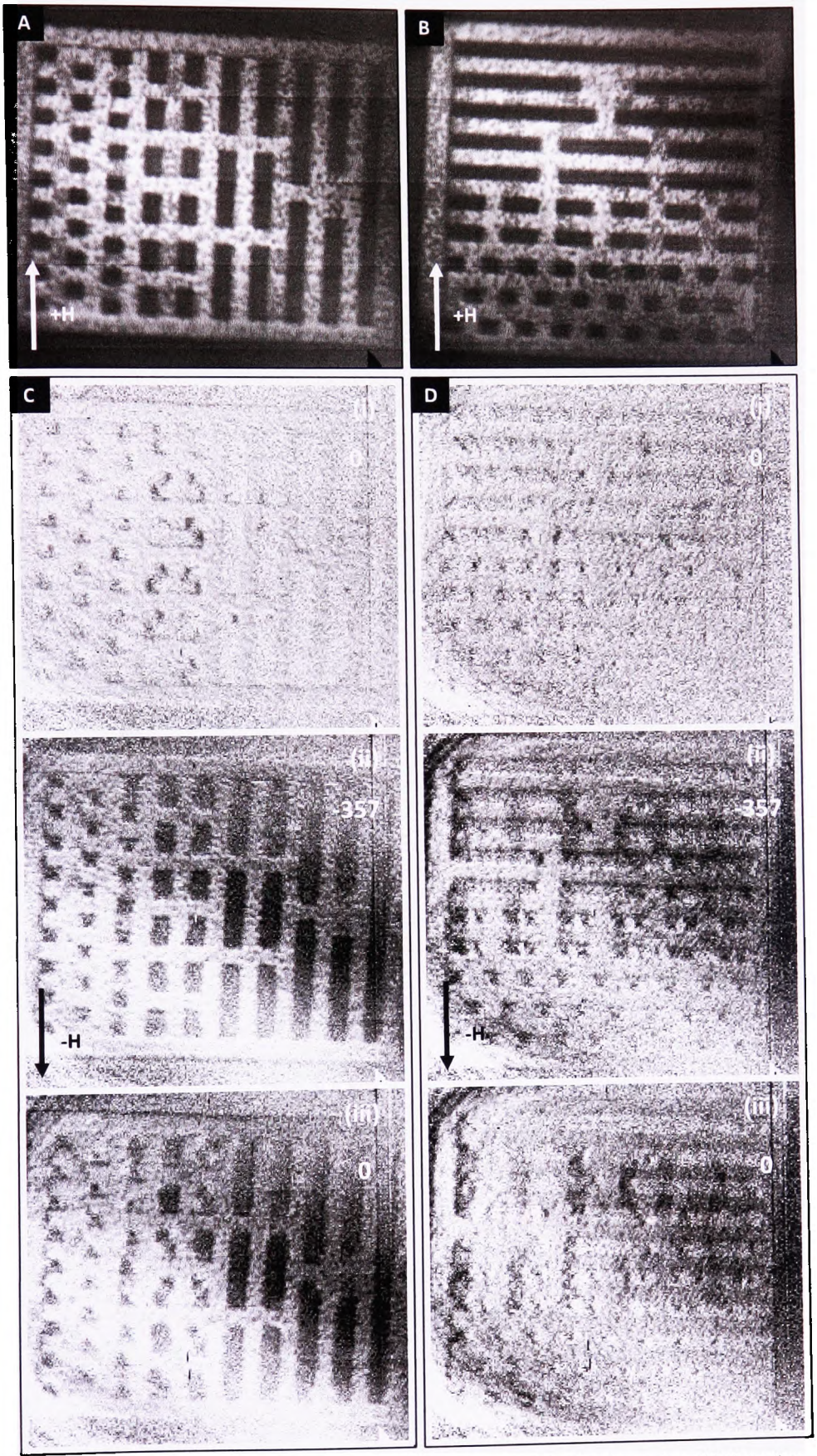

Figure 6.4.2 – *A* and *B*: MTXM images of 0.4 μm wide Fe elements with lengths ranging from 0.4 μm to 6.8 μm. Sequential difference XMCD *C* and *D* show the domain formation at various points in the cycle. **H** is shown (in Oe) in each image.

The shape anisotropy of the rectangles allowed them to become almost saturated along their easy-axes at +369 and -357 Oe, but it is evident that higher fields would be required to saturate the squares, in which closure domains were still present. On removal of the field, image *C*, (iii) shows that the longer strips again remained magnetised parallel to their length, while the smaller elements relaxed back into flux closure states. *D*, (iii) shows that the clusters of Fe still retained a component of magnetisation along the field direction, but across the majority of the pattern the elements revert back to energetically favourable states determined by their shape anisotropy.

6.4.2 Magneto-Optical Properties

SEM images of three arrays consisting of slightly larger elements than those in Fig. 6.4.2, fabricated for the purpose of magneto-optical characterisation are shown. The pattern in Fig. 6.4.3*A* is referred to as a "chessboard" while those in *B* and *C* are termed "elongated chessboards". The Fe (bright) and etched (dark) elements in *A* measure approximately 0.725 μm × 0.725 μm, while those in *B* and *C* have been elongated in the *y*-direction such that they measure 2.9 μm and 5.8 μm in length, respectively. Each array covers a large area of film 58 μm × 58 μm in size. Since the width of each element is slightly larger than the wavelength of the light, complex polarisation effects should be reduced.

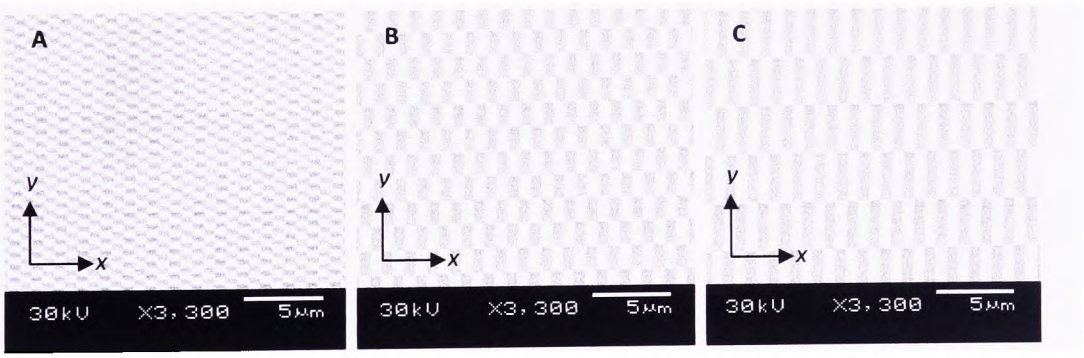

Figure 6.4.3 – SEM images of the chess-board-style patterns. The Fe (bright) and etched (dark) elements are 0.725 μm in width and 0.725 μm (*A*), 2.9 μm (*B*) and 5.8 μm (*C*) long.

Faraday rotation hysteresis loops generated by each pattern are shown in Fig. 6.4.4. The magnetic reversal characteristics of the chessboard pattern in *A* appear similar along both axes. Not considering the excessive thermal drift during one of the measurements, the two orientations result in slightly different loops, which could be a result of off-axis alignment when mounting the sample. The loops in Figs. 6.4.4, *B* and *C* show that the elongated elements behave in a similar manner to the gratings in section 6.2. The easy-axis loops (**H** //

y) exhibit high squareness and sharp switching of the magnetisation. The hard-axis loops (**H** // *x*) reveal low values of coercivity between 25 and 40 Oe, and slightly higher remanence than previously observed with the gratings. This may be a consequence of domain formation between the connected corners of the Fe rectangles allowing for a larger component of **M** along the direction of **H**.

The ε_F loops for the same three patterns are shown in Fig. 6.4.5. In the case of the square chessboard pattern, the shape of each ε_F loop seems to reflect that of the corresponding θ_F loops. Considering the results in previous section, where ε_F seemed to be more sensitive to the reversal mechanism, the lack of any conspicuous features in the loops would suggest an absence of any second-order magneto-optical effects or irregular domain formation, as might be expected if the squares support flux-closure domains, such as the Landau state.

The elongated patterns again generate irregular ε_F loops similar to those produced by the gratings and thus do not always represent the true **M** versus **H** behaviour. The easy-axis loops measured using *s*-polarised light do not reveal the sharp switching of **M** as indicated by the Faraday rotation. Instead, just prior to switching, a small step in the ellipticity angle occurs (indicated by the arrows in Figs. 6.4.5, *B* and *C*). Corresponding features can also be seen in the θ_F loops but they manifest as small peaks rather than steps. The same features can also be seen in the loops produced by the gratings in section 6.2 and may be indicative of the switching mechanism, however, no domain structure that could potentially be responsible was observed in the XMCD images of the gratings.

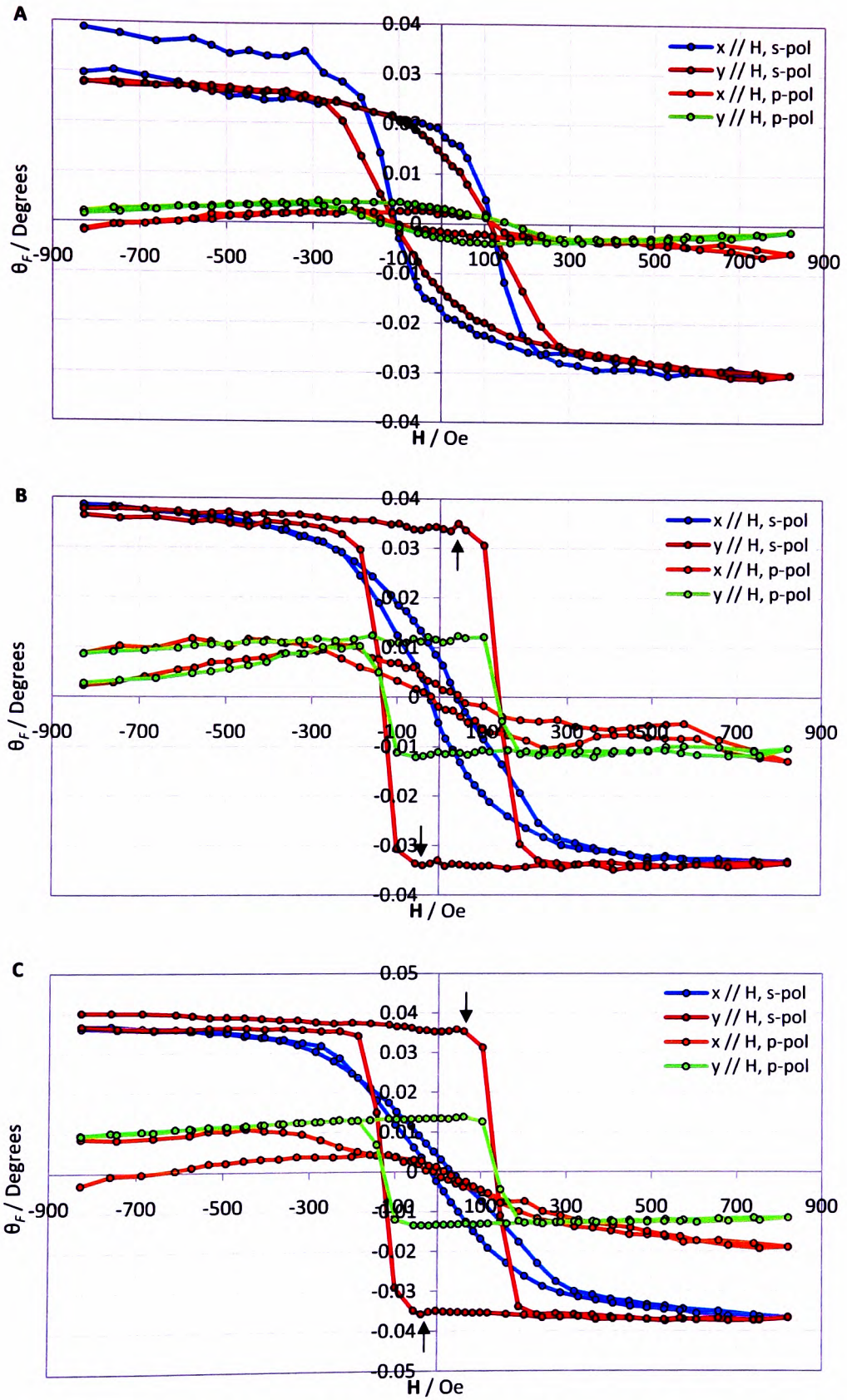

Figure 6.4.4 – Hysteresis loops showing the θ_F generated by the arrays of square elements (*A*), and elongated 2.9 μm (*B*) and 5.8 μm (*C*) long elements. The black arrows indicate small peaks in the loops prior to switching.

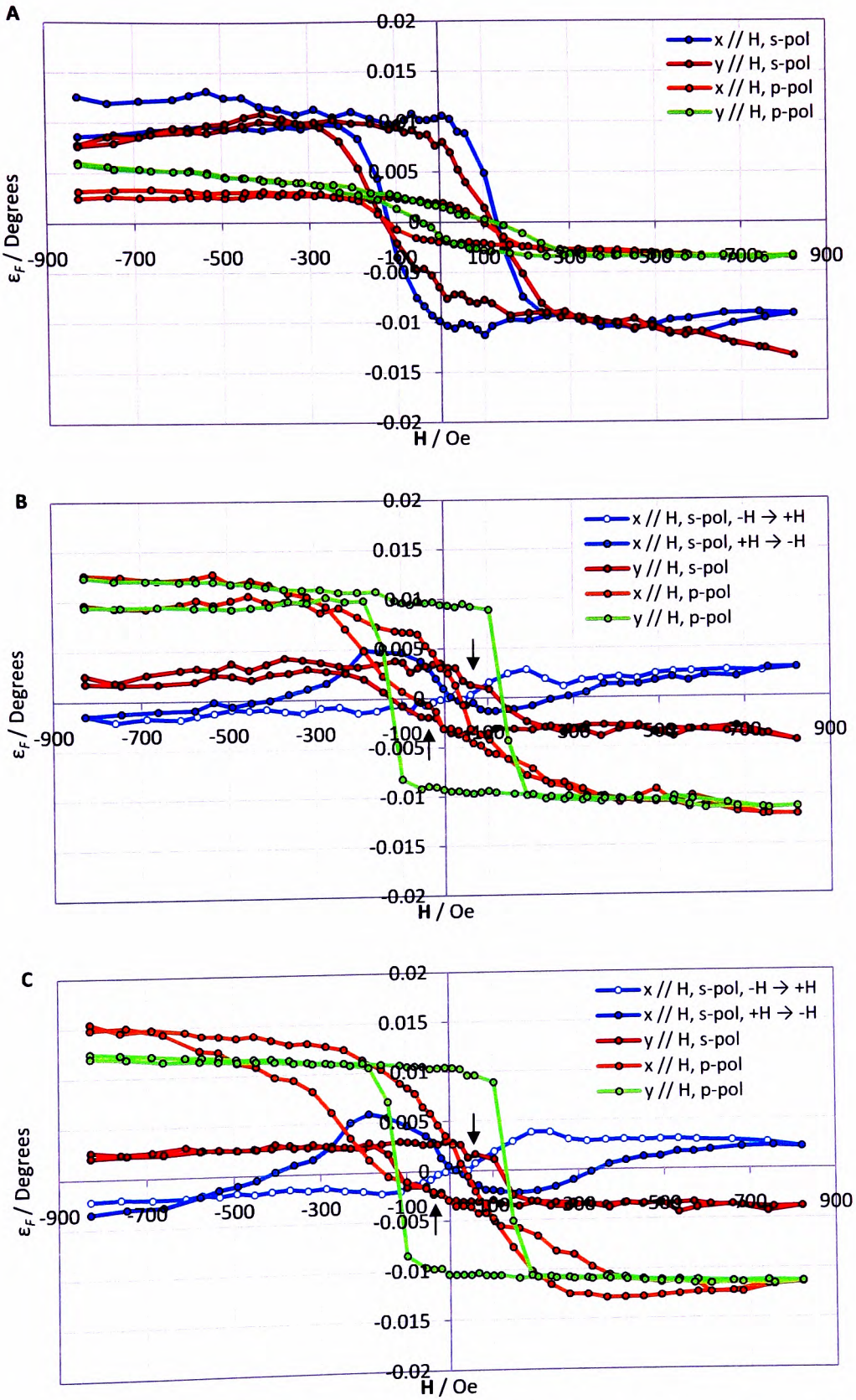

Figure 6.4.5 – Hysteresis loops showing the ε_F generated by the arrays of square elements (*A*), and elongated 2.9 μm (*B*) and 5.8 μm (*C*) long elements. The two branches of the hard-axis cycles measured with *s*-polarised light, (**-H** → **+H**) and (**+H** → **-H**), have been plotted using different symbols for clarity.

6.5 *Anti-Dot Arrays*

Arrays of holes have been milled into nanocrystalline Fe films in square, rectangular and rhomboidal lattice geometries as shown schematically in Fig. 6.5.1. TEM images of the square and rectangular arrays are shown in Fig. 6.5.2. They reveal the holes have a blade-like shape measuring approximately 465 nm in length and 160 nm in width. The square array had a 1 μm period along both axes, while the rectangular array had a reduced *y*-axis period of 0.5 μm. The distance between nearest anti-dots in the rhomboidal lattice was 1.4 μm.

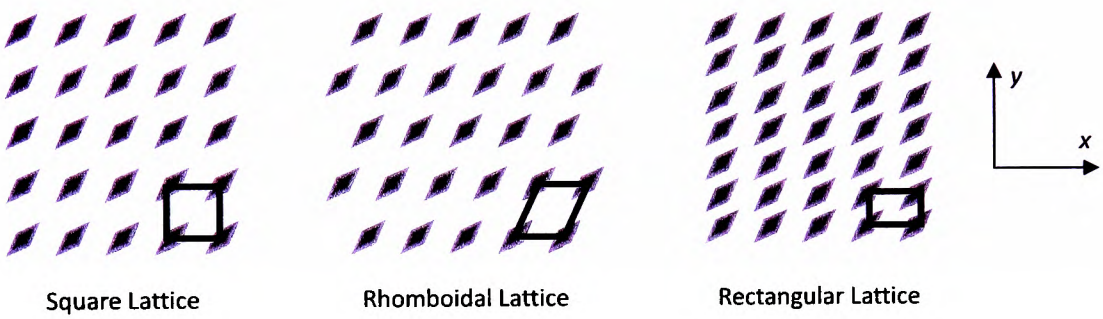

Figure 6.5.1 – Schematic illustration of the anti-dot arrays (not to scale).

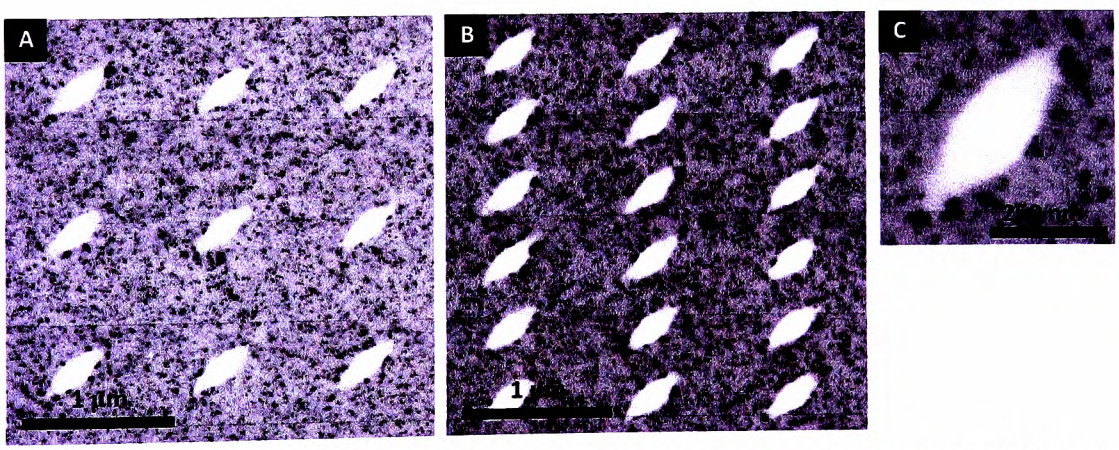

Figure 6.5.2 – TEM images of the anti-dot arrays arranged in square (*A*) and rectangular (*B*) lattices. A magnified image of one of the anti-dots is shown in *C*.

The θ_F loops measured when the arrays were magnetised along the two axes are shown in Fig. 6.5.3. The square and rhomboidal lattices both have a coercivity on the order of 40 Oe, which is not significantly greater than that of the Fe film in its as-grown state (10-30 Oe); an observation also reported by Vavassori *et al.*[6.10]. It is also apparent that these two arrays yield similar shaped loops with **H** applied along either axis. While this may be expected from the

square lattice, owing to the asymmetry of the rhomboidal lattice one might presume a certain degree of anisotropy to be observed[6.17]. The lack of any anisotropy may be due to the relatively large lattice period in comparison with the anti-dot size, allowing the domain walls to propagate more freely than in an array of larger or closer packed anti-dots[6.17-20]. The anti-dots tend to affect the magnetic properties of the film closer to saturation, where both the rhomboidal and rectangular arrangements show an apparent hardening of the magnetic properties, which is likely to be a result of pinning around the holes. In bulk samples, blade domains often form around holes or voids in order to reduce the surface energy[6.21] as illustrated schematically in Fig. 6.5.4*A*. Domain walls lie perpendicular to the bisector of the two adjacent magnetisation directions in order to minimise dipolar energy[6.22] as indicated by the dotted lines. For a single anti-dot, a trade off between dipolar and domain wall energies results in the formation of blade-shaped domains. Using the vector-MOKE technique, Vavassori *et al.* concluded that such domains were formed around 200 nm circular anti-dots arranged in a 2μm square lattice based on the appearance of small "oscillations" in the m_t versus **H** Kerr rotation loops at the switching fields[6.10]. If the anti-dots are closer together the domains may coalesce to produce band domains that run diagonally across the array[6.22, 23] as schematically illustrated in Fig. 6.5.4*B*.

In some cases, the shape anisotropy of the array will dictate the domain formation[6.17, 20, 22, 23]. The separation between the edges of the anti-dots in the rectangular lattice arrangement as shown in Fig. 6.5.2, measures just 280 nm in the *y*-direction, and is thus narrow enough to force the magnetisation to lie parallel to the dot edges. It is evident from the hysteresis loops that the coercivity of the rectangular array is higher along the *x*-direction and the shape of the loop shows step-by-step reversal at low field values, suggesting stronger pinning. This is followed by a sharp reversal of the magnetisation and saturation at 140 Oe. The much reduced squareness signifies domain formation across a significant portion of the array, suggesting a remanent state more akin to the band domain structure rather than individual blade domains. The apparent asymmetry of the loop may be a result of the sample alignment since the square and rhomboidal lattices did not show such an effect. Low coercivity along the *y*-axis of the rectangular lattice can be attributed to the initial easy displacement of the domain walls between the rows of anti-dots. However, after applying a field of 55-60 Oe, the film becomes much harder to magnetise, requiring a field in excess of 600 Oe in order to reach saturation. Owing to the reduced period of the lattice along this direction and the

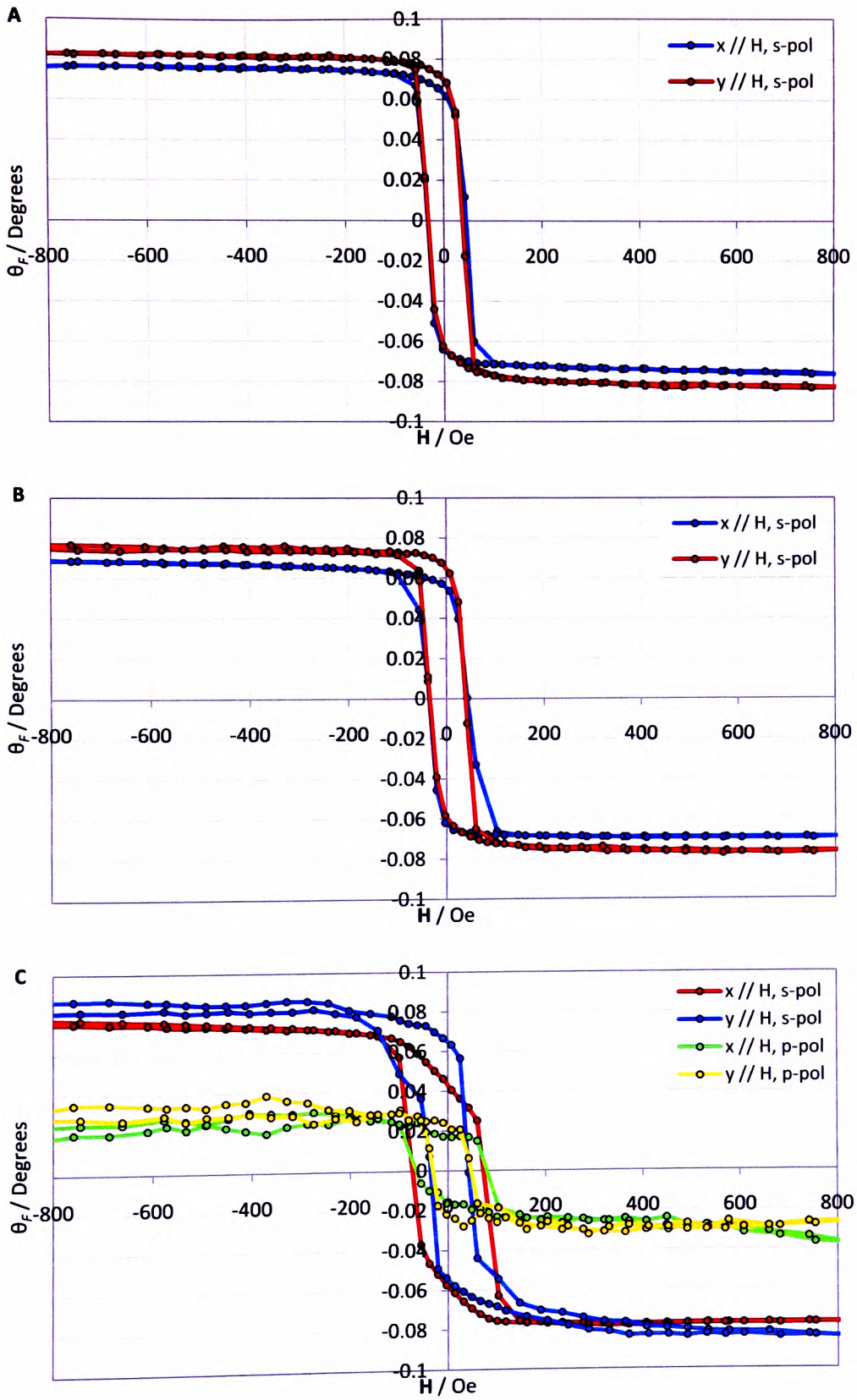

Figure 6.5.3 – Hysteresis loops showing θ_F produced by the square (*A*), rhomboidal (*B*) and rectangular (*C*) arrays.

elongated shape of the anti-dots, the demagnetising fields between any two anti-dots will resist the rotation of the magnetisation.

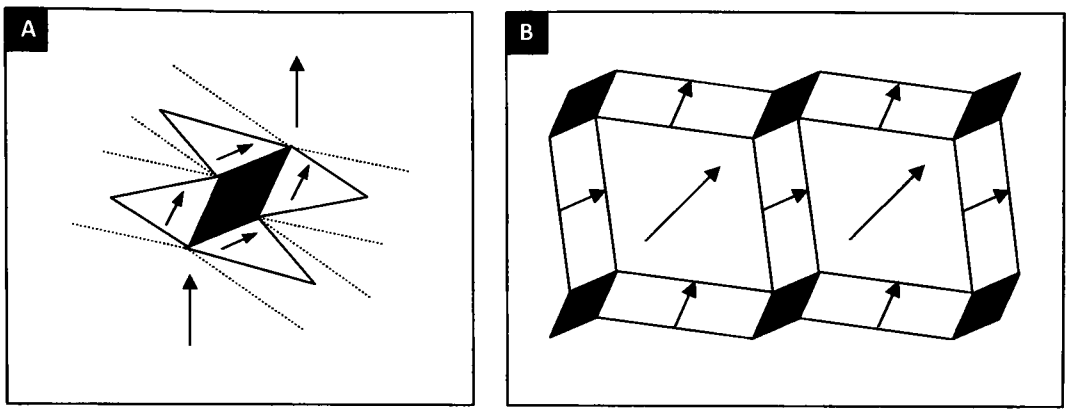

Figure 6.5.4 – Schematic illustration of blade domains that can form around holes in order to minimise surface energy (*A*). In an array of holes the blade domains may coalesce to form band domains (*B*). Not to scale.

Hysteresis loops produced from the ε_F measurements on the square, rhomboidal and rectangular lattices are shown in the Figs. 6.5.5, *A*, *B* and *C*, respectively. Again, irregular features that may be associated with domain formation are apparent. As previously seen with the coupled Fe/Fe-Ga gratings, peaks in the loops manifest at $\mathbf{H} = 0$. These were previously attributed to the formation of domains that may not necessarily be aligned parallel or perpendicular to the applied field direction, giving rise to contributions from second-order effects. This is possible evidence of the blade domains that have been observed by others. In addition, anomalous "oscillations" in the loops are also observed at field values corresponding to points where the average magnetisation (as judged from the Faraday rotation) of the array switches or is close to zero (indicated by the arrows in Figs. 6.5.5, *A* and *B*). The asymmetry of these loops is rather more exaggerated than in the case of the coupled gratings and could be interpreted as increased contributions from higher diffraction orders, since diffraction effects generated by the anti-dots are likely to be more pronounced. D-MOKE measurements on anti-dot arrays[6.10, 22, 23] have been found to exhibit a strong and varying dependence of the diffracted light on the domain structure through the magnetic-form factor (Eqn. 3.2.8).

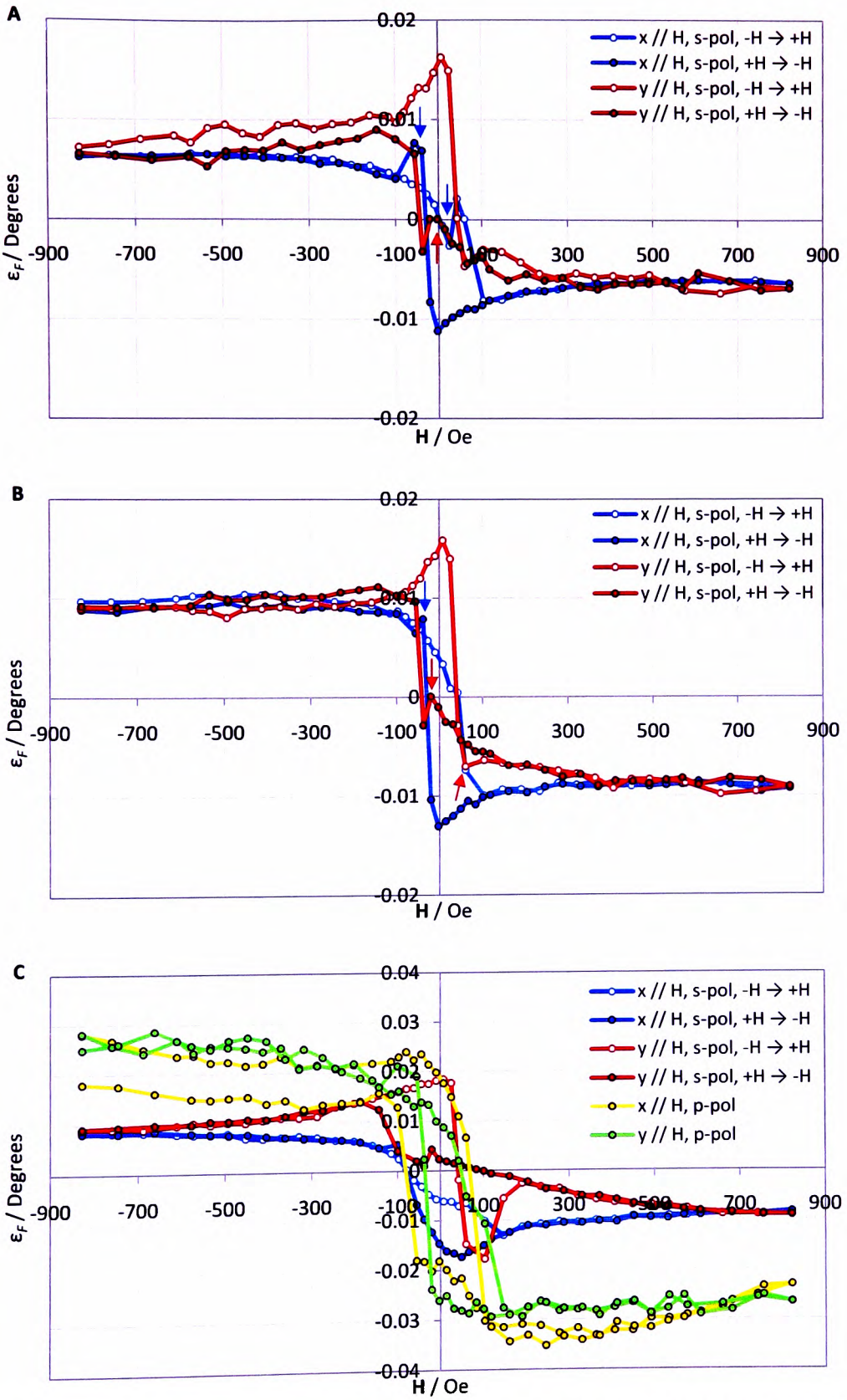

Figure 6.5.5 – Hysteresis loops showing the ε_F generated by the square (*A*), rhomboidal (*B*) and rectangular (*C*) arrays. In some cases the two branches of the cycle, (**-H** → **+H**) and (**+H** → **-H**), have been plotted using different symbols for clarity.

6.6 *Summary and Conclusions*

In section 6.2, the physical structure of FIB-milled sub-micron gratings was briefly explored, where it was found that the ion beam tails can cause significant and undesirable milling along the edges of the Fe strips, resulting in poorly defined transitions from magnetic to non-magnetic regions. Differences in the microstructure along the edges of each Fe strip and Fe-Ga clusters within the intermediate spacing regions may have been responsible for the wide range of coercivities observed using the MTXM. The short grating period (0.8 μm) may also have allowed magnetostatic interactions to take place between neighbouring strips, leading to unpredictable switching behaviour.

Gratings were patterned over larger areas for magneto-optical characterisation. Higher ion doses were applied to the spacer strips such that all Fe-Ga were removed. During magnetisation along the easy-axis (**H** along the strips) the gratings produced very square θ_F loops. Considering such a loop represented the collective behaviour of over 40 individual strips, averaged over 30 cycles of the applied field, the high squareness indicates that the reversal process was actually very consistent across the whole grating. During hard-axis magnetisation (**H** perpendicular to strips), the magneto-optical measurements yielded asymmetrical loops that could not be related directly to the actual **M** vs. **H** behaviour. The asymmetry was partly attributed to rotation of the average magnetisation vector, producing second-order magneto-optical effects that are quadratic in **M**. Also, diffraction was considered, although this was not verified explicitly.

One rather striking aspect of the magneto-optical properties of the gratings was the variation in the behaviour of θ_F and ε_F as functions of the applied field strength. To explore these differences further, several other simple patterns were milled into the Fe films. In section 6.3, gratings with alternating Fe and Fe-Ga strips were produced using various ion doses. The θ_F measurements produced regular loops generally fitting with what would be expected from such patterns. However, again the ε_F loops appeared different and exhibited varying degrees of asymmetry depending on the ion dose used to form the Fe-Ga strips. Surprisingly, the gratings produced with the lowest ion doses, where diffraction effects produced by the structural periodicity were considered to be minimal, generated asymmetrical loops with small peaks at remanence. These were attributed to domain formation based on the observed

reduced squareness of the corresponding θ_F loops. Such domains were not likely to correlate strongly with the periodicity of the grating, but perhaps form rather randomly such that the average magnetisation makes an oblique angle with the plane of incidence. This was illustrated with an XMCD image of a similarly dosed Fe/Fe-Ga grating (Figs. 6.3.3 and 6.3.5). At higher ion doses, the gratings developed well-defined hard-axes, which consequently produced different features in the ε_F loops, similar to those seen with the discrete gratings. Some anomalous features in the loops were quite clearly attributable to diffraction, such as the apparent increase in M_S as the Fe and Fe-Ga strips became better defined.

Further evidence that second order effects could be significant came from the chess-board patterns in section 6.4. The chess-board pattern consisted of an array of small squares, slightly larger than the wavelength of the light. Flux closure states that form within such small magnetic elements keep the magnetisation perpendicular to the applied field and accordingly, the second-order magneto-optical effects should be minimal. This was indeed the case. It was found that both the θ_F and ε_F measurements on the chessboard array yielded similarly shaped loops that were free of the anomalous features observed with other patterns. Elongating the chess-board pattern to reintroduce shape anisotropy again resulted in asymmetrical hysteresis loops. Considering that the elements were slightly larger than the wavelength of the light, would indicate such effects are not linked to diffraction.

Finally, anti-dot arrays were measured. The θ_F and ε_F loops produced by the square and rhomboidal lattices are very similar to those produced by the Fe/Fe-Ga gratings, indicating domain formation at remanence and possibly occur as a result of the second-order effects. However, diffraction cannot be ruled out and further work, either experimental or theoretical, micromagnetic simulations for example, is required in order to properly determine the contribution of the diffracted light.

References

6.1 D. E. Bangert and H. P. Hughes, Journal of Magnetism and Magnetic Materials **156** (1-3), 189-190 (1996).

6.2 T. Schmitte, K. Westerholt and H. Zabel, Journal of Applied Physics **92** (8), 4524-4530 (2002).

6.3 A. Westphalen, K. Theis-Bröhl, H. Zabel, K. Rott and H. Brückl, Journal of Magnetism and Magnetic Materials **302** (1), 181-189 (2006).

6.4 J. B. Kim, Y. H. Lu, M. H. Cho, G. J. Lee, Y. P. Lee, J. Y. Rhee and C. S. Yoon, Applied Physics Letters **94** (15), 3 (2009). J. B. Kim, Y. H. Lu, M. H. Cho, Y. P. Lee, J. Y. Rhee, J. H. Lee and K. M. Ho, Journal of Applied Physics **106** (9), 3 (2009).

6.5 Y. H. Lu, M. H. Cho, J. B. Kim, G. J. Lee, Y. P. Lee and J. Y. Rhee, Optics Express **16** (8), 5378-5384 (2008).

6.6 M. Inoue, K. Isamoto, T. Yamamoto and T. Fujii, Journal of Applied Physics **79** (3), 1611-1624 (1996).

6.7 M. Ouyang, Y. Cao, H. Gao, J. Shi, J. Zhou and D. Liu, Optics and Laser Technology **40** (1), 201-207 (2008).

6.8 S. J. Blundell, C. Shearwood, M. Gester, M. J. Baird, J. A. C. Bland and H. Ahmed, Journal of Magnetism and Magnetic Materials **135** (1), L17-L22 (1994).

6.9 R. M. Osgood, S. D. Bader, B. M. Clemens, R. L. White and H. Matsuyama, Journal of Magnetism and Magnetic Materials **182** (3), 297-323 (1998). R. M. Osgood, B. M. Clemens and R. L. White, Physical Review B **55** (14), 8990-8996 (1997).

6.10 P. Vavassori, V. Metlushko, R. M. Osgood, M. Grimsditch, U. Welp, G. Crabtree, W. J. Fan, S. R. J. Brueck, B. Ilic and P. J. Hesketh, Physical Review B **59** (9), 6337-6343 (1999).

6.11 S. S. Yan, R. Schreiber, P. Grünberg and R. Schäfer, Journal of Magnetism and Magnetic Materials **210** (1-3), 309-315 (2000).

6.12 C. M. Soukoulis, S. Linden and M. Wegener, Science **315** (5808), 47-49 (2007).

6.13 P. Fischer, G. Denbeaux, T. Eimuller, D. Goll and G. Schutz, IEEE Transactions on Magnetics **38** (5), 2427-2431 (2002).

6.14 P. Fischer, D. H. Kim, B. L. Mesler, W. Chao and E. H. Anderson, Journal of Magnetism and Magnetic Materials **310** (2), 2689-2692 (2007).

6.15 H. Youk, G. -W. Chern, K. Merit, B. Oppenheimer and O. Tchernyshyov, Journal of Applied Physics **99** (8), 3 (2006).

6.16 O. A. Tretiakov, D. Clarke, G. W. Chern, Y. B. Bazaliy and O. Tchernyshyov, Physical Review Letters **100** (12) (2008).

6.17 C. C. Wang, A. O. Adeyeye and N. Singh, Nanotechnology **17** (6), 1629-1636 (2006).

6.18 R. P. Cowburn, A. O. Adeyeye and J. A. C. Bland, Journal of Magnetism and Magnetic Materials **173** (1-2), 193-201 (1997).

6.19 N. Owen, H. Y. Yuen and A. Petford-Long, IEEE Transactions on Magnetics **38** (5), 2553-2555 (2002).

6.20 L. J. Heyderman, F. Nolting, D. Backes, S. Czekaj, L. Lopez-Diaz, M. Kläui, U. Rüdiger, C. A. F. Vaz, J. A. C. Bland, R. J. Matelon, U. G. Volkmann and P. Fischer,

Physical Review B **73** (21) (2006).

6.21 H. J. Williams and W. Shockley, Physical Review **75** (1), 178-183 (1949).

6.22 I. Guedes, M. Grimsditch, V. Metlushko, P. Vavassori, R. Camley, B. Ilic, P. Neuzil and R. Kumar, Physical Review B **66** (1), 9 (2002).

6.23 I. Guedes, N. J. Zaluzec, M. Grimsditch, V. Metlushko, P. Vavassori, B. Ilic, P. Neuzil and R. Kumar, Physical Review B **62** (17), 11719-11724 (2000).

CHAPTER 7 FIB-Induced Deposition of Tungsten on Ferromagnetic Thin Films

FIB-induced deposition (FIBID) of tungsten using a $W(CO)_6$ gaseous precursor was briefly introduced in Chapter 2. Precision milling and deposition of conducting material is a unique combination of lithographic techniques offered by the FIB that potentially allows one to fabricate entire electronic devices for magnetoresistive studies on a sub-micron scale. Such a process may involve forming electrical contacts on top of magnetic elements, which is only feasible if the deposition process does not interfere with the magnetic behaviour of the device. Here the results of a brief, preliminary exploration of the effects of FIBID on the magnetic behaviour of Fe and Ni/Fe thin films are presented.

7.1 The Ideal Deposition Parameters

Although modern FIB systems are often supplied with suggested beam parameters for deposition purposes, in this case only very limited information was provided. Therefore, an initial search for suitable beam parameters was required.

Different combinations of ion beam current, scan speed and beam-defining aperture size were used to deposit a set of tungsten wires measuring 60 μm × 0.6 μm, upon a Si substrate with a 67 nm thick SiO_2 insulating layer. Each wire was deposited between 300 nm thick Au electrical contact pads, deposited beforehand using UV photolithography, thermal evaporation and lift-off procedures. These allowed the current-voltage (I-V) characteristics of each wire to be measured and used, in addition to SEM observations, as a judge of the deposition quality.

The probe current and spot size were controlled by adjusting the condenser lens voltage and beam-defining aperture size. Two apertures were used, measuring 50 μm and 100 μm in diameter. Then by adjusting the condenser lens voltage, more or fewer ions were focussed through the aperture in order to adjust probe current and ion flux. For each aperture/condenser lens combination, the scan frequency along the length of the deposition

was varied from 0.5 kHz to 20 kHz, equating to average scanning speeds between 0.06 m s^{-1} and 2.4 m s^{-1}. The scanning frequency along the width of the deposition area was kept at 0.02 Hz (2.4×10^{-8} m s^{-1}). To enable a direct comparison between each beam configuration, the total charge applied to each area was kept constant at approximately 110 nC (1.9×10^{18} cm^{-2}). The total deposition time was varied according to the probe current, ranging from 145 minutes for the lowest current, down to just 4 minutes when using the highest current.

The effectiveness of each beam configuration could be judged roughly from SEM observations of the resulting wires, some of which are shown in Fig. 7.1.1. As a test of the overall quality of each wire, the current-voltage (I-V) characteristics were measured and were found to be linear in all cases, although the resistance varied substantially as shown in Fig. 7.1.2 and Table 7.1.1. It is apparent, from the very thin deposits (vertical strips) in Fig, 7.1.1, *A* and *D* that the lower probe currents were much less effective at cracking the precursor; this is reflected in the resistance measurements. Consequently, slower scanning speeds were required in order to form better conducting wires when low probe currents were used, as evident from Fig. 7.1.2*B*. The importance of ion flux becomes clear when comparing the resistance values of the wires numbered 11-15 and 20-24. The larger aperture used for wires 20-24 produced a larger spot, but the probe current remained almost unchanged and consequently the ion flux was lowered. This resulted in a three- to five-fold increase in resistance and the difference in deposition yields can be seen visually in Figs. 7.1.1, *C* and *D*.

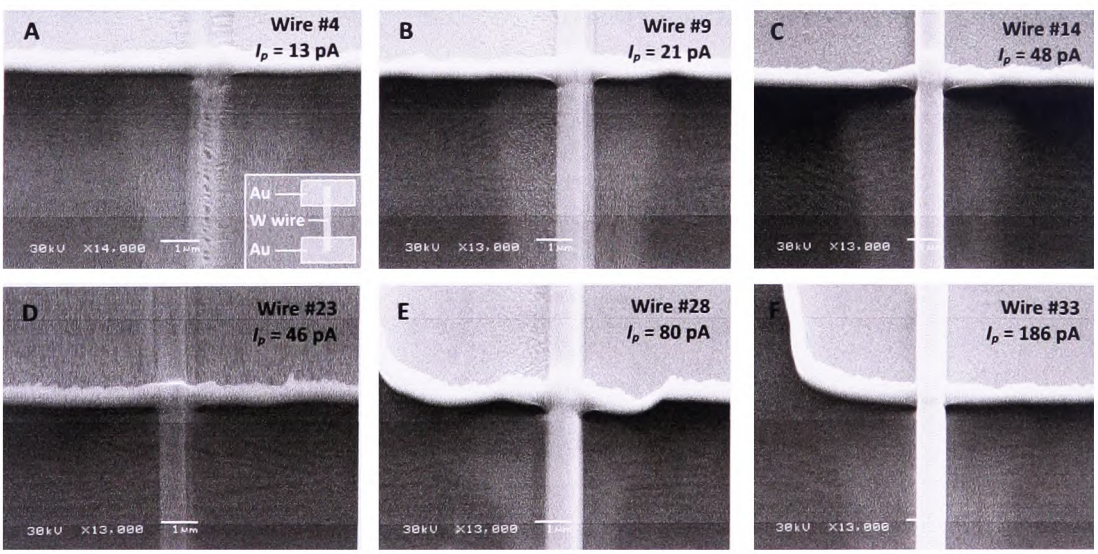

Figure 7.1.1 – SEM images showing some of the tungsten wires deposited using a scanning speed of 1.2 m s^{-1} and 50 μm (*A* to *C*) and 100 μm (*D* to *E*) beam-defining apertures. A schematic illustration showing the position of the wires in relation to the Au contact pads is given in *A* (inset). The wire numbers in each image correspond to the resistance measurements in Table 7.1.1.

Figures 7.1.2, *B* and *D* seem to suggest that where higher ion fluxes were used, the resistance was less dependent on scanning speed, although generally, faster beam movement was more effective. In nearly all cases, the slowest scanning speed produced wires with the highest resistance, probably as a result of overexposure and subsequent sputtering. The optimum current density was achieved using the 100 μm aperture with a probe current of 186 pA, where the wire resistance was reasonably low for all scanning speeds, measuring approximately 260 Ω at its lowest. In some cases it is not possible to use the optimum conditions. If a shorter element is required, the same scanning frequency will equate to a slower average speed, which has to be compensated for with other settings. Unfortunately, there is no single setting that will satisfy all conditions when using analogue systems. Digital systems are preferable in this respect, since they work in terms of pixel dwell time and step size. Any given combination of these settings will result in a beam speed that will be independent of scan area.

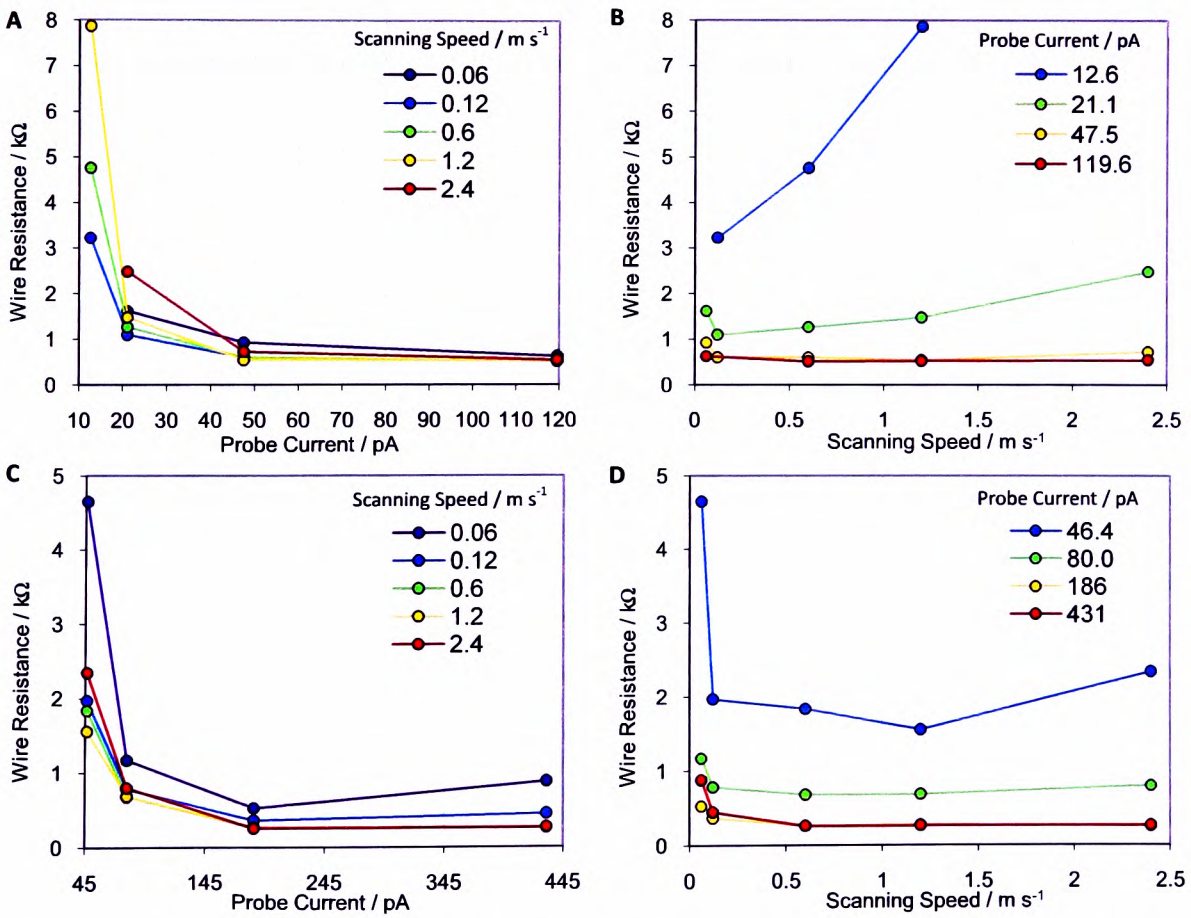

Figure 7.1.2 – Resistance measurements of the wires deposited using the 50 μm (*A* and *B*) and 100 μm (*C* and *D*) apertures with different probe currents and scanning speeds.

Wire #	Aperture Diameter (μm)	$\langle I_p \rangle$ (pA)	Scanning Speed (m s^{-1})	Resistance (Ohms)
1	50	12.64	0.06	1 M
2			0.12	3221
3			0.6	4761
4			1.2	7870
5			2.4	8.8 M
6		21.1	0.06	1620
7			0.12	1098
8			0.6	1266
9			1.2	1478
10			2.4	2479
11		47.52	0.06	928
12			0.12	602
13			0.6	600
14			1.2	543
15			2.4	725
16		119.58	0.06	629
17			0.6	513
18			1.2	525
19			2.4	543
20	100	46.4	0.06	4652
21			0.12	1969
22			0.6	1837
23			1.2	1558
24			2.4	2343
25		80	0.06	1173
26			0.12	785
27			0.6	681
28			1.2	687
29			2.4	802
30		186	0.06	529
31			0.12	366
32			0.6	263
33			1.2	274
34			2.4	258
35		431	0.06	880
36			0.12	449
37			0.6	261
38			1.2	264
39			2.4	268

Table 7.1.1 – Combinations of aperture size, probe current and scanning speed yield wires of varying resistance.

7.2 *Tungsten Deposition on Fe and Ni/Fe Films*

As was discussed in the previous section, non-ideal ion beam parameters can lead to undesirable milling of the substrate during deposition. This must be minimised if FIBID is to be used to form electrical interconnects between delicate structures. The ion dose required for deposition of a substantial thickness of tungsten is around one to two orders of magnitude greater than that which has previously been shown to affect the magnetic properties of Fe films. Most of the ion-induced damage is likely to occur during the initial deposition of the interfacial layer, which begins as a discontinuous deposit comprising clusters tens of nanometres in size[7.1, 2]. Once these initial clusters grow to form a continuous film, the deposition may already be over 100 nm thick[7.2] and should then provide ample protection against further ion irradiation. The issue here is whether the deposition forms fast enough in order to prevent the magnetic properties of the sample from being significantly modified.

In order to address this point, magneto-optical measurements were performed on an as-grown Ni/Fe bi-layer and two different areas of W/Ni/Fe, where the W layers were formed using two sets of ion beam conditions. Each tungsten deposit covered an area of 60 μm × 60 μm and was formed using a total charge of 990 nC (approximately 1.7×10^{17} ions cm^{-2}). The two ion beam configurations were: i) 50 μm aperture and 104 pA probe current, and ii) 100 μm aperture and 550 pA probe current. In both cases, a high beam scanning speed of 2.4 m s^{-1} was used since slower beam movement was found to compromise the integrity of the silicon nitride membrane. At 0.12 m s^{-1} the ion beam milled through the full thickness of the membrane, highlighting the potential for significant substrate milling to occur if the parameters are not set accordingly. The composition of each deposition was determined using EDX in a scanning transmission electron microscope (STEM). As shown in Table 7.2.1, the composition of the two deposits did not differ significantly, but it is apparent that the magnetic layers were marginally better preserved using the higher probe current, probably owing to the much shorter exposure time. The levels of

	50 μm Aperture, 104 pA	100 μm Aperture, 550 pA
Element	At. %	At. %
O	16.62	13.12
Ga	25.59	24.63
Fe	4.7	6.88
Ni	1.93	3.23
W	51.17	52.15

Table 7.2.1 – Approximate compositions of the FIB-deposited W films. Carbon is also likely to be present but the amount is difficult to quantify using EDX.

tungsten and Ga content are not drastically different to those observed by others[7.1, 3], but there appears to be an elevated level of oxygen. Depending on its chemical state, it may be detrimental to the Fe layer, possibly causing oxidation.

Magneto-optical measurements performed on the two tungsten deposits revealed that the underlying Ni/Fe remained magnetic, although the saturation magnetisation was reduced considerably in comparison to that of the as-grown Ni/Fe (Fig. 7.2.1). The magnetic signal from the area irradiated using the lower probe current was almost masked completely by thermal drift, while there is a small but definite loop from the area irradiated using the higher probe current. The coercivity doesn't appear to be greatly increased in either region, which is surprising considering the high doses that were applied, although such low signals are not sufficient to draw a meaningful conclusion regarding the magnetisation reversal mechanisms.

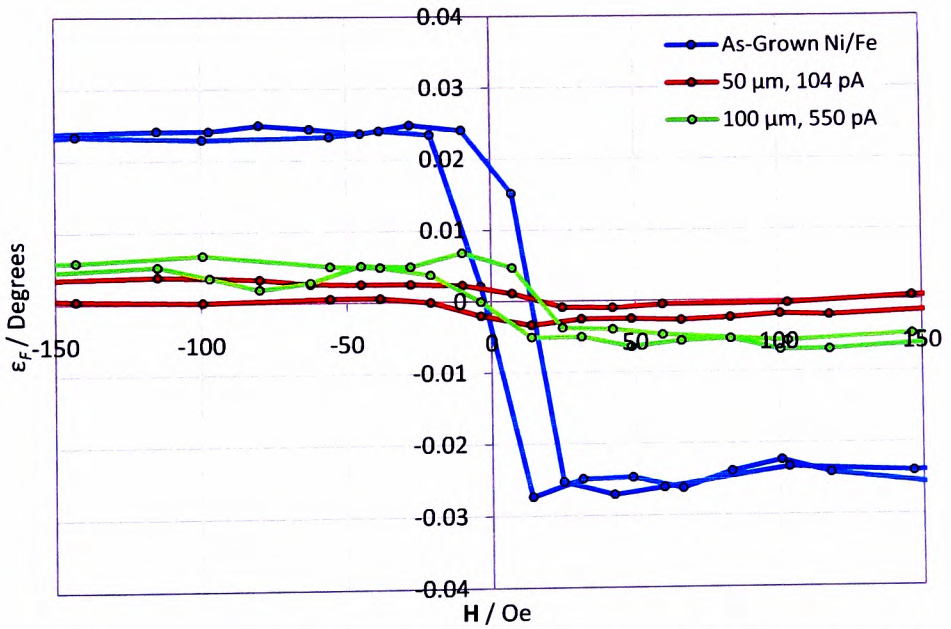

Figure 7.2.1 – Hysteresis loops plotting the θ_F produced by the Ni/ Fe film in its as-grown state and beneath the FIB-deposited tungsten layers.

An STXM OD image of a tungsten deposit running across a 6.8 nm thick Fe grating is shown in Fig. 7.2.2*A*. The 2 µm wide, 35 µm long tungsten wire was produced using a 50 µm aperture, 128 pA probe current and a beam scanning speed of 0.7 m s^{-1}. Surface profiles of the grating with and without the overlying deposition are plotted in Fig.7.2.2*B*, from which a thinning and apparent widening of the Fe strips is clearly seen. The ion dose applied during deposition was approximately 2.3×10^{17} ions cm^{-2}, but the Fe thickness was reduced by only 1.4 nm. According to the thickness versus dose plots in Chapter 5, this equates to an effective

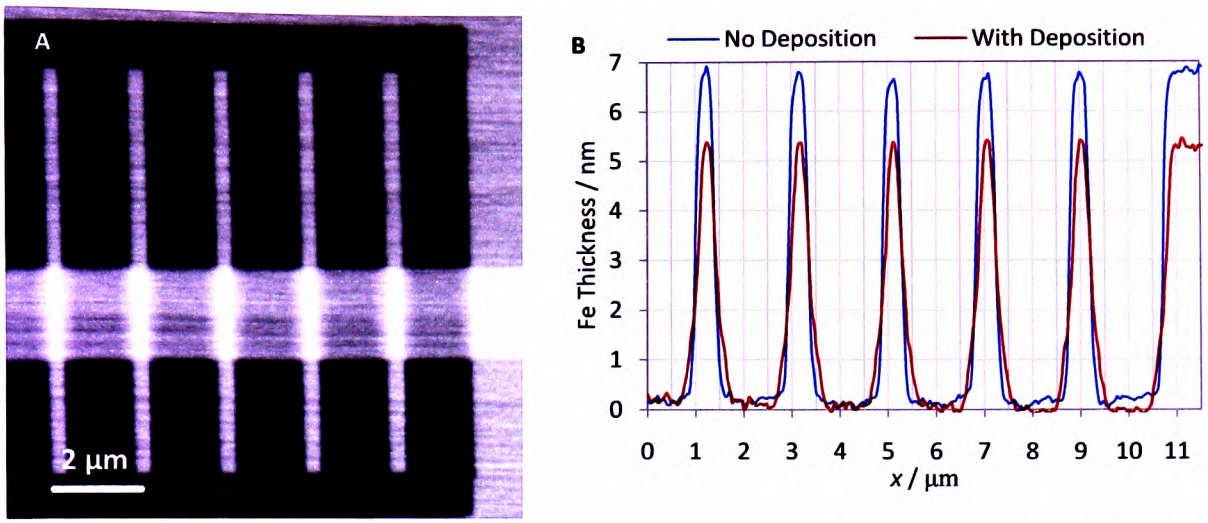

Figure 7.2.2 – *A*: STXM OD image of an Fe grating with a 2 µm wide FIB-deposed W strip. *B*: Surface profiles of the Fe strips with and without the overlying deposition.

dose of roughly 1.2×10^{16} ions cm^{-2} applied to an uncapped Fe film. Sputtering during the interfacial growth stage has resulted in a portion of the Fe becoming trapped within the tungsten deposit, which has migrated out 125 nm either side of the strips. It is also likely that tungsten, carbon and oxygen have been implanted into the Fe. XAS measurements, however, did not reveal any formation of Fe compounds.

Observations made in the earlier chapters indicate that Ga implantation at 1.2×10^{16} ions cm^{-2} should be not be detrimental to the magnetic properties of 10-12 nm thick films, but in this case with the initial Fe thickness being just 6.8 nm, the combination of sputtering and Ga implantation will most likely have had a greater impact on the magnetic properties. In addition, as previously discussed, atomic mixing with a non-magnetic layer may expedite the decline of the ferromagnetic properties.

A higher resolution MTXM image of the grating is shown in Fig. 7.2.3*A*, in which the Fe layer can clearly be seen beneath the tungsten deposit. The XMCD images of the reversal process in *B* to *E* show that the Fe strips switch at fairly high field values in excess of 450 Oe. Pinning of the domains at the edges of the deposit appears to isolate the sections of Fe on either side of it. In fact, no XMCD contrast is apparent beneath the tungsten, which suggests the two sections of each Fe strip are magnetically isolated. On a side note, the spacer regions between the Fe strips appear much cleaner compared to those previously shown in Fig 6.2.2. As a result there is no longer any pinning of domain walls because of the edge roughness.

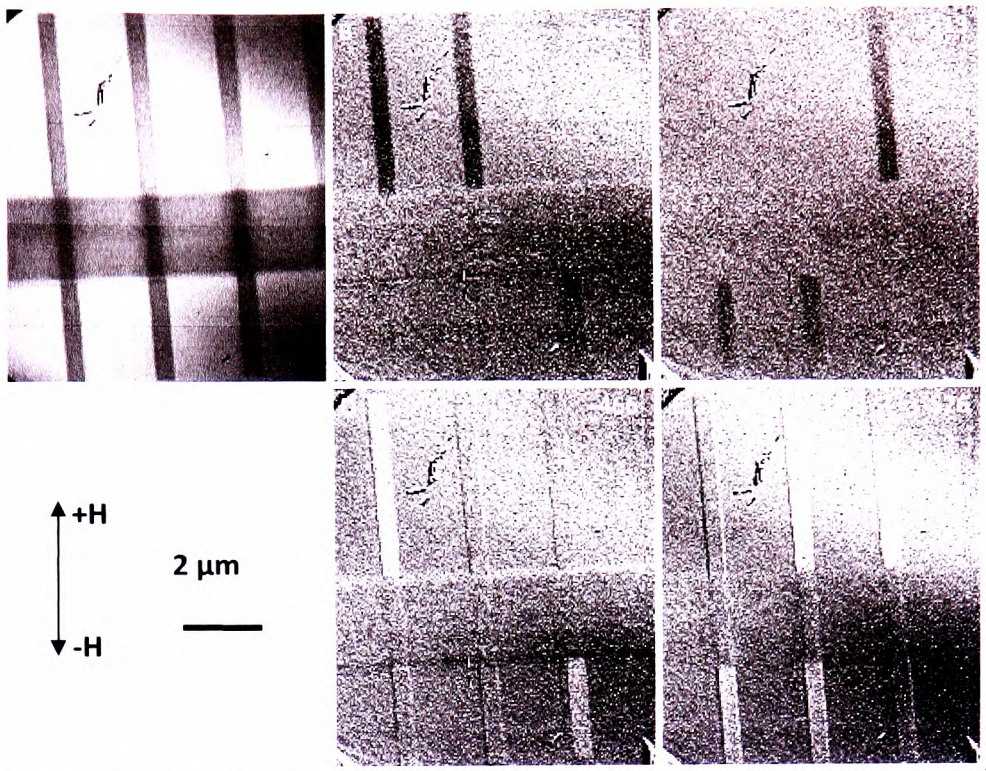

Figure 7.2.3 – *A*: MTXM image of an Fe grating with a 2 µm wide FIB-deposited tungsten strip (not an OD image). *B* to *E*: XMCD sequential difference images showing pinning of the magnetisation at the deposition edges. Field values (in Oe) are indicated in the images.

t is quite clear that forming electrical contacts upon "active" areas of magnetic devices by IBID should be avoided, unless the magnetic layers are thick enough to withstand the ion lose required to form the initial deposition. Even then, subsequent irradiation may result in lloying of the deposited and magnetic layers. It can be imagined how electrical contacts leposited either site of a domain wall trap[7.4-6], as illustrated schematically in Fig. 7.2.4, if ormed by FIBID could effectively isolate the trapping element and prevent the device from unctioning as intended. Moreover, the two contacts may themselves form a trapped state in he intermediate section.

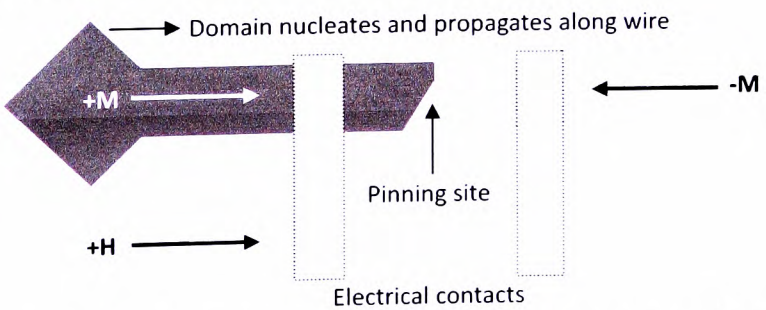

Figure 7.2.4 – Schematic illustration of a simple domain wall trap[7.4]. The domain nucleates in the large pad at the left, and then propagates along the wire until it becomes pinned at the notch. The resistance of the wire measured between the two contacts decreases when the domain wall is present.

References

7.1 D. W. K. Jenkins, G. C. Allen, P. D. Prewett and P. J. Heard, Journal of Physics-Condensed Matter **3**, S199-S206 (1991).

7.2 H. Langfischer, B. Basnar, H. Hutter and E. Bertagnolli, Journal of Vacuum Science & Technology a-Vacuum Surfaces and Films **20** (4), 1408-1415 (2002).

7.3 E. S. Sadki, S. Ooi and K. Hirata, Applied Physics Letters **85** (25), 6206-6208 (2004).

7.4 M. Y. Im, L. Bocklage, P. Fischer and G. Meier, Physical Review Letters **102** (14), 4 (2009).

7.5 H. T. Zeng, D. Read, D. Petit, A. V. Jausovec, L. O'Brien, E. R. Lewis and R. P. Cowburn, Applied Physics Letters **94** (10), 3 (2009).

7.6 C. Brownlie, S. McVitie, J. N. Chapman and C. D. W. Wilkinson, Journal of Applied Physics **100** (3), 9 (2006).

CHAPTER 8 Conclusions and Further Work

8.1 *Conclusions*

This work, for the most part, was concerned with two aspects of patterned magnetic media research, namely, the fabrication and characterisation. A commercial Ga-FIB system was employed as a general purpose magnetic patterning tool for the production of magnetic elements on a sub-micron scale. The physical and magnetic properties of theses artificial structures were then explored with a potentially novel combination of a modern approach to the well-established magneto-optical methods and the relatively new X-ray microscopy techniques.

The effects of quasi-homogeneous Ga ion irradiation on the structure of nanocrystalline Fe films were studied using TEM and STXM, while the magnetic hysteresis properties were determined using magneto-optical Stokes polarimetry. Various magnetic patterns were also created by fully or partially etching away the Fe, such that arrays of physically isolated Fe elements or coupled Fe and Fe-Ga elements were created on a sub-micron scale. The magnetisation reversal processes occurring within the small elements was investigated using MTXM, which aided in the interpretation of the magneto-optical hysteresis loops. In addition, FIBID was investigated as a possible means of forming electrical contacts to magnetic elements for magneto-electronic applications.

TEM observations of the Ga irradiated nanocrystalline Fe film revealed that even low doses of 7.68×10^{15} ions cm^{-2} can affect the microstructure, increasing the average grain size from around 15 nm to 26 nm. The film remained nanocrystalline and continuous until a dose of 2.29×10^{16} ions cm^{-2} was applied, where discontinuities became apparent. At higher doses isolated clusters of Fe-Ga, approximately 60 nm in size, were formed. Ga incorporation into the Fe crystal structure was considered as a possible reason behind the observed increase in lattice parameter 0.6 % after a dose of 1.15×10^{16} ions cm^{-2}, but changes in the stress cannot be disregarded. A higher dose of 2.29×10^{16} ions cm^{-2} resulted in a relaxation of the lattice

parameter back down to the nominal value. This was concomitant with disappearance of preferential ordering, which was possible a result of recrystallisation.

During the investigations of the patterned media, a magneto-optical Stokes polarimeter was specially constructed for the purpose of measuring the small areas of FIB-patterned magnetic film. The rudimentary two-lens microscope, while providing only limited spatial resolution owing to a considerable amount of laser speckle, allowed areas 40 μm × 40 μm in size to be easily measured independently of the surrounding film. The polarimeter provided a full characterisation of the polarisation state of the light, allowing for a direct comparison between the Faraday effects produced by different samples to be made without any normalisation.

Such an absolute measurement of the polarisation state is only possible if the polarimeter is properly calibrated. The conventional linear regression approach to calibration, while it is simple in theory, is extremely restrictive in terms of the allowed PEM configuration, i.e. the peak retardation values and the relative angle between PEM axes. In practice it was shown to yield inferior results in comparison to an alternative, recently developed calibration method, referred to here as the "four-state calibration method", which allows a completely free and arbitrary choice of the PEM retardation values. Consequently, errors associated with these settings are eliminated. Furthermore, this freedom allows for optimisation of the desired signals to potentially enhance the signal-to-noise ratio. The relative angular settings of the PEMs are still restricted however.

A new approach to calibration has been developed during the course of this work which potentially allows for total freedom in the choice of polarimeter configuration, including the angular settings of the PEMs which in principle can be unknown. The new approach uses a non-linear multi-parameter optimisation routine that iteratively trials different values of the calibration constants in order to find the ideal solution. The algorithm used is a standard function in the widely available Microsoft Excel application and thus requires no programming knowledge in order to replicate the results obtained here. In general, the procedure provided results comparable with those obtained using the four-state calibration approach and in one case improved on the accuracy considerably. However, if the polarimeter configuration permits, it would be advantageous to perform the first stage of the four-state calibration procedure in order to obtain trusted values for most of the constants for comparison; however, this is not strictly necessary. The real advantage to the non-linear

optimisation, apart from the possible improvement in accuracy, is its potential to relieve the experimentalist of the task of accurately configuring the angular dispositions of the PEMs, which can be time consuming and costly, if precision rotary mounts or specialised PEMs are purchased in order to minimise the error in alignment.

Using the magneto-optical microscope, a study of the effects of quasi-homogeneous Ga ion implantation on the magnetic properties of Fe films was conducted. The results correlated well with the TEM images of a similarly irradiated film. At low ion doses up to 1.15×10^{16} ions cm^{-2} the coercivity increased without evidence of domain wall pinning. This was attributed to the enlargement of the grains. Discontinuities, as observed in higher dosed areas were thought to further increase coercivity by providing domain wall pinning sites. Doses higher than 2.87×10^{16} ions cm^{-2} then reduced the coercivity due to the increasing separation between Fe. In comparison with reports on the irradiation of permalloy films of similar thickness, the Fe studied here was somewhat more resistant to irradiation damage, where the Fe-Ga was seen to remain ferromagnetic even after high doses of 4×10^{16} ions cm^{-2}.

Areas of film that were topographically patterned, in some cases, exhibited hysteretic behaviour that did not appear to be symmetrical about zero-field. This was noticed particularly where the patterns were anisotropic. It was proposed that second-order magneto-optical effects could be present as a result of coherent rotation of the magnetisation where domain nucleation is restricted by the physical dimensions of the magnetic elements, in narrow strips for example. MTXM images, although they did not reveal domain structure during magnetisation along the hard axis (field perpendicular to the strips), contained a definite dichroic signal between images recorded at opposing fields, confirming some rotation of the magnetisation.

Contributions from the diffracted beams could not be determined separately, in a manner analogous to D-MOKE, although it was shown that certain features in the ellipticity angle loops became more pronounced as the grating became better defined in terms of the difference in transmittance between the Fe and Fe-Ga regions. This was considered to be indirect evidence that the increasing magnitude of such features was attributed to contributions from the diffracted light.

Some of the patterns produced features in the hysteresis loops at zero-field which were attributed to domain formation. While these were present on the Faraday rotation loops, in many cases they were barely noticeable. On the other hand, they are quite clearly visible on the ellipticity angle loops, to such an extent that in some cases the loops did not describe the true **M** vs. **H** behaviour of the sample. This would suggest that the ellipticity is more sensitive to the reversal mechanism and domain structure, while the Faraday rotation, as generally accepted, yields the average magnetisation of the measured area.

Finally, a preliminary investigation of FIBID as a means of forming electrical contacts to magnetic elements for magnetoresistive applications was conducted. The various analytical techniques used here all indicate that the process of depositing tungsten on magnetic layers can significantly affect their structural and magnetic properties. STXM images reveal a thinning of the magnetic layer beneath the deposit and as a result, domain wall pinning occurs as observed using the MTXM. In fact an overlying deposit is as effective at pinning the magnetisation in a thin magnetic strip as a lateral constriction almost the complete width of the strip. FIBID is only likely to be a viable approach to contact formation if the magnetic layer is thick enough to withstand the ion dose required to form the initial interfacial layer, which may require doses in excess of 10^{16} ions cm^{-2}.

8.2 *Proposed Further Work*

There are a number of interesting aspects to this work that would be worthwhile pursuing further, one of which is the development of the magneto-optical Stokes polarimeter. Unfortunately, as is often the case in research, limited funds restricted the progress to a stage where it was functional and fit for the purpose, but its true potential was far from realised. Even without any serious effort to minimise noise, measurements of the azimuth and ellipticity angles with a precision on the order of 10^{-3} degrees or even less was possible. With a few fairly simple modifications, the performance and functionality could be improved considerably.

Using *p*-polarised light with the sample in the longitudinal Faraday orientation (as used throughout this work) can provide simultaneous measurement of both longitudinal and transverse components of magnetisation, where the polarisation state is proportional to m_l and the intensity proportional to m_t. For such a measurement to be made, the Stokes parameter I needs to be independent of laser output, which is currently not the case. Fluctuations in intensity over a typical data acquisition timeframe currently swamp any magnetic signals. With the addition of a reference beam that bypasses the sample, a second photodiode and differential amplifier would allow the measurement of I as a function of sample magnetisation only.

Several steps could be made to improve the resolution of the microscope for domain imaging purposes. Laser speckle is currently a performance limiting factor, which could easily be resolved with the addition of a spatial filter to remove the diffraction orders produced by imperfections in the optics. Also, improving the optics further, with the combination of a beam expander and longer focal length condenser and objective lenses would allow them to be removed from the magnetic field, eliminating their troublesome contributions to the Faraday rotation measurements. A shorter wavelength light source, a blue laser for example, would also improve spatial resolution to less than half a micron. With a straight forward adjustment of the sample orientation to the transverse geometry (see Chapter 3), such optical improvements would make conventional magnetic domain imaging (i.e. recording the intensity variations) possible in addition to the polarisation-sensitive mode used in this work.

Development could be taken even further with the addition of a scanning sample stage. Scanning the sample laterally while using a small fixed aperture located at the image plane would allow a spatially resolved map of the Stokes parameters to be obtained. The new stage would likely combine widely available stepper-motor and piezoelectric scanning mechanisms to provide relatively quick coarse and fine imaging. Such images would provide maps of the absolute Faraday rotation and ellipticity angles, allowing a quantitative characterisation of the sample properties.

Regarding the patterned media, further work is required in order to determine the origin of the asymmetrical nature of some of the hysteresis loops. Without modification of the magneto-optical set-up, measurement of the hysteresis loops as a function of incident angle would reveal the first and second-order contributions. As the angle of incidence approaches zero, the first order effects would disappear while the second-order effects would increase. However, as explained in Ref. (8.1) these second-order effects should be observable in the specular and the diffracted light, while domain information only appears in the diffracted light. Thus, perhaps a more certain conclusion could be drawn from a measurement of the specular beam alone. This would require placing a pinhole-aperture at the focal point of the objective lens (the Fraunhofer diffraction plane). Spatial filtering could then be achieved such that only the desired order was measured. If for example, all asymmetry disappears when the zeroth-order is measured, then this would suggest diffraction effects were responsible. If it persisted, it would suggest second order effects.

Alternatively, the current data may be supported by additional theoretical work, with micromagnetic simulations for example. Perhaps an adaption of the theoretical approaches of Inoue *et al.*[8.2] and Lu *et al.*[8.3] for thin gratings with in-plane anisotropy may provide some insight into the very different behaviour observed when measuring the Faraday rotation and the ellipticity angles.

Using a scanning Stokes polarimeter as described above, would make it possible to image the FIB-patterned media to provide further information about the domain structure. For instance, by performing spatial filtering at the Fraunhofer plane, the zeroth-order light could be blocked, leaving only the diffracted light at the imaging plane. What would be observed is an image revealing the diffracting elements of the sample which may include the magnetic domains. In this case the image would change with applied field as a result of the changes in

the domain structure, potentially proving addition information about the reversal mechanism.

Of course domain imaging could easily be achieved with additional MTXM measurements, but exploring the various ways in which magneto-optical techniques can be used may be of some benefit for the future commercialisation of patterned magnetic recording media. Production of the media on an industrial scale would also require development of quality control techniques that would have to be suitable for use within an industrial environment; optical methods are ideal in this respect. Since the individual magnetic bits could not be observed directly, measuring their collective properties could provide a characteristic "fingerprint" that when compared to an ideal media, would provide a quick check of the pattern quality.

Not too far afield from the work in this thesis is the area of meta-materials research. The FIB lithography technique could easily be used to fabricate planar chiral meta-materials such as those studied by Potts *et al.*[8.4, 5]. Potts and co-workers found that the handedness of planar patterns can influence the polarisation state of diffracted components of linearly polarised incident light. Imaging such a pattern using a scanning Stokes polarimeter, as described above, would provide a detailed map of the polarisation states originating from each part of the pattern. This map could be broken down into the specular and diffracted components using spatial filtering, maybe providing some insight into the critical areas of the patterns that are responsible for inducing the unusual polarisation effects.

On a broader note, the scanning polarimeter would not only be useful for characterising patterned media, but could also be used as a potentially powerful biological imaging technique. Since biological materials can exhibit birefringence[8.6] and optical activity[8.7] as a result of their structure, an imaging technique that is sensitive to such effects can reveal structural contrast that is not normally observed in conventional optical microscopy[8.6].

References

8.1 T. Schmitte, K. Westerholt and H. Zabel, Journal of Applied Physics **92** (8), 4524-4530 (2002).

8.2 M. Inoue, K. Isamoto, T. Yamamoto and T. Fujii, Journal of Applied Physics **79** (3), 1611-1624 (1996).

8.3 Y. H. Lu, M. H. Cho, J. B. Kim, G. J. Lee, Y. P. Lee and J. Y. Rhee, Optics Express **16** (8), 5378-5384 (2008).

8.4 A. Potts, A. Papakostas, N. I. Zheludev, H. J. Coles, R. Greef and D. M. Bagnall, Materials and Devices for Optoelectronics and Microphotonics **722**, 293-297 (2002).

8.5 A. Potts, A. Papakostas, D. M. Bagnall and N. I. Zheludev, Microelectronic Engineering **73-4**, 367-371 (2004).

8.6 J. F. de Boer, T. E. Milner, M. J. C. vanGemert and J. S. Nelson, Optics Letters **22** (12), 934-936 (1997).

8.7 D. Keller, C. Bustamante, M. F. Maestre and I. Tinoco, Proceedings of the National Academy of Sciences of the United States of America **82** (2), 401-405 (1985).

APPENDIX

Appendix 1: A simple transimpedance preamplifier

A simple transimpedance preamplifier was built for the purpose of amplifying the small current signal from the photodiode into a larger voltage signal that could be detected by the lock-in amplifiers and *dc* electrometer. The design was based around the Texas Instruments OPA2380 operational amplifier[1]. Although the amplifier was not used for measurements, as will be explained below, details are included here for those who wish to improve on the design.

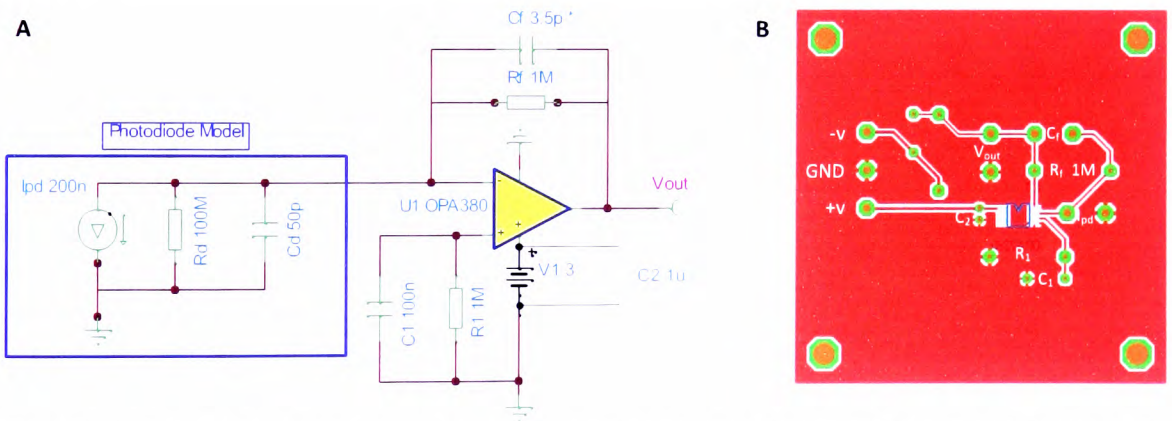

Figure A1.1 – *A*: A schematic circuit diagram of a simple transimpedance amplifier using an OPA380 op-amp. For circuit simulation purposes, a photodiode model was also included as shown in the blue box. *B*: The component side of the printed circuit board layout (actual size). Red areas indicate the copper layer on the rear side and green represents solder pads. The OPA2380 is in the form of a surface-mount package that is soldered directly to the copper side.

A schematic circuit diagram and printed circuit board layout is shown in Fig. A1.1. For circuit simulation purposes, the photodiode was modelled using a current source (I_{pd}), a resistor (R_d), and capacitor (C_d). R_d and C_d represent the photodiode resistance and parasitic capacitance, the actual values of which are unknown, so typical values have been used. The gain of the amplifier is set by R_f. A value of 1M results in a gain of 10^6 V A^{-1}. The feedback capacitor, C_f, compensates for C_d and prevents oscillation. Since C_d was unknown, the ideal

[1] Texas Instruments, "Precision, high-speed transimpedance amplifier," Data sheet SBOS291G, 2007. [Online]. Available: http://focus.ti.com/lit/ds/symlink/opa380.pdf. [Accessed Aug, 2008].

value could not be calculated, thus a 3.5 pF variable capacitor (1-3.5 pF) was used to allow for tuning of the response. The simulated[2] *ac* transfer characteristics of the amplifier with various values of C_f are shown in Fig. A1.2.

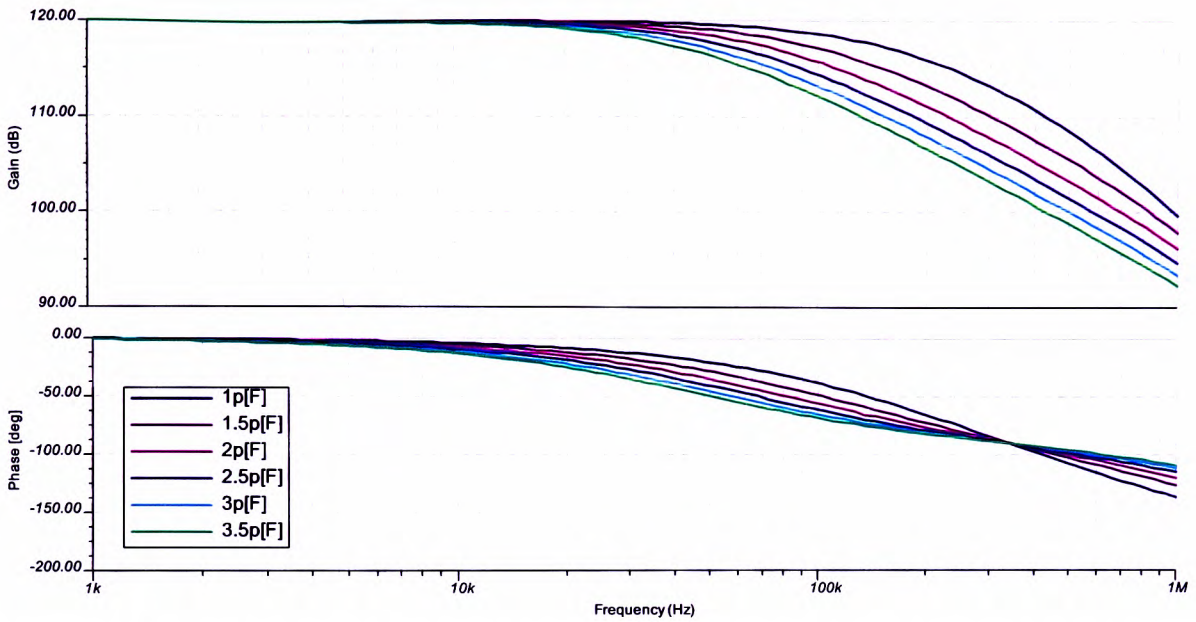

Figure A1.2 – Simulated *ac* transfer characteristics of the amplifier in Fig. A1.1 with various values of C_f.

With C_f = 1 pF, the simulation suggests a bandwidth of 164 kHz, which should be sufficient to measure all PEM signals, so long as the photodiode capacitance does not increase much above 50 pF. However, when fabricated, the amplifier exhibited a somewhat distorted signal at 84 and 100 kHz. This became evident when observing the stability of the S_{dc}, S_{QU1} (84 kHz), S_{QU2} (100 kHz) and S_V (42 kHz) signals, as illustrated in Fig. A1.3. Each signal should follow S_{dc} as is seen to be the case with S_V (apart from the inversion). Some of the more prominent noise features can be matched to those in the plot of S_{dc}. The S_{QU1} signal appears similar, but does not follow S_{dc} as closely, while the plot of S_{QU2} appears quite different. It is also apparent that noise fluctuations are much lower in the S_{QU2} signal, which suggests some smoothing and hence distortion of the waveform. This is quite possibly linked to a higher value of C_d than expected. In its current state the amplifier is only suitable for lower frequency measurements and for this reason it was not used for sample measurement, but with modifications, an extension of the bandwidth may be possible.

[2] Design-Soft, *TINA-TI*, Version 7. [Online] Dallas, TX.: Texas Instruments, 2007. Available: http://focus.ti.com/docs/toolsw/folders/print/tina-ti.html.

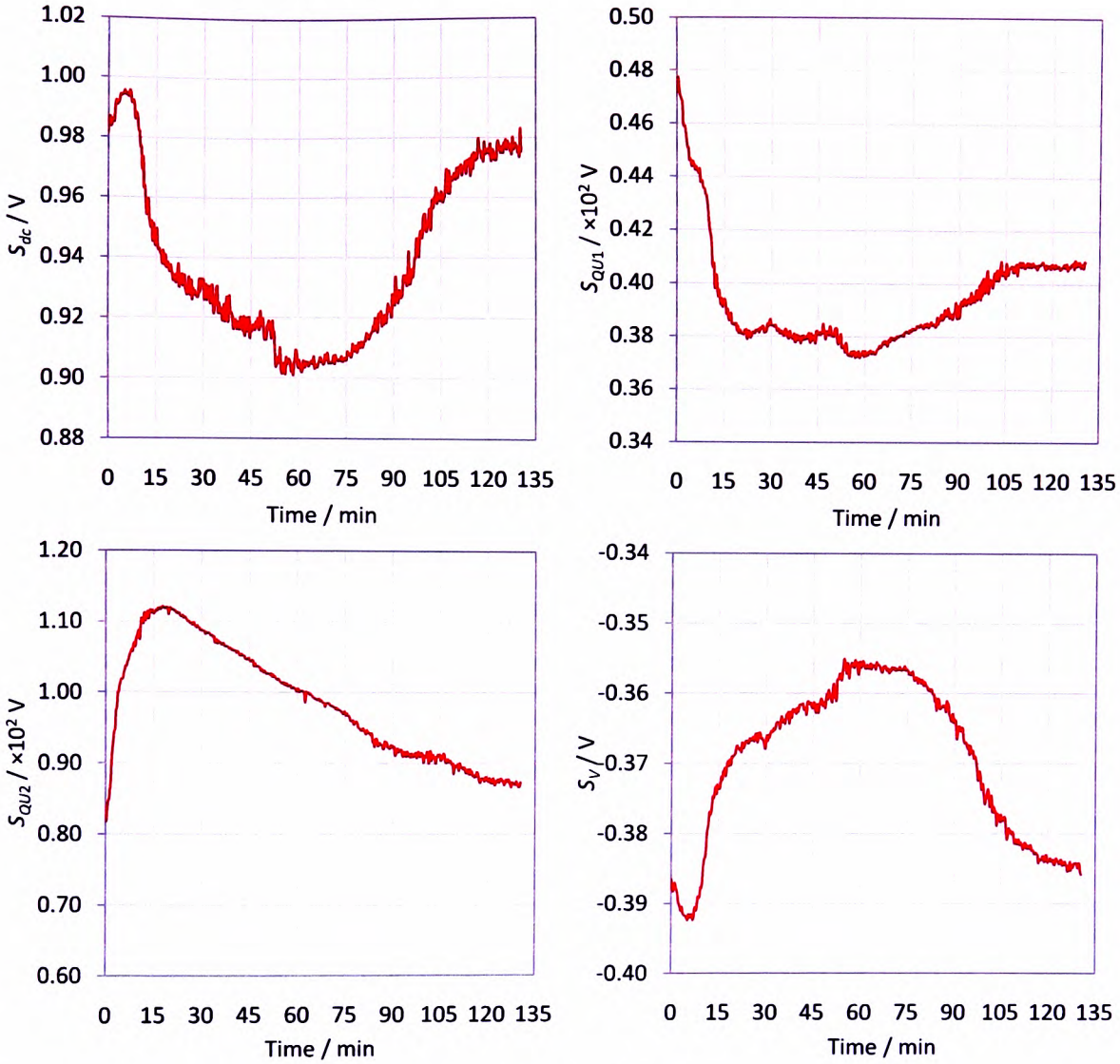

Figure A1.3 – Variations in the S_{dc}, S_{QU1}, S_{QU2} and S_{QU2} signals over time.

Appendix 2: Polarimeter calibration data

The following calibration data was collected using the polarimeter configuration where: $\alpha = 45°$ and $\delta_{10} = \delta_{20} = 2.4048$ rad.

Sub-Set	θ (Deg)	S_{dc} (V)	S_v (V) (Ω_1 = 42 kHz)	S_{QU1} (V) ($2\Omega_1$ = 84 kHz)	S_{QU2} (V) ($2\Omega_2$ = 100 kHz)
1	0	6.5945E-01	1.4388E-03	2.5056E-01	-3.2985E-04
	45	6.4937E-01	-2.0970E-04	-2.4936E-05	3.0301E-01
	90	6.0652E-01	-1.3992E-03	-2.5215E-01	4.0750E-04
	-45	6.4627E-01	3.3197E-04	-2.9029E-04	-3.5194E-01
2	0	6.8231E-01	1.3709E-03	2.5942E-01	-6.3625E-04
	45	6.7553E-01	-2.7725E-04	-1.5475E-04	3.1494E-01
	90	5.8490E-01	-1.2415E-03	-2.4352E-01	2.8395E-04
	-45	6.6046E-01	2.5802E-04	1.6947E-04	-3.5889E-01
3	0	6.9772E-01	1.2318E-03	2.6544E-01	-8.5590E-04
	45	6.9410E-01	-2.3159E-04	-1.1611E-04	3.2377E-01
	90	5.9480E-01	-1.2547E-03	-2.4745E-01	4.9465E-04
	-45	6.5998E-01	2.4401E-04	-1.2861E-04	-3.5824E-01
4	0	6.9396E-01	1.2505E-03	2.6398E-01	-7.3390E-04
	45	6.9314E-01	-2.6921E-04	2.3522E-05	3.2321E-01
	90	6.0225E-01	-1.3047E-03	-2.5043E-01	4.3550E-04
	-45	6.5349E-01	2.3921E-04	-1.0666E-04	-3.5467E-01
5	0	6.8875E-01	1.2557E-03	2.6197E-01	-9.1875E-04
	45	6.9339E-01	-2.2155E-04	1.2467E-04	3.2363E-01
	90	6.0888E-01	-1.3392E-03	-2.5310E-01	4.4920E-04
	-45	6.4961E-01	2.2352E-04	-9.5889E-05	-3.5188E-01

Table A2.1 – Data Set *A*: Linearly polarised states at θ = 0°, 90° and ±45°.

S_{dc} (V)	S_v (V) (Ω_1 = 42 kHz)	S_{QU1} (V) ($2\Omega_1$ = 84 kHz)	S_{QU2} (V) ($2\Omega_2$ = 100 kHz)
7.6794E-01	1.4623E-03	2.9324E-01	7.2025E-04
7.2607E-01	5.3414E-02	2.7224E-01	8.0729E-03
6.7413E-01	9.5780E-02	2.4053E-01	1.3868E-02
6.1281E-01	1.2662E-01	2.0136E-01	1.8294E-02
5.4416E-01	1.4436E-01	1.5840E-01	2.0868E-02
4.6996E-01	1.4900E-01	1.1492E-01	2.1574E-02
4.2723E-01	1.4685E-01	9.0962E-02	2.1451E-02
3.9729E-01	1.4280E-01	7.5798E-02	2.0896E-02
3.6091E-01	1.3593E-01	5.8439E-02	1.9911E-02
3.2339E-01	1.2673E-01	4.2176E-02	1.8547E-02
2.5328E-01	1.0457E-01	1.6659E-02	1.5271E-02
2.1525E-01	9.0313E-02	5.6906E-03	1.3175E-02
1.8969E-01	8.0025E-02	-3.1810E-04	1.1660E-02
1.9107E-01	8.0542E-02	-3.1993E-04	1.1992E-02
2.5590E-01	1.0557E-01	1.6846E-02	1.5798E-02
3.2615E-01	1.2773E-01	4.2503E-02	1.9159E-02
4.0137E-01	1.4418E-01	7.6534E-02	2.1660E-02
4.7728E-01	1.5096E-01	1.1693E-01	2.2714E-02
5.5219E-01	1.4628E-01	1.6078E-01	2.2078E-02
6.2285E-01	1.2830E-01	2.0482E-01	1.9442E-02
6.8716E-01	9.7141E-02	2.4540E-01	1.4836E-02
7.3947E-01	5.4242E-02	2.7740E-01	8.6815E-03
7.8399E-01	1.4093E-03	2.9934E-01	7.9515E-04

Table A2.2 – Data Set *B*: Arbitrary elliptically polarised states.

θ (Deg)	S_{dc} (V)	S_v (V) (Ω_1 = 42 kHz)	S_{QU1} (V) ($2\Omega_1$ = 84 kHz)	S_{QU2} (V) ($2\Omega_2$ = 100 kHz)
0	1.9107E-01	8.0542E-02	-3.1993E-04	1.1992E-02
5	2.5590E-01	1.0557E-01	1.6846E-02	1.5798E-02
10	3.2615E-01	1.2773E-01	4.2503E-02	1.9159E-02
15	4.0137E-01	1.4418E-01	7.6534E-02	2.1660E-02
20	4.7728E-01	1.5096E-01	1.1693E-01	2.2714E-02
25	5.5219E-01	1.4628E-01	1.6078E-01	2.2078E-02
30	6.2285E-01	1.2830E-01	2.0482E-01	1.9442E-02
35	6.8716E-01	9.7141E-02	2.4540E-01	1.4836E-02
40	7.3947E-01	5.4242E-02	2.7740E-01	8.6815E-03
45	7.8399E-01	1.4093E-03	2.9934E-01	7.9515E-04

Table A2.3 – Data Set *C*: Linearly polarised states at known values of θ.

Appendix 3: XMCD images

A3.1 Fe-Ga grating

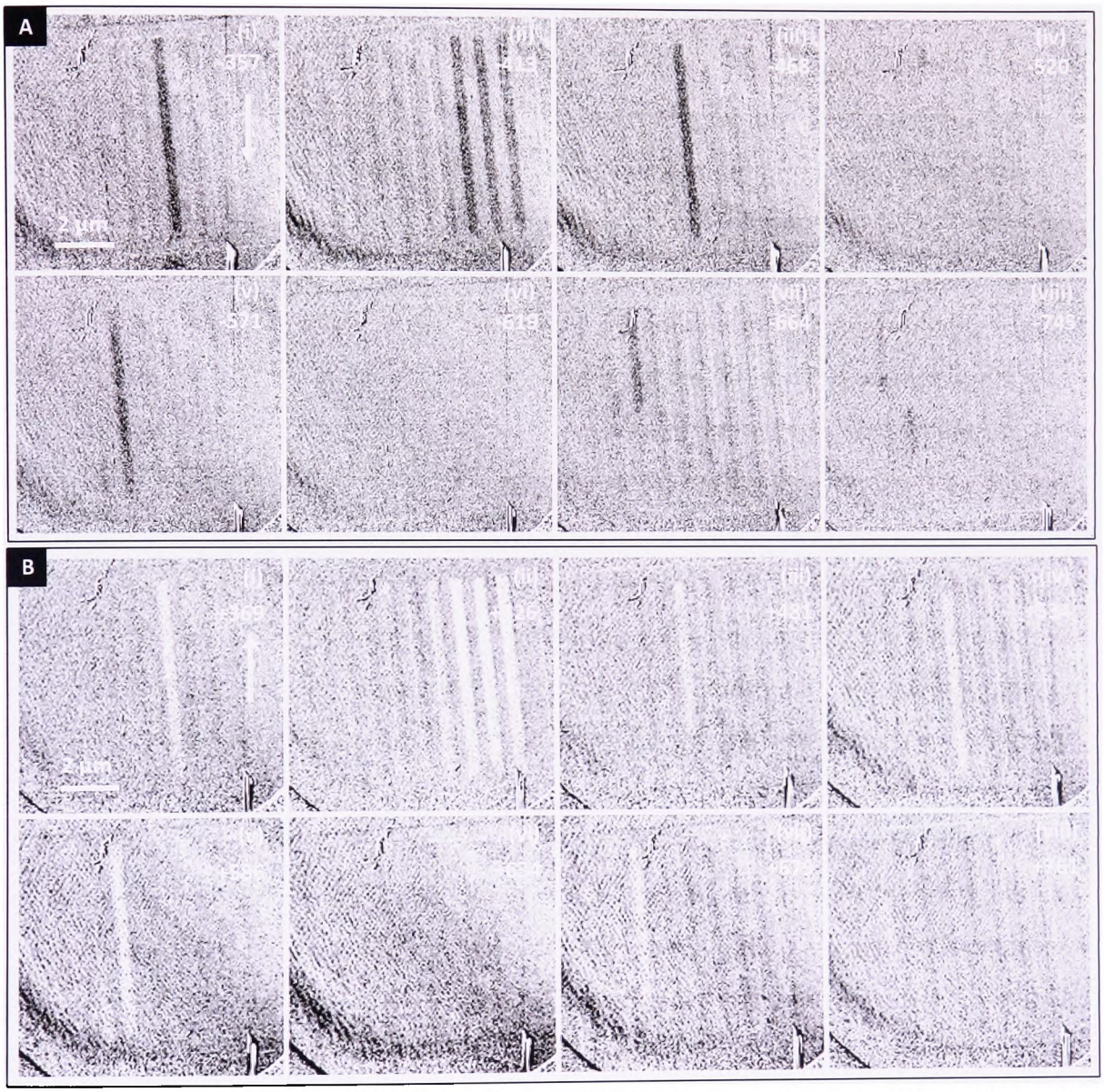

Figure A3.1.1 – XMCD sequential difference images showing the magnetisation sequence of the grating previously discussed in Chapter 6 (Fig. 6.2.1). Each strip was irradiated with a different ion dose. From right to left, the doses applied to the strips were: 0, 0.52, 0.77, 1.15, 1.72, 2.29, 2.87, 3.44, 4.01 and 5.16 $\times 10^{16}$ ions cm^{-2}. The highest dosed strips cannot be seen to switch, probably because the film thickness has been reduced significantly. It is evident the coercivity of the lower dosed strips does not correlate with ion dose. The field directions and scale bars are shown in *A* and *B*, (i).

A3.2 Composite Fe and Fe-Ga grating

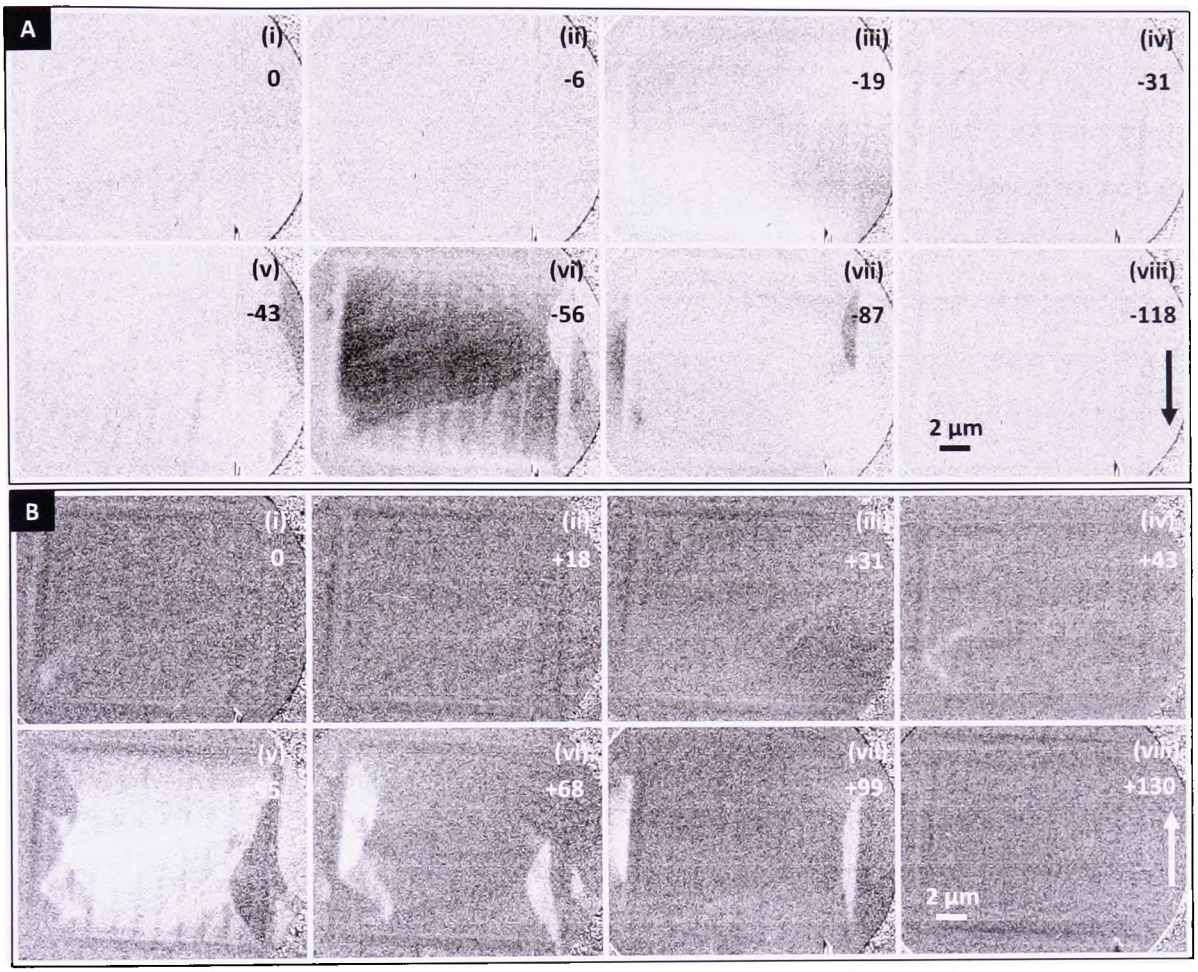

Figure A3.2.1 – XMCD sequential difference images showing the magnetisation process of a grating comprising Fe and Fe-Ga strips of width 0.4 µm. The Fe-Ga was created using a Ga dose of 2.5×10^{16} ions cm^{-2}. It is clear that the formation of the magnetic domains is influenced much more by the shape of the frame that surrounds the grating than the grating itself. Although a degree of pinning along the length of the strips is evident in some images. At remanence in *A* and *B*, (i), faint contrast can be seen in the lower region of the grating. Here the magnetisation has rotated very slightly in some of the Fe-Ga strips to produce faint banding. This is most noticeable in *A*, (i).

A3.3 Fe elements with different aspect ratios

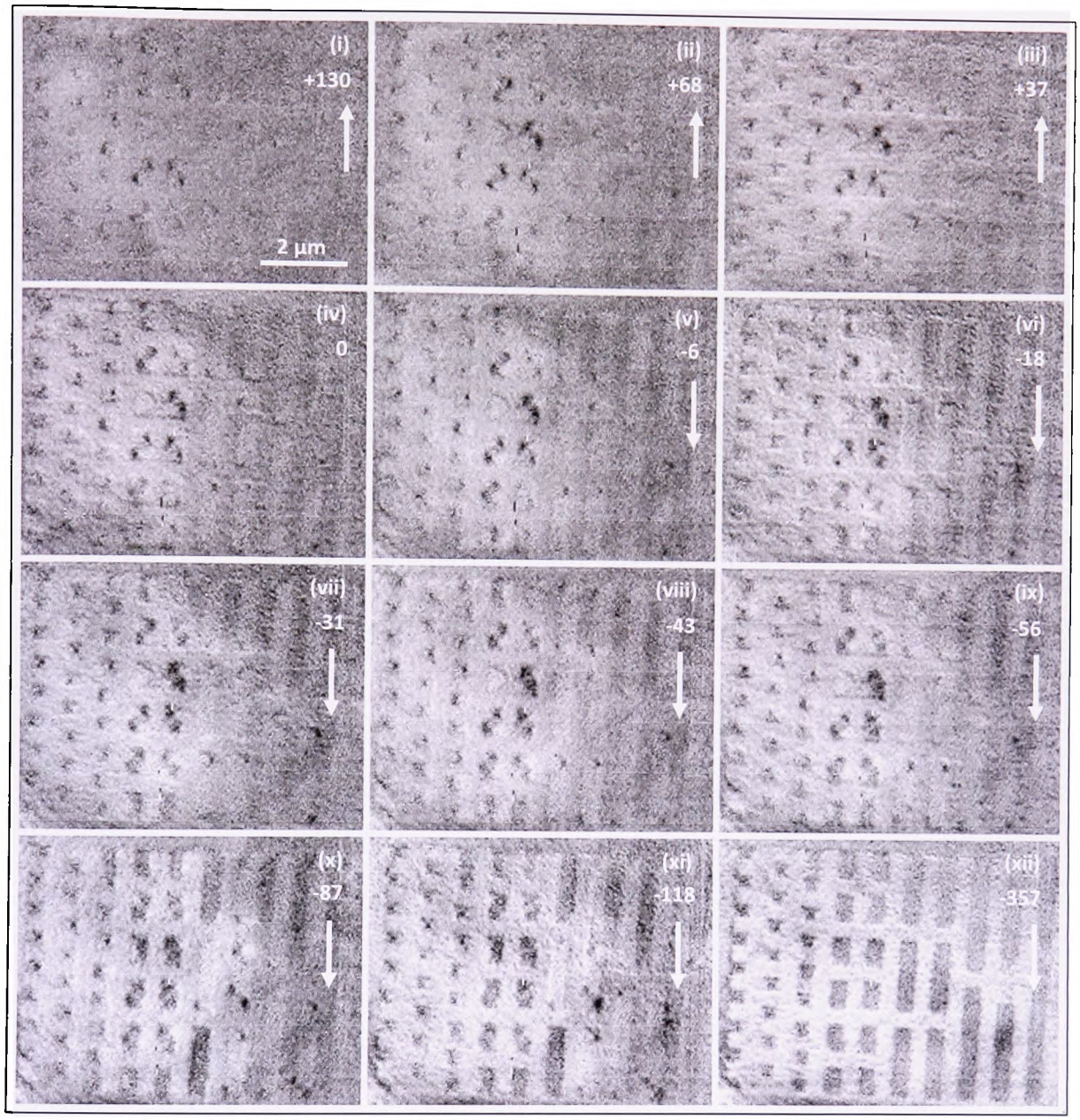

Figure A3.3.1*A* – Half of a magnetisation cycle showing the magnetic domain structure within small Fe elements with different aspect ratios. Each image compares the magnetic state at a particular field value (marked on the images in Oe) to that at **H** = +369 Oe. In (i) to (iii), the smaller elements begin to relax into flux closure states as **H** is reduced down to zero, indicated by the dark areas. The corresponding domains have their magnetisation aligned anti-parallel to **H**. As **H** becomes negative and approaches -357 Oe, the darker regions expand to cover larger areas as the domains grow in size. Domain structure can still be seen in the smallest squares even at the highest field, although the longer elements are saturated.

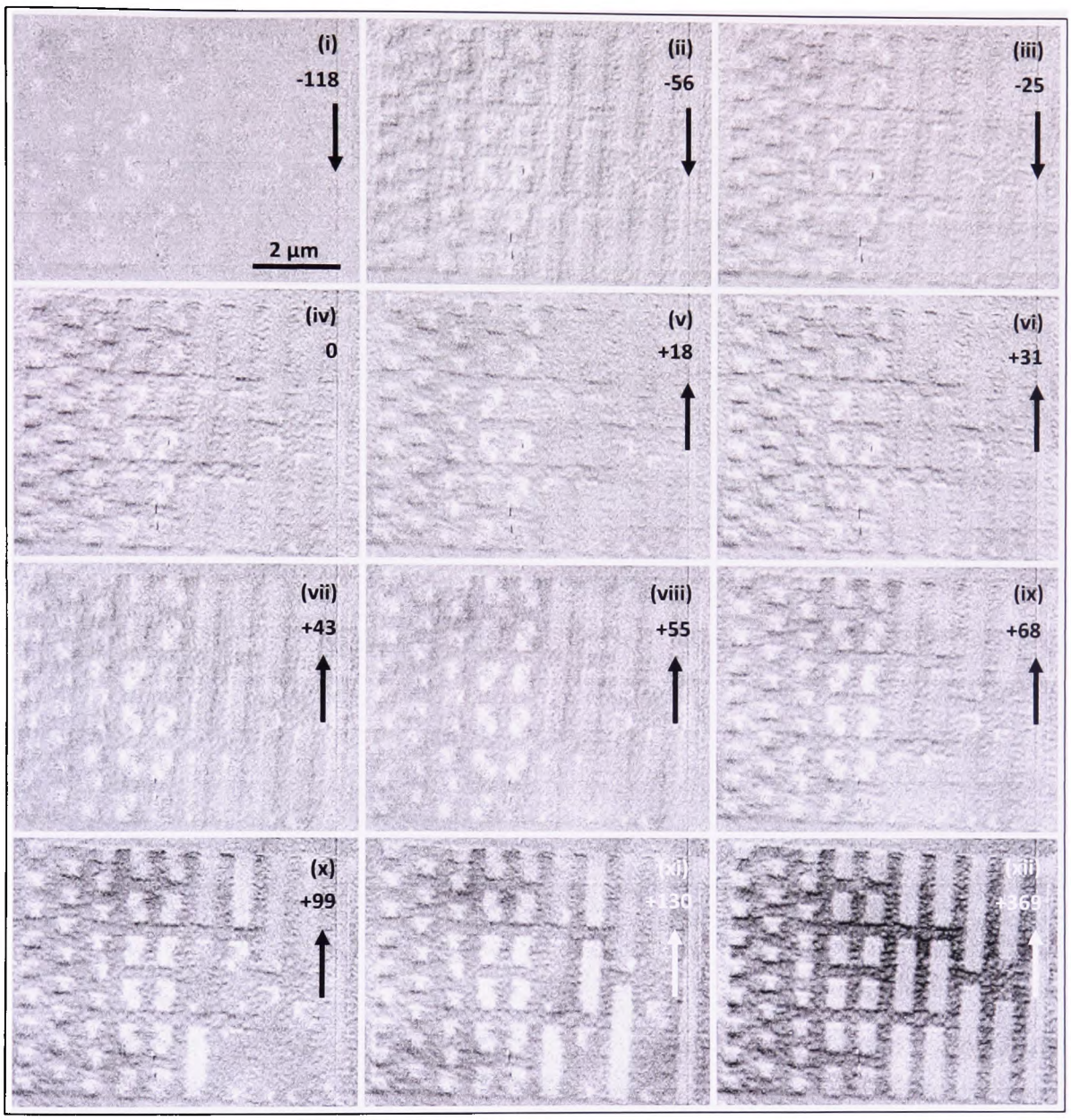

Figure A3.3.1*B* – In this second half of the magnetisation cycle, each image is compared with that recorded while applying a field of -357 Oe. The switching areas now appear brighter.

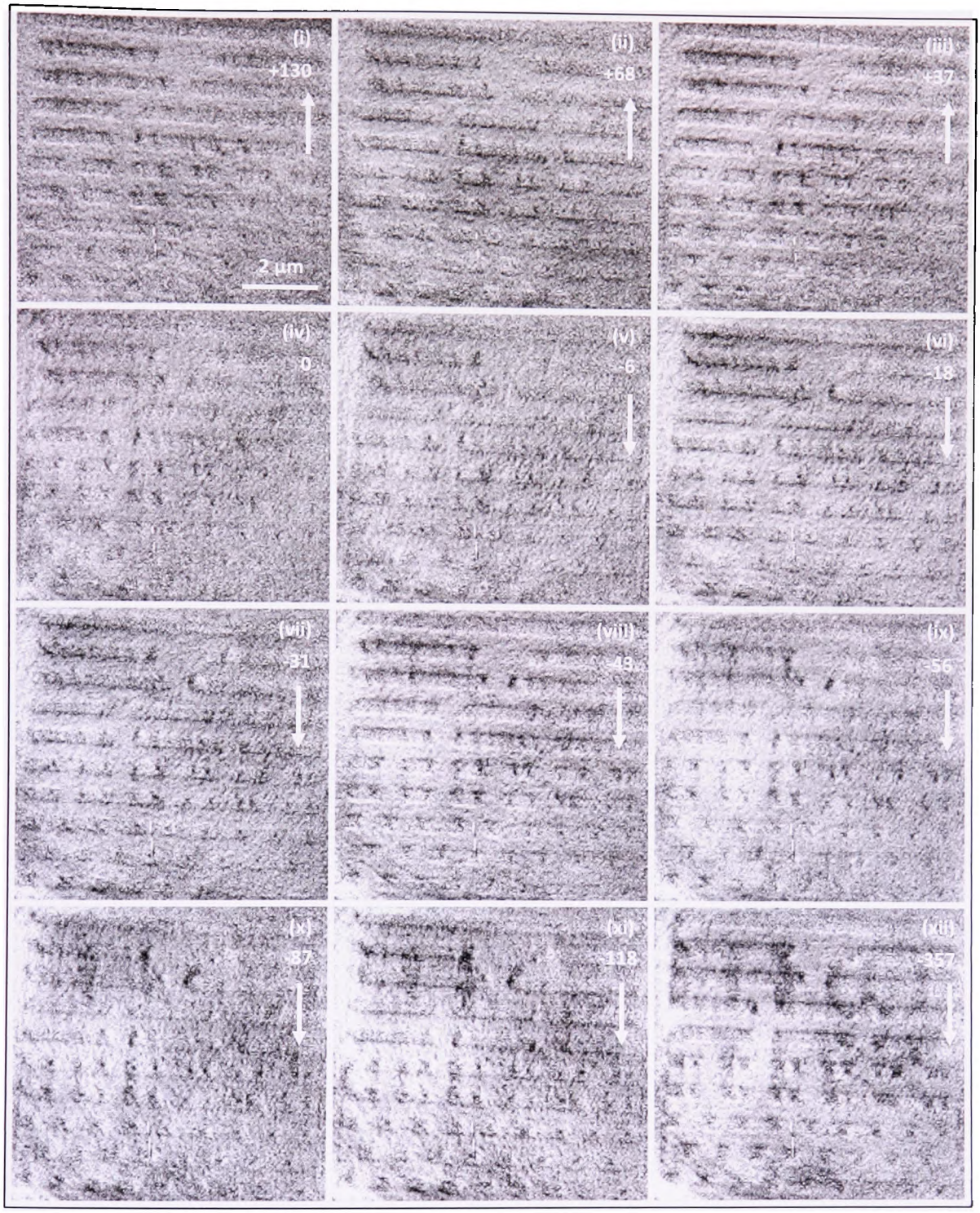

Figure A3.3.2*A* – Half of a magnetisation cycle showing the magnetic domain structure within small Fe elements with different aspect ratios. The images compare the domain structure at each field value (marked on the images in Oe) with that at +369 Oe. Small dark spots within some of the elements indicate vortex states. In (iv) to (xii), as **H** approaches -357 Oe, the darker regions, which are magnetised parallel to **H** begin to expand very slowly. In most images the changes are hardly noticeable. None of the elements become saturated and all contain areas where the magnetisation remains anti-parallel to **H**. In (ix) to (xii), some of the Fe-Ga grains that remain between the Fe strips are reversed, appearing as dark patches running vertically across the grating. This allows a direct interaction between neighbouring Fe strips. At no point does the longest strip at the very top of the pattern develop any strong contrast. This suggests that the magnetic structure did not change significantly during reversal of **H**.

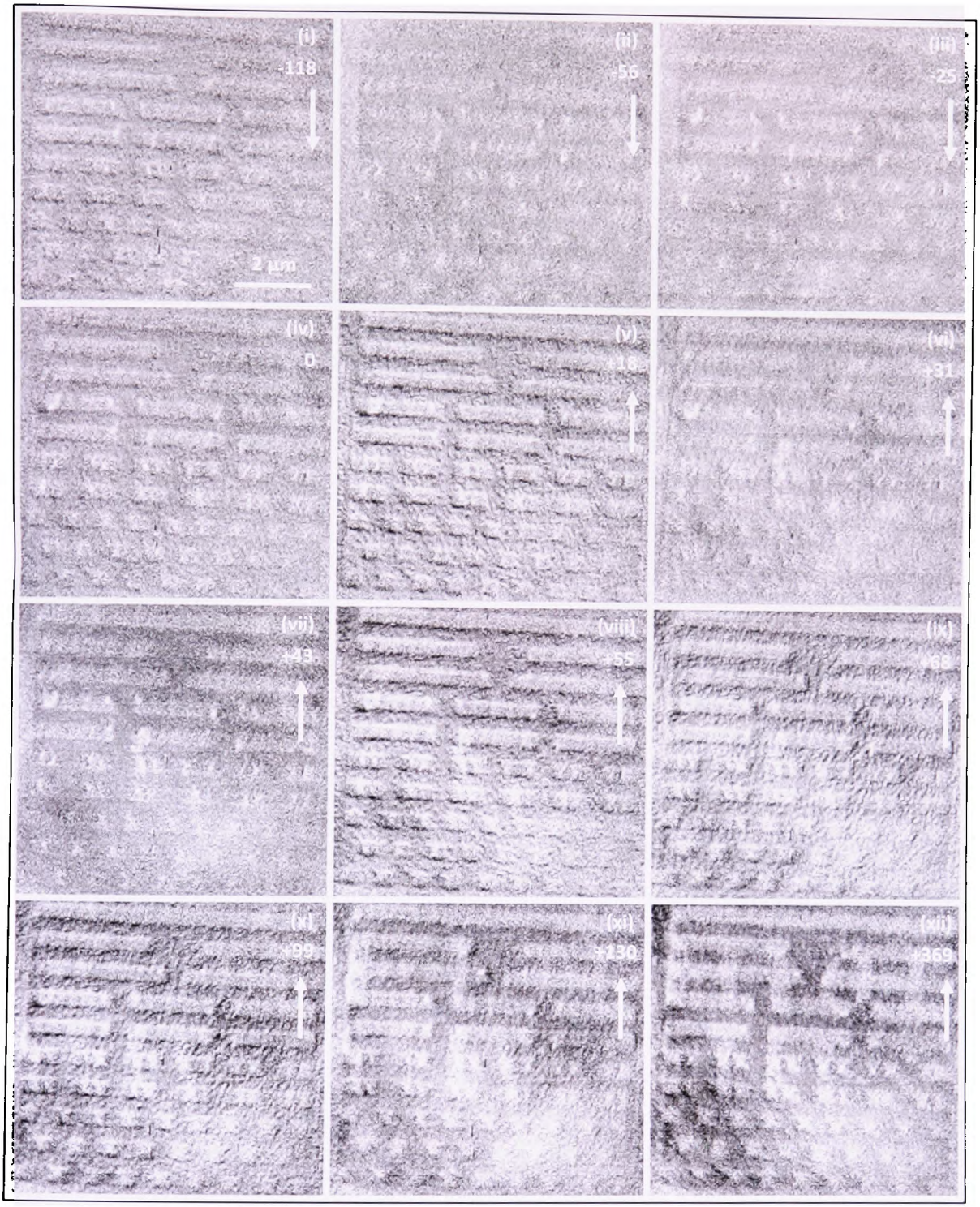

Figure A3.3.2*B* – The second half of the magnetisation cycle compares the magnetic structure occurring at each field value (shown in the images in Oe) with that at **H** = -357 Oe. The areas that reverse appear brighter.